Rotation and Impurity Studies in the presence of MHD activity and Internal Transport Barriers on TCV

PAR

Lucia Isabel FEDERSPIEL

(EPFL
ÉCOLE POLYTECHNIQUE
FÉDÉRALE DE LAUSANNE

Suisse
2014

"The universe is a pretty big place. If it's just us, seems like an awful waste of space."
Carl Sagan, Contact

"The cosmos is within us. We are made of star-stuff. We are a way for the universe to know itself."
Carl Sagan

"Life is about courage, and going into the unknown."
James Thurber, The secret life of Walter Mitty

Abstract

This thesis focuses on measurements of toroidal rotation and impurity profiles in improved plasma scenarios and in the presence of MHD activity. These experiments were performed on TCV, the Tokamak à Configuration Variable in Lausanne.

In TCV, plasma rotation is measured by the charge exchange recombination spectroscopy diagnostic (CXRS). The CXRS is associated with a low power diagnostic neutral beam injector (DNBI) that provides CX emission from the hot plasma core, without perturbing the plasma with additional torque. The beam is observed transversally by the CXRS diagnostic so that local ion temperature, density and intrinsic velocity measurements are obtained.

During this work, a pre-existing CXRS diagnostic was improved and automated. The three systems composing the present day CXRS2013 diagnostic cover the entire TCV radial midplane with up to 80 measurement locations separated by around 7mm with a time resolution ranging from 2-30ms. The main upgrades concerned the installation of new sensitive cameras, the overhaul of the toroidal HFS system, the extended-chord configuration and the automation of the acquisition and analysis processes. These new CXRS capabilities permitted the investigation of more complex scenarios featuring low intensity and/or fast events, like the low density electron internal transport barriers (eITBs) and the sawtooth (ST) instability discussed in this work.

For the first time, a comparison between rotation profiles measured over several sawtooth events and across a "canonical" sawtooth cycle has been undertaken in limited L-mode plasmas in this thesis, in order to identify the effect of the various ST phases on the rotation profile, and thus momentum transport. It is shown that the main ST effect on momentum is not simply a rotation profile flattening, as might be conjectured from their effect on electron temperature and density (consistent with a ST reconnection model), but results appear more complicated. The averaged rotation profiles obtained with the upgraded CXRS diagnostic show that ST restrict the maximum attainable $|v_{\varphi,max}|$ and that, in the plasma core, inside the q=1 surface, the rotation profiles are flattened and almost always display a small co-current contribution. It is this effect that results in the $1/I_p$ scaling observed in TCV limited L-mode plasmas. The co-current core contribution is identified to be related to the ST crash, whilst, during the quiescent ramp of the sawtooth period, a plasma recoil outside the mixing radius is observed. A high degree of momentum conservation, up to 80-90%, is measured, suggesting that a supplementary torque accompanying the ST crash is not required to explain the experimental observations. This study demonstrates the importance of including fast perturbating effects such as MHD modes in momentum transport models to build a complete picture, since they are likely to generate strong and rapid fluxes inside the plasma.

Extensive work on transport barriers has been performed to better understand the formation and characteristics of eITBs on TCV, using, for the first time, toroidal and poloidal rotation measurements. During this work, the poloidal rotation, E_r and the $E \times B$ shearing rate have been derived systematically from the asymmetry of the toroidal rotation measurements at the HFS and LFS. Since the position of the CXRS diagnostic view is at Z=0cm, two scenarios, a central barrier and a strong off-axis eITB, similar to previous targets investigated at Z=21cm, were developed to facilitate CXRS analysis during this thesis. The effect on the barrier strength and on the rotation profiles of several parameters, such as the central and total power, Ohmic current perturbations and MHD activity is investigated for both targets. The barrier strength

increases with cnt-CD applied on axis, higher total power and negative Ohmic perturbations. Indeed, for the strong co-CD off-axis eITB, a barrier in T_e at 7keV and n_e with a 23cm barrier width, confinement factor $H_{RLW} = 5.4$ and $|R/L_{Te}| = 45$ was achieved. No special dependence is found between the experimental $|\omega'_{E\times B}| \propto 10^4 s^{-1}$ and the confinement factor H_{RLW} or the maximum $|R/L_{Te}|$, confirming that on TCV, the barrier improvement is not linked to higher $|\omega'_{E\times B}|$ values. The experimental $E \times B$ shearing rates were compared with the growth rate of the most unstable mode for these discharges (TEM) obtained with the GENE code. The growth rate is found always one order of magnitude larger than the measured $E \times B$ shearing rates, confirming that the $E \times B$ shearing rate is not the cause of the formation of eITBs on TCV. This result supports previous theoretical studies concluding that the reversed shear profile is mainly responsible for the eITB formation. The comparison between the experimental ion temperature profiles and the results obtained with a quasi-linear model applied to TCV eITBs has shown some discrepancies. The $|R/L_{Ti}|/|R/L_{Te}|$ ratios measured at the barrier position are much lower than expected from the model, and no ion barrier is observed in these discharges. The installation of a new NB heating in 2015 will allow direct heating of the ion channel and may elucidate these discrepancies.

Version abrégée

Cette thèse porte sur les mesures de rotation toroïdale et de profils liés aux impuretés, dans les scénarios améliorés en présence d'une activité MHD. Ces expériences ont été réalisées sur TCV, le Tokamak à Configuration Variable, localisé à Lausanne.

Dans TCV, la rotation du plasma est mesurée via le diagnostic de spectroscopie à échange de charge (CXRS). Le CXRS est associé avec un injecteur de neutres (DNBI) de faible puissance qui assure les émissions de CX depuis le coeur chaud du plasma, sans perturber le plasma avec un couple. Le faisceau est observé de manière transversale par le diagnostic CXRS de manière à obtenir des mesures locales de la température ionique, de la densité et de la vitesse intrinsèque.

Pendant ce travail, un diagnostic CXRS pré-existant a été amélioré et automatisé. Les trois systèmes composant le diagnostic CXRS2013 couvrent la totalité du plan radial médian de TCV avec jusqu'à huitante points de mesures séparés de sept millimètres avec une résolution temporelle allant de deux à trente millisecondes. Les principales améliorations concernent: l'installation de nouvelles caméras sensibles, la refonte du système de mesure toroïdal du coté du champ magnétique fort (*high field side*, HFS), la configuration étendue des lignes de visée et l'automatisation des processus d'acquisition et d'analyse. Ces nouvelles fonctionnalités du CXRS permettent l'étude de scénarios plus complexes avec des évènements de faible intensité ou potentiellement rapides, tel que les barrières de transport internes (eITBs) de basse densité et les instabilités en dents de scie (*sawtooth*, ST) présentés dans ce travail.

Pour la première fois, une comparaison entre les profils de rotation mesurés sur plusieurs périodes ST ou pendant un cycle ST a été effectuée dans cette thèse pour des plasmas limités de type mode L (*L-mode*), afin d'identifier l'effet des différentes phases du ST sur le profil de rotation, et donc sur le transport de la quantité de mouvement. On a montré que le principal effet des ST sur la quantité de mouvement ne se limite pas uniquement à un aplatissement du profil de rotation, comme supposé par leur effet sur les profils de température et densité électroniques (en accord avec le modèle de reconnexion des ST). Les profils moyénnés obtenus avec le diagnostic CXRS amélioré montrent que les ST limitent la valeur maximale de $|v_{\varphi,max}|$ et que dans le coeur, à l'intérieur de la surface q=1, les profils de rotation sont aplatis et présentent une petite contribution dans le sens du courant. Cet effet contribue à ce que $|v_{\varphi,max}|$ soit proportionnel à $1/I_p$ pour les plasmas limités de type mode L de TCV. La contribution dans le sens du courant au coeur du plasma est identifiée comme étant liée à l'effondrement du ST, tandis que pendant la calme rampe de la période ST, un recul du plasma au dehors du rayon de mélange (*mixing radius*) est observé. Un haut degré de conservation de la quantité de mouvement jusqu'à 80-90% est mesuré, ce qui suggère qu'un couple supplémentaire accompagnant l'effondrement ST n'est pas nécessaire pour expliquer les observations expérimentales. Cette étude montre l'importance d'inclure les effets d'événements perturbateurs rapides, comme les modes MHD, dans les modèles du transport de la quantité de mouvement, afin de construire une image complète, car ceux-ci peuvent générer des flux rapides et forts dans le plasma.

Un travail intensif sur les barrières de transport a été réalisé afin de mieux comprendre la formation et les caractéristiques des eITBs sur TCV, en utilisant, pour la première fois, les mesures de rotation toroïdale et poloïdale. Pendant ce travail, la rotation poloïdale, E_r et le taux de cisaillement $E \times B$ ont été systématiquement déduits de l'assymétrie des mesures de rotation poloïdale à l'HFS et LFS. Comme la position du CXRS se trouve à Z=0cm, deux scénarios principaux, une barrière centrale et une

forte eITB hors-axe (*co-CD off-axis eITB*), ont été développés pour faciliter l'analyse CXRS durant cette thèse. Les effets, sur la force de la barrière et sur les profils de rotation, de plusieurs paramètres, tel que la puissance centrale et totale, les perturbations du courant ohmique et l'activité MHD ont été étudiés pour les deux cibles. Il a été observé que la force de la barrière augmente avec du courant EC appliqué dans le sens opposé du courant (cnt-CD) sur l'axe, une puissance totale augmentée et des perturbations ohmiques négatives. En effet, pour la forte eITB, une barrière en n_e et à $T_e = 7keV$ avec largeur de 23cm, un facteur d'amélioration du confinement $H_{RLW} = 5.4$ et $|R/L_{Te}| = 45$ a été atteint. Aucune tendance particulière n'a été trouvée entre les valeurs expérimentales de $|\omega'_{E \times B}| \propto 10^4 s^{-1}$ et le facteur de confinement H_{RLW} ou le maximum de $|R/L_{Te}|$, confirmant qu'en TCV l'amélioration du confinement n'est pas liée à des valeurs plus grandes de $|\omega'_{E \times B}|$. La valeur expérimentale du taux de cisaillement $E \times B$ a été comparée avec le taux de croissance des modes les plus instables (TEM) pour ces plasmas, obtenus avec le code gyro-cinétique GENE. Le taux de croissance était toujours un ordre de grandeur plus grand que $|\omega'_{E \times B}|$. Ce résultat confirme l'effet négligeable du taux de cisaillement $E \times B$ sur la formation de ces barrières internes et supporte les études théoriques précédantes concluant que le profil de cisaillement inversé est le principal responsable de la formation des eITB sur TCV. La comparaison entre les profils expérimentaux de température ionique avec les résultats d'un modèle quasi-linéaire appliqué aux eITBs de TCV, révèle quelques désaccords. Les rapports $|R/L_{Ti}|/|R/L_{Te}|$ mesurés à la position de la barrière sont bien plus petits que ceux prédits par le modèle, et aucune barrière ionique n'est observée pour ces décharges. L'installation du nouveau chauffage par injection de neutres (NBH) pour 2015, va permettre de directement chauffer le canal ionique et pourrait ainsi clarifier ces désaccords.

Mots clés: fusion nucléaire, plasma, tokamak, TCV, rotation intrinsèque, rotation toroïdale, rotation poloïdale, impureté, ions, temperature, densité, transport de quantité de mouvement, échange de charge, spectroscopie, diagnostic, CXRS, carbone, activité MHD, sawtooth, dents de scie, instabilité, TEM, barrière de transport interne, eITB, scénario de confinement amélioré, courant bootstrap, courant ohmique, chauffage, ECH, ECCD, courant induit, cisaillement inversé, profil du facteur de sécurité, taux de cisaillement $E \times B$, taux de croissance.

Sintesi

Questa tesi si concentra sulla misurazione di profili di rotazione toroidale ed impurità in scenari ottimizzati ed in presenza di attività MHD. Questi esperimenti sono stati eseguiti su TCV, il Tokamak a Configurazione Variabile di Losanna.

In TCV, la rotazione del plasma è misurata tramite la diagnostica di spettroscopia di scambio carica (CXRS). Il CXRS funziona in associazione ad un iniettore di un fascio di neutri a bassa potenza (DNBI), che assicura la presenza di emissione di scambio carica nel plasma, senza perturbare il plasma stesso imprimendo un momento aggiuntivo. Il DNBI è osservato trasversalmente dal CXRS, in modo da ottenere misure locali della temperature, densità e velocità intrinseca ionica.

Durante il corso di questa tesi, una diagnostica di CXRS preesistente è stata migliorata ed automatizzata. I tre sistemi che compongono la diagnostica CXRS2013 coprono l'intero piano mediano radiale in TCV, con 80 punti di misura lontani 7 mm gli uni dagli altri con una risoluzione temporale che varia da 2 a 30 ms. I miglioramenti più importanti consistono nell'installazione di nuove camere con migliore sensibilità, nella revisione del sistema toroidale della zona di campo magnetico più elevato (HFS), nella configurazione estesa delle linee di vista e nell'automatizzazione del sistema di acquisizione ed analisi. Queste nuove caratteristiche del CXRS permettono lo studio di scenari più complessi, inclusi eventi a bassa intensità e/o alta velocità, come le barriere di trasporto interne elettroniche (eITBs) a bassa densità, e l'instabilità a denti di sega (*sawtooth*, ST), che saranno presentate in questo lavoro.

Per la prima volta, in questa tesi è stato effettuato un confronto tra i profili di rotazione misurati su diversi periodi di attività ST o durante un ciclo ST per plasmi L-mode limitati (*limited*), in modo da identificare l'effetto delle varie fasi di un ST sui profili di rotazione e sul transporto del momento angolare. È stato mostrato che il principale effetto dei ST sul momento angolare non consiste soltanto in un semplice appiattimento dei profili, come suggerito dal loro effetto sui profili elettronici di temperatura e densità (in accordo con il modello di riconnessione dei ST), ma esso risulta essere più complesso. I profili mediati di rotazione ottenuti con la diagnostica CXRS migliorata mostrano che i ST limitano la velocità massima $|v_{\varphi,max}|$ raggiungibile e che, nel cuore del plasma, all'interno della superficie q=1, i profili di rotazione sono appiattiti e quasi sempre mostrano una piccola contribuzione nel senso della corrente. Questo effetto conduce ad un rapporto di scala $1/I_p$ osservato per i plasmi L-mode limitati di TCV. La contribuzione nel senso della corrente è identificata come legata al crollo del dente di sega, mentre durante le lente rampe del periodo ST, un rinculo del plasma al di fuori del raggio di mescolamento (*mixing radius*) è osservato. Un alto grado di conservazione del momento angolare fino a 80-90% è misurato. Esso suggerisce che un momento supplementare accompagnante il ST crash non è necessario per spiegare queste osservazioni sperimentali. Questo studio dimostra l'importanza di includere gli effetti di rapidi perturbatori, come i modi MHD, nei modelli del trasporto di momento in modo da costruire un'immagine completa, dato che essi possono generare forti e rapidi flussi all'interno del plasma.

È stato condotto un esteso lavoro di studio sulle barriere di trasporto per migliorare la comprensione della formazione e delle caratteristiche degli eITBs in TCV, usando, per la prima volta, misurazioni toroidali e poloidali della rotazione. Nel corso di questo lavoro, la rotazione poloidale, E_r e lo shear $E \times B$ sono stati derivati sistematicamente a partire dalla asimmetria della rotazione toroidale tra la zona di forte campo magnetico (HFS) e quella di debole campo (LFS). Siccome l'orientazione della diagnostica

CXRS permette di studiare il plasma attorno a Z=0cm, nel corso di questa tesi due scenari, una barriera centrale ed un forte eITB fuori asse (*co-CD off-axis eITB*), simili a precedenti target studiati a Z=21cm, sono stati sviluppati per facilitare l'analisi con il CXRS. L'effetto sulla forza della barriera e sui profili di rotazione di numerosi parametri, come la potenza deposta nella parte centrale e la potenza totale, le perturbazioni di corrente ohmica e l'attività MHD, è stato investigato per entrambi i target. Si è osservato che la forza della barriera aumenta se viene applicata sull'asse magnetico una corrente EC nel senso opposto alla corrente del plasma (cnt-CD), se si ha una potenza totale maggiore e se si hanno perturbazioni ohmiche negative. Infatti, per il caso del forte eITB, si è ottenuta una barriera in n_e e in T_e a 7keV con una larghezza di 23cm, un fattore di confinamento $H_{RLW} = 5.4$ e $|R/L_{Te}| = 45$. Nessuna particolare tendenza è stata riscontrata tra i valori sperimentali di $|\omega'_{E \times B}| \propto 10^4 s^{-1}$ ed il fattore di confinamento H_{RLW} od il massimo valore di $|R/L_{Te}|$. Questo conferma che su TCV il miglioramento della barriera non è legato a dei valori più elevati di $|\omega'_{E \times B}|$. I valori sperimentali del shear $E \times B$ sono stati confrontati con i tassi di crescita dei modi più instabili (TEM), predetti tramite simulazioni girocinetiche con il codice GENE. Il tasso di crescita trovato è di un ordine di grandezza più grande rispetto lo shear $E \times B$. Questo risultato conferma che lo shear $E \times B$ non è la causa della formazione di barriere elettroniche a TCV. Inoltre questo risultato si allinea a studi precedenti che sostengono come lo shear magnetico inverso sia il principale responsabile della formazione degli eITBs. Infine, un confronto fra i profili ionici di temperatura con i risultati ottenuti tramite un modello quasi-lineare applicato agli eITB in TCV ha rivelato alcune discrepanze. I rapporti $|R/L_{Ti}|/|R/L_{Te}|$ misurati alla posizione della barriera sono molto inferiori rispetto a quelli predetti dal modello, e nessuna barriera ionica è osservata in questi plasmi. L'installazione di un nuovo sistema di riscaldamento tramite fascio di neutri (NBH) per il 2015 permetterà il riscaldamento diretto del canale ionico e potrebbe chiarire queste discrepanze.

Parole chiave: fusione nucleare, plasma, tokamak, TCV, rotazione intrinseca, rotazione toroidale, rotazione poloidale, impurità, ioni, temperatura, densità, trasporto del momento angolare, scambio carica, spettroscopia, diagnostica, CXRS, carbonio, attività MHD, dente di sega, instabilità, TEM, barriera di trasporto interna, scenario di confinamento ottimizzato, corrente bootstrap, corrente ohmica, riscaldamento, ECH, ECCD, shear inverso, profilo di q, tasso di $E \times B$ shear, tasso di crescita.

Contents

CONTENTS

Chapter 1

Introduction

After the Fukushima accident in 2011, the world has renewed a fear of nuclear power, immediately associating dramatic images with any energy system, or device, advertising the term *nuclear*. When I talk with friends and people outside the scientific field (and many inside it too...), there are few people that are really able to distinguish nuclear fission and nuclear fusion.

Nuclear fission of heavy elements (often uranium), disintegrate into lighter elements after collision with a neutron particle. The elevated energy release coming from each collision has been exploited for over 60 years by commercial fission reactors, presently spread around the world. It has to be recalled that, even in Switzerland, land of mountains and lakes, 40% of the total electrical energy comes from fission energy. Nevertheless, this source of energy suffers from many drawbacks such as a limited availability of uranium, long lifetime radioactive waste production, related problematic waste storage and the danger of the intrinsically unstable fission reaction (chain reaction). This latter can lead to a possible loss of the reaction control (and to a related overheating) as a consequence of unpredictable events (like the recent earthquake and tsunami in Japan) or any improper actions from the operating teams (such as that in Chernobyl). To this list must be added the problem of nuclear weapon proliferation that remains an important concern among any State or potential terrorist-like association that wants to obtain or pretends to already be part of the present day world hegemony.

Fusion is the opposite process to nuclear fission, where light nuclei (such as hydrogen isotopes) fuse together to form heavier elements, with consequent release of energy. Nuclear fusion is the basic process governing the solar energy production and what makes our Earth habitable and our existence possible. It is interesting to ponder that, since the universe was essentially born as light element gases, virtually everything around us is the result of Fusion. This form of energy on Earth, after decades of study, is still at the research phase, but has achieved considerable progress. This energy source has several advantageous features: higher safety level for a power plant (explosive events are excluded because of the low fuel quantities involved and the impossibility of a chain reaction), short-lived radioactive waste (mainly coming from the vessel elements) and practically unlimited availability of fuel, which may be obtained

directly from oceanic water (and rainwater too).

To sustain the future world energy demand, a pragmatic solution will need to employ a mixture of several energy sources. In parallel to the so called "renewable sources" such as hydroelectric, geothermic, wind and photoelectric, both nuclear energy sources merit being pursued. One of the main objectives that mankind must attain, on a relatively short time scale, to ensure a healthy and sustainable future for future generations, is to decarbonise our society using all possible means.

Hereafter, our discussion will focus on the promise of poorly understood nuclear fusion, interestingly enough, the source of more or less everything.

1.1 Nuclear fusion

Fusion is the basic process taking place in the core of any star of the universe, including our Sun. The dominant fusion reactions occurring in the Sun are the following:

$$^{1}_{1}H + ^{1}_{1}H \rightarrow ^{2}_{1}D + e^{+} + \nu_e \tag{1.1}$$

$$^{2}_{1}D + ^{1}_{1}H \rightarrow ^{3}_{2}He + \gamma \tag{1.2}$$

$$^{3}_{2}He + ^{3}_{2}He \rightarrow ^{4}_{2}He + 2^{1}_{1}H \tag{1.3}$$

In all these reactions the final total mass loss is converted to energy radiated toward the external layers of the Sun through successive absorption and re-emission processes. In order to obtain a commercial source of energy on Earth, different possible fusion reactions have been considered and analyzed. Among them the D-T reaction is the currently envisioned for the first commercial fusion reactor, since it displays the largest cross section at the lowest energy of the reacting nuclei and is therefore the most efficient reaction. This reaction fuses two isotopes of hydrogen, D and T, to form helium and a neutron:

$$^{2}_{1}D + ^{3}_{1}T \rightarrow ^{4}_{2}He(3.5 \ MeV) + ^{1}_{0}n(14.1 \ MeV) \tag{1.4}$$
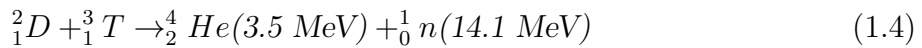
Because of quantum mechanical tunneling, D-T fusion occurs at energies somewhat less then that required to "overcome" the Coulomb potential barrier (i.e. the repulsion force of positively charged nuclei). The critical ignition temperature of this reaction lies above a few keV ($10^{7}K$).

Deuterium is available in bulk quantities from ordinary water, whereas tritium is not present in nature because of its short radioactive half-life (12.3 years). An attractive scheme for generating the necessary tritium is to surround a fusion reactor with a lithium blanket (breeder blanket layer), where fission reactions induced by the fusion-generated neutrons result in the generation of tritium. The reactions exploited are therefore:

$$^{7}_{3}Li + ^{1}_{0}n \rightarrow ^{4}_{2}He + ^{3}_{1}T + ^{1}_{0}n - 2.47 \ MeV \tag{1.5}$$

$$^{6}_{3}Li + ^{1}_{0}n \rightarrow ^{4}_{2}He(2.05 \ MeV) + ^{3}_{1}T(2.73 \ MeV) \tag{1.6}$$
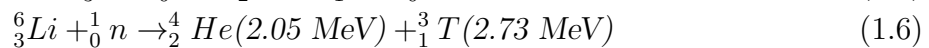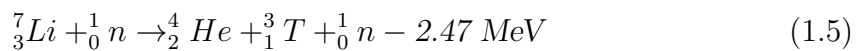
The relative abundances of the two lithium isotopes $^{7}_{3}Li$ and $^{6}_{3}Li$ are 92.6% and 7.4% respectively. Natural resources of deuterium and lithium isotopes dissolved in the sea

water are estimated to meet the global energy requirements for several million years at todays annual global electricity consumption rates. Thus, nuclear fusion promises to be a practically inexhaustible source of energy.

1.2 Magnetic confinement

At the temperature required for fusion, most substance will exist as a completely ionized gas, the so called plasma. Globally, the electrostatic charge of the ions is neutralized by an equal number of electrons. Locally, the charged particles are subjected to the Lorentz force, which bends the particle trajectory to a helical one around the magnetic field lines (see Fig.1.1). The radial extent, or gyro-radius, of this trajectory for a particle of mass m and charge q is given by:

$$\rho = \frac{v_\perp}{\Omega_c} = \frac{mv_\perp}{qB} \tag{1.7}$$

where Ω_c is the cyclotron angular frequency and $v_\perp$ is the velocity of the particle perpendicular to the magnetic field B. In the case of a homogeneous velocity distribution, $v_\perp$ can be expressed by the plasma temperature T as $v_\perp = \sqrt{2kT/m}$ with the Boltzmann constant k. This effect is used as a method to protect the wall of a reactor
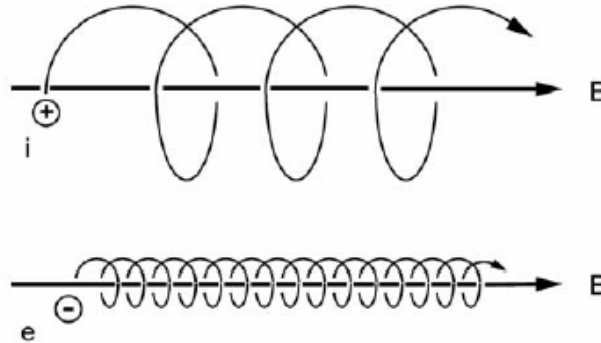
Figure 1.1: Trajectories of charge particles in a homogeneous magnetic field. Notice the larger gyro radius for the ion particles.

from the high temperatures of the fusion plasma, by introducing a gap between the outer plasma surface and the reactor wall. The presence of the magnetic field highly restricts the perpendicular direction of motion, whereas the parallel is unaffected (see Fig.1.1). Collisions among particles, however, introduce a diffusive perpendicular cross field transport of particles and also give rise to a resistivity in the parallel direction

1.3 The tokamak principle

A straight magnetic field configuration suffers from plasma losses at both ends. This can be avoided by either compressing the plasma column at its extremities with an

additional magnetic field (the so called *magnetic bottle*) or by reconnecting one extremity of the magnetic field lines with the other in form of a torus. Only this latter configuration confines sufficiently well particles with high velocities parallel to the magnetic field lines and is used for the so called *Tokamak* design, the Russian acronym for "Toroidalnaja Kamera s Magnitnymi Katuskami" or "Toroidal chamber with magnetic coil" (for a detailed description see also [1]).

The reconnection of the magnetic field lines in the form of a torus leads to a bending of them and hence creates an inhomogeneity in their distribution, i.e a compression of the field lines on its inner side and a decompression on the outer side. This curvature and gradient of the field leads to drift motions of ions and electrons in opposite vertical direction, resulting in a separation of charge and consequently creates an electric field. The electric field is perpendicular to the magnetic field and causes an outward $E \times B$ drift of the entire plasma (see Fig.1.2). This cause of the outward drift is canceled
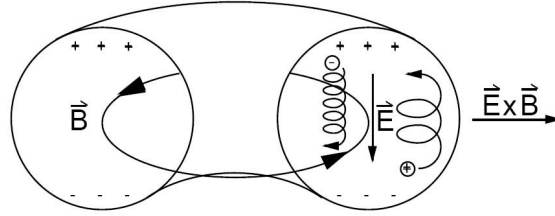
Figure 1.2: Particle drift motion in a toroidal magnetic field.

by a toroidal plasma current I_p producing a poloidal magnetic field B_{pol} which, together with a toroidal magnetic field B_{tor}, leads to a twisted magnetic field topology (see Fig.1.3). An additional vertical magnetic field B_v (where $B_v < B_{pol} < B_{tor}$) is
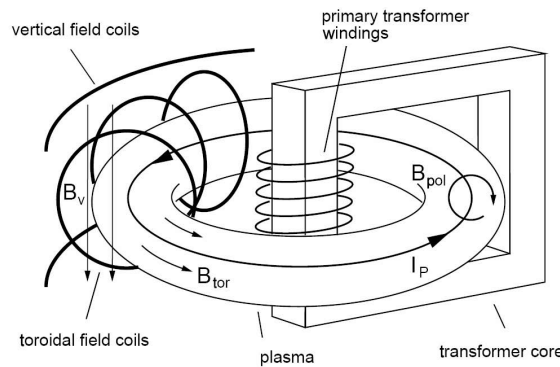
Figure 1.3: Schematic of the coil configuration of a tokamak.

required to attain the balance in the radial forces. The plasma pressure gradient ∇p gives rise to a radial expansion of the plasma ring and therefore to an outward directed force that is canceled out by the Lorentz force resulting from B_v.

In a tokamak, the primary transformer coil is used to drive the inductive plasma current and to heat the plasma. The central solenoid acts as the primary circuit and the

plasma ring as the secondary circuit with a single winding. This has the advantage of retaining the toroidal symmetry, but the induction of the plasma current allows only pulsed operation, which is undesirable for a future fusion power plant based on the tokamak principle. Thus, a major effort is being undertaken to develop alternative ways of driving the plasma current, such as beam-wave driven or pressure gradient driven currents.

The magnetic structure in a tokamak consists of an infinite set of nested toroidal magnetic surfaces centered on the magnetic axis, the so called flux surfaces. These surfaces represent regions of constant pressure and poloidal magnetic field flux ψ. In this axisymmetric configuration, heat and particles are transported much faster along the magnetic field lines than across the field. Therefore to first approximation, temperature and density are uniform on magnetic surfaces and may thus be described as a function of a radial coordinate, that labels the flux surfaces. The radial flux label that will be used throughout this work to describe the ion profiles is the normalized poloidal flux:

$$\rho_\psi = \sqrt{\frac{\psi - \psi_0}{\psi_a - \psi_0}} \tag{1.8}$$

where ψ is the poloidal flux and ψ_0, ψ_a the poloidal flux at the magnetic axis and plasma boundary respectively. The twist of the field lines in each surface is characterized by the safety factor q, given by:

$$q = \frac{\Delta\varphi}{2\pi} = \frac{rB_\varphi}{R_0 B_\theta} \tag{1.9}$$

where r and R_0 are the plasma minor and major radii and B_φ and B_θ are the toroidal and poloidal magnetic fields. Here $\Delta\varphi$ denotes the change in toroidal angle φ associated with a change of 2π in the poloidal angle, when following the field lines on a magnetic surface. The profile of q is mainly determined by B_θ, or the current density j_p (see Sec.1.7), and plays a crucial role in the magneto-hydrodynamic (MHD) stability. Usually the radial q profile has its minimum value at, or close to, the magnetic axis and increases outwards. A non-monotonic q profile is observed to be related to improved confinement and to the formation of internal barriers (as will be discussed in Sec.1.7 and Chapter 5). For rational values of $q = m/n$, when the field lines close on themselves after m poloidal loops and n toroidal loops, the development of resonant magnetic perturbations is facilitated. These latter can cause the onset of MHD instabilities [2, 3] leading to the destabilization of parts or even of the whole plasma. These events can develop on a fast time scale ($\cong$ms), decrease the plasma performance and can damage components of the tokamak, which makes it indispensable to study their very nature. In this work, some of these MHD modes (mainly sawtooth inside q=1, 2/1 and 3/1 modes), will be observed during the study of the various discharges and their effect on plasma rotation (for an introduction to plasma rotation see Sec.1.8) and impurity profiles will be investigated.

1.4   Plasma shape and boundary

In modern tokamaks additional poloidal field coils carrying a toroidal current are used for shaping the poloidal cross section of the plasma. It has been found that the plasma shape also influences the stability and transport properties of the plasma. Elongated and triangular plasma shapes, for example, exhibit superior properties compared to circular plasmas [1, 4, 5, 6]. The elongation κ is defined as the ratio of the vertical to the horizontal semi-axis of the plasma, while the triangularity δ is a parameter describing the deformation of the plasma cross section into a D. Negative values of δ correspond to a plasma whose D-shaped cross-section is left to right inverted.

Another important task for a plasma confining device is to control the interaction of the plasma with the first wall. There are two main configurations used to separate the plasma from the vacuum vessel wall. In the first configuration the outer boundary of the plasma (last closed flux surface, LCFS) is defined using a material limiter (see Fig.1.4.a). In the second configuration the magnetic field structure is modified to induce separation between the inner closed flux surfaces and the outer region with open field lines that can intercept the vessel walls (see Fig.1.4.b). This scrape off layer (SOL) region constitutes the interface between the confined plasma and the first wall. The separatrix surface is designed to transport heat and particles away from the main plasma region to an especially designed wall interaction region known as a divertor.
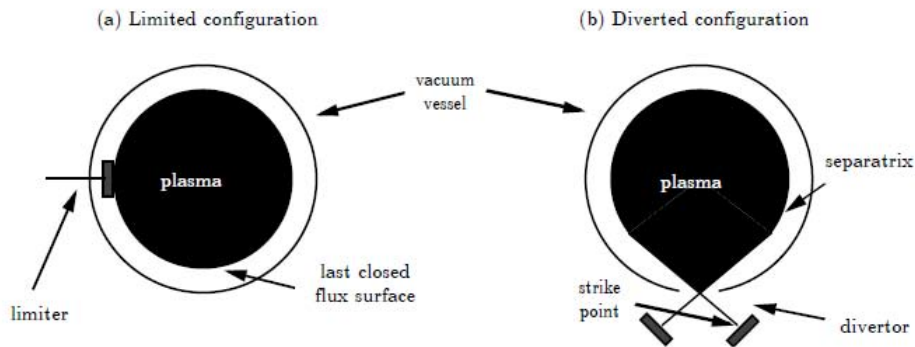
Figure 1.4: The two plasma boundary configurations in a tokamak. a) A limiter scrapes the plasma off and defines the last closed flux surface (LCFS). On TCV the walls are limiting the plasma in this configuration. b) In diverted configurations the LCFS is determined through additional magnetic coils that shape the magnetic flux surfaces such as to create an X-point, where the poloidal magnetic field has a null. The magnetic flux surface passing through this X-point is called the separatrix. The region below the X-point may be loosely defined as the divertor. The points at which the separatrix strikes the wall are known as the strike points.

The *Tokamak à Configuration Variable* (TCV) at the Centre de Recherches en Physique des Plasmas (CRPP) in Lausanne is well suited to study a large variety of plasma shapes in limited and diverted configurations. A detailed description of this experimental facility is given in Chapter 2.

1.5 External plasma heating

Owing to the plasma resistivity η, the toroidal plasma current also heats the plasma. The Ohmic heating power density is given by:

$$P_{ohmic} = \eta j_p^2 \tag{1.10}$$

where j_p is the plasma current density. The plasma resistivity, however, decreases with increasing plasma temperature as $T^{-3/2}$ and the maximum current density j_p is limited by MHD stability (see [1, 2, 7]). The plasma temperature reached by Ohmic heating is not sufficient to start and sustain a fusion reaction. Thus, additional plasma heating is required.

One method of additional plasma heating consists of injecting energetic particles into the plasma by means of neutral beams of hydrogen or deuterium. The neutral particles travel unaffected by the magnetic field until they collide with ions and electrons in the plasma, which will ionize them. The beam attenuation depends on the plasma density profile and the beam geometry. The resulting ions and electrons are afterward confined by the magnetic field and deposit their energy via further collisions to the rest of the plasma.

A second method of additional heating is the injection of high energetic electromagnetic waves into the plasma. Once the wave has coupled to the plasma, its energy is absorbed at fairly high rate at the resonance frequencies, first or higher harmonics, of ion or electron cyclotron frequencies (like on JET [8] and on TCV [9] respectively) or lower hybrid frequency (like on Tore Supra [10]).

1.6 Power plant concept and improved scenarios

As observed in Sec.1.1, each D-T nuclear fusion reaction delivers an amount of energy $\Delta E = E_\alpha + E_n = 17.6 MeV$ shared between the helium nucleus (α-particle) and the neutron.

In a future fusion power plant the plasma temperature is assumed to be maintained by energy transfer from the α-particles (created by the fusion process) to the combustibles D and T. The magnetic field has to confine the charged α-particles long enough so that they can transfer their energy via collisions and equilibrate their energy with the bulk plasma before leaving the plasma. In contrast to the α-particles, the neutrons leave the plasma without any interaction and should be absorbed in a blanket surrounding the reactor vessel to bread the tritium from lithium (see Eq.1.5 and 1.6). The heat is carried away by a suitable coolant and used to drive steam turbines.

A power balance gives an estimate for the plasma parameters required for a fusion power plant and culminates in the triple product or Lawson criterion [1]:

$$n_e T \tau_E > 5 \times 10^{21} \; keV \; s \; m^{-3} \tag{1.11}$$

where T and n_e are the plasma temperature and density, and τ_E the energy confinement time. This relation shows that in order to produce enough energy for commercial

interest we need to satisfy three conditions. The first condition is to attain a high temperature T (several tens of millions of degrees Celsius, i.e. a plasma state). The second condition is that the density n_e is sufficiently high. Finally, it is necessary that the plasma can keep its energy for a time τ_E sufficient for the reaction rate to generate more power than is supplied to it.

Present-day tokamaks have demonstrated the feasibility of the temperatures and densities required for break-even and ignition, the confinement time remaining the parameter to be increased further. As τ_E increases with device size and total plasma current, the worldwide magnetic fusion community has come together around a single, large device constituting the next generation of tokamaks. The ITER tokamak, the first prototype of fusion reactor, currently under construction in France (see Fig.1.5.a and b), is designed to exceed the break-even condition and produce ten times more fusion power than the required input power.
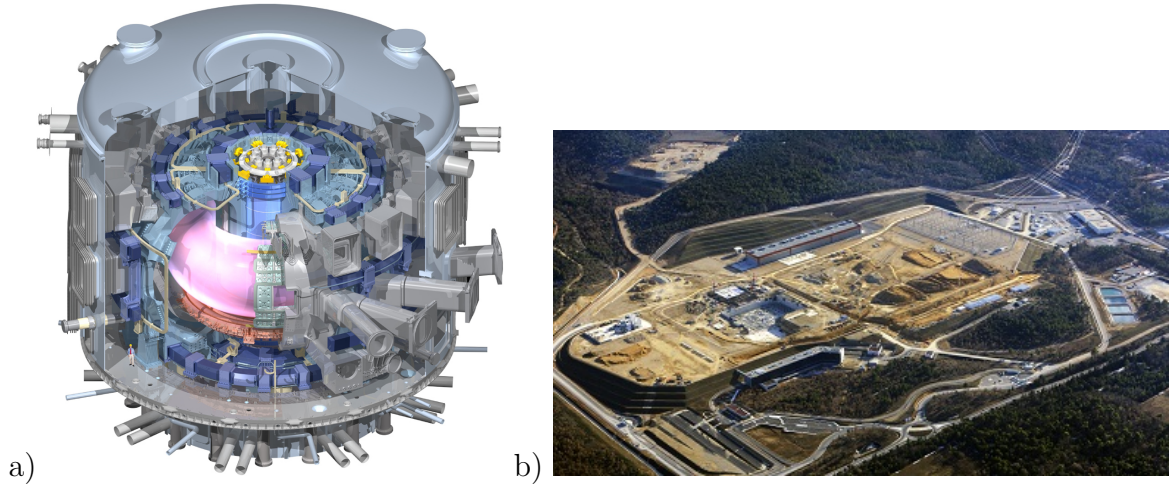
Figure 1.5: a) The ITER tokamak design. The first plasmas are planned for 2020. b) Present picture of the ITER platform in Saint-Paul-les-Durance (Cadarache). (Source: ITER Organisation, 2013)

We recall that high plasma power can be achieved by auxiliary heating and by energy transfer from the α-particles. The dependence of Eq.1.11 on the energy confinement time gives reason to develop the so-called "improved plasma scenarios", such as high-confinement mode (H-mode) or plasmas with internal transport barriers (ITB), in which radial transport properties decrease significantly, minimizing the power loss of the plasma.

As we will discuss in Chapter 5, electron and ion ITB scenarios feature high core confinement combined with a non-negligible self-generated current fraction, the so called bootstrap current (see Sec.1.7.3), while operating at high normalized pressure and moderate current. This regime suggests a potential route to the steady-state mode of operation desirable for fusion power plants. Therefore, a better understanding of the ITB formation and sustainment related to rotation profiles is an important step towards the exploitation of this improved scenario.

1.7 Determination of the plasma current density shaping the q profile

Knowing the plasma current density profile is essential to derive the safety factor profile, which plays a crucial role in the MHD stability of a plasma. Moreover, in order to obtain eITBs on TCV (described in Chap.5), the shape of the total plasma current density is manipulated to generate a non-monotonic q profile, which leads to the barrier development. To create a hollow plasma current density j_p, several contributions are summed:

$$j_p = j_{OH} + j_{ECCD} + j_{BS} \tag{1.12}$$

where j_{OH} is the Ohmic inductive current, j_{ECCD} the current generated from the electron cyclotron resonance heating (ECRH) system and j_{BS} the bootstrap current. In the following paragraphs we briefly describe each contribution.

1.7.1 Ohmic current

The current driven inductively by the Ohmic transformer j_{OH} is proportional to $T_e^{3/2}$ in steady state. Thus, co-Ohmic (co-OH) current induced in an eITB is mainly deposited in the center of the plasma, leading to a peaked current density and a monotonic q profile. When increasing the OH current contribution, the T_e profiles are reduced and become narrower [11]. This effect can be seen in the scan of small Ohmic perturbations performed in Sec.5.5.1, where even a small positive dI_{OH}/dt ramp causes a weakening of the barrier.

1.7.2 EC current drive

When injecting in the plasma the EC waves with a non-zero toroidal launcher angle (e.g. the azimuth angle of TCV launcher beams, see Sec.2.2), most of the power is absorbed by the electrons (since the wave frequency is a multiple of the electron cyclotron frequency) and a toroidal current j_{ECCD} is also generated (while the rest of the power is lost on the wall). This current is determined by the dependence of the electron-electron collisions frequency on the electron velocity (proportional to v^{-3}). More details of these principles can be found in [12, 13]. Imposing a central counter-ECCD component during the eITB formation adds a contribution that opposes the Ohmic current, while a co-ECCD off-axis current increases the off-axis current contribution resulting in a hollower profile. A correctly localized ECCD current is, therefore, essential to develop a strong barrier.

1.7.3 Bootstrap current

The bootstrap current density j_{BS} plays an important role in the sustainment of ITBs. The bootstrap current is related to the inhomogeneity of the magnetic field strength ($B \propto 1/R$) [14]. It is a current parallel to the magnetic field, driven by the radial

pressure gradient (resulting from both the density and temperature gradients). j_{BS} is carried by the passing particles (both ions and electrons) and is generated through collisional processes between trapped and passing particles. The bootstrap current density is given by [14]:

$$j_{BS} \approx \sqrt{\epsilon} \frac{c}{B_\theta} \left[\frac{dp_i}{dr} + \frac{dp_e}{dr} \right] \tag{1.13}$$

where $\epsilon = r/R$ is the inverse of the aspect ratio with r the radius of the magnetic surface and R the major radius. In order to obtain a rough estimate of the total bootstrap current I_{BS}[1] compared to the total plasma current I_p in a circular tokamak, we can express it using the pressure gradient [14]:

$$I_{BS} \propto \sqrt{\epsilon} \frac{a \langle p \rangle}{B_\theta} \qquad\qquad I_p \propto a B_\theta \tag{1.14}$$

where the angle brackets denote a volume average. From the above equations, we can derive the bootstrap fraction $f_{BS} = I_{BS}/I_p$ (see [14]).

In tokamaks, the bootstrap current is always present (due to $B \propto 1/R$ and the non zero radial pressure gradients), but was first experimentally reported only in 1988 [15]. In advanced scenarios, like ITBs with negative shear, this current can be exploited to sustain a steady-state plasma without requiring an inductive current. ITBs with negative central shear are characterized by a non-monotonic q profile that results from a hollow current profile. Moreover, ITBs are also characterized by strong pressure gradients that produce a bootstrap current peaked at the location of the maximum pressure gradient. Since the bootstrap current is naturally peaked off-axis, it is essential in the creation of this hollow current profile. A broad pressure profile is necessary for the bootstrap current to create a large hollow profile, which improves the plasma confinement, and also increases MHD stability [16]. This example shows the importance of the bootstrap current. It requires the synergism between a correct bootstrap current alignment (between the q_{min} and max ∇p_i locations), a strong confinement and an increased MHD stability for the cases of reversed shear eITBs [16], like the one studied on TCV.

---

[1]A total current is defined as $I = \int j_\varphi dA$.

1.8 Thesis motivation

In a tokamak, the radial transport of heat and particles, between the plasma core and plasma edge, has a direct effect on the physical and economic feasibility of a fusion reactor, through the effective plasma confinement and in determining the fusion reaction constituent densities and temperatures. A large part of the commonly observed "anomalous" transport in tokamak plasmas is nowadays considered to be driven by turbulence related to small scale instabilities. Other important, often detrimental, effects derive from macroscopic instabilities, the so-called MHD modes, that alter the magnetic equilibrium, with consequences for both plasma confinement and stability.

The study of momentum plasma transport mechanisms from measurements of the resulting plasma rotation has recently become intense. One of the main reasons for this is the recent availability of high spatial and temporal resolution rotation measurements on many machines worldwide. It is relatively rare that a main plasma parameter can be measured directly with small uncertainty and, furthermore, be compared between experimental devices with a range of configurations. Various experiments have demonstrated that plasma rotation has a beneficial effect on both confinement and stability and changes in the measured rotation are found to correlate with changes in the plasma behavior. High rotation is found important to avoid detrimental impurity accumulation in the core, since it keeps high-Z elements safely located in the low field side region. Additionally, high rotation is required at rational q surfaces in order to maintain the plasma stability against locked modes. An accurate rotation profile prediction has become one of the main research goals in the field.

Progress has been made in understanding the role of plasma rotation. Together with the basic questions of momentum conservation and distribution, rotation shear is thought to reduce, and even suppress, some of the anomalous transport effects of turbulence [17] and, in this way, reduce the threshold for transiting to the high confinement regime (H-mode,[18]) or in the formation of internal transport barriers (ITB,[19]). These are known as improved confinement scenarios. It should be recalled that, operation in an H-mode regime, is presently considered the most likely operational scenarios to achieve the plasma performance required by the ITER device. ITBs, with their high core confinement at moderate current, combined with a non-negligible bootstrap current component, may provide an alternative route to steady-state mode of operation for a fusion power plant.

The last few years have shown that TCV, together with its highly developed CXRS diagnostic, is well able to characterize thermal ion behavior over a wide range of plasma conditions [20, 21, 22]. With the recent CXRS diagnostic improvements, it has become possible to measure the ion parameters in plasmas with an internal transport barrier, where the low power diagnostic neutral beam is strongly attenuated and the measured signal weaker. As the TCV neutral beam only slightly perturbs the plasma, the carbon velocity is interpreted as a measurement of the intrinsic ion motion in the plasma, i.e. the motion of the ions in the absence of any externally applied force. This intrinsic rotation is expected to constitute the main component of plasma rotation in next generations devices such as ITER, where the effectiveness of neutral beam heating

is expected to be diminished [23].

This thesis firstly describes the enhancements of TCV's CXRS diagnostic system together with a thorough analysis of its spectroscopic components in a attempt to identify where further improvements may still be possible. The main aim of this thesis is to then use the diagnostic in an enhanced study of TCV plasma rotation both as a mechanism in affecting plasma performance and as a monitor of changes in plasma performance. The work addresses two subjects:

- An investigation of the role of MHD modes on radial momentum transport. This work examines the effect of one of the strongest and best known MHD mode, the sawtooth, on momentum transport with a view to completing pragmatic momentum transport models that mostly neglect this phenomenon that is already well known to affect many other plasma parameters.

- The role of rotation in the formation of the internal transport barriers. TCV analysis before this work did not require a strong role for rotation, and its shear effect, to obtain a transport barrier in contradiction to conclusions from other machines (i.e. $E \times B$ shear flows). This work attempts to measure directly the plasma rotation across eITB barrier formation to directly probe the role of rotation on TCV's eITBs.

One of the major problems in this endeavor is the physical vertical position of the CXRS diagnostic on the central TCV axis, whereas most of the H-mode and ITB discharges have, to date, been obtained with the plasma centered at Z=+21 cm where the CXRS diagnostic does not have access up to the plasma core.

An important goal of this thesis was therefore to achieve, for the first time on TCV, measurements of both toroidal and poloidal velocity and impurity density profiles across the whole transport barrier width (and beyond) and to track fast changes associated with the barrier formation. To achieve this, a strong effort to optimize the CXRS diagnostic system was performed, including the purchase of new sensitive CCD cameras (to increase the time resolution) and a complete overhaul of the three CXRS spectroscopic systems (to maximize their radial coverage).

Although the measurements themselves were complicated and required original optical and real-time timing solutions, they were eventually found to be quite straightforward. The main difficulty was found in the development of plasma scenarios that were both reproducible and stable in TCV operations whilst providing a correctly positioned plasma with the correct plasma parameters. In all this work, highly precise ECH heating and ECCD current drive were employed to achieve these configurations. This involved the use of the full array of TCV's actuator and control possibilities and, it must be noted, a large amount of machine run time. As most experimentalists must realize, the reliability of these systems can be precarious and several periods of many months occurred without the possibility of machine operation on these topics.

The second main achievement of this thesis, not directly related to a physics analysis, was in the development and routine operation of such configurations that should now be accessible for future experiments.

1.9 Outline of this thesis

This first chapter has provided an introduction to nuclear fusion, plasma physics and the tokamak concept. The rest of this thesis is structured as follows:

- Chapter 2 describes the TCV tokamak where all the experimental work reported in this thesis was carried out. The magnetic coil system, main diagnostics, heating system and TCV real-time control system are presented, in addition to the two main post-shot analysis tools used during this work.

- Chapter 3 is devoted to the CXRS diagnostic. First the measurement principles are discussed. Following this, the present status of the diagnostic is described, with the main upgrades performed during this thesis (new cameras and other optical elements, acquisition process,...). Finally, the analysis procedure for data acquired during TCV discharges is presented and an example of the measurements with carbon and boron impurities is given.

- Chapter 4 discusses the effect of sawteeth on rotation profiles and momentum transport in limited L-mode discharges with CXRS measurements taken over several sawtooth events or between sawteeth. The special fast acquisition configuration and the relevant modifications of the CXRS diagnostic are presented. The contributions related to the ST crash and the quiescent ramp of the sawtooth period that strongly affect the rotation and momentum are described and interpret.

- Chapter 5 is dedicated to the role of rotation in the formation of eITBs. First an introduction to internal transport barriers explains the main motivation of this task. A large section is devoted to the validation of the method used to determine the electric radial field and $E \times B$ shearing rate in this work. The two main scenarios (a central barrier and a strong eITB) developed during this thesis are described and compared with previous barriers performed at Z=21cm. The effect on the barrier strength and on the rotation profiles of several parameters, such as the central and total power, Ohmic current perturbations and MHD activity are successively investigated for both targets. In reply to the original motivation, a comparison of the experimental $E \times B$ shearing rate with the growth rate of TCV most unstable modes, predicted by gyrokinetic simulations, is discussed. Finally, the impurity ion temperature and density profiles are described and compared with the results of a quasi-linear model applied to TCV eITBs.

- Chapter 6 concludes this thesis summarizing the main achievements and providing a brief outlook for future investigations.

- Appendix A summarizes the work performed during the first year of this thesis on the TORPEX device.

- Appendix B describes the theoretical estimation of the main losses of the CXRS systems compared with experimental measurements.

- Appendix C contains some complements to Chapter 4.

- The validation of the E_r indirect method is given in Appendix D. In this appendix the effect of a global oscillation in both eITB scenarios is also discussed.

- Some additional Figures related to Chapter 5 are finally shown in Appendix E.

Chapter 2

The TCV tokamak

2.1   The TCV device

This thesis was carried out on the *Tokamak à Configuration Variable* (TCV), a medium size tokamak in Lausanne. TCV was built in 1992 with the main aim of investigating the effect of plasma shape on confinement and stability. The stainless steel vacuum vessel has an elongated cross section designed to allow a large variety of plasma shapes and ∼90% of the vessel interior is covered by around 1700 carbon tiles (see Fig.2.1.b). The main machine parameters are summarized in Table 2.1.

a)   b)
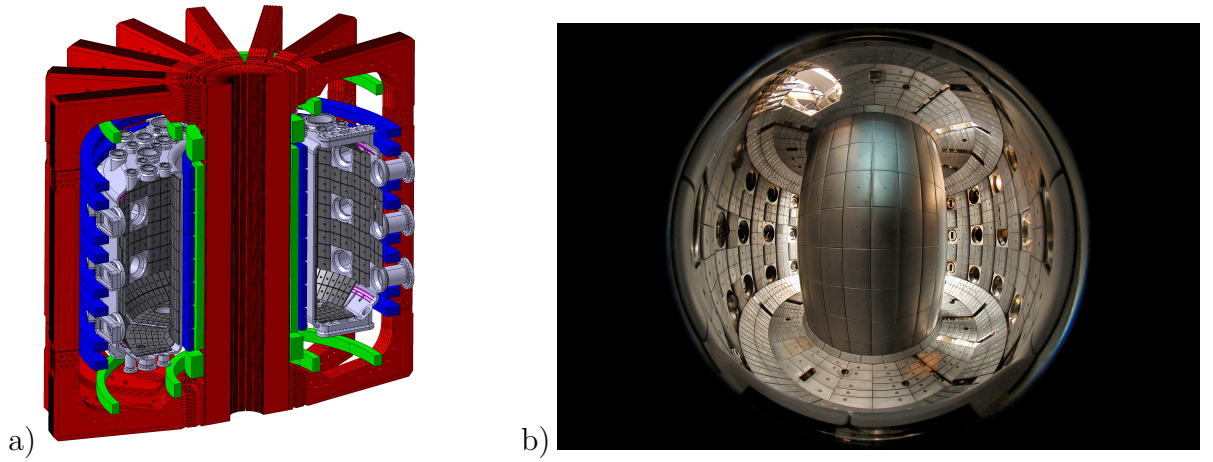
Figure 2.1: The TCV tokamak: a) vacuum vessel and diagnostics ports surrounded by the set of coils and b) inner wall covered by carbon tiles.

TCV's plasma shaping is achieved by 16, independently power supplied, poloidal field (PF) coils which are mounted in two vertical stacks on both sides of the plasma, outside the vacuum chamber (shown in blue, see Fig.2.1.a). The vertical stability, particularly for high elongated plasmas, is ensured by two sets of in-vessel toroidal coils (shown in pink, see Fig.2.1.a). The toroidal field (TF) is provided by 16 poloidal coils (shown in red, see Fig.2.1.a). A set of 7 Ohmic coils located around the central column constitute a primary circuit of the transformer that is used to induce the toroidal plasma current

Parameter	Symbol	Value
Major radius	R_0	0.88 m
Minor radius	a	0.25 m
Aspect ratio	$\varepsilon^{-1} = R_0/a$	up to 3
Vessel internal full width	$R_{max} - R_{min}$	0.56 m
Vessel internal full height	$z_{max} - z_{min}$	1.54 m
Toroidal field on axis	B_0	≤ 1.54 T
Plasma current	I_p	≤ 1 MA
Typical shot duration	t_{shot}	2 s
Central electron temperature	T_{e0}	< 15 keV (EC heated)
Central ion temperature	T_{i0}	≤ 0.1 - 1 keV
Density range	n_e	$\leq 0.5 \times 10^{19} - 20 \times 10^{19}$ m^{-3}
X2 ECH heating	P_{X2}	≤ 2.8 MW
X3 ECH heating	P_{X3}	≤ 1.4 MW
Installed peak power	P_{MT}	200 MW
Ohmic heating	P_{Ohm}	200-300 kW
Radiated power in snowflake (SF) divertor	P_{rad}	100-200 kW

Table 2.1: Main parameters of the TCV tokamak and its plasmas.

(shown in green, see Fig.2.1.a). In addition, TCV is equipped with a powerful and flexible electron cyclotron resonance heating (ECRH) system, which is used to heat the varied plasma configurations at the second and third harmonics of the electron cyclotron frequency. TCV has the flexibility to operate with combinations of high plasma elongation $\kappa \leq 2.8$, high positive and negative triangularity $-0.77 \geq \delta \leq 0.86$, high squareness $\lambda \leq 0.5$, in pear and doublet shape, in double null and various upper and more advanced lower single null divertor shapes like the most recent snowflake shape.

2.2 Electron cyclotron heating system

In TCV, plasma heating, provided by the plasma current, permits the plasma to attain electron temperatures up to 1 keV. An auxiliary heating system is also available on TCV and is based on the resonant interaction between microwave beams and plasma electrons. The microwave energy is transmitted to the electrons, since the wave frequency is a multiple of the electron cyclotron frequency. This permits the heat deposition to be localized along an approximately vertical resonance layer whose position is determined by the magnetic field.

The flexible electron cyclotron heating (ECH) and current drive (ECCD) system installed on TCV consists of six 82.7 GHz gyrotrons for heating at the second harmonic of the electron cyclotron frequency, and three 118 GHz gyrotrons that heat at the third harmonic (see Fig.2.2). Each gyrotron provides a nominal power of 500kW for a total of 4.5 MW injected power. For optimal power coupling, the EC waves are usually

polarized in the extraordinary mode (X2, X3), i.e. with the oscillating electric field orthogonal to the confinement magnetic field.

The X2-system allows us to heat and drive current in plasmas with a density up to the cut-off density of $n_{e,cut-off,X2} = 4.25 \times 10^{19} m^{-3}$. There are two launchers (L1, L4) mounted in equatorial ports and four launchers (L2, L3, L5, L6) in upper lateral ports. Each launcher has two steering axes, whose combination allows a wide variety of poloidal and toroidal injection angles. The gyrotrons are grouped into two clusters of three gyrotrons each. Cluster A (L1, L2, L3) and Cluster B (L4, L5, L6) have separate power supplies, permitting two different power traces. More specifically, the gyrotrons from the same cluster inject the same nominal power. The modification of the poloidal and toroidal angles allows a localized power deposition across most of the plasma cross section. Nevertheless the X2-system has some limits in coverage and exploitation for particular scenarios at Z=0cm (as for eITBs, see Chap.5)

The gyrotrons from the X3-system are combined in one launcher at the top of the TCV vessel and heat plasmas with a density up to a cut-off density of $n_{e,cut-off,X3} = 11.5 \times 10^{19} m^{-3}$. The microwave beam is injected nearly tangentially to the resonant surface in order to increase the absorption path length as it has relatively weak absorption. The launcher mirror can be moved radially and steered poloidally in order to optimize this injection angle and the position of the beam path with respect to the resonant layer. The X3 power deposition is thus less localized compared with X2. All X3 gyrotrons are powered by the same supply which does not allow power ramps.

During this thesis work, the EC system was used extensively, particularly the X2 launchers for the electron internal transport barriers and sawteeth studies.
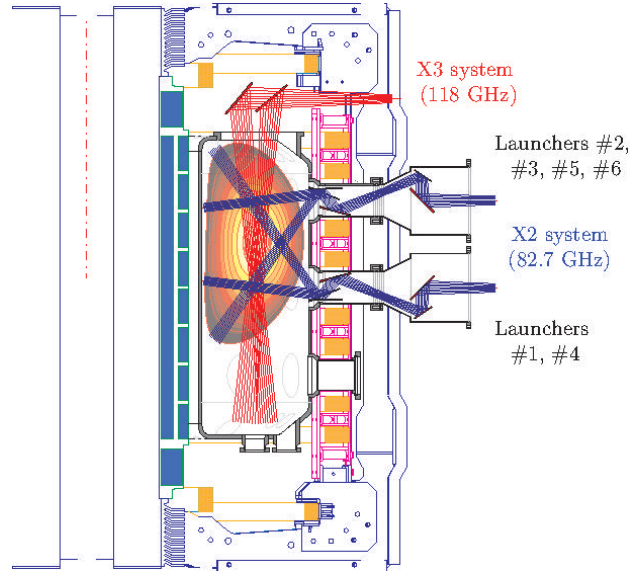
Figure 2.2: TCV plasma heating system. The X2 launchers are placed on the two equatorial (L1, L4) and four upper lateral ports (L2, L3, L5, L6). Two degrees of freedom in the launcher mirror angles allow a wide range of poloidal (ECH) and toroidal angles (ECCD). The X3 launcher is placed on the top of the device and has two degrees of freedom to optimize the injection angle radially and poloidally (the toroidal angle is fixed to 0°.)

2.3 Turbo-alternator and flywheel

The installed peak power requirement of TCV is about 200MW, which is equivalent to the total consumption of the Lausanne city (1kW/inhabitant). In order to avoid a black-out at every discharge, a turbo-alternator (*Machine Tournante*) and a flywheel (∼60 tonnes) are installed to decouple TCV's pulsed needs from the public electrical distribution grid. The electricity needed to perform a pulse is therefore extracted from the kinetic energy stored in the rotor and flywheel. During the discharge the rotation frequency decreases by ∼30% and takes around 5-10min in order to regain nominal speed (120Hz). A fast power supply (FPS) is installed to supply the G1 and G2 coils that are responsible for the fast vertical stabilization of the plasma. Note that the 200MW peak power is mostly required to supply the IOH coils of the transformer, even though the heating power generated in a plasma on TCV is only around 300kW in the flat-top.

2.4 Main diagnostics used for this thesis

A rich and versatile set of diagnostics is installed in TCV, which allows the measurement of many important plasma parameters for the various shapes and positions explored on TCV. A diagnostic is classified as active or passive depending on its effect on the plasma. An active diagnostic directly interacts with the plasma electrons or ions and can slightly affect the plasma behavior, such as an injected laser beam or neutral beam (see Thomson scattering, CXRS,...), whereas a passive diagnostic only observes the plasma and measures some emitted quantity without affecting it (visible camera, soft X-ray cameras,...). The following paragraph describes the main active and passive diagnostics used during this thesis.

2.4.1 Magnetic diagnostics

TCV is equipped with a large number of magnetic probes and flux loops [24, 25]. The magnetic probes (pick-up coils) are located inside the vacuum vessel, between the wall and the graphite tiles, and measure the time derivative of the poloidal magnetic field tangential to the vacuum vessel. Their signals are not only used for real-time plasma shape and position control and plasma equilibrium reconstruction, but also in the analysis of plasma MHD modes. The in-vessel magnetic probes are arranged in toroidal and poloidal arrays. There are four complete poloidal arrays of 38 probes each, toroidally separated by 90 degrees. Three toroidal arrays are installed especially for MHD studies. One is located at the mid-plane, and the others 35 cm above and below, respectively. Each toroidal array consists of 8 equidistant probes on the high field side (HFS) and 17 on the low field side (LFS), which allow the measurement of toroidal mode numbers $n \leq 16$. Acquisition frequencies up to 1 MHz are available, but usually a frequency between 125-250 kHz was chosen during this thesis. The choice of the toroidal array depends on the position of the plasma in the vessel, which was mainly ∼Z=0 cm for the experiments presented here. The flux loops are located

outside the vacuum vessel but on its surface and measure the time derivative of the poloidal magnetic flux. They are used for the plasma equilibrium reconstruction.

A conducting loop poloidally encircling the plasma, termed the diamagnetic loop (DML), is also installed on TCV [26]. It measures the time derivative of the toroidal magnetic flux that can be directly related to the total plasma energy. The DML signal is used therefore as a supplementary constraint on the plasma equilibrium reconstruction code LIUQE [27] used on TCV (see Sec.2.4.5).
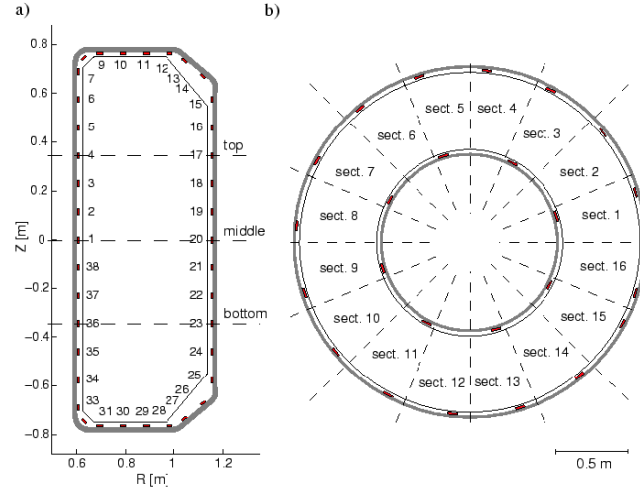
Figure 2.3: a) Poloidal and b) toroidal cross-sections of the TCV vessel, showing the layout of the fast magnetic probes.

2.4.2   Electron and impurity diagnostics

Thomson scattering

The Thomson scattering (TS) diagnostic measures both local electron temperature (T_e) and density (n_e). The profiles are determined by spectrally analysing the light scattered from electrons in their interaction with a laser beam. From the intensity of the scattered light it is possible to calculate the electron density [28]. The Thomson scattering installed on TCV comprises three pulsed Nd:YAG lasers traversing vertically the vacuum vessel at a wavelength of 1064 μm with a laser beam pulse energy of about 1.5 J [29, 30]. The diagnostic has a sample time of a few nanoseconds but a repetition frequency of 20 Hz. In low density plasmas (like eITBs), the lasers may be fired together every 50ms in order to increase the signal to noise ratio. The electron temperature and density are measured at 35 different local positions along the vertical laser beam path (Fig.2.4.a). Radial profiles are obtained by mapping the measurements on the reconstructed magnetic equilibrium. By rearranging the position of the optical fibers, and thus the viewing chords, the spatial resolution at the edge (TS-edge, magenta lines in Fig.2.4.a) can be increased in order to better measure the H-mode pedestal profiles [30] or to study the X-point location in a snowflake divertor configuration. Note that, the TS-edge channels permit T_e measurements between 10eV-1.2keV, while the central

TS-main channels measure between 100eV-15keV. The Thomson density profiles are cross-calibrated against FIR measurements (see Sec.2.4.2). The Thomson scattering is the most important diagnostic for electron temperature measurements on TCV and is essential for the post-shot analysis of many parameters, such as the confinement parameters or impurity density profiles.
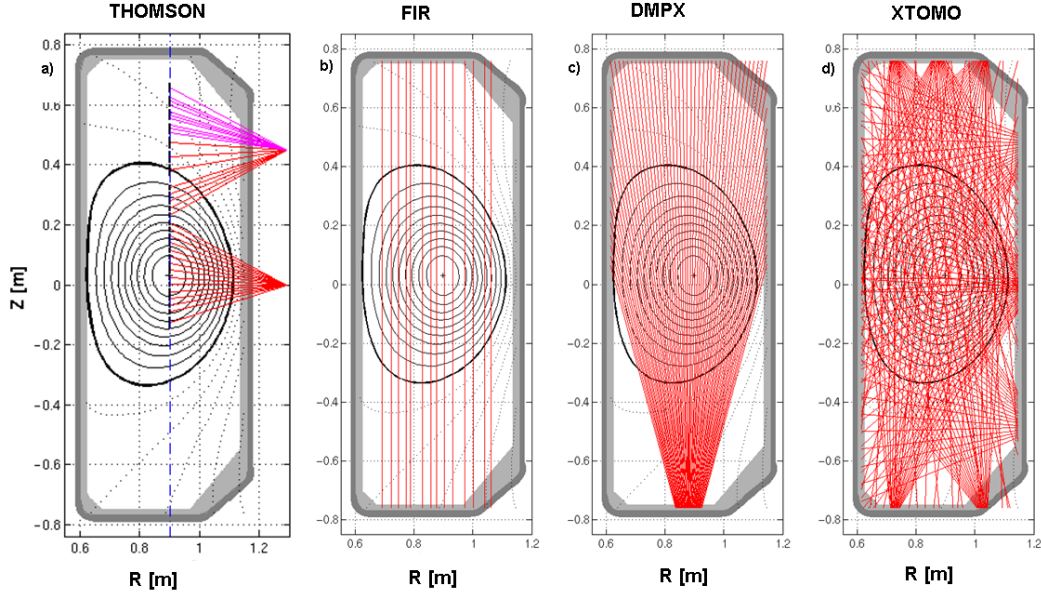
Figure 2.4: Viewing chords of the a) Thomson scattering (TS) in standard configuration, b) FIR, c) DMPX, d) XTOMO diagnostics. The TS-main channels, better covering the plasma center, are highlighted in red and the high resolution channels of the TS-edge system are highlighted in magenta. The vertical blue line shows the laser path.

Far infrared interferometer (FIR)

The FIR interferometer is a Mach-Zender $\lambda = 214\mu m$ interferometer and provides line integrated electron density along 14 vertically aligned chords (see Fig.2.4.b) with an acquisition rate of 20 kHz [31]. The electron density is evaluated from the phase delay of 14 laser beams passing through the plasma and a reference beam that is frequency shifted. The phase delay results from traversing the plasma that has a refractive index that is proportional to the integral of the electron density along the beam path. From the equilibrium reconstruction, the line average density along each chord can be estimated. Using tomographic inversion, the n_e profiles on the flux surfaces ρ_ψ defined by LIUQE (see Sec.2.4.5), can be reconstructed from the line-integrated FIR measurements. This is done by Minimum Fisher regularization on a finite difference discretization or by least squares inversion on a set of basis functions from SVD analysis of Thomson profiles. The central viewing line at R=0.9 m is used in the control system as the density value for feedback control using the gas valve actuator.

Electron cyclotron emission and CECE diagnostics

Electron cyclotron emission (ECE) diagnostics on TCV study the electron temperature time evolution with high spatial and temporal resolution. ECE diagnostics are widely used to obtain information on heat transport, magnetohydrodynamic (MHD) phenomena and fast electron dynamics. A second harmonic X-mode ECE, comprising two separate heterodyne radiometers on both the LFS and HFS was installed (and working) on TCV until 2011 and ensured a full radial coverage of the plasma cross-section with a high sampling rate [32]. Two alternative lines-of-sight, perpendicular to the magnetic field (at Z=0 cm and Z=+21 cm), were used by both radiometers to measure the ECE radiation temperature giving the electron temperature. We recall that, at the second harmonic EC frequency, the plasma is optically thick, i.e. the EC emission is a black body radiation. This condition is essential to determine T_e, since according to Rayleigh-Jeans law, the long wavelength approximation of Planck's law, the intensity of black body radiation is related to the temperature. The ECE intensity $I(\nu)$, as a function of frequency, is therefore proportional to the electron temperature $T_e(R)$, as a function of major radius R, derived from the definitions of the electron cyclotron frequency Ω_e and the magnetic field B.

At the end of 2012, the LFS radiometer was upgraded with four additional channels and, at present, a new 6-channel correlation electron cyclotron emission (CECE) has been installed on TCV to investigate the electron temperature component of the turbulent transport through spectral decorrelation [33]. The system exploits the same two perpendicular view lines at vertical position Z=0 cm and Z=+21 cm and has a spatial coverage from the LFS wall to the center of TCV. The RF stage is protected by two notch filters at the second and third harmonic of the EC frequency in order to reduce the direct radiation from the gyrotrons. A local oscillator at 63 GHz is installed, combined with 6 remotely controllable YIG filters (Yttrium Iron Garnet, see [34]) in the 6-18 GHz range that covers the LFS region. The radial and vertical resolution of the diagnostics are of 0.3-1 cm and of 3-5 cm respectively with an acquisition frequency of 1.75 MHz. Broadband turbulence in TCV often appears in the range 10-150 kHz. Considering only the adjacent correlations, the 6 separated channels allow the simultaneous study at 5 locations.

CXRS

TCV is equipped with a charge exchange recombination spectroscopy (CXRS) diagnostic that provides local measurements of impurity temperature, density, toroidal and poloidal rotation through the analysis of the spectral moments of impurity line radiation [20, 35]. The CXRS typically observes the CVI line (529.1nm), emitted when a charge exchange (CX) reaction takes place between the intrinsic impurity (carbon C^{6+} from the tiles) and a neutral H^0, injected by a low power, high energy, diagnostic neutral beam injector (DNBI). This active component is summed with the passive CX emission mainly coming from the plasma edge. The DNBI is weak enough not to perturb the plasma significantly, permitting CX measurements to be obtained in the absence of an external input torque. The optimization and maintenance of this diag-

nostic constituted an important part of this thesis. The diagnostic will be described in detail in chapter 3.

Neutral particles analyzers

Although most of the particles of a tokamak plasmas are ionized, in TCV there are some neutrals present in the plasma core. These neutrals arise from atoms and molecules released from the vessel wall, penetrating into the plasma after multiple consecutive charge-exchange reactions with hotter ions from which they gain thermal energy. The process stops when the neutral is ionized or when it leaves the plasma without further interaction. Two neutral particle analyzers (NPA), installed on TCV, analyze such neutrals and determine their velocity distribution from the measured flux energies.

The 5-channel NPA observes the neutral charge-exchange fluxes of hydrogen isotopes, generated in the plasma, along a fixed central vertical chord. The 5 detection channels, combined with an energy sweeping analyzer, allow an ion energy coverage between 0.6-8 keV with a time resolution of 0.05-2 ms.

A compact neutral particle analyzer (CNPA) is used to analyse hydrogen, deuterium or helium atoms in the energy range of 0.5-50 keV. It is composed of two arrays of 11+17 energy channels, such that two species can be separately measured simultaneously (H/D or D/He). The diagnostic is currently installed at the midplane and can be set to two possible view lines: perpendicular to the plasma current (the default position) and tangential (45°) in order to study the properties of the perpendicular or parallel distribution function.

The NPA and CNPA provide complementary measurements of the ion energy distribution function [36] and can be contrasted to the CXRS measurements. One system uses the tail of the velocity distribution to diagnose the bulk, whereas the other measures the bulk distribution directly. From the lower part of the energy spectrum of the NPA, an estimate of the on axis ion temperature can be obtained. NPA measurements are line integrated quantities, so Monte-Carlo codes (such as DOUBLE-TCV [37]), are needed to predict the atomic neutral density profiles inside the plasma.

2.4.3 Soft X-ray diagnostics

The soft X-ray (SXR) radiation spectrum (with photon energy < 30 keV) is the sum of bremsstrahlung losses (charged particle acceleration during Coulomb collisions), line radiation from heavy impurities (emission by bound electrons transiting to a lower energy state) and electron-ion recombination (free electron becoming bound to ions). Several diagnostics, installed on TCV, detect SXR with high temporal and spatial resolution with large spectral coverage. The two most important diagnostics on TCV are the DMPX and XTOMO. They provide much information on the MHD instabilities developed in the plasmas, such as the sawtooth inversion radius or their spatial structure.

Duplex multiwire proportional X-ray detector (DMPX)

The duplex multiwire proportional X-ray counter (DMPX) is a 64-channel soft X-ray detector located underneath TCV viewing the plasma vertically [6, 38]. The diagnostic houses two superimposed wire-chambers, and is equipped with a beryllium filter in order to cut-off the low-energy photons, and therefore is sensitive to soft X-ray emission in the range between 1-30 keV. The DMPX is characterized by a high time and spatial resolution with a sampling rate of 200 kHz and an 8 mm horizontal resolution at the midplane (see Fig.2.4.c). The wire-chambers operate in the proportional regime, such that the measured signal, integrated along the lines-of-sight, is proportional to the mean power of the measured photons. The DMPX is also connected to the TCV digital control system and can be used in order to determine in real-time the sawtooth cycle and the sawtooth inversion radius.

Tomographic soft X-ray diagnostic (XTOMO)

The SXR XTOMO diagnostic consists of 10 cameras, placed at the same toroidal location, each having 20 photodiodes for a total of 200 lines of sight [39](see Fig.2.4.d). A beryllium absorption foil is placed in front of each camera so that the cameras are sensitive in the energy range between 1-15 keV. The signals are acquired with a spatial resolution of 3-4 cm and an acquisition rate of 100 kHz. The 200 chords provide full poloidal coverage and are used to obtain a tomographic reconstruction of localized SXR emission in the poloidal plane.

2.4.4 Real-time control systems

Two control systems are presently in use on TCV: the first is the original system installed on TCV, the so-called hybrid control system[1] and is accompanied by a new real-time fully digital distributed control system (SCD, *système de contrôle distribué*) envisaged to eventually replace the legacy system at a future time. The SCD is able to perform advanced control, such as driving the ECRH actuators (power and launcher angles) in real-time. Real-time (RT) algorithms are programmed in the flexible and powerful block programming software Simulink. The SCD is described in detail in [40, 41, 42]. In the following paragraphs we briefly describe two applications of the SCD that were used during this thesis.

CXRS triggering on sawtooth crash detection

Typically sawtooth (ST) crashes are characterized by sudden drops of the core X-ray emission, which can be observed by the SXR diagnostics installed on TCV. In order to study the rotation in between ST events with the CXRS diagnostic (see Chap.4), a real-time sawtooth detector was developed capable of triggering the CXRS synchronously with the ST crash time. The detector algorithm uses the central SXR signal of the DMPX or XTOMO diagnostics and detects a crash if two conditions are fulfilled. The

---

[1]The name *hybrid* comes from a hybrid combination of analog and digital processes in the system.

SXR signal must cross an absolute intensity threshold in the negative direction and the intensity of the drop slope must also exceed a given threshold level. Only when the SXR intensity drop is sufficiently abrupt and large, is a crash detected and a series of 2 ms triggers generated by the d-tACQ196 card sent to the CXRS diagnostic. This unique technique was fundamental in obtaining the first rotation measurements just before and after a sawtooth crash on TCV (see Sec.4.3).

IOH control

To create steady state plasmas, the Ohmic transformer coil current must be set to a fixed value so that the plasma current it induces is negligible. During the TCV operation mode called *IOH feedback*, this was obtained by feedback controlling the OH coil current to a constant reference value at a specified time in order to reduce any induced current. In standard operation, the IOH coil is the *Ip feedback* in which its ramp rate is feedback controlled to maintain the desired plasma current. The study and development of eITBs required the utilization of the new SCD IOH control system (see Chap.5). The IOH current was set to a constant value just after the start of the EC heating. In addition, a range of positive and negative IOH ramps were imposed to study the effect of the Ohmic perturbations on the ITB strength. The new SCD IOH control can switch from the Ip feedback to the IOH feedback operation dynamically, i.e. without continuously adjusting the IOH reference value to the IOH current from the previous discharge, as was necessary with the old controller that led to sudden spikes in V_{loop} that perturbed the plasma (for more details see Appendix A of [42]).

2.4.5 Post-shot analysis tools

Two important post-shot analysis codes used at TCV are briefly introduced in this section.

Magnetic equilibrium reconstruction

The plasma magnetic equilibrium reconstruction is computed by the LIUQE [2] code [27] after each discharge, using the poloidal magnetic flux measurements provided by the magnetic probes and flux loops located inside and outside the vessel described in Sec.2.4.1. The code iteratively solves the Grad-Shafranov equation in order to obtain a poloidal flux description with the closest match to all measurements. The quality of the reconstruction can be improved by imposing additional constraints, such as the pressure profile (from Thomson scattering diagnostic) and the toroidal flux (total energy) measured by the DML.
Knowledge of the shape and positions of the flux-surfaces is crucial to the analysis performed during this thesis. In particular, the method of the indirect derivation of the poloidal rotation (see Sec.5.2.2) is based on the precise measure of the HFS and LFS toroidal rotation determined on the same flux surface. Unfortunately, it has

---

[2]EQUIL spelled backwards

been observed that the LIUQE equilibrium reconstruction converges with increasing difficulty in plasmas with low Ip and reverse q profile, such as those with an eITB.

Ray tracing

The ECRH beam trajectories and power deposition locations can be calculated with the ray-tracing code TORAY-GA [43]. The code determines the ECH absorption regions and the current drive efficiencies for a particular discharge configuration and launcher orientation. The plasma description used in TORAY is based on the measured Thomson density and temperature profiles, coupled to a MHD magnetic equilibrium calculated with the CHEASE code [44] starting from the LIUQE result. TORAY is extremely useful in order to analyze the already performed shots, as well as to prepare new targets by predicting in advance the deposition regions of the beams from the ECRH launchers.

Chapter 3

The CXRS diagnostic on TCV

A reliable study of the intrinsic rotation and impurity profiles in limited L-mode plasmas and in electron internal transport barriers is based on measurements at high spatial and temporal resolution. In most tokamak devices, these measurements are performed with the charge exchange recombination spectroscopy (CXRS, also known as CHERS), which obtains local measurements of impurity ion temperature and velocity, from the observation of Doppler shift and line broadening of the impurity line emission. Impurity ion densities are obtained from the line intensities of the measured spectra. In the large devices, charge-exchange (CX) emission is provided by the interaction of neutral beams heating (NBH) with the fully ionized impurity ions present in the plasma. In this way the neutral beam injectors ensure abundant CX emission but, at the same time, they directly affect the ion channel and can exert an applied torque that affects the rotation profiles. Since on TCV the installation of an auxiliary ion heating is planned only after 2014 (so far the main ion heating on TCV is due to the electron-ion collisions), the TCV CXRS diagnostic installed in 2004 works with a diagnostic neutral beam injector (DNBI) that provides sufficient CX emission from the hot plasma core without perturbing the plasma.

During these nine years, the original design of the CXRS diagnostic has been initiated and continually upgraded. The initial status was reported in the thesis work of Bosshard [35] and was operational for the period 2004-2006. The diagnostic system was completed during 2006-2009 by Bortolon [20] with the installation of a poloidal system, an increase in the number of measured chords and the introduction of a routine wavelength calibration after each shot.

This chapter reports on the upgrades performed during this thesis between 2010-2013 that mainly concern the installation of new EMCCD cameras, the reinstallation of the toroidal HFS system and the optimisation-automation of the CXRS acquisition and analysis routines for TCV daily operation.

The CXRS-DNBI system of TCV was used for all impurity ion temperature, intrinsic rotation and density profiles measurements discussed in this work.

In the first part of this chapter, Sec.3.1, the principles of CX spectroscopy are introduced and a description of the present system is given. In Sec.3.2, the main up-

grades to the hardware and software system performed during this work are discussed, such as the installation of the new cameras, the reinstallation of the THFS system, the extended double slit (DS) configuration and the CXRS acquisition process. Some essential calibration and checks needed to optimize the CXRS systems are discussed in Sec.3.3. Finally, the CXRS analysis routines and the calculation of the ion profiles from the raw spectra are briefly explained in Sec.3.4, with examples for the carbon and the recent boron diagnostic configurations. In Appendix B, a theoretical estimation of the main transmission losses along the complete CXRS optical path is discussed and compared with the measured signal.

3.1   The CXRS systems on TCV: principle and present status

3.1.1   The principle of CXRS measurements

The charge exchange reaction takes place between a plasma ion (usually the most studied C^{6+}, B^{5+}, He^{2+} and O^{8+}) and a neutral atom (H^0 or D^0). The result of this reaction is a transfer of an electron from the neutral to an excited state of the target ion, characterized by principal quantum number n and orbital quantum number l. The CX reaction tends to populate high n energy and angular momentum levels, and the probability (cross section) is highest for approximately $n_{max} = Z^{3/4}$ [45]. The CX recombination process mostly exploited on TCV involves the neutral atoms H^0 from a low power DNBI [46] and fully ionized carbon impurity ions:

$$H^0 + C^{6+} \rightarrow H^+ + C^{5+}(n,l) \tag{3.1}$$
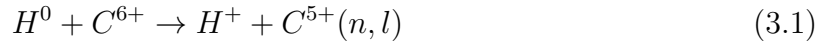
This reaction leaves the resulting ion in an excited state (n,l) which subsequently decays through a cascade of transitions (n-1,l-1) accompanied by photon emission of multiple characteristic lines. For common low-Z hydrogenic ions such as C^{5+}, B^{4+}, He^+ and O^{7+}, these spectral lines have wavelengths which range from the extreme ultraviolet to the visible spectral regions. From the spectral analysis of the Doppler shift, line broadening and line intensity of the considered CX line emission, the evolution of the temperature, velocity and density of the initial recombining ion population can be recovered in the visible range by means of spectrometers and CCD detectors. On TCV, the CXRS diagnostic is optimized for the observation transition of the CVI (n=8→7) line at λ =529.059 nm (i.e. green light)[1]. Carbon is the main impurity in TCV as it constitutes the near full graphite tiles that covers the inner TCV vessel. Carbon

---

[1]Note that the CXRS diagnostic is based on the measurement of the probability distribution function (PDF) of the bulk of the distribution and is to be distinguished from diagnostics such as the NPA (discussed in Sec.2.4.2) that instead use the tail of the distribution to determine the bulk temperature value $T_i(0)$ (for more details see [36]). The CXRS temperature is then obtained by assuming, with good approximation, a Gaussian shape for the ion velocity PDF and using its FWHM. This procedure is much less likely to fail when there is a relatively small fast (or slow) ion contribution, compared with the "tail" diagnostics such as the NPA, which may largely overestimate the central temperature.

concentrations of 1-2% are often present in TCV. This quantity reduces strongly after a boronization process, when the first wall is covered by a thin boron/boron-oxide layer and the carbon tiles pores are obscured by boron. After a boronization it usually takes around two weeks of TCV operation to recover a sufficient level of carbon active signal on the CXRS system. Recently, in order to exploit the CXRS diagnostic during this period, the spectrometers were aligned to observe the BV ($n = 7 \rightarrow 6$) line at $\lambda =$ 494.467 nm. This allowed enough CX emission for the CXRS measurements and provided an estimate of the evolution of the carbon and boron amount inside TCV (see Sec.3.4.4).

The DNBI, responsible for what is termed the "active" CX reactions occurring in the plasma core, is observed transversally by the CXRS diagnostic (see Fig.3.1). This position in the TCV vessel can recover local ion measurements, since they refer to the ions contained in a specific emitting volume defined by the intersection between the neutral beam and the CXRS view lines (this is called a "cross-beam" technique). The DNBI that features relatively low power ($P_B = 80kW$) and high energy 50.3 keV-H^0 injected atoms provides sufficient CX emission for the CXRS diagnostic measurements, without strongly perturbing the plasma by additional external momentum or direct ion heating. Preliminary ASTRA simulations have shown that the DNBI causes a negligible torque of $0.03 N/m^3$ (1km/s) and a 20-30eV temperature increase during the beam injection pulses. Due to the high ion velocity, the bulk of the beam power is deposited on the electrons [47]. The advantage of a low power beam with negligible applied torque is somewhat offset by the disadvantage of obtaining an often small emitted intensity.

3.1.2 Main plasma ions and impurity species profiles

The CXRS diagnostic on TCV measures the carbon species temperature, density and toroidal/poloidal velocity profiles. In TCV, the main plasma ions (deuterium) and the impurity species (carbon, boron) are expected to be thermalized, since the ion-ion energy equilibration timescale ($\approx$1 ms) is much faster than the heating through collisions with electrons ($\approx$100 ms). This was confirmed experimentally (see [36, 48]), through an extensive comparison between ion temperature measurements from the NPA (deuterium) and CXRS (carbon). Therefore, the CXRS carbon temperature measurements can be considered as an indirect measure of the main ion temperatures (see Sec.3.4.4 also for boron).

For the plasma rotation, the question is more delicate, since from neoclassical theory, the main ions and impurities are expected to rotate with different velocities, in particular in the presence of large pressure gradients (see Kim, Diamond & Gröbner [49]). Previous toroidal rotation studies on TCV [20, 22] have shown that the main ion toroidal rotation predicted by neoclassical theory does not differ substantially from the carbon measurements. Note that the approximate formulas in [49] applied to TCV discharges tend to overestimate Δv_φ (see [20, 50]).

The poloidal rotation offers a different picture [51]: NEOART [52] simulations of Ohmic and ECH heated TCV L-mode plasmas have shown a good agreement between

the neoclassical and measured carbon poloidal rotation profiles. In particular, the predicted deuterium rotation is observed to be lower than the carbon poloidal rotation. Recently, in the DIII-D tokamak, a diagnostic capable of measuring directly deuterium rotation has been commissioned. The diagnostic, which analyses the charge exchange recombination spectrum of the D_α emission, has been exploited to compare main ion and impurity flow [53]: different core toroidal rotations of carbon and deuterium species were measured, with a slightly more cnt-current rotation for the main ion species. Interestingly, some discrepancies with the neoclassical theory were observed in the plasma core, which may indicate an inaccurate prediction of the neoclassical poloidal flow that does not include anomalous effects (such as turbulent transport). Other studies on DIII-D combining Mach probe measurements in the plasma edge, indicated that, in the region close to the separatrix, the differences between carbon and deuterium rotations can be explained with purely neoclassical terms [54].

The several comparisons of measured carbon poloidal flow and neoclassical theory performed for other devices also shows a mix of reasonable agreement [55, 56, 57, 58] and large disagreement [59, 60, 61].

In spite of several theoretical and experimental studies, the debate is still open. Ultimately, an accurate measurement of the deuterium poloidal and toroidal rotation profiles across the whole plasma radius simultaneously with the carbon profiles is required to elucidate this issue.

3.1.3 The CXRS diagnostic present status (2013)

As explained in the introduction, the CXRS diagnostic was installed on TCV in 2004. From the original design [35, 20] up to today the diagnostic system has evolved with continual upgrades and optimizations. In this section, the main characteristics of the present diagnostic are described with the related upgrades of the hardware components performed during this thesis between 2010-2013.

The CXRS diagnostic on TCV consists of three observation systems covering the plasma core and edge (see Fig.3.1):

- Toroidal low field side (TLFS, also simply named LFS, in magenta)

- Toroidal high field side (THFS, also simply named HFS, in red)

- Poloidal low field side (PLFS, also simply named VER, in green)

Each system comprises 40 observation chords arranged in pairs in a double slit (DS) configuration (see Sec.3.2.4), for a total of 120 viewlines covering the entire vessel mid-plane (toroidally and poloidally). The toroidal systems have a radial resolution of ± 1.5cm, while the vertical system's resolution is ± 0.8cm

In standard acquisition, the systems acquire with an integration time of $t_{int} = 10 - 30ms$, which gives a time resolution of $t_{res} = 30 - 90ms$. The CXRS acquisition is synchronized with the DNBI pulses via a trigger (positive edge). The DNBI duty cycle is of 30% with a series of OFF-ON-OFF pulses. This is used to determine the CX active signal A (i.e. the CX emitted photons) that must be obtained by subtracting
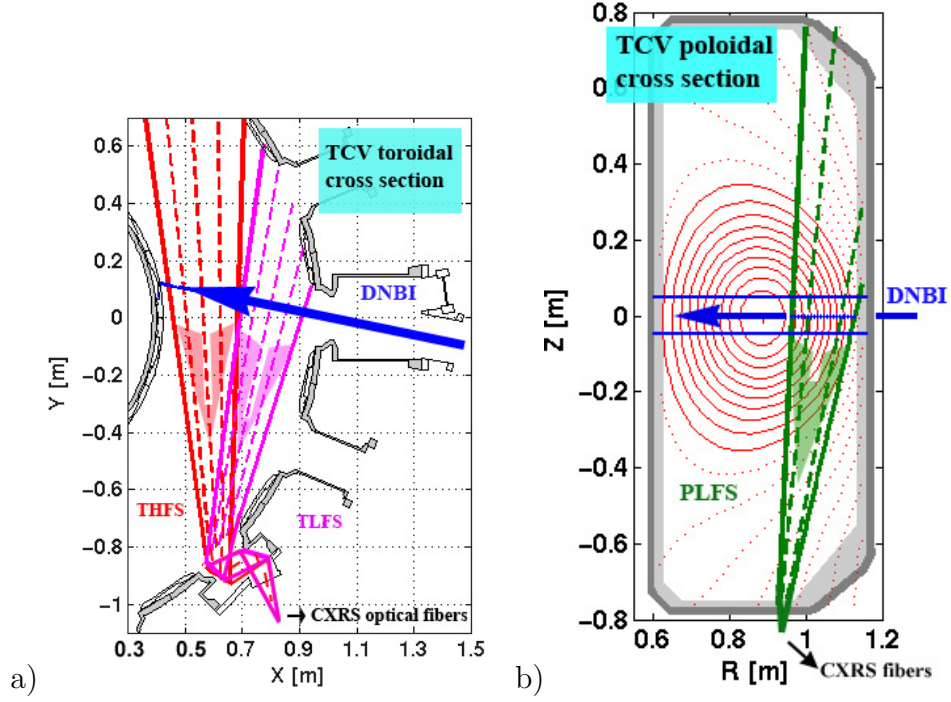
Figure 3.1: a) Toroidal and b) poloidal cross-section view of the three CXRS observation systems on TCV. The beam direction is indicated in blue.

the passive signal P (background emission) before and after the beam ON pulse from the spectrum acquired during the beam (A+P). Depending on TCV conditions and investigated plasmas, the Active/Passive ratio can range from 5-100%. A more detailed description of this technique and of the related analysis can be found in Sec.3.4. In the fast acquisition configuration, the system can operate with $2ms$ resolution. Since the DNBI has a lower ON pulse limit of around 10ms, during this configuration the beam can be used synchronized with a system (the PLFS, set to standard acquisition) and not synchronized with another (the TLFS, set to fast acquisition). This configuration was used with a RT sawtooth trigger (see Secs.2.4.4 and 4.3.1) for the experiments related to the rotation measurements during sawtooth cycles. In Sec.4.3.2 more details on the CXRS configuration required for these measurements are described.

The neutral beam is injected at the horizontal mid-plane Z=0cm, almost perpendicular to the torus, to maximize the beam penetration and minimize the toroidal injected momentum. A small toroidal injection angle of 11.25° is however retained, in order to avoid significant trapped ion population among the injected particles. The CXRS coverage (from the core to the edge) is therefore optimized for plasmas vertically centered around Z=0cm. This constraint required a strong effort in the development of the two electron internal transport barrier scenarios centered at Z=0cm studied in this thesis (see Sec.5.4 and 5.5). Indeed, this position is not optimal for creating eITBs, because of vertical stability and ECH launcher specifics.

The set of optical elements comprising each system is described in detail in Appendix B, during the estimation of the photons transmission from the plasma to the CCD

cameras.

3.2 CXRS upgrades during this thesis

At the start of this thesis in 2009, the TLFS and PLFS systems were fully commissioned and equipped with two Xcam Ltd cameras (each with a e2v CCD 57-10 chip) and with a double slit configuration for the 40 chords (see [20] for a detailed description of the CXRS09 status). Due to some optical problems in the THFS system, this remained off-line awaiting a complete optimization. In a preceding thesis work, many interesting rotation measurements were acquired with the CXRS09 system, but these results also exposed system limitations concerning the rapidity and sensitivity of the installed cameras.

Motivated by the need to measure the rotation profiles during fast events (2-5ms), such as between sawteeth crashes and during the barriers formation with the maximum available radial resolution over the entire mid-plane, upgrades of the CXRS diagnostic were applied. These diagnostic upgrades concerned both the hardware and software. The main modifications made to improve the acquired signal quality and to increase the CXRS exploitation range were:

- installation of two Andor ^{TM} iXon $^{EM+}$ DU897D-CSO-BV cameras with EMCCD gain (see Sec.3.2.1)

- installation of new optical image reducers in front of the Andor cameras (see Sec.3.2.1)

- reinstallation and optimisation of the THFS system (see Sec.3.2.3)

- in vessel mirror replacement for the tangential views (see Sec.3.2.2)

- cooling system replacement (see Sec.3.2.1)

- extended double slit configuration (see Sec.3.2.4)

- new CXRS acquisition program and triggering (see Sec.3.2.5)

- update of CXRS analysis routines employing density coefficients for all three systems (see Secs.3.4 and 3.3.2)

The main listed upgrades are described in the next paragraphs.

3.2.1 EMCCD gain cameras

The most important improvement of the CXRS diagnostic is related to the installation at the end of 2010 of two new cameras on the TLFS and PLFS systems (see Fig.3.2). The existing spectrometers were equipped with CCD cameras featuring on-chip gain (model Andor ^{TM} iXon $^{EM+}$ DU897D-CSO-BV) resulting in improved sensitivity and time resolution, together with a much easier and faster reliable exploitation.
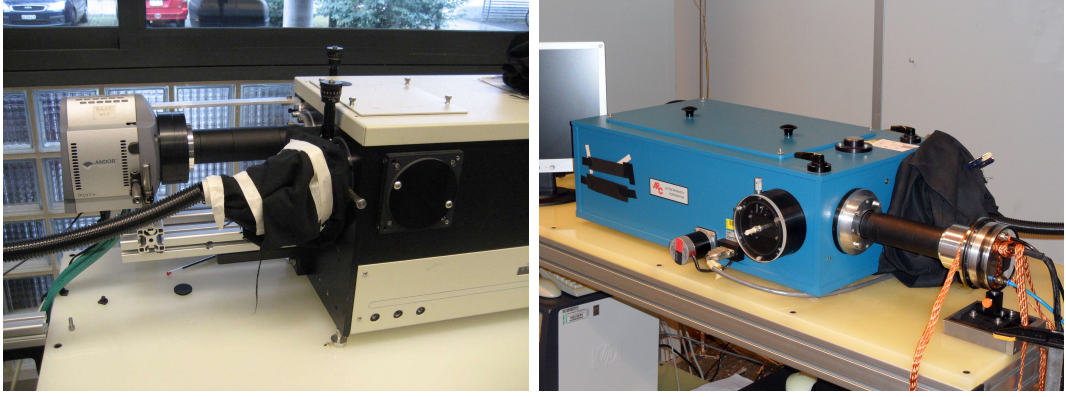
Figure 3.2: The CXRS TLFS (same as PLFS, left) and THFS (right) spectrometers and cameras. The TLFS system is equipped with the new Andor camera, whereas the THFS is still equipped with the legagy Xcam Ltd camera. Notice also the new reducers placed in front of each camera (black tube).

Parameters	Andor cameras (2013)	Xcam cameras (2009)
Back illuminated detectors	e2v CCD97	e2v CCD57-10
Electron multiplying gain	up to 300	no
Preamplifier gain	$\times 1 - \times 5$	no
CCD image area	$8.2 \times 8.2 mm^2$	$6.656 \times 6.656 mm^2$
Pixel size	16 μm	13 μm
Quantum efficiency	95 %	85 %
Frame transfer time	0.25 ms	0.34 ms
Integration time in 512×20 frame transfer format	1.7 ms	12 ms

Table 3.1: Comparison between the main characteristics of the new and old CXRS cameras.

The EMCCD is a recent quantitative digital camera technology, capable of detecting a single photon event whilst maintaining high quantum efficiency [2] [62, 63]. A solid state electron multiplying (EM) register is usually added to the end of the conventional readout register and it is characterized by several hundred stages that use higher than normal clock voltages (see Fig.3.3). The charge transfer through each stage exploits avalanche breakdown within the silicon to produce secondary electrons (and hence produce the EM gain). The photonic signal is multiplied before readout noise is incurred by the output pre-amplifier, rendering the readout noise negligible, even for high readout speeds particularly for low intensity signals. Note that the avalanche process of the EM register introduces an additional noise factor of about $\sqrt{2}$, as observed in [64]. The main characteristics of the Andor cameras compared to the old Xcam Ltd cameras are elucidated in Tab.3.1. During the first CXRS data acquisition with the new cameras, some limitations in the cameras performance were observed, in particular a non-linear dependence of the amplification gain on the CCD illumination. With a high applied

---

[2]The quantum efficiency (QE) of a CCD detector is the ratio of the number of incident photons to the number of electron-holes pairs created (measured in $e^-/photons$).
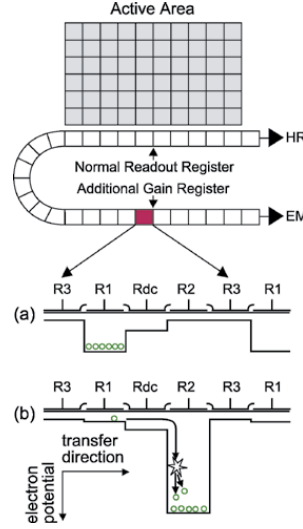
Figure 3.3: Schematic of the EMCCD principle: the EM register is added to the end of the normal register and is characterized by hundreds of stages that use higher clock voltages (a). The charge transfer through each stage exploits the impact ionization to produce secondary electrons (b). The photonic signal is multiplied before readout noise is incurred by the output pre-amplifier (source [62]).

EM gain (see Fig.3.4 for a PreAmpGain=1) the spectra displayed a saturation (peak flattening, in yellow and red) before attaining the CCD chip's limit of $2^{14} = 16384$ counts [3]. A scan of the EM gain, PreAmplifier (PreAmp) gain, exposure time, horizontal and vertical clock speed was performed with a Neon PenRay lamp and with a He-Ne laser to derive the optimal camera parameters for the fast ($t_{int} = 2 - 4ms$) and standard ($t_{int} = 10 - 30ms$) acquisition. For a PreAmpGain=1 it was suggested to adjust the main parameters for a maximal ADC count-rates of 8000 (see Fig.3.4 in blue), while 16000 for the PreAmpGain=2.4 and 5 cases.

The new cameras have largely improved the CXRS temporal resolution as they enable 40 chords full range acquisitions (i.e. 512×20 frame transfer format) with integration times of 1.7 ms (compared to 12 ms before). Even the sensitivity was improved with a Signal/Noise ratio increased by a factor of 8.

In order to maximize the image area arriving on the CCD detector, reducers (consisting of 4 lenses) were installed between the spectrometers and the cameras (see Fig.3.2). This optical element allowed to increase the proportion of the incoming light that reached the CCD.

Additionally, a new water cooling system has been installed to evacuate the heat generated by the Peltier elements inside the cameras. The CCD detectors can now be regularly cooled down to optimal temperatures of -85°C (green tubes in Fig.3.2).

These new cameras have, during this thesis, permitted the detection of faster events in

---

[3]The Andor cameras are 14-bit digital cameras, therefore the analog signal from the CCD is digitized with 14-bit depth by the on-board A/D converter. This signifies that the signal received by each single pixel is converted to a bit sequence (i.e. in numbers). The larger the bit number, the more accurate is the quantization of the signal. If n is the number of bits, the outgoing signal can assume 2^n different values ($2^{14} = 16384$).
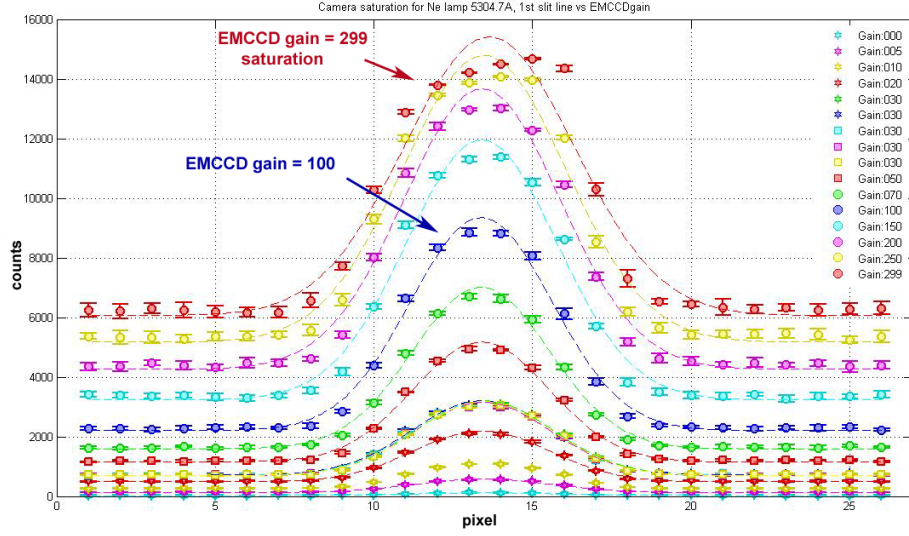
Figure 3.4: Saturation problem observed during a EMCCD gain scan with a Neon PenRay lamp (5304.7A). The camera parameters were: Track:10, Tint:0.3s, Horizontal speed:3(1MHz), Vertical speed:4($3.3\mu s$), PreAmpGain:1, Temp:-82.0°C. An acquisition limitation is observed for the largest gains (200-299).

scenarios where the beam is strongly attenuated and the active signal weaker or more irregular (just after the sawtooth crashes and in low density plasmas featuring eITBs). At present, the cameras can be rapidly tuned between TCV discharges, to increase the measurement quality by choosing the EM or conventional register, the PreAmp gains and various readout-speeds.

The installation of the new cameras has required a modification of the entire CXRS acquisition process and of the data analysis. Their control systems were then integrated into the TCV plant control system (see Secs.3.4 and 3.2.5).

3.2.2   In vessel mirrors replacement

During the TCV opening of November 2010, the aluminum-SiO_2 coated mirrors of the horizontal CXRS systems, damaged by glow exposure in 2008, were replaced with a pair featuring a beral coating. The re-installation of the CXRS diagnostic also required a verification of the mirror positions on an optical table and then inside TCV (chords alignment, see Sec.3.3.1, before and after the modification). Fig.3.5 shows the entire CXRS observation window on the optical table for the alignment tests. The mirrors are shown and it is possible to distinguish some damage traces on their surface. After this incident, a system of shutters was introduced in order to protect the mirrors and avoid further destructive manipulation. The change of the in vessel mirrors required an absolute calibration in order to account for the new mirror surfaces in the CXRS acquisition (see Sec.3.3.2).
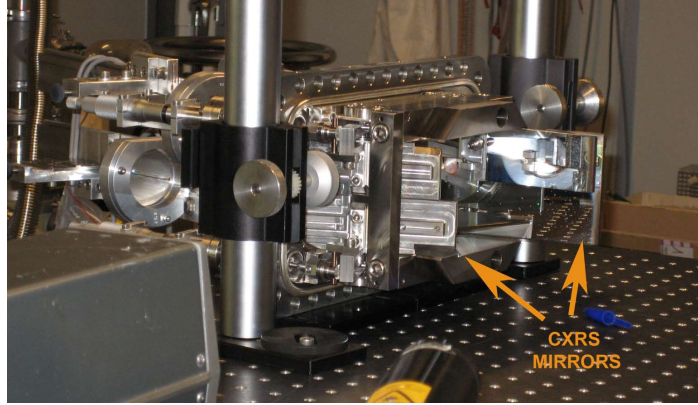
Figure 3.5: Verification of the mirrors positions on the optical table using a laser before the mirror replacement. The damages on the mirrors can be distinguished at their extremities.

3.2.3 Reinstallation of the THFS system

In the second half of 2011, considerable effort was employed in reviving the toroidal high field side system (see Fig.3.2). Together, the THFS and TLFS systems measure across the entire TCV midplane and were used to exploit the toroidal rotation asymmetry in a derivation of the poloidal rotation and the radial electric field, essential in the eITB study (see Sec.5.2). The previous TLFS Xcam camera with an e2v CCD57 detector was installed on the Czerny-Turner spectrometer ACTON AM-506 $f/\#_{spex} = 5.5$ aperture in first order and a 0.66 m focal length. An optical reducer, consisting of three lenses, similar to that used by the other two systems, was installed at the slit exit to fit the image size to the detector's surface.
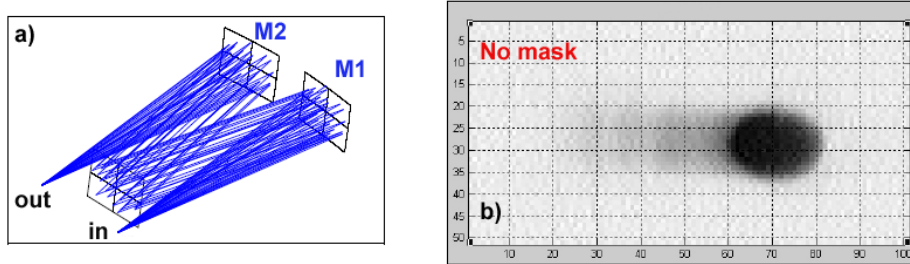
Figure 3.6: Tests to identify the THFS system optical defect. A HeNe laser ($\lambda = 543.5nm$) is injected into a fiber ($\phi = 200\mu m$ and $NA = 0.4$) placed in front of the spectrometer. a) Schematic light path: the light inside the spectrometer is reflected by the first mirror M1, attains the grating and finally is reflected by the second mirror M2. b) Light spot detected by the camera CCD: the spot is clearly not focused.

Unfortunately, the spectrometer mirrors appear to have strong defects (incorrect astigmatism, coma effect,..) already observed in [20, 35] and do not correctly focus the analyzed light (see Fig.3.6 without any mask). Various tests were performed to identify the error (coming from the first M1 or second M2 mirror or the grating). These tests have concluded that M1 is a parabolic astigmatic mirror, whereas M2 is a parabolic stigmatic mirror. By placing masks on various regions of the first mirror surface (see
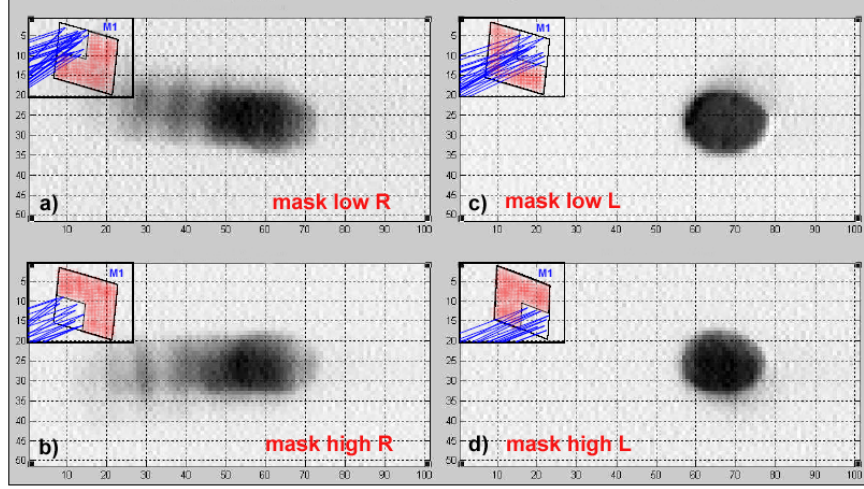
Figure 3.7: Tests to identify the THFS system optical defect. A HeNe laser ($\lambda = 543.5nm$) is injected into a fiber ($\phi = 200\mu m$ and $NA = 0.4$) placed in front of the spectrometer. a-d) By placing different masks on various regions of the first mirror surface M1, a better focusing is identified when the left side of the mirror is covered.

Fig.3.7), a better focal was obtained when the left side of the mirror is covered (see Fig.3.7.c and d). For this, a laser HeNe ($\lambda = 543.5nm$) was injected into a fiber ($\phi = 200\mu m$ and $NA = 0.4$) placed in front of the spectrometer. This resulting image on the detector indicates the presence of a clear defect on the left side of the optical element (note the large non focused spots in Fig.3.7.a and b), but it is still unclear from which element the main error originates (it appears to be a superposition of several defects). Due to the high request of the CXRS systems operation and a lack of time, it was decided to partially mask the first mirror (30% of the left side), in order to reduce the main defects (but this also reduced the light throughput). Other solutions, like using a corrective cylindrical lens at the spectrometer exit were attempted, but did not result in a clear improvement. During the upcoming TCV opening in 2014 further tests are planned to identify the defect sources and find a permanent correction.

The THFS acquisition was synchronized with the TLFS and PLFS systems and the related acquisition routines modified to be compatible with the existing TLFS and PLFS acquisition process. All three spectrometer systems are now integrated into the TCV plant control system (Sec.3.2.5).

3.2.4 Double slit extended configuration

During this thesis, the three CXRS systems were routinely operated with a double slit configuration for the optical fibers. We recall that the 40 optical fibers are divided in two bundles of 20 fibers each, which are fixed adjacently (see Fig.3.8 and [20]). The fibers are arranged in pairs, so that two fibers collect the light at the same radial position (see Fig.3.9.c). To improve the data quality and reduce the profiles uncertainties in low density or irregular plasmas, such as plasmas with eITBs, a binning between the coupled measurements was often employed.

Figure 3.8: Example of a double slit. The two arrays of 20 fibers each are fixed together and placed at the entrance slit. Notice that this configuration allows to form 20 pairs of measurements.

During the reinstallation of the THFS, the second slit, which was initially covered by a mask, was "opened" in order to acquire simultaneously with all 40 fibers.

In October 2013, an extended double slit configuration for the THFS and TLFS systems was tested. The two fibers arrays were displaced to position the fibers of the first slit in between the fibers of the second slit. In this way, a near double radial resolution was attained (of around 7-8mm) covering the entire midplane. In Fig.3.9.a-b an example of this extended configuration applied to shot #49573 is illustrated. The locations of the 2×40 collecting volumes are shown in Fig.3.9.a, determined after an alignment verification (see Sec.3.3.1). A small displacement of the upper chords towards the LFS of about 7mm was determined. From the measured toroidal rotation profiles, it is possible to observe the increased radial resolution ($\pm 7 - 8$mm instead of ± 15mm) of the diagnostic. The entire TCV midplane is covered by 80 separated measurements. The THFS profiles display larger errorbars, which are mainly due to the lower quality of the ACTON spectrometer and to the weaker active signal acquired (the beam is considerably attenuated in the HFS region). Note that shot #49573 is a repetition of a previous discharge #40130 that will be discussed in Sec.4.2.1 in Fig.4.1 (multiplied by $sign(I_p) = -1$, showing only the LFS). For this discharge, the CXRS diagnostic was configured with the normal double slit configuration (Fig.3.9.c), with the 2×40 chords placed in pairs for a total of 40 radial positions measurements covering the entire midplane.

This improved spatial resolution of the CXRS diagnostic will be used in the future in order to study the evolution of small radial extended structures in the plasma.

3.2.5 Triggering and CXRS implementation in TCVPC system

During 2012, the synchronization of the THFS system with the TLFS and PLFS was optimized and integrated into the same acquisition routines. Due to problems with erratic triggering times, during December 2011 the acquisition of the three systems was only possible with a single common exposure time. In an effort to correct the simultaneous trigger of the CXRS cameras, the four CXRS triggering cards were revised and a counting error in the electronics corrected.
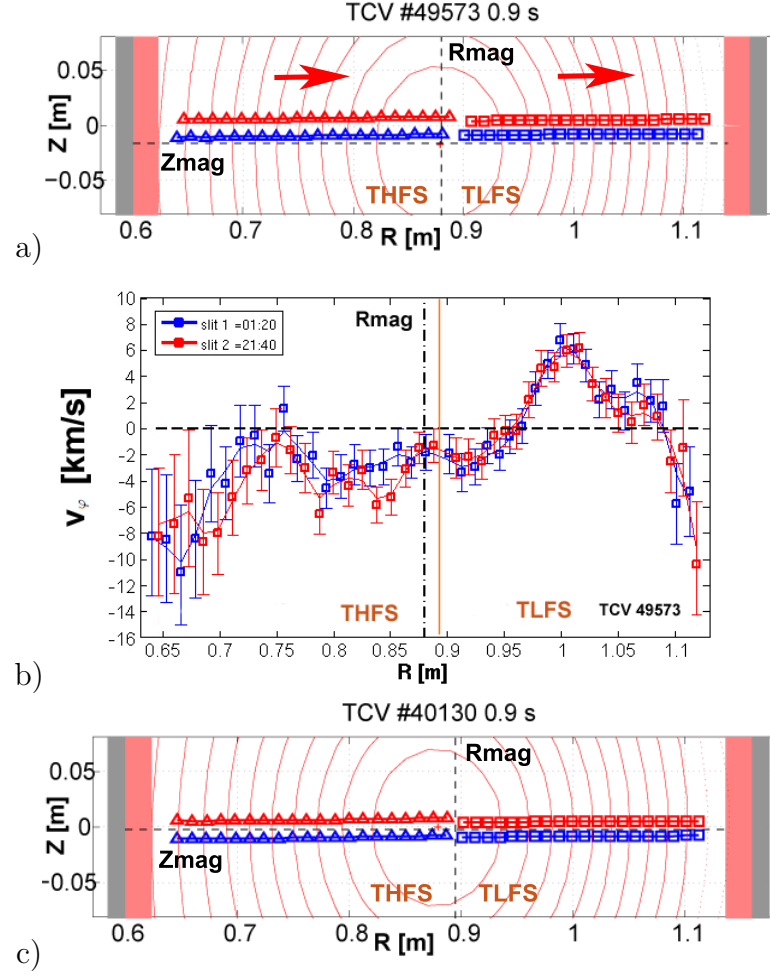
Figure 3.9: a) CXRS measurements positions with the extended double slit configuration for shot #49573. A small displacement of the upper chords towards the LFS of about 7mm can be noticed. b) Toroidal rotation profiles in function of R for both THFS and TLFS systems with the extended configuration. A total of 80 measurements positions covers the entire TCV midplane. c) CXRS measurements positions with the standard DS configuration for similar shot #40130. The chords are placed in pairs for a total of 20 radial positions for each system.

Presently, the three systems are synchronized with the DNBI and are simultaneously triggered at each beam ON pulse (positive edge triggering). During the experiments of rotation measurements in between sawteeth, the TLFS system was no longer synchronized with the DNBI but triggered by the RT-control sawtooth trigger (see Sec.4.3.1). A recent RT-control sawtooth trigger modulation developed on TCV that results in a constant ST period [65], is also being tested at the time of writing, and may lead to a new solution for future sawtooth related experiments. Although a RT DNBI trigger was also suggested during this thesis [66], further work is required to develop this concept. All these different trigger methods illustrate many possibilities remaining to enlarge the CXRS exploitation in future TCV operation.

Finally, the CXRS diagnostic, previously integrated into the TCV plant control system (TCVPC) as a component of the DIAG system, was modified to become an

independent system (as are DNBI or Thomson diagnostics) and implemented into the modified TCVPC sequence. This separation allows the CXRS system to be controlled independently of the main TCV diagnostic sequence allowing for faster configuration modification and system recovery.

The TCVPC system is the central component that coordinates TCV daily operation. It consists in a series of routines that control the operation of several sub-systems (turbo generator, ECRH, diagnostics, timers, MDS acquisition,...) integrated within several state machines. It controls and monitors the execution of individual pieces of codes that every system must perform within each state, for a complete TCV plasma cycle. To avoid problems during the TCV discharge sequence, it was essential to implement the code for these various states that, although time-consuming, resulted in error-free operation.

3.3 Alignment verification and absolute calibration

In order to include the CXRS diagnostic status in the calculation of the measured carbon density profiles, two important controls were periodically performed on the CXRS. These are the alignment verification and the absolute calibration. The first precisely set the positions of the CXRS chord measurements and corrects for any displacement between the optical elements. The second monitors the transmission of the optical elements and is used to derive the transmission coefficients for the density profiles.

3.3.1 Chords alignment verification

During the TCV opening in 2012, a complete alignment of all systems was performed inside the TCV vessel, instead of the usual, less precise alignment, performed through a port from outside the TCV vessel. Two plastic targets covered with a millimeter

Figure 3.10: Illuminated targets for the CXRS alignment of the a) HFS and b) LFS toroidal systems, c) Light spots on TCV tiles from the back-illuminated fibers of the VER system.

paper, one for the toroidal systems and the other for the vertical system, were placed at various TCV inner ports for the alignment. By back-illuminating the fibers with a green laser, the targets were illuminated by 40 spots corresponding to the CXRS
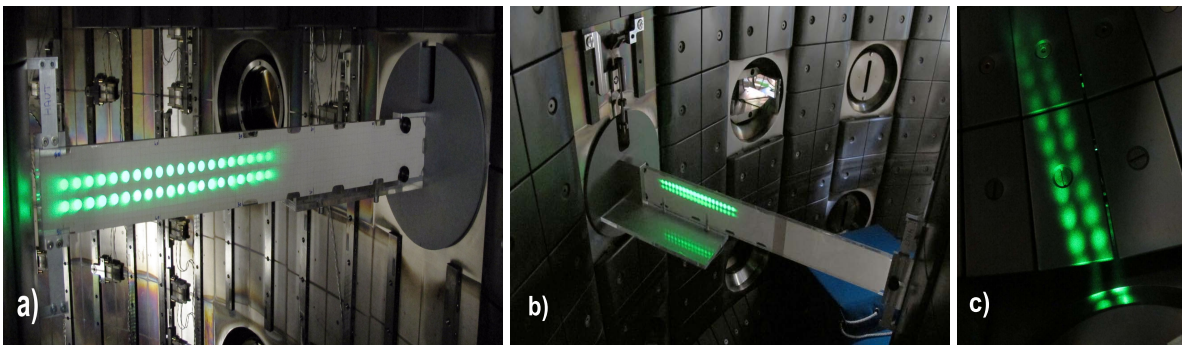
lines of sight (see Fig.3.10.a-b). The illuminated target was placed at two positions for every system and photographed. By reconstructing with AutoCAD and Matlab the spots positions on the targets and on TCV tiles (see Fig.3.10.c), the directions of all CXRS view lines inside TCV were determined. The combination of these data with the beam direction was used to derive the positions of the CXRS-DNBI crossing points for all the three systems in TCV spatial coordinates to within a few mm.

A correct estimation of each measurement position for the three systems is particularly important in the determination of the radial electric field. The E_r calculation is based on a precise mapping of both HFS and LFS impurity profiles (see Sec.5.2 for more details). A simple method to cross-check sufficient alignment of the three systems can be performed by comparing the ion temperature profile of the vertical system with the toroidal LFS and HFS system, which should be identical as they correspond to the same measured radial LFS region.

3.3.2 Absolute calibration

During this thesis several absolute calibrations of the CXRS diagnostic have been performed using different methods, depending on whether or not it was possible to work inside the TCV vessel.

A first calibration was performed in 2011 from outside TCV. Due to the limited TCV port size, an integrating sphere, together with a support structure, were homebuilt in order to place the sphere inside the TCV vessel through a lateral port (see Fig.3.11.a). Acquisitions of this light source were performed at several positions to illuminate the entire fiber set. The fabricated sphere was successively calibrated against a commercial integrating sphere (Labsphere Ltd, Model US-060-SF) equipped with a lamp of known radiance as a function of wavelength. Despite the effort to build an homogeneous illuminating sphere, during the analysis of the data an irregular intensity emitted by the sphere was obtained. This effect was deduced to be caused by the only partially homogeneous paint applied on the inner surface of the sphere and to frequent lamp overheating during the acquisition. These results did not turn out to be completely exploitable.

During the TCV opening in 2012, an absolute calibration for all three systems was performed from inside the TCV vessel using the commercial integrating sphere with a movable support built to displace the sphere inside the tokamak vacuum vessel (see Fig.3.11.b). Many acquisitions of this light source were performed for several sphere positions so that the entire fiber set was illuminated. During the first calibration acquisition, a strange linear decrease in the fiber intensity was observed that, after some lab tests, was corrected by increasing the time between the EMCCD gain set and the spectrum acquisition. The absolute calibration depends on the camera configuration and the mirror state and determines the total loss of the optical system (i.e. the experimental ϵ_{tot}, see Appendix B.1.6 for a detailed discussion of the estimated and measured values). It is, therefore, essential in order to derive reliable density profiles. Note that this was the first time that all three CXRS systems were simultaneously calibrated with the new Andor cameras.
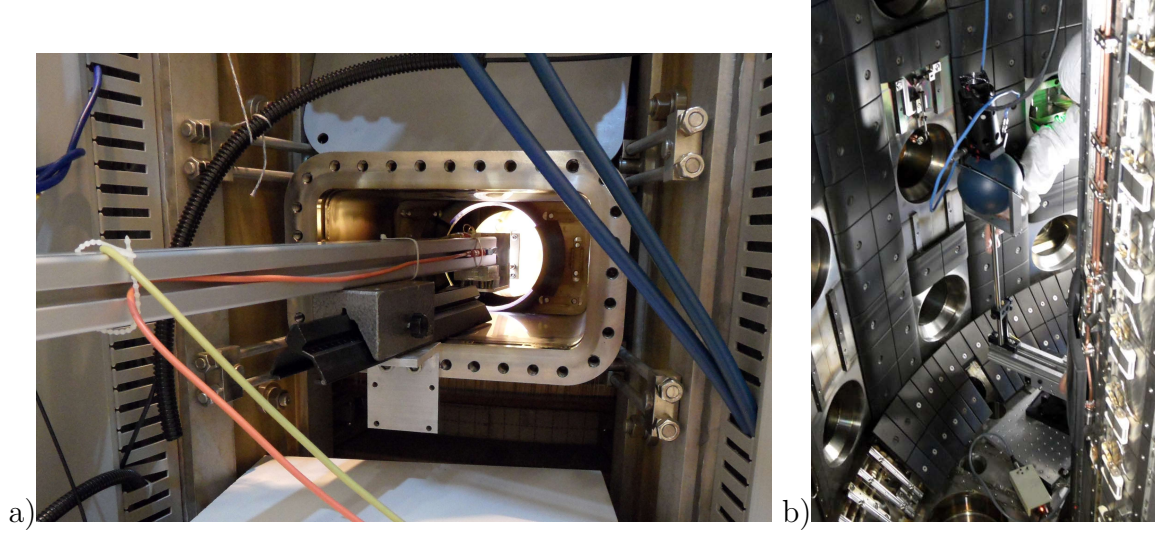
Figure 3.11: a) Hand-built integrating sphere and support inserted inside TCV through a port b) Integrating sphere (in blue) placed inside TCV for the absolute calibration.

For completeness, we shortly summarize the general analytical procedure to determine the calibration coefficients, which were used to calculate the carbon density profiles. As explained previously, the CXRS absolute calibration is performed with a calibrated lamp of known radiance R_{labsph} $[ph/s/nm/m^2/sr]$. The radiance is integrated over the range of wavelength covered by the detector (around [527-531]nm), which gives R_{cal} $[ph/s/m^2/sr]$. In parallel, an integration over the same wavelength range is performed for each measured absolute calibrated spectra S_{cal} $[counts/s]$. The calibration factors, essential to obtain the carbon density, are therefore derived by the relation $Cf = R_{cal}/S_{cal}$ $[ph/counts/m^2/sr]$.

During normal TCV operation, the radiance R_{meas} (integrated on the same lambda range) of each emitting sampling volume measured by the CXRS cameras S_{meas} is obtained from $R_{meas} = C_f \cdot S_{meas}$ $[ph/s/m^2/sr]$. Note that here, each C_f coefficient accounts for the total losses and the etendue of each fiber. At the same time, the radiance of an extended source can be obtained by integrating its emissivity $E_{\Phi,v}$ $[ph/s/m^3/sr]$ along the observing chord. In the specific case we have:

$$R_{meas} = \int E_{\Phi,v} dl = (1/4\pi) \int n_C \cdot n_B^{E_0} \cdot r_{cx87} dl \; [ph/s/m^2/sr] \tag{3.2}$$

with $n_B^{E_0}$ the beam density, n_C the carbon density and r_{cx87} the excitation rate for the $n = 8 \rightarrow 7$ transition of C^{6+} (similarly to Eq.B.3 in Appendix B). Note that only $n_B^{E_0}$ is assumed to vary along the observing chord coordinate dl in the small sampling volume. Hence, we can write

$$R_{meas} = (1/4\pi) \cdot n_C \cdot r_{cx87} \cdot n_{Bl}^{E_0} \; [m^{-3} \, m^3/s/m^2/sr \equiv ph/s/m^2/sr] \tag{3.3}$$

where $n_{Bl}^{E_0} = \int n_B^{E_0} dl$ is the chord integral of $n_B^{E_0}$. The carbon density is finally obtained from;

$$n_C = \frac{R_{meas}}{r_{cx87} \cdot n_{Bl}^{E_0}} \, [m^{-3}] \tag{3.4}$$

where R_{meas} has been calculated using the determined calibration coefficients C_f and the measured spectra S_{meas}.

3.4 CXRS profiles analysis

During this thesis, to accomodate a continuous increasing demand for the CXRS data during TCV operation and, following the installation of the new Andor cameras, a strong effort was undertaken in order to upgrade and automate the analysis process. In this section we summarize the main steps of the CXRS analysis from the acquired raw spectra to the final carbon temperature, density and rotation profiles. An application to discharge #42422 (studied in Appendix B) is briefly described. For more details on the complete analytical procedure, the reader is invited to consult [20].

In order to derive the carbon parameters profiles, a sequence of steps must be followed starting from the raw acquired CXRS spectra:

- CCD offset subtraction

- determination of the passive CX spectra (P) during the DNBI pulses

- calculation of the active CX spectra (A)

- determination of the instrumental function (IF) from the wavelength calibration spectra (acquired after each shot)

- gaussian fit of the active spectra using the instrumental function

- calculation of the carbon local measurements from the fit parameters

- mapping of the measurements positions using the data from the alignment verification (R, Z, ϕ, Sec.3.3.1) and the LIUQE magnetic equilibrium reconstruction (ρ_ψ, See.2.4.5), taking into account the beam attenuation

3.4.1 Determination of the active spectra

The passive spectra (P) during the DNBI pulses are obtained by interpolating the spectra acquired before and after an ON pulse. The active spectra (A) are then calculated by subtracting these passive components to the spectra acquired with the ON pulse (A+P), as shown in Fig.3.12.b. This method relies on there being a small variation of the passive signal during an entire OFF-ON-OFF cycle. If the background varies rapidly during a fast event, like in the formation of eITBs, the active signal can be affected. This can be partly overcome by reducing the CXRS acquisition time. For

slow variations, this effect is well compensated by interpolating the passive spectra with a cubic spline fit [20]. An example of the DNBI OFF-ON-OFF pulses and of the total acquired CXRS signal time evolution is shown in Fig.3.12.a. With the new acquisition routines, it is possible to immediately visualize and deselect some problematic pulses (no DNBI, fast ramps or disruptions (like at 1.4s)) before starting the calculation of the active signal. From Fig.3.12.b, the presence of a strong passive CX contribution on

a)   b)
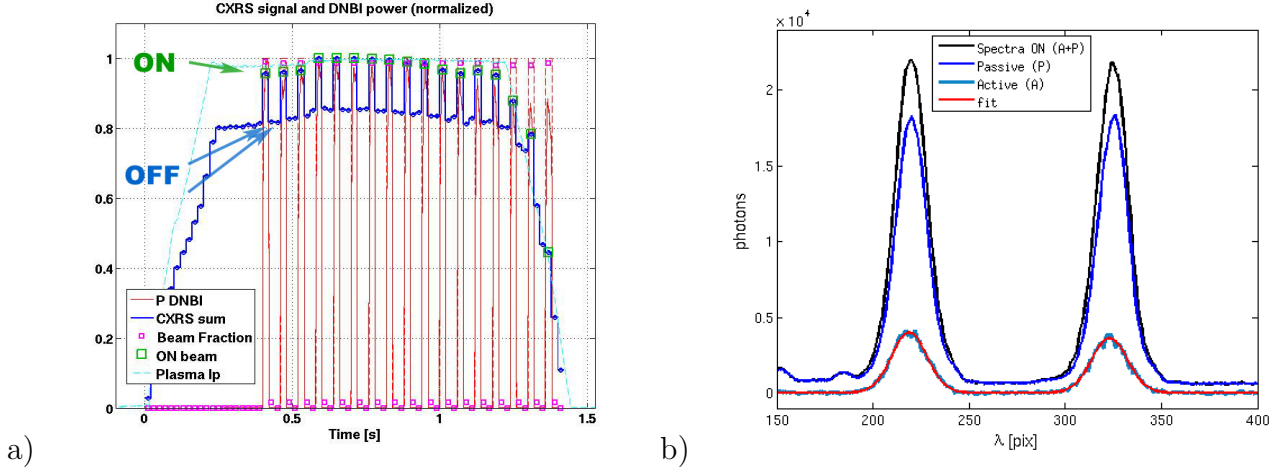
Figure 3.12: a) Visualisation of the DNBI pulses and CXRS signals during a discharge (#42422). A deselection of the problematic aquisition intervals can be performed at this stage. b) Passive (P), active (A) and A+P (ON pulses) signals measured at 1s with a double slit configuration (each peak corresponds to a slit). In red the fitted profile of the active spectrum is also shown. Notice the initial CCD offset of the spectrum ON signal to be subtracted.

TCV (in blue), which is much higher than the active contribution from the DNBI (in azure) is visible. Previous studies have identified the main contribution to the passive signal as coming from electron impact excitation and the interactions of fully stripped impurity ions with the thermal $n = 2$ population present at the edge of the plasma. In addition, the free electron recombination appears also to have a non negligible role [35].

3.4.2 Wavelength calibration and determination of the instrumental function

The full frame calibration spectra (see Fig.3.13.a) acquired after each shot with a Neon Pen-Ray lamp are needed to perform a precise wavelength calibration. During this calibration, known calibration lines observed by each slit are identified and their pixel positions are associated with the corresponding wavelength via the dispersion relation $\lambda(x_{CCD})$ [20]. In Fig.3.13.b the four main calibration reference lines used to determine the dispersion relation are indicated with their corresponding wavelength. The vertical line in blue is the reference of the CVI transition line $\lambda = 529.059$nm seen by each slit. Note that the dispersion relation slightly differs from the official specifications and can vary for each considered chord and slit. This effect may be due to

the environment conditions (temperature, humidity) or the wear of the instruments. Therefore the wavelength calibration is essential to correctly determine the position of each emission line. We quickly recall that all detected spectral line profiles result
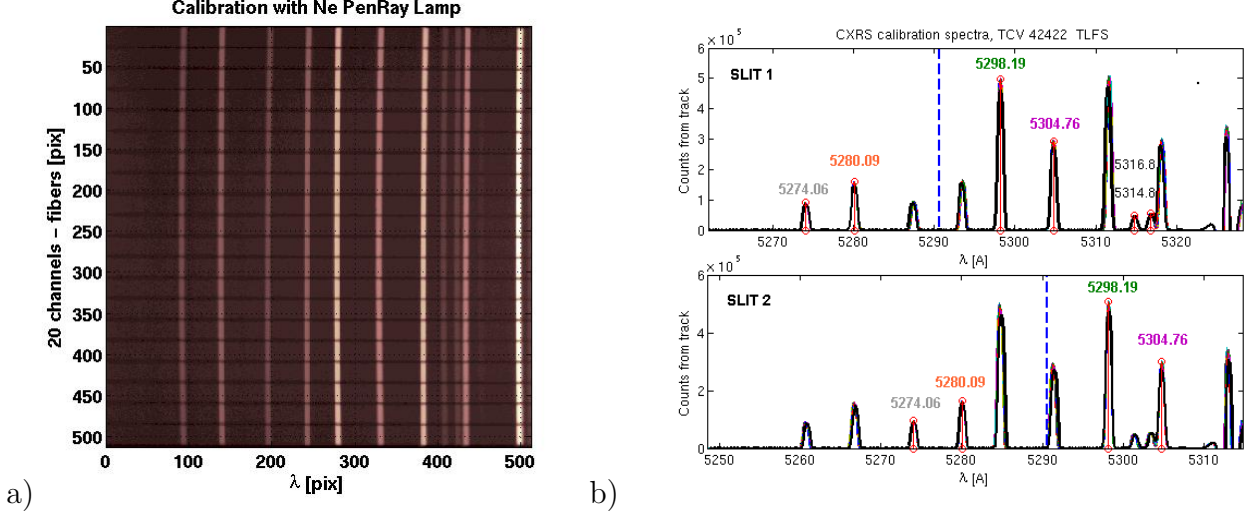
Figure 3.13: Wavelength calibration spectra: a) Full frame calibration spectra showing the 20 regions of interest for the two slits b) Profile of the calibration spectra for each slit, with indicated the wavelength of the reference lines associated to the CCD pixels via the dispersion relation $\lambda(x_{CCD})$. The vertical lines in blue indicate the CVI transition line λ =529.059nm seen by each slit.

from the convolution of the real spectrum with the instrumental function IF. Therefore the IF is essential since it accounts for the distortion of the spectral profile (broadening, displacement, a/symmetry) induced by the optical elements, and its width is also affected by the entrance slit aperture. The instrumental function for each chord of each slit is obtained from the nearest calibration line to the CVI line (on TCV the strongest line λ =529.8nm, in green), normalized, and then fitted by a gaussian and rectangular functions in order to determine the centroid position (see Fig.3.14.a). The instrumental function FWHM obtained for the three systems, determined by the entrance slit aperture and the spectrometer distortion, range between 5.7-6.3 pix (TLFS, see Fig.3.14.b), 10.3-11.3 pix (THFS) and 6.1-6.8 pix (PLFS) [67]. By applying the IF on all the calibration reference lines, the final corrected wavelength positions and the related dispersion relations are determined. The dispersion relation measured for the TLFS and the PLFS cameras is of about 0.13Å/pix, while for the THFS it is of 0.11Å/pix.

3.4.3 Fitting of the active spectra

The calculated active spectra with the double slit configuration are successively fitted with the convolution of the previously derived instrumental function and a gaussian spectrum profile (least-squares fit). In Fig.3.12.b, the passive (P), active (A), A+P spectra and fitted profiles are shown for one chord at the selected DNBI pulse (1s).

a)   b)
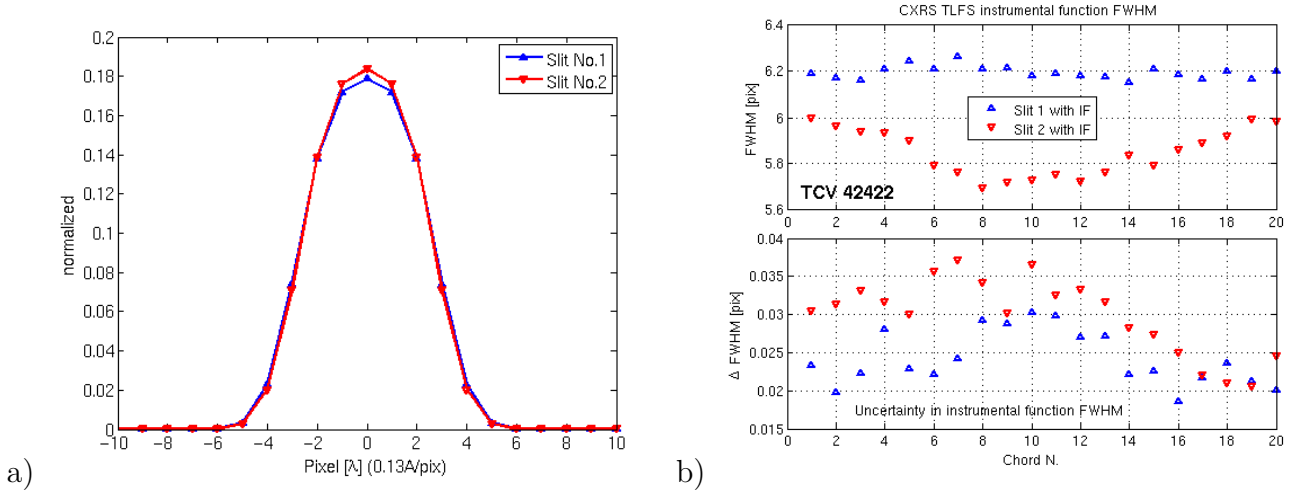
Figure 3.14: a) Instrumental function associated to chords N.1&21 (slit 1&2). b) Instrumental function FWHM and related uncertainties as a function of the chords number for both slits (#42422). A variation of the IF width along the input slit can be observed. The dispersion relation measured for the TLFS cameras is of about 0.13Å/pix.

A zoom of the same active spectra and the applied fitting (showing also the spectrum uncertainties) is illustrated in Fig.3.15. From the gaussian fitting parameters, the Doppler shift and Doppler broadening are calculated, which measure the carbon rotation and temperature. Finally, from the active signal intensity and the absolute calibration coefficients (see Sec.3.3.2), the carbon density and Z_{eff} profiles are derived, assuming carbon being the main impurity. An example of the carbon profiles derived from the presented analysis process is shown in Fig.3.16 for the studied discharge.
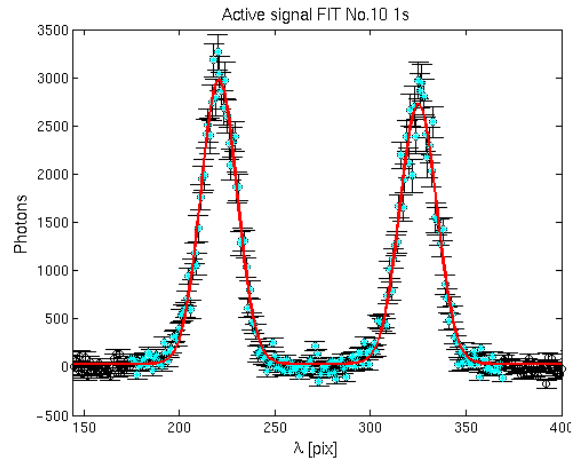
Figure 3.15: Fitting of the active signal for shot #42422 at 1s for the chord N.10.

A calculation of the main uncertainties of the ion profiles shows that most of the error comes from the active signal fitting [67]. Indeed, almost 85% is due to the determination of the FWHM broadening (for T_i) and of the Doppler shift (for v_φ) from the
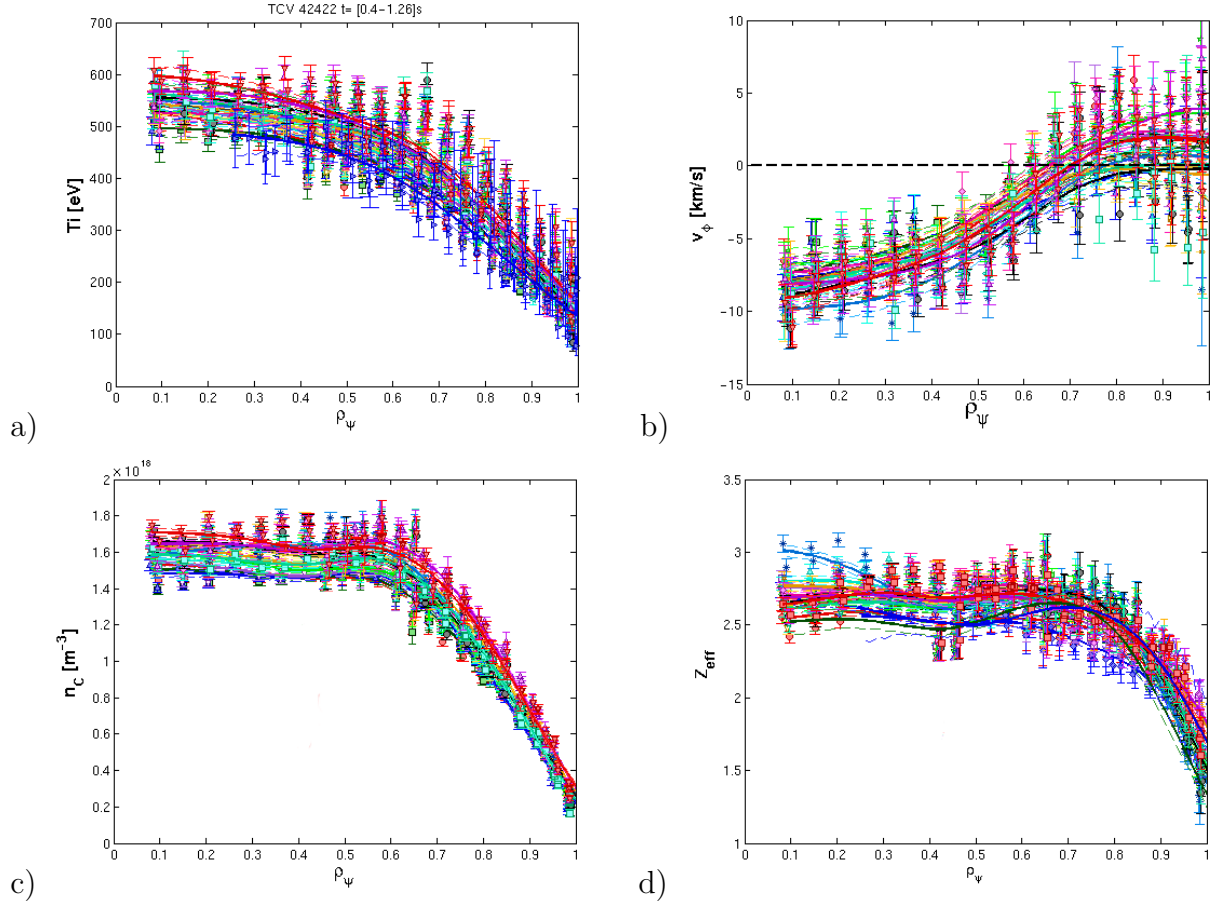
Figure 3.16: a) Carbon temperature, b) toroidal rotation, c) density and d) Z_{eff} for shot #42422 (t=[0.4,1.26]s).

fit sequence. For the T_i profiles, the multiplet corrections and the IF shape affect also the uncertainties, but are minor compared to the fitting. The measured errors in the plasma core usually range between $\Delta T_i = 5 - 30 eV$ and $v_\varphi = 1 - 2.5 km/s$ (this latter corresponding to a shift of 0.03-0.4 pixel $\sim$ 0.004-0.052Å). By comparing the TLFS and PLFS systems, a small difference of about 20eV has been identified between the corresponding T_i profiles. For the density profiles, the main errors are due to the passive photon determination (photon statistics, <5%) and the uncertainties of the calibration coefficients (10-30%, from absolute calibration, see Sec.3.3.2) and of the beam attenuation estimation (<10%). Other sources of errors are discussed in more details in [20, 67], like the Zeeman and Stark broadening (causing a $\Delta_{Zeeman} \cong 0.2$Å and $\Delta_{Stark} < 0.1$Å) or the effects due to the energy-dependent CX cross-section and the gyro-motion effects. These latter are found negligible (< 0.001Å of wavelength shift) and are not included in the CXRS analysis (as done in [68]).

For standard TCV operation, the central carbon temperature can range between 100-600eV, while the density varies between $0.5 - 2 \times 10^{18} m^{-3}$. The toroidal rotation can be observed in the co and cnt-current direction with peak values up to 40km/s, varying significantly from Ohmic or heated plasmas, L-mode or H-mode plasmas, high/low

current and plasma density. Usually the poloidal rotation profile is much lower than the toroidal rotation (as predicted by neoclassical theory) with values up to 5km/s in the clockwise or counter clockwise direction.

3.4.4 Boron and carbon profiles measurements after boronization

During the first weeks following TCV boronization conditioning in November 2012, the TLFS and PLFS spectrometers were set to observe the BV ($n = 7 \rightarrow 6$ at λ =494.467nm) emission line. Note that other devices, such as ASDEX Upgrade (AUG) and Alcator C-Mod, use the BV rather than the CVI emission (n=8→7 at λ =529.059nm) used on TCV. For the first time, active signals from the BV impurity have been acquired and information on the impurity content and radial profiles obtained for comparison with the C profiles.

In order to acquire the B^{4+} emission line, the TLFS and PLFS spectrometers were set to wavelengths 4939.7/4941.7Å(TLFS/PLFS-VER) instead of the usual 5286.0/5288.0Å for the C^{5+} emission line. For comparison, the THFS system was kept on the standard carbon configuration. In order to determine the boron profiles, some modifications in the analysis routines were performed (i.e. wavelength calibration, IF, excitation rate $r_{CX} = < \sigma v >_{CX}$ for BV(n=7→6)). Similar Ohmic shots with $I_p = -290kA$, line
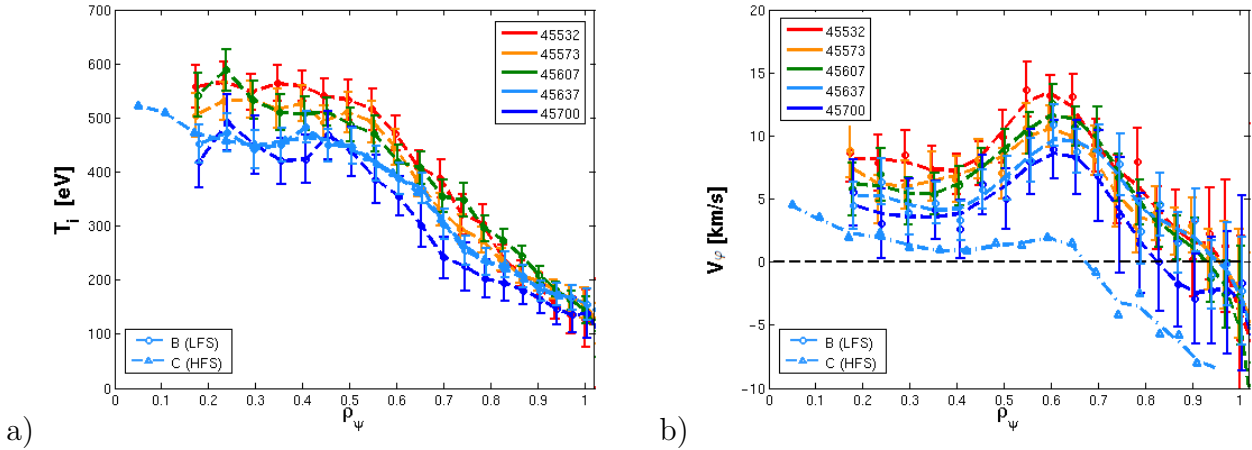
Figure 3.17: Boron a) temperature and b) toroidal rotation from TLFS measurements (circle) for similar discharges #45532, #45573, #45607, #45637 and #45700 taken at $t = [0.6, 0.8]s$. For comparison the THFS carbon profiles (triangle in azure) for shot #45637 are also added.

averaged density from FIR $n_{e,av} = 2.1 - 2.7 \times 10^{19}m^{-3}$, $\kappa_a = 1.35$, $\delta_a = 0.28$ at $Z = 1cm$ were repeated during the first 200 discharges following the boronisation. In Figs.3.17.a,b and 3.18.a,b are plotted the boron profiles measured for a selection of these discharges at $t = [0.6, 0.8]s$. The profiles for the THFS system, set to the carbon line, are also added for shot #45637 (in azure). Note the close superposition of the T_B and T_C profiles, indicating that both boron and carbon ions are thermalised with the main deuterium impurity (and that the diagnostic analysis appears to be working

well). By comparing the boron density profiles n_B obtained with the TLFS system
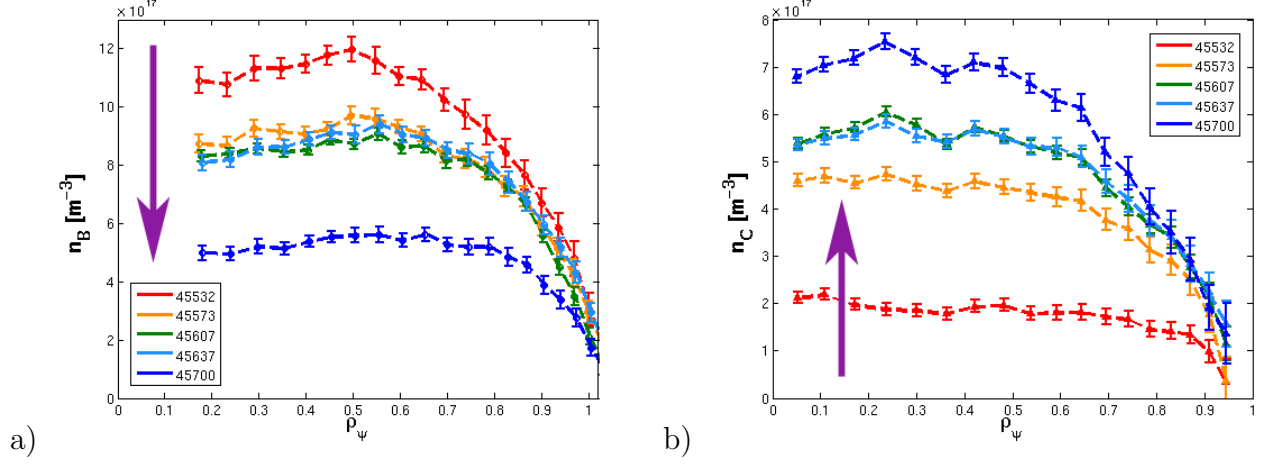
Figure 3.18: a) Boron and b) carbon density profiles for similar discharges #45532, #45573, #45607, #45637 and #45700 measured at $t = [0.6, 0.8]s$. Notice that the boron density decreases with the number of shot, while the carbon density increases.

and the carbon density profiles n_C obtained with the THFS system, a reduction of n_B and an increase of n_C is clearly visible. This trend is more evident in Fig.3.19, where the central density of both ions (i.e. $\rho_\psi \cong 0.2 - 0.3$) is plotted as a function of the discharge number (time). As expected, the boron content (in cyan) reduces with TCV operation, while the carbon content (in violet) increases. This plot shows that the CXRS acquisitions during TCV restart can be used to observe the gradual decrease of the B^{5+} impurity density (from the boronization) simultaneous with the increase of the C^{6+} impurity (from the tiles).
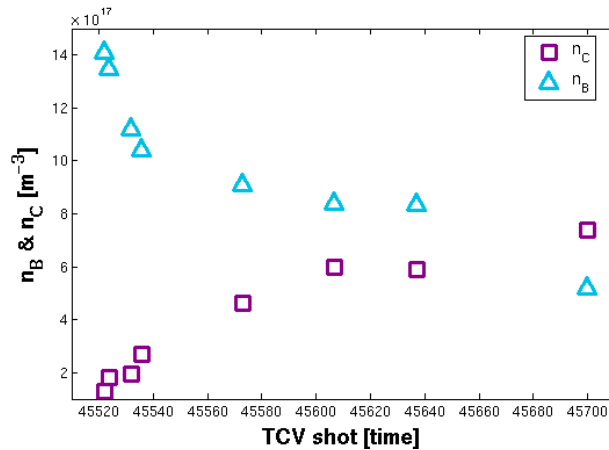
Figure 3.19: Carbon/boron core ($\rho_\psi \cong 0.2 - 0.3$) density evolution as a function of TCV shot number (#45522-#45700).

Finally, two identical Ohmic shots with $I_p = -140 kA$, line averaged density from FIR $n_{e,av} = 2.2 \times 10^{19} m^{-3}$, $\kappa_a = 1.37$, $\delta_a = 0.38$ at $Z = 1 cm$ were acquired with the boron

and carbon configurations. In Fig.3.20 the carbon and boron profiles measured at the LFS at $t = [1.2, 1.35]s$ are plotted (circle) together with the carbon profiles measured at the HFS for shot #45651 (triangle). The carbon and boron toroidal rotations are
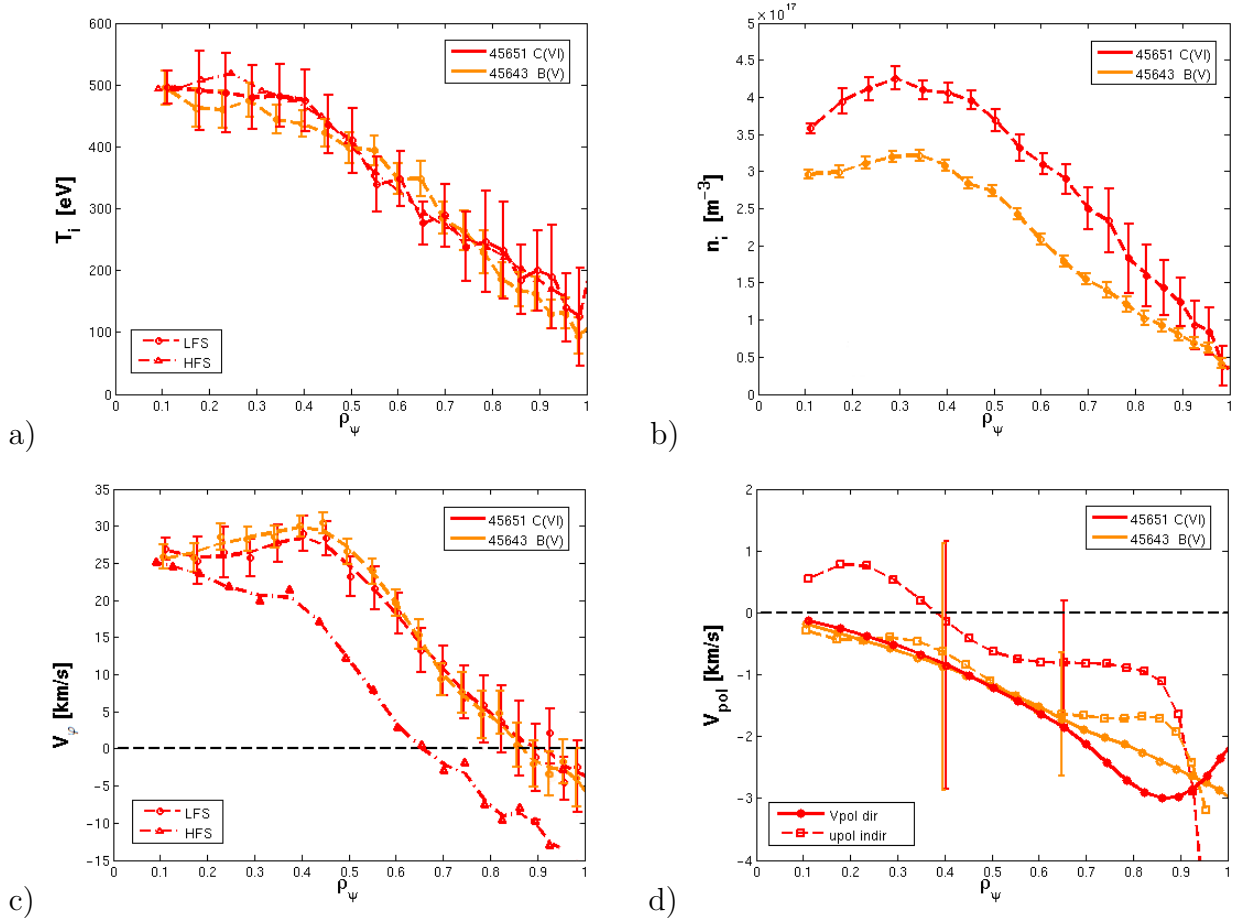
Figure 3.20: Carbon(red)/boron(orange) a) temperature, b) density, c) toroidal rotation and d) poloidal rotation for discharges #45651 and #45643 at $t = [1.2, 1.35]s$ measured at the LFS (circle). The carbon profiles measured at the HFS for shot #45651 (triangle) are also added. Notice that $T_B = T_C$ and $v_{\varphi,B} = v_{\varphi,C}$ on the LFS within the error bars.

identical on the LFS to within error bars (see Fig.3.20.c). The same is also observed for both impurity ion temperature profiles (Fig.3.20.a), while n_C is higher than n_B (Fig.3.20.b, and as observed in Fig.3.19). Moreover, no significant modification is observed for the poloidal rotation with the direct measurements, with $v_{\theta,B}$ and $v_{\theta,C}$ that range between 0.2-3km/s in the counter clockwise direction (see Fig.3.20.d), but a small difference of 1km/s is observed with the poloidal rotation indirect profiles (see Sec.5.2.2). For a more detailed study on the behavior of the carbon and boron density profiles as a function of I_p or plasma density (out of this work), the reader is invited to consult [69].

This example shows that, even if the CXRS diagnostic is optimized for the CVI ($n = 8 \rightarrow 7$) line, in the future it may be exploited immediately after a boronization by measuring the BV ($n = 7 \rightarrow 6$) line, without a delay of a few operational

weeks for a sufficient carbon density, as in the past. The new obtained profiles demonstrate the thermalisation of both boron and carbon ions, so that $T_B = T_C$ with a high accuracy. In addition, $v_{\varphi,B} = v_{\varphi,C} = v_{\varphi,i}$, which shows that the friction term between the two impurities and the main ions is similar. Furthermore, the simultaneous measurements of boron and carbon density during the first 200 TCV discharges can be used to estimate the evolution of both quantities following wall conditioning. Notice that for a precise determination of the boron density, an absolute calibration with the spectrometer set to the boron emission line is required, in order to correctly determine the losses inside the spectrometer and the related absolute coefficients. Even without this, the acquired boron temperature and velocity profiles can be used for rotation and impurity studies.

3.5 Conclusions

In this chapter the CXRS diagnostic on TCV has been described in the present configuration after a series of upgrades performed during this thesis. The main upgrades of the hardware and software system have been presented and discussed, mainly concerning the installation of new cameras, reinstallation of the THFS system, extended double slit configuration and modifications of the CXRS acquisition process.

The new Andor cameras have largely improved the CXRS time resolution since they enable 40 chord full range acquisitions with integration times of 1.7 ms (compared to the 12 ms before). The sensitivity was also improved with a Signal/Noise ratio increased by a factor of 8.

With the reinstallation of the THFS system, the coverage of the entire TCV midplane became possible, allowing an exploitation of the toroidal rotation asymmetry to derive the poloidal rotation and the radial electric field, essential for this work.

In addition, the recent extended double slit configuration demonstrated the possibility to improve the radial spatial resolution of the CXRS diagnostic to almost 7mm for a total of 80 separated measurements locations along TCV midplane. This configuration may be further exploited in the future to study the evolution of radial structures inside the plasma (barrier width and max ∇T_e region, blobs,...).

The installation of the new cameras required modification of the entire CXRS acquisition process and an automation of the data analysis. Their control systems have been successively integrated into the TCV plant control system in order to facilitate routine CXRS exploitation during TCV operation.

The CXRS analysis routines and the calculation of the ion profiles starting from the raw spectra have been briefly explained, demonstrating the high accuracy of the wavelength calibration and of the related signal fitting. The recent developed diagnostic set up for the BV ($n = 7 \rightarrow 6$) line has shown the possibility to measure boron profiles immediately after a boronization, instead of waiting a few operational weeks for the CVI line. The great advantage of using a low power beam with negligible applied torque unfortunately results in a disadvantage of a limited emitted active signal. The simultaneous measurements of boron and carbon density during the first discharges

after the boronization was used to track the evolution of both quantities after a wall reconditioning.

The theoretical estimation of the main transmission losses along the complete CXRS optical path discussed in Appendix B shows a theoretical efficiency of 3% for the TLFS system, compared with 0.7% from the measured signal. An experimental verification of each optical element transmission would be required to determine the presence of any additional loss and better estimate the initial photon flux. Nevertheless, this efficiency is still sufficient to acquire enough active signal to obtain the intrinsic rotation, temperature and density profiles in many TCV plasmas scenarios, but it requires the use of high sensitivity and time resolution cameras, like those installed during this thesis.

With all these improvements, the original CXRS system is now complete and, together with the recently optimisation-automation, is able to operate for a large proportion of TCV experiments. During this thesis the CXRS diagnostic was used to detect faster events in scenarios where the beam is strongly attenuated and the active signal weaker or more irregular, as for sawtooth crashes or in low density plasmas with an eITB, which will be discussed in the following chapters.

Chapter 4

Toroidal rotation and momentum transport studies related to sawteeth events

4.1 Review of main rotation studies and present model of momentum transport

4.1.1 General overview on rotation studies

As discussed in Sec.1.8, the goal of this chapter is to initiate a study on the effect of MHD activity on momentum transport that is well known to have a strong effect upon plasma transport in magnetic confinement devices.

Most work on rotation and momentum transport concentrates on understanding the resulting measured profiles during quiescent plasma conditions. CXRS provides ion parameter profiles, often using existing neutral beam heating systems, which exert an external torque. Therefore, to date, many main studies have focused on the rotation generation and on the induced toroidal torque [70, 71, 72, 73]. Benefiting from an extended radial coverage, CXRS has become the most common diagnostic presently used to measure the physical parameter profiles of impurities. Recent studies use a DNBI or NBH blips to estimate the intrinsic rotation such as on TCV and AUG respectively [20, 68, 74, 75]. Both techniques result in impaired CXRS performance in terms of available temporal resolution, but do not have a strong effect on the measured parameters themselves. As on several other devices, TCV has measured peaked toroidal profiles that are sustained even in the absence of externally applied torque [20] showing the intrinsic or self-developed plasma torque to be non-negligible. This intrinsic rotation is expected to be important, and possibly dominant, on ITER, since the torque applied by the installed heating beams will be minor compared to the present day machines [23, 71]. In conclusion, understanding, and hopefully predicting, intrinsic plasma rotation in a magnetically confined plasma remains a subject of strong interest to designers and operators of machines whose goal is to test fusion power production.

4.1.2   Present momentum transport model

The presence of the intrinsic rotation demonstrates that momentum transport must include contributions that are not only proportional to the rotation gradient (often termed non-diagonal or non-diffusive contributions). At present, several studies suggest that the candidate most likely to dominate momentum transport is perpendicular momentum flux arising from plasma turbulence.

The presently most accepted model, (discussed in detail in [76] and ref. therein), describes the toroidal momentum flux as consisting of various contributions: a diagonal-diffusive term, proportional to the rotation gradient (with $\chi_i \sim \chi_\varphi$, [77, 78]), a small convective contribution (Coriolis pinch, [76, 79]), proportional to the toroidal rotation and directed inwards, and a residual stress component. This last term results from symmetry breaking due to perpendicular sheared flows [80], up-down asymmetric effects [79] and/or global effects (ρ_*, [81, 76]). Residual stress is also assumed to provide a seed rotation at the plasma boundary that is convected by the pinch to balance the diagonal contribution and sustain the entire rotation gradient profile [82].

With respect to the work in this thesis, it should be noted that the above model treats quiescent or near-quiescent states where transport, in the form of flows and gradients, is in some kind of balance. To date, neither the source/sinks terms nor the boundary conditions assumed by the model are well understood, and the mechanism of coupling/transport from edge to confined plasma still is under intense scrutiny.

The effect of changing the boundary conditions in a relatively simple manner resulted in recent studies aimed at isolating, and thus interpreting, some of the simpler or more easily identified physical processes involved. Up-down asymmetry plasma shapes were studied on TCV in [79] in order to identify a turbulent up-down asymmetry residual stress. More recently, during the write up stage of this thesis, the effect on edge flow resulting from changing the X-point radial location with respect to the plasma core radius was investigated on TCV and was shown to track a relatively simple edge flow model [83]. The boundary conditions have thus been shown to play an important role in providing a rotation "source", but it remains difficult to obtain accurate measurements in the edge region. TCV is, as are other machines, developing tools designed to provide high spatial resolution imaging spectroscopy in the edge region together with reciprocating probes to measure the flows outside the confined plasma in order to get a handle on the important physical processes involved.

4.1.3   Rotation and momentum averaged measurements

We recall that the investigated rotation profiles are mostly obtained over an averaged, stationary, phase and fast perturbative events such as edge localized modes (ELMs) or MHD events are not resolved and, thus, rarely explicitly included in the models. Measurement of the rotation profiles do not provide a measurement of the momentum flows, which is where the physics processes exert their effect, which have to be deduced, mainly from the rotation profile gradients. Various experiments, modeling and theoretical works have been performed in the past years, but these studies often only mirror general trends and rarely, dynamic effects. When completed, they must

also be compared with some clearly reproduced and "challenging" experimental observations, such as the rotation reversals observed on TCV [21] and Alcator C-Mod [84]. In this example, an extremely strong effect on the whole measured rotation profile was reported for a quite minor change in a single plasma parameter (the plasma density in this case). There are clearly some effects that are mirrored in the plasma rotation profile that are not obviously related to a strong change in any other plasma parameter but, conversely, it is reasonable to expect that some strong changes in main plasma parameters could result from changes to the self-induced plasma rotation.

Despite this complexity, some global tendencies of the intrinsic rotation profiles have been deduced. The maximum toroidal rotation, and to some degree their profiles, are observed to scale with the plasma current [22, 50, 74, 84, 85] in agreement with what is sometimes termed the *Rice scaling* (discussed in more detail later in Sec.4.1.5).

In other devices, such as AUG, an attempt to understand the transport process as a change from domination by one turbulence domain to another, in particular from ITG to TEM, has been proposed [75, 86, 87, 88]. Again, for these experiments, only average, quiescent plasma conditions are considered. Inevitably, this approach results in models for interpreting momentum transport that look for transport regime changes with plasma conditions. As an example, when applying ECRH in H-mode AUG plasmas, a rotation flattening due to a cnt-current residual stress contribution is observed, together with a related electron and impurity density peaking and a transition towards TEM modes [75]. A correlation between the intrinsic toroidal rotation gradient and the density peaking (i.e. R/L_{ne}) is found for AUG plasmas, and the plasma rotation tends to reverse for large R/L_{ne} values [86].

In a similar approach [89], it was suggested that, above a critical collisionality value, a transition between linear ohmic confinement (LOC) and saturated ohmic confinement (SOC) regimes occurs simultaneously in position and time with other major changes, such as a turbulence regime change, rotation reversals and modified heat transport. This work suggests that a sign change of the residual stress term may be responsible for the rotation reversal.

These works are providing a physically modeled insight into processes affecting the processes determining momentum transport, which are then reflected in changes in the rotation profiles. They demonstrate strong progress in describing momentum transport in a manner coherent with other plasma transport processes.

4.1.4 MHD and sawtooth instability

MHD activity has long been observed to affect plasma transport. Whereas turbulence may be seen as setting a transport rate (non-neoclassical, i.e. anomalous), MHD events have the potential to create "discontinuities", e.g. as they do for heat and particle transport. There is no reason to expect that momentum transport would be an exception. Nevertheless, as previously commented, strong phenomena related to MHD are usually not included in the transport calculations as a possible source or sink term, or as a redistribution/transport mechanism.

In this thesis we will show that the effect of MHD is strong and can dominate the

measured rotation profiles. We will focus in particular on one specific MHD mode: the sawtooth (ST) instability. To examine the physical processes at play, the rotation profile evolution will be probed as a function of the MHD (ST) phase.

As a short reminder, the sawtooth instability is a periodic MHD instability that has been observed on practically all tokamaks and was first reported in the mid 70s on the ST tokamak [90]. More precisely, the sawtooth crash results from the instability of a m = 1/n = 1 kink mode in a core plasma region with q < 1. The instability manifests itself as a fast (Alfvén time scale) crash, better known as a *sawtooth crash* that often results in a sequence of periodic magnetic relaxation events (ST crashes) separated by quasi-quiescent periods (often with n_e and T_e ramps) during which the plasma pressure increases. Widely accepted sawtooth reconnection models show that, at the sawtooth crash, the magnetic field lines break and reconnect accompanied by a strong particle and energy mixing (inside a so-called mixing radius) and the expulsion of a heat and particle pulse outwards from the high pressure plasma core [91]. An example of the main effect of ST on macroscopic parameters on TCV, such as electron density and temperature, is shown in Fig.9 of [92]. At the ST crash, the temperature and density profiles sharply decrease within the mixing radius, corresponding to a sharp degradation of the plasma confinement, often resulting in a macroscopic increase of these parameters outside this radius. While the sawtooth instability is detrimental to core confinement, it may prove useful in fusion plasmas to prevent accumulation of thermalized alpha particles (helium ash) and impurities in the plasma core, where they reduce the fusion energy reaction rate and, if they accumulate, extinguish the fusion reactor.

Sawteeth are common in TCV daily operation since, for sufficient plasma current, large regions with q < 1 develop within which the plasma pressure grows until a ST instability, and then crash, occur. A ST occurs when a threshold is reached, either by a build up of the plasma pressure or after strong diamagnetic stabilization of a precursor mode [93]. The sawtooth period τ_{ST}, i.e. the time between two subsequent crashes, can be influenced by a number of physical effects. In this chapter we will see that well localized co-ECCD and ECH deposition in the region of the q=1 surface has a stabilizing effect on the sawteeth, increasing τ_{ST} from a few ms to over 15ms. Recent TCV studies have focused on computer assisted real-time control of the ST instability [42, 65], where it was observed that sufficiently large ST are associated with the appearance of neoclassical tearing modes (NTM), for which they provide the seed island [94, 95].

The first CXRS toroidal rotation profiles measurements on TCV recorded that the location of the sawtooth instability affects the plasma rotation profiles [22, 50]. Since the control of the rotation profile is associated with plasma mode stabilization and locked mode avoidance, this work attempts to probe how rotation and momentum are modified by sawteeth.

Using the ST reconnection model, it would be reasonable to expect that the large, and sudden, increase in cross field heat and particle transport, associated with the ST, might have a similar "averaging" on the plasma momentum. More interestingly, since the rotation direction can change sign, its redistribution during ST could be more

complex. Testing this conjecture forms the basis of this chapter.

4.1.5 Previous measurements averaged over several sawtooth periods in limited TCV L-mode plasmas

Before presenting the measurements from the improved CXRS diagnostic, described previously, a short description of the relevant published measurements from TCV is provided. Since new data of a similar nature are presented later in the chapter, the previous figures are not reproduced but simply referenced for completeness. As cited in Sec.4.1.3, the maximum toroidal rotations have been reported on TCV and Alcator C-Mod to scale with the plasma current [22, 50, 74, 84, 85].

More precisely, in previous TCV studies it was shown that, when the plasma current is increased, the toroidal rotation profile is flattened, or slightly bulged in the co-current direction, inside the ST-inversion radius that is ascribed to the effect of the sawteeth. This was concluded to effectively limit the maximum toroidal rotation which is leveled at the ST-inversion radius leading to the $1/I_p$ scaling observed in TCV Ohmic L-mode plasmas (see Fig.2 of [22] and [50, 74]). The maximum core toroidal rotation was also found to be approximately proportional to the core ion temperature[1] (Fig.3 of [22]). Further investigations of the intrinsic rotation profiles for limited and diverted TCV plasmas as a function of various plasmas parameters (plasma current, density and shape) were performed in [20], showing unexpected features such as a rotation reversal for plasmas with $q_{95} < 3$ [22].

We recall that the typical integration time of the CXRS diagnostic used for previous studies (about 20ms for 8 radial chords with the old Xcam cameras) largely exceeded the typical sawtooth period τ_{ST} for TCV Ohmic plasmas (a few ms), so, here again, the measurements are effectively "ST-averaged". The ST behavior itself did not display strong or reproducible discontinuities with changing plasma rotation (the ST amplitude and phase were not interrupted, even during rotation reversal), so the rotation profiles, averaged across many sawteeth, were used in the study of the physics governing this $1/I_p$ scaling.

Many of the previously published data [22, 50] lacked detailed simultaneous core and edge CXRS measurements, providing only partial rotation profiles, particularly in the edge and core regions. This motivated us to repeat in this work some of these measurements, as illustrated below in Sec.4.2 using the augmented CXRS diagnostic.

4.2 Toroidal rotation averaged over several sawtooth periods in limited L-mode plasmas

As described above, previous TCV experiments (discussed in Sec.4.1.5) were repeated in this thesis (see also [96]) using the newly available increased radial accuracy of the CXRS core-edge measurements, previously reported in Chap.3.

---

[1]We recall that, on TCV, ion heating is determined by electron-ion collisions as there is no direct ion heating.

4.2.1 Plasma current effects on toroidal rotation profiles in limited Ohmic L-mode plasmas

In order to better distinguish the effect of MHD activity and of momentum transport on rotation profiles, a limited Ohmic scenario with line averaged density $n_{e,av} = 2.2 - 2.7 \times 10^{19} m^{-3}$ (from FIR measurements), $q_a = 3.2 - 3.6$, $\delta_a = 0.17 - 0.3$ and $\kappa_a = 1.4 - 1.5$ was developed on TCV, whilst attempting to obtain continuous and constant MHD activity during the discharge's stationary phase.

Using this target, a plasma current scan between $I_p = [-325, -126]kA$ (corresponding to $q_a = [2.7, 7.3]$) was performed with greater precision than before [22, 50]. To facilitate the following discussion, this I_p scan is grouped into two sets: the low I_p discharges ($I_p = [-279, -126]kA$) and the high I_p discharges ($I_p = [-325, -279]kA$). The toroidal rotation profiles v_φ (multiplied by $sign(I_p)$ to have co-current rotation with positive values) measured for this plasma current scan are shown in Fig.4.1 and Fig.4.3. The associated electron temperature and density profiles are illustrated in Figs.4.2.a-c and Figs.4.4.a-c. Note that the plasma current was negative throughout.

Figure 4.1: Carbon toroidal rotation ($sign(I_p)v_\varphi$) profiles in limited OH plasmas for low plasma currents I_p: #40117/-126kA, #40118/-177kA, #40119/-228kA, #40130/-279kA. The plotted dashed lines indicate the q=1 surface position, while the dotted lines the inversion radius for each discharge. The plasma currents of the main shots studied in this section are also indicated.

Starting from the low I_p discharges, see Fig.4.1, we observe a peaked counter-current (cnt-Ip) toroidal rotation profile for all cases. More precisely, rotation profile peaking increases as I_p decreases. With decreasing plasma current, the $q = 1$ surface is displaced inwards (a low I_p corresponds to high q_a), with more peaked (and higher) absolute core toroidal rotation values attained (up to -36km/s). The mid-radius rotation gradient ∇v_φ, covering the region from ρ_{inv} up to $\rho_\psi \cong 0.85$, which we continue to assume is determined by turbulent momentum transport, appears similar for all these I_p values. Thus, at low I_p, a significant residual stress component ([76]) is required to sustain the peaked cnt-Ip rotation profile. Inside $\rho_{q=1}$ (dashed lines), a clear feature

can be observed for these discharges: the local ∇v_φ changes sign and a flattish central rotation profile results. The profile flattening and this particular feature appears to be affected by the sawtooth activity inside the inversion radius. From Fig.4.2.a we can

Figure 4.2: a) Electron temperature, b) normalized electron temperature, c) normalized electron density profiles in limited OH plasmas versus low plasma currents I_p: #40117/-126kA, #40118/-177kA, #40119/-228kA, #40130/-279kA. The associated carbon temperature profiles are plotted in Fig.4.7.

see that the electron temperature (and therefore the electron total thermal energy W_e) increases with I_p, but the T_e transport remains independent of the plasma current. Indeed, the normalized T_e at $\rho_\psi \cong 0.85$, plotted in Fig.4.2.b, does not vary between ρ_{inv} and $\rho_\psi \cong 0.85$ [97]. The normalized electron density in Fig.4.2.c shows a similar trend, but with a broader effect (even beyond ρ_{inv}) of the sawtooth activity on the profiles.

For the high I_p discharges, see Fig.4.3, the toroidal rotations display a flat co-current (co-Ip) profile. Finally, above a certain value of I_p ($|I_p| > 300kA$), the rotation profile does not vary further (see #41385/-301kA and #41386/-325kA with $v_\varphi = 1-6km/s$). The main gradient ∇v_φ seems to gradually reduces near the q=1 surface for these plasmas. Even for the high I_p values, the same clear rotation feature can be distinguished inside $\rho_{q=1}$, with a negative local ∇v_φ and a flat central profile that is presumed to result from sawtooth activity (see below). From Fig.4.4.a, the central electron temperatures remain flat with I_p inside ρ_{inv}, and again the T_e transport is independent of I_p (see Fig.4.4.b from ρ_{inv} up to $\rho_\psi \cong 0.85$). Similar to the low I_p discharges, the
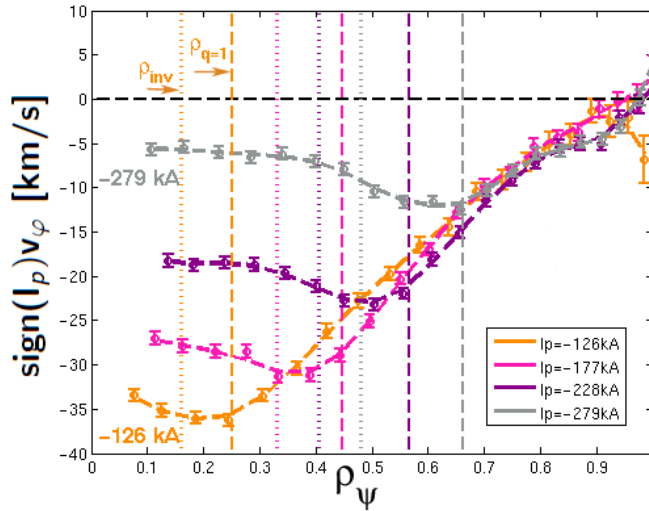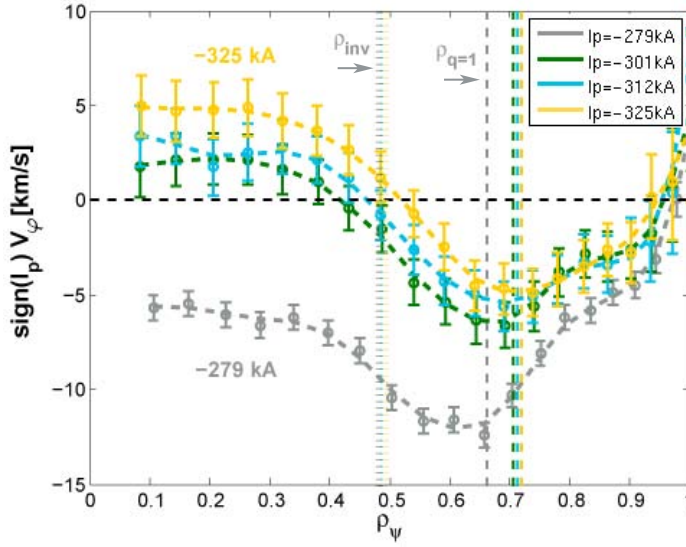
Figure 4.3: Carbon toroidal rotation ($sign(I_p)v_\varphi$) profiles in limited OH plasmas for high plasma currents I_p: #40130/-279kA, #41385/-301kA, #41388/-312kA, #41386/-325kA. The plotted dashed lines indicate the q=1 surface position, while the dotted lines the inversion radius for each discharge. The plasma currents of the main shots studied in this section are also indicated.

normalized electron density in Fig.4.4.c shows a similar trend, but with a broader effect of the sawtooth activity on the profiles.

In Fig.4.5.a the entire set of plasma current values are plotted together. In general, these measurements are completely consistent with those previously reported from TCV. By considering the maximum rotation values $|\nabla v_\varphi|$ for the low I_p cases (colored circles), the $1/I_p$ scaling observed in TCV Ohmic limited L-mode plasmas is recovered. Indeed, Fig.4.5.b clearly shows that the $|v_{\varphi,max}|$ near the q=1 surface, whose value is concluded to be restricted by the sawtooth activity, decreases linearly with I_p as reported in [22, 50]. The intermediate-region rotation gradient $|\nabla v_\varphi|$ was calculated for $0.8 > \rho_\psi > 0.65$ as a function of the applied plasma current (see Fig.4.6). Again, as previously observed in Fig.4.1 and Fig.4.3, $|\nabla v_\varphi|$ is constant for $q_{95} > 3$ (i.e. at low I_p values), and reduces gradually for $q_{95} < 3$ (i.e. at high I_p). For the high I_p values, the mixing radius ρ_{mix} becomes extremely large (up to $\rho_\psi \cong 0.9$) and the effect of the q=1 surface, and/or sawteeth, is stronger. Previous TCV work showed that v_φ reversals result for $q_{95} < 3$ in limited OH plasmas [22], further indicating a strong effect of several phenomena, including ST, in these regions. For $q_{95} > 3$, the constant gradient $|\nabla v_\varphi|$ suggests that the properties of the turbulence, supposed to be sustaining this gradient (residual stress based), do not seem to be significantly modified.

The negative, local, $|\nabla v_\varphi|$ just inside the q=1 surface for all plasma currents, together with the flat core rotation profiles, suggest that the sawtooth has the effect of a co-current v_φ contribution inside $\rho_{q=1}$ that may extend beyond $\rho_\psi \cong 0.85$ for high I_p cases, possibly initiating an effect on the intermediate-region $|\nabla v_\varphi|$.

The carbon density and temperature profiles are also plotted in Figs.4.7.a-d for completeness. Note that, for low I_p values (#40117/-126kA in orange and #40118/-177kA
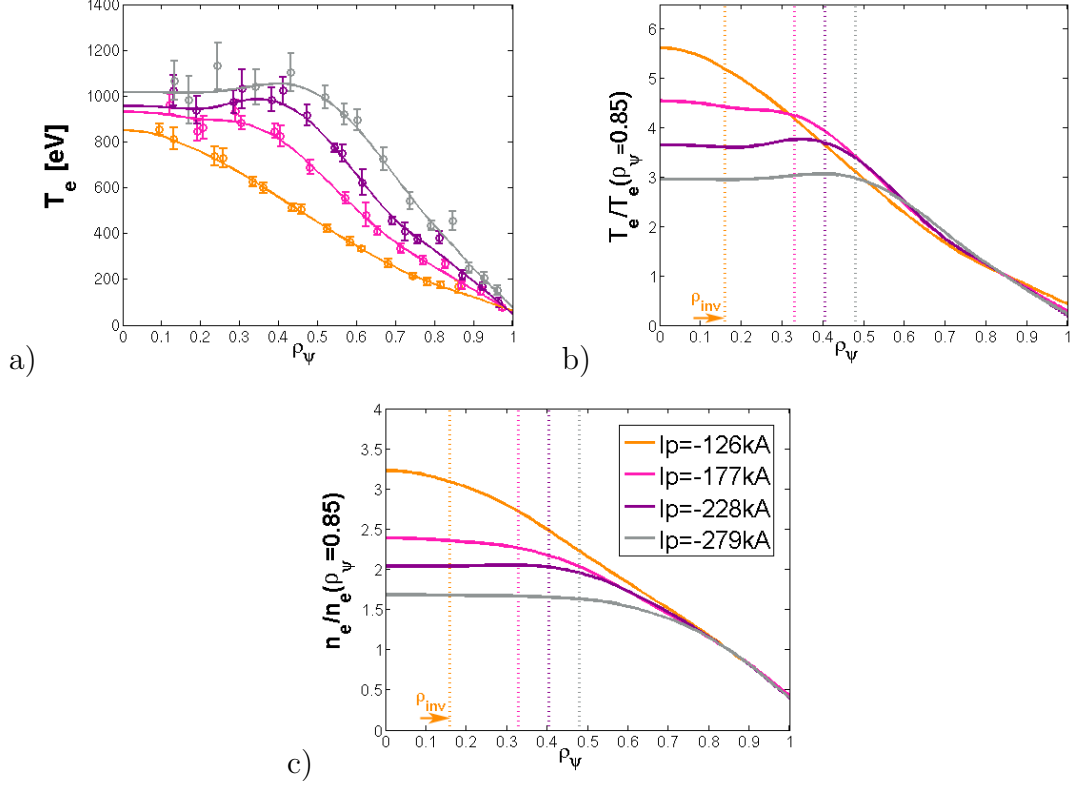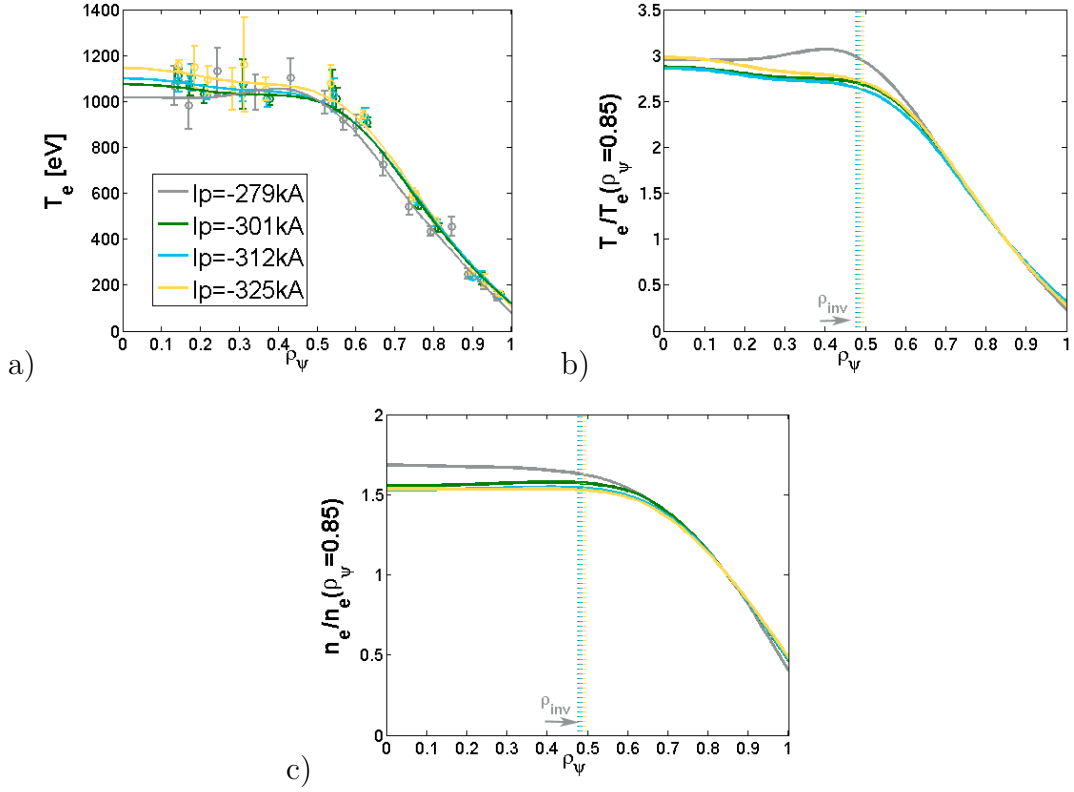
Figure 4.4: a) Electron temperature, b) normalized electron temperature, c) normalized electron density profiles in limited OH plasmas versus high plasma currents I_p: #40130/-279kA, #41385/-301kA, #41388/-312kA, #41386/-325kA. The associated carbon temperature profiles are plotted in Fig.4.7.
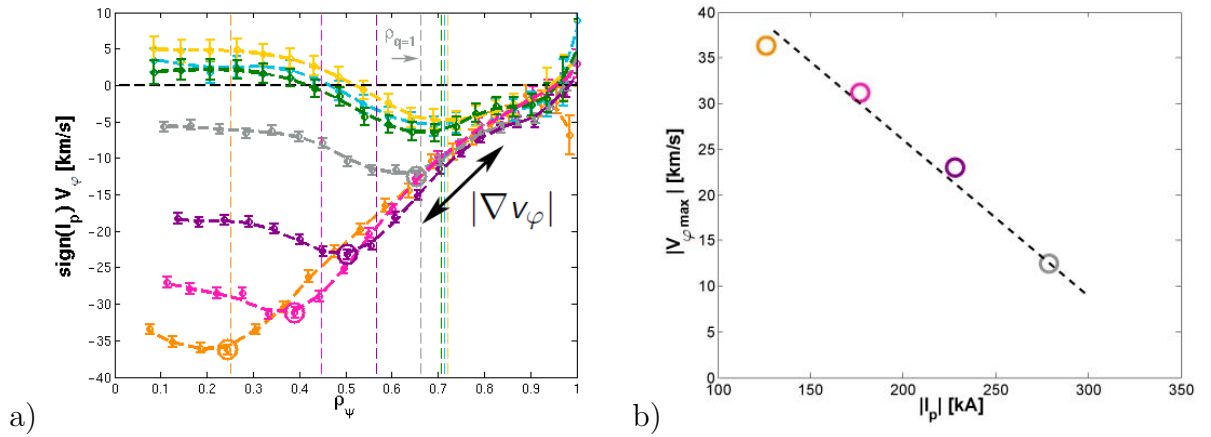
Figure 4.5: a) Carbon toroidal rotation $(sign(I_p)v_\varphi)$ profiles in limited OH plasmas versus all I_p values. b) Maximum carbon toroidal rotation $|v_{\varphi,max}|$ as a function of I_p for the low I_p cases: #40117/-126kA, #40118/-177kA, #40119/-228kA, #40130/-279kA.

Figure 4.6: $|\nabla v_\varphi|$ in limited OH plasmas versus plasma current I_p: #40117/-126kA, #40118/-177kA, #40119/-228kA, #40130/-279kA, #41385/-301kA, #41388/-312kA, #41386/-325kA. It can be observed that the main $|\nabla v_\varphi|$ remains constant for $q_{95} > 3$ (i.e. at low I_p values), while it reduces gradually for $q_{95} < 3$.

in pink), the carbon density profiles are strongly peaked, whereas for higher plasma currents they are relatively flat and clearly affected by the sawtooth activity (Figs.4.7.a and c, see also [98]). For all discharges, the core ion temperatures varied between 400-580eV. Even here, the low I_p cases have a slightly peaked profile (see Figs.4.7.a and d), whereas the higher I_p cases present a flat profile in the core (up to $\rho_\psi \cong 0.5$), possibly again explainable by an effect of sawtooth activity and the outer displacement of ρ_{inv} with I_p. The main $|\nabla T_i|$, calculated in the region from $0.85 > \rho_\psi > 0.55$ in Fig.4.7.b, increases with I_p and then stays constant at high I_p. Preliminary ASTRA simulations, with as input the experimental T_e and n_e profiles, indicate that the measured ion temperatures are consistent with neoclassical calculations of χ_i [99].

This section has clearly demonstrated that the effect of MHD activity can be strong and may even dominate the measured rotation profiles, particularly in certain radial regions of the plasma profile (e.g. the plasma core for the ST instability). This appears to result in core profile flattening and, further, what appears as a co-current contribution. Returning to the ST reconnection model (for T_e and n_e), we see that the ST "mixing" alone can not explain the observed co-Ip bulge, but is consistent with the observed profile flattening inside the q=1 surface, as conjectured in the chapter introduction.

From these observations, we can suggest two contrasting possibilities concerning the main effect of ST. ST activity results in an average effect on the momentum transport coefficients or causes a change in the dominant turbulence characteristics, etc. Or it exerts a rapid and strong effect, most probably at the time of the ST crash.

In order to understand how (and when) the ST exerts its effect on the plasma rotation profile, it is essential to study the rotation profile evolution as a function of the ST phase, i.e across the ST crash and during the ST ramp periods. Since ST are relatively short (a few ms) and the CXRS requires at least $\sim$ 2ms to obtain meaningful data,
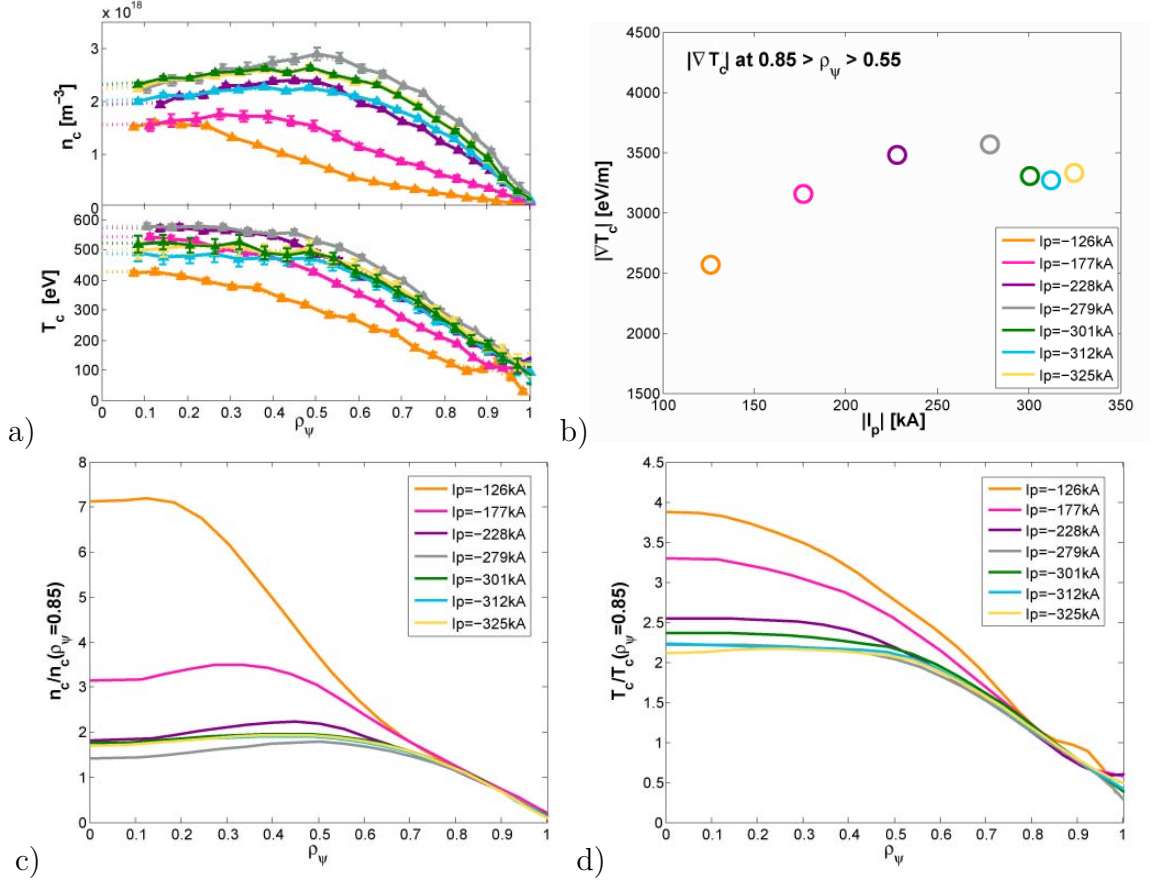
Figure 4.7: a) Carbon temperature and density profiles, b) $|\nabla T_i|$ at $0.85 > \rho_\psi > 0.55$, c) normalized carbon temperature and d) normalized carbon density pro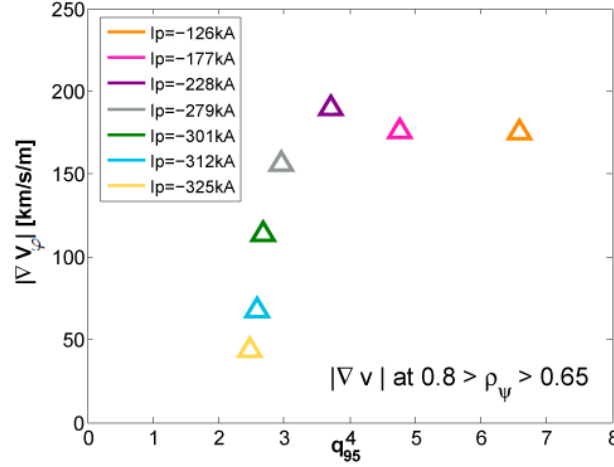files in limited OH plasmas versus plasma current I_p: #40117/-126kA, #40118/-177kA, #40119/-228kA, #40130/-279kA, #41385/-301kA, #41388/-312kA, #41386/-325kA.

slowing down (stabilizing) the ST is a possible option so long as this process does not change the ST effect we hope to study.

4.2.2 Effect of ECH on toroidal rotation profiles in limited L-mode plasmas and developed scenario

A scenario was developed for this work that featured an extended sawtooth period and large sawtooth inversion radius ρ_{inv}.

As already documented, depositing co-current ECCD just near $q = 1$ together with power deposition in the plasma core, partially stabilizes the sawteeth resulting in a sawtooth period τ_{ST} ranging from a few ms to over 15ms [100, 92, 65, 42].

A limited plasma configuration similar to discharge #41386 was chosen, by sequentially imposing three values of B_φ/I_p [2] pairs during the discharge: -1.44T/-342kA,

---

[2]Note that the coordinates φ or simply t indicate the toroidal direction (positive when anticlockwise from the top).

-1.19T/-282kA and -1.11T/-263kA. The same B_φ/I_p ratio is chosen to maintain the same $q = 1$ surface position. Finally, 450kW of ECRH was injected from 0.35s at constant angle to generate ECH and co-current drive.

Figs.4.8.a-d show the DMPX, I_p, B_φ and $n_{e,av}$ time traces of shot #48884 with the corresponding B_φ/I_p values. The EC deposition during the three phases is indicated in Fig.4.8.e. Recall that, for this discharge, the ECH injection angles are constant, but the reduction in the magnetic field B_φ displaces the EC deposition towards the LFS. During the initial phase -1.44T/-342kA (0.7s, in blue), the deposition is inside $q = 1$, for -1.19T/-282kA (1.2s, in lilac) it is near the $q = 1$ surface and for -1.11T/-263kA (1.5s, in azure) it is outside $q = 1$. All cases generate a negative I_{CD}, corresponding to co-CD in the plasma. In the intermediate phase, with the EC deposition near the q=1 surface, a sequence of regular sawteeth with a 11-14ms period is achieved (see Fig.4.8.a highlighted in lilac). The corresponding toroidal rotation and electron tem-
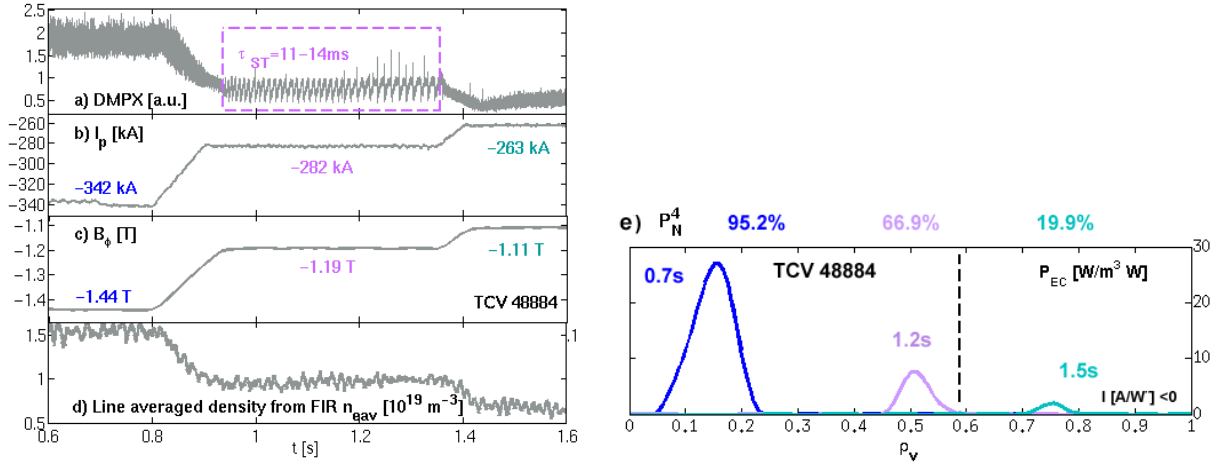
Figure 4.8: a) DMPX, b) I_p, c) B_φ and d) $n_{e,av}$ time evolution for shot #48884. The three B_φ/I_p values are indicated, so as the intermediate stationary phase with long sawteeth of 11-14ms period. e) EC power and co-current drive deposition of a 450kW EC beam for the three B_φ/I_p values in shot #48884: -1.44T/-342kA (0.7s, in blue), -1.19T/-282kA (1.2s, in lilac) and -1.11T/-263kA (1.5s, in azure). The above values indicate the percentage of absorbed EC power for each phase. The $q = 1$ surface remains constant and is defined by the vertical black line. The change in B_φ/I_p results in the EC deposition to be shifted outward. NB: $\rho_v = \sqrt{V/V_a}$ is the normalized volume coordinate.

perature and density profiles are plotted in Fig.4.9.a and Fig.4.10.a-b. The rotation profiles have a small component directed in the co and cnt-Ip direction for the three cases. We recall that, on TCV, the CX photon count near the edge at $\rho_\psi = 0.9 - 1$ is small, due to the low power beam and low ion density. The error bars are large at the edge and $\pm 3km/s$ values cannot be unambiguously separated. Although the rough shape at the edge profiles is probably close to reality, small offsets remain possible. The error bars shown in Fig.4.9 are only due to fitting uncertainties and not the, larger, absolute value.

For completeness the Ohmic discharges corresponding to the same B_φ/I_p pairs are illustrated and discussed in Fig.C.1.a of Appendix C.1.1. They show that, for cases
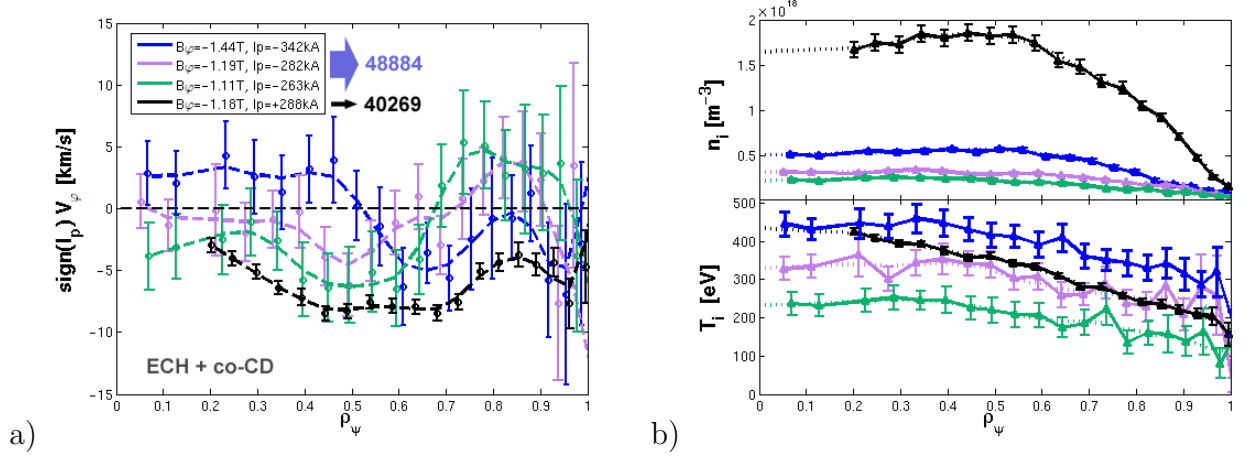
Figure 4.9: a) Carbon toroidal rotation ($sign(I_p)v_\varphi$), b) carbon density and temperature profiles in limited plasmas for three different B_φ/I_p values in shot #48884: -1.44T/-342kA ([0.5,0.8]s), -1.19T/-282kA ([0.9,1.35]s) and -1.11T/-263kA ([1.4,1.7]s). A beam of 450kW in co-CD is injected from 0.35s during the entire discharge. Since the B_φ/I_p ratio is not modified, the position of the $q = 1$ surface remains constant, but the ECH deposition is displaced outwards (LFS). The discharge #40269 with a positive plasma current (B_φ/I_p = -1.18T/+288kA), similar to the intermediate interval, is also shown (in black). The error bars shown only pertain to fitting uncertainties.

with medium-high I_p values, adding ECH near $q = 1$ or off-axis does not modify significantly the rotation profiles, but only results in a small shift in the cnt-Ip direction. This is particularly valid for the discharge pair -1.19T/-282kA pair (in lilac), with long regular ST, where the rotation for both case is not affected. For all three B_φ/I_p values, the local negative ∇v_φ is again observed. Although we have, indeed, changed the ST by stabilizing them by up to an order of magnitude, the overall phenomenological effect of ST on the rotation profile appears unchanged.

Nevertheless, we observe that with more central EC deposition, the electron temperature increases, from direct electron heating, as shown in Fig.4.10.a. The electron density also increases (see Fig.4.10.b and Fig.4.8.d), due to increased I_p, which leads to higher carbon temperatures for the centrally heated case (430eV), compared to the off-axis heated phases (220eV, see Fig.4.9.b). As described in the previous section, the central ion density profiles are relatively flat.

To exploit ST stabilizing, we developed a scenario with a 700ms stationary phase of regular ST with $\tau_{ST} = 14ms$, shown in Fig.4.11 for #40271. We note that discharges #40271 and #40269, discussed in the rest of the chapter, are intended to be identical, during which a fast or standard CXRS acquisition cycle was performed to ensure that CXRS with increased temporal resolution did not introduce any systematic effect on the measurement. These discharges are also similar to the intermediate phase of shot #48884 (Fig.4.8.a), but with $I_p > 0$. For this scenario, $q_a = 2.8$ is obtained with a plasma current $I_p = 288kA$, $n_{e,av} = 0.9 \times 10^{19}m^{-3}$ density and an elongation of $\kappa_a = 1.42$. The toroidal field B_φ was reduced from the standard 1.44T to 1.18T with the EC beam launched from the equatorial plane locating the ECH resonance on the
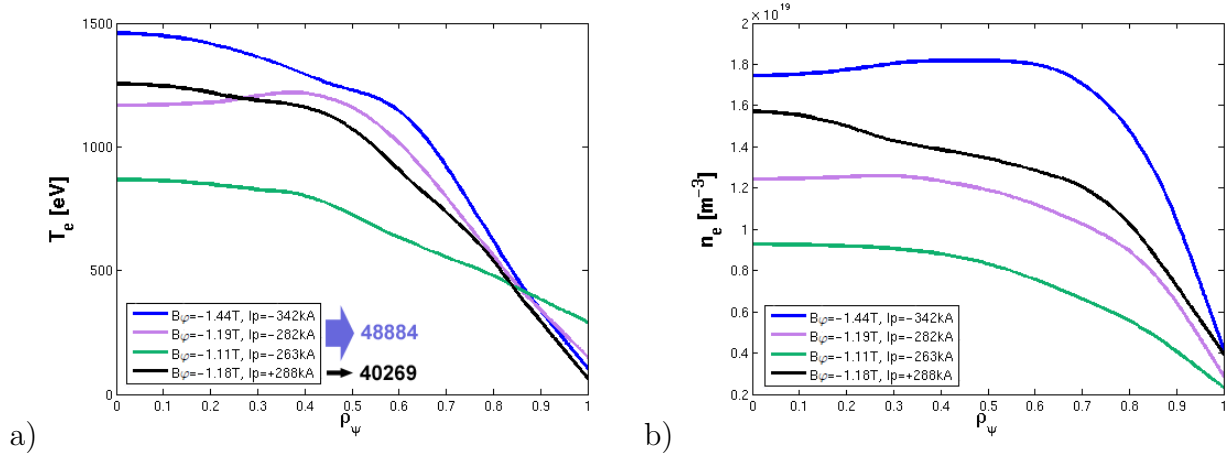
Figure 4.10: a) Electron temperature and b) electron density profile in limited plasmas for three B_φ/I_p values in shot #48884: -1.44T/-342kA ([0.5,0.8]s), -1.19T/-282kA ([0.9,1.35]s) and -1.11T/-263kA ([1.4,1.7]s). The discharge #40269 with a positive plasma current ($B_\varphi/I_p =$ -1.18T/+288kA), similar to the intermediate interval, is also added.
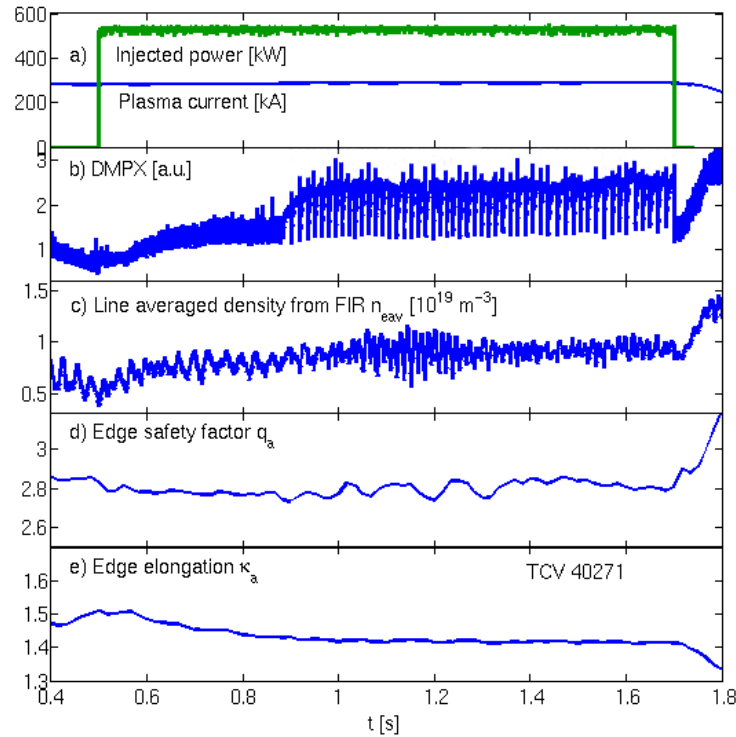
Figure 4.11: Main traces for shot #40271. A stationary phase with $\tau_{ST} = 14ms$ is created starting from 1s.
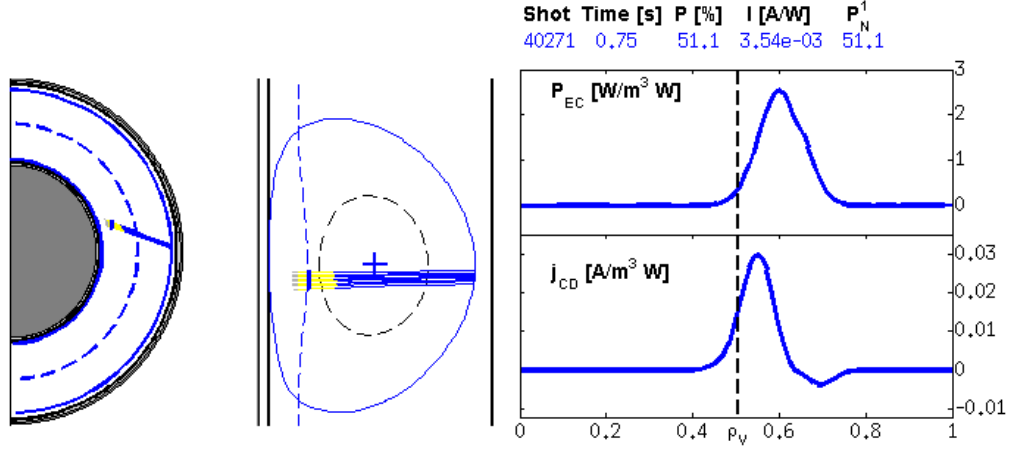
Figure 4.12: Power and ECCD current density deposition scheme reconstructed with TORAY. The beam is mostly deposited just outside the q=1 surface at the HFS. The ECCD current drive is in the co-current direction.

plasma HFS and reducing q_a thus obtaining an increased sawtooth inversion radius. The power and deposition profiles are estimated using the ray tracing TORAY-GA code (see Sec.2.4.5) and the radial location of the current drive is positioned by using fine scans of B_φ whilst keeping the ratio B_φ/I_p, and thus q_a, constant or by sweeping the ECCD launcher angle. The power and current density deposition profiles for discharge #40271 are plotted in Fig.4.12. 500kW is injected off-axis at 0.5s. The co-ECCD deposition is localized just outside the q=1 surface at the HFS, shown as a black vertical line at $\rho_v \cong 0.5$ (i.e $\rho_\psi \cong 0.4$). This procedure tracks the observed ST length to determine the optimal ECH deposition location and proved reproducible for subsequent discharges.
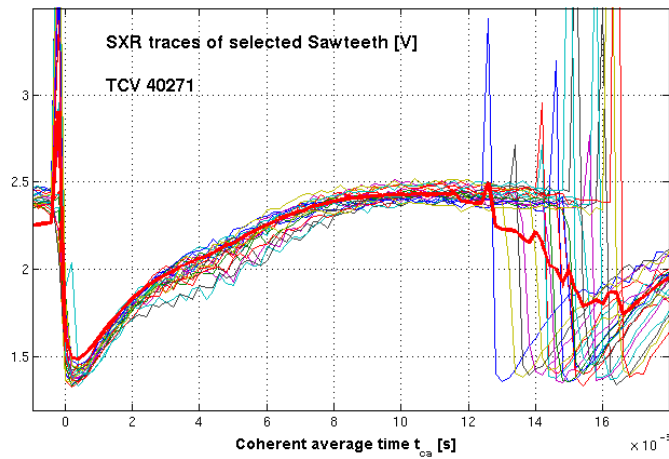
Figure 4.13: SXR traces of selected sawteeth to be analyzed with conditional average sampling (discussed in Sec.4.3.2).

The regularity of the ST obtained for shot #40271, is demonstrated in Fig.4.13 with

stabilized ST of period ∼14ms. Some sawteeth exhibit a "partial" crash during the pressure ramp.

To compare the average rotation profiles, discharge #40269, with a positive plasma current (B_φ/I_p = -1.18T/+288kA) is added to Figs.4.9.a and b (in black). Note that, even for positive plasma currents, the rotation profile is in the cnt-current direction and is similar to the -1.19T/-282kA phase of shot #48884. The $\nabla v_\varphi < 0$ feature inside $\rho_{q=1}$ is always present. The small rotation difference of discharge #40269 is ascribed to the small variation in the B_φ/I_p ratio or the increased core plasma density and possibly changed edge boundary conditions. For completeness, to ascertain the similarity among the rotation profiles in Ohmic and EC heated plasmas for high I_p values, the discharge #40269 has been plotted in Fig.C.2, together with the entire I_p scan discussed in Sec.4.2.1.

4.3 Toroidal rotation and momentum transport studies in between successive sawtooth crashes

In the previous Sec.4.2.2, we demonstrated long relatively regular stabilized ST by injecting ECH and ECCD near the $q = 1$ surface, that did not unduly affect the measured rotation profiles. Using the real time sawtooth crash trigger discussed in Sec.2.4.4 and the fast acquisition CXRS acquisition configuration ($\sim 2ms$), it is now possible to measure the rotation evolution as a function of the ST phase to examine the effect of ST on momentum.

To obtain time resolved velocity measurements between sawteeth crashes [101], several modifications to the CXRS acquisition, analyses and standard TCV operation were developed. The specific RT-trigger and related CXRS modifications are now described.

4.3.1 Sawtooth trigger concept

During the plasma discharge, the sawtooth crash, detected from the soft X-ray emission (from DMPX or XTOMO), is monitored by a RT control digital system [40, 41]. Following the detection of a ST crash, a sequence of regularly spaced triggers (2ms), is generated by the d-tACQ196 card. The CXRS triggering after ST detection was described in Sec.2.4.4. An example of the CXRS RT trigger, based on the DMPX, is shown in Fig.4.14, where the sequence of CXRS triggers, with a 5V amplitude and $200\mu s$ width, following the ST crash, is shown in red.

4.3.2 CXRS set up and data analysis: time and spatial resolutions and conditional average sampling

For these experiments, the CXRS diagnostic is configured for fast acquisition, since the standard 20ms integration time for 20 radial chords cannot resolve the sawtooth period. To reduce the detector integration time to 2ms, the number of sampled chords was reduced, but on-chip "pixel binning" (from 20 to 5 or 6) was employed to record
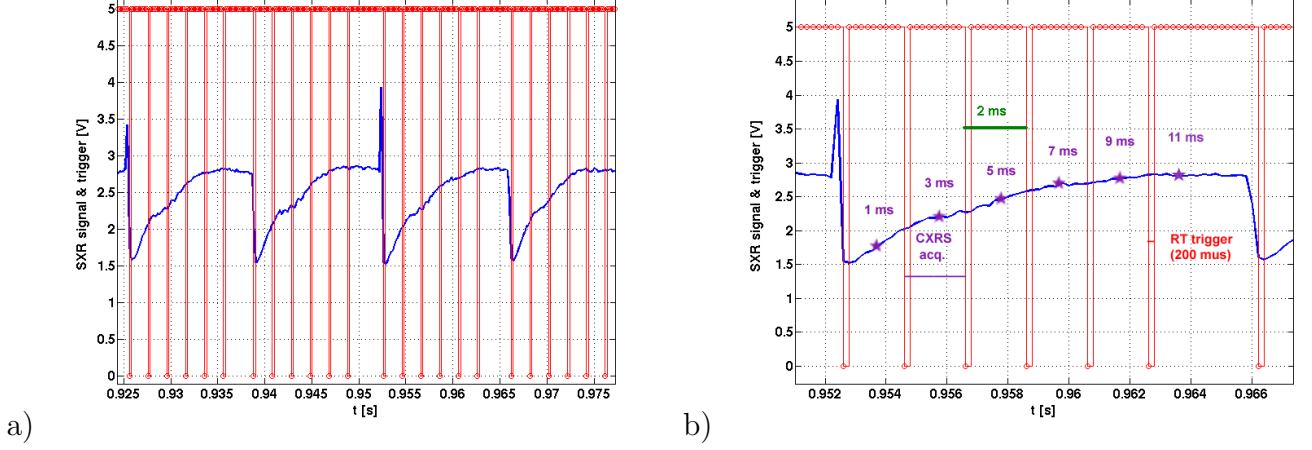
Figure 4.14: a) DMPX traces (in blue) and RT triggers (in red) on ST crashes to the CXRS detectors. b) Zoom of a typical ST crash with the trigger sequence generated by the d-tACQ card noted as $t_{ca} = [1, 3, 5, 7, 9, 11]ms$, i.e. the central time of each triggered CXRS acquisition interval with respect to the first initial trigger (as an index for conditional averaging). At each trigger, the CXRS cameras perform a "frame-transfer" then readout and store in slightly less than 2ms. Depending on the ST period, the number of triggers to be sent after the crash is set, but in this implementation, a single value must be pre-chosen (6 for this discharge).
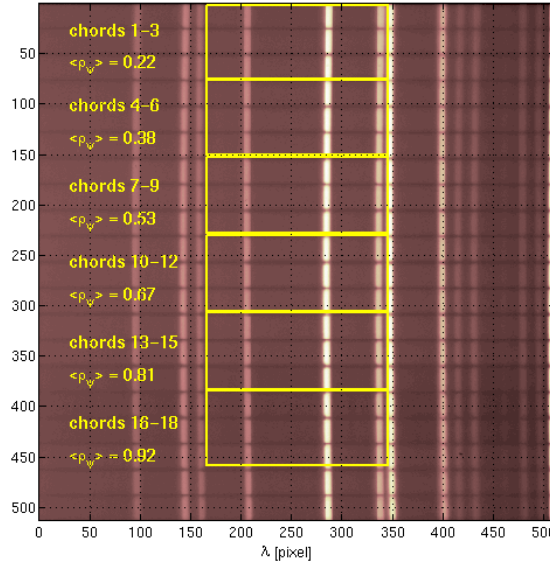
Figure 4.15: Selection of the CXRS fast acquisition chords. Each group of chords is indicated with the corresponding averaged value of ρ_ψ.

the strongest possible signal at the expense of spatial resolution. Furthermore, the spectral range was reduced from 512 to 180 pixels, see Fig.4.15. The reduction in the spatial resolution and acquired light intensity can be partially mitigated by combining adjacent chords and choosing effective observation chords distributed equally across the plasma minor radius, covering the core, intermediate, and peripheral regions. To compensate for the reduction in signal with the reduced integration time, a conditional average (CA) sampling technique was applied in which the signals from several sawtooth crashes are summed as a function of the sawtooth phase. As explained above, each detected ST sends a regularly spaced trigger pulse train to the CXRS. The CXRS CCD cameras integrate the incident signal until a trigger arrives upon which a read-out and storage cycle occurs. Thus, the first trigger after a ST from the RT system, is almost entirely a measurement of the plasma rotation immediately before the ST crash and subsequent triggers measure the average plasma rotation during successive 2ms integration periods. Finally, for these experiments, the DNBI injector operated with a regular 12ms ON /12ms OFF duty cycle that was not synchronized to the sawteeth events. Each 2ms acquisition period was then sorted with respect to its time from the preceding sawtooth crash ($t_{ca} = [1, 3, 5, 7, 9, 11, ...]ms$, i.e. the central time of each CXRS acquisition, see Fig.4.14.b). By averaging the spectra in each group and extracting the active spectra from the difference between acquired spectra with or without the DNBI (see Fig.4.16), the evolution of an average, or more correctly "canonical", sawtooth was constructed.

An example of the experimental CXRS spectra, obtained for discharge #40271, is shown in Fig.4.16. The averaged spectra with and without DNBI for the most central
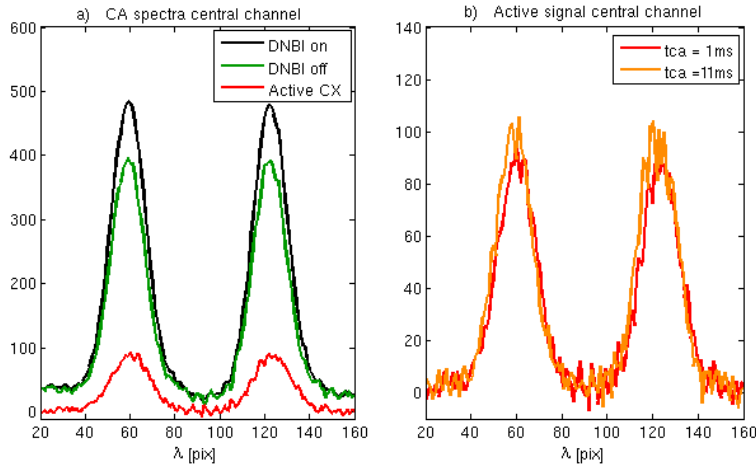
Figure 4.16: a) Conditional averaging of CXRS spectra for the most central channel (ch.1) and $t_{ca} = 1ms$ (# 40271). The two peaks are obtained using the double slit configuration of the optical fibers. b) Active signals measured at $t_{ca} = 1ms$ and $t_{ca} = 11ms$ for the same central channel. A small Doppler shift of a few pixels can be seen even from the raw data, indicative of a rotation change at the ST crash.

channel are plotted together with the active spectra. On-chip binning is necessary to obtain a sufficient signal during the active signal for a statistically meaningful analysis.

A comparison between the active spectra measured at $t_{ca} = 1ms$ (just after the crash) and $t_{ca} = 11ms$ (rotation at the end of the ST) for the same central channel already displays a clear Doppler shift (Fig.4.16.b).

4.3.3 Experimental rotation and momentum across a ST cycle

From the averaged spectra shown in Fig.4.16.a-b, the temporal and spatial evolution for the averaged sawtooth in discharge #40271 can be derived in Fig.4.17. In the upper plot, the toroidal rotation profiles evolving during the ST phase are shown for all acquired time intervals. In bold are highlighted the profiles measured just after the crash ($t_{ca} = 1ms$, blue), near the middle of the sawtooth period ($t_{ca} = 5ms$, green) and near the end of the sawtooth period ($t_{ca} = 11ms$, red).
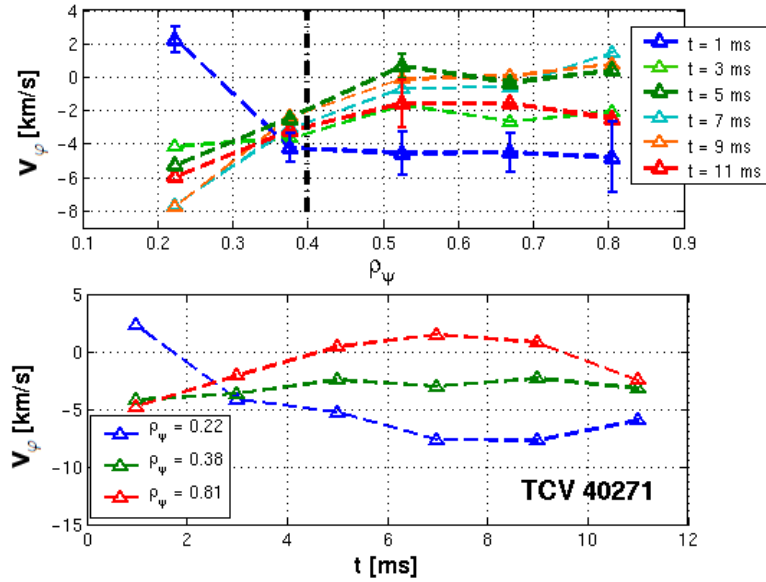
Figure 4.17: Toroidal rotation at 1,3,5,7,9 and 11ms after the ST crash (top); evolution of the rotation at three radial positions (bottom) for shot #40271. A set of error bars is plotted for $t_{ca} = 1ms$.

A clear co-current "kick" in the core region is seen at the sawtooth crash ($v_\varphi > 0$ corresponds to a co-current direction), then the profile rapidly relaxes and evolves more slowly until the next crash. This behavior is also visible in the lower plot where the toroidal velocity at three radial locations is shown as a function of the ST phase. Near and outside the sawtooth inversion radius ($\rho_{inv} \cong 0.4$), the toroidal rotation evolves slower across the sawtooth period and we observe a small counter current acceleration at the ST crash affecting the profile up to $\rho_\psi = 0.8$.

This co-current kick explains the origin of the co-current "bulge" inside ρ_{inv} observed for the I_p scan in Fig.4.9. Note that the acquisition interval $t_{ca} = 11ms$ corresponds to the last acquired profile during the ST cycle, i.e. the profile measured just before the ST crash, with the ST crash occurring only 2-3ms after this acquisition. This time delay may explain why the rotation profile acquired at $t_{ca} = 11ms$ (in red) does not

completely recover the first profile (in blue). If the experiment worked perfectly, the rotation profile deduced before the ST crash should be close to that at the end of the ST period but the variable delay, resulting from RT-triggering, of the pre-crash profile is thought responsible for the remaining difference.
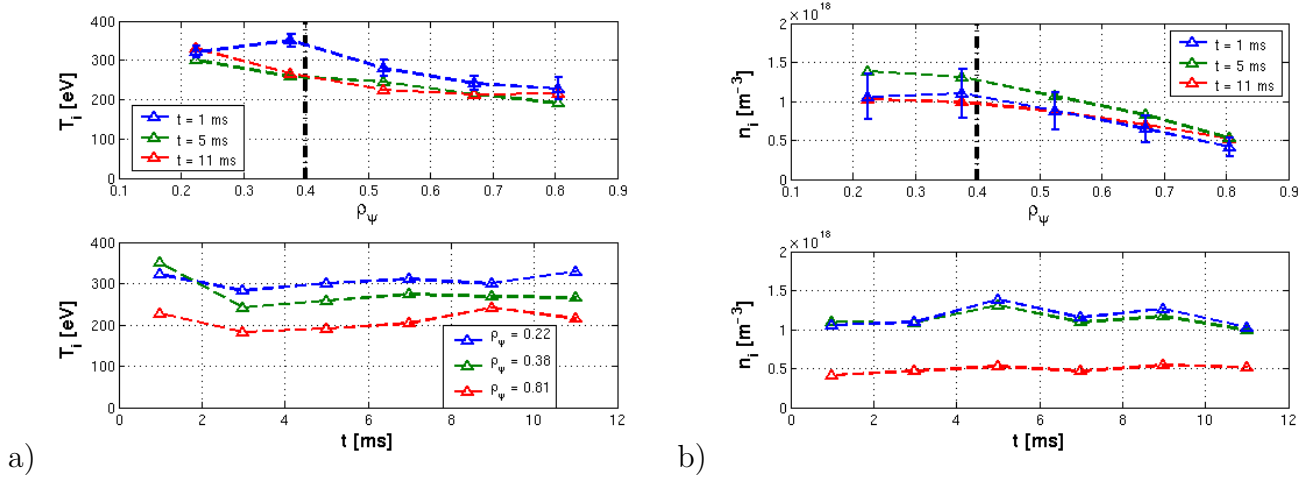
Figure 4.18: Impurity carbon a) temperature and b) density at 1, 5 and 11ms after the ST crash (top); evolution of both profiles at three radial positions (bottom) for shot #40271. A set of error bars is plotted for $t_{ca} = 1ms$.

These rotation profiles suggest that the ST crash has a strong and rapid effect on momentum transport and creates an effective co-current torque in the plasma core. Nevertheless, this result also demonstrates a strong degree of momentum conservation across the plasma profile, with the plasma outside ρ_{inv} accelerating in the opposite direction to the core (on longer timescales).

The impurity temperature and density, measured in between the ST, are plotted in Fig.4.18. The temperature profile ($T_i(0) \cong 300eV$) broadens and increases by about 20-30% just after the ST crash around ρ_{inv}, while the density reacts later and is higher after 3-5ms. Both profiles then slowly reduce and narrow during the rest of the sawtooth period. Recall that, after the ST crash the plasma profiles are flattened. Finally, the impurity density measurements seem to indicate some preferential expulsion of the carbon impurities that merits further exploration that may help in the understanding of impurity transport in Tokamak plasmas.

From the impurity temperature, density and toroidal rotation profiles obtained with the fast acquisition, the radial electric field can be estimated in between the ST crash using the force balance equation (see Sec.5.2.1). The radial electric field shows a sharp change in the plasma core inside the sawtooth inversion radius (see Fig.C.4 in App.C.2.1). Before the crash E_r is in the inward direction ($E_r < 0$) and, immediately after the crash, evolves towards an outward direction. During the ST ramp, the profile then relaxes towards an inward central constant value of $E_r = -1kV/m$. Therefore, after a ST crash, the acceleration in the toroidal direction occurs simultaneously with a modification (even reversal) of the radial electric field. This effect implies a reduction or reversal of the $E \times B$ drift velocity, which is directed downward for the ions before

the crash. More details on the calculated radial electric field can be found in App.C.2.1. The reproducibility of this experimentally challenging result is demonstrated in Fig.4.19, where the toroidal rotation profile change across the ST crash is plotted for several discharges with the same sawtooth inversion radius. The plot shows the difference between the first rotation profile following the sawtooth crash and a best estimation of the profile just before the crash. The profile appears to pivot around ρ_{inv} with the core
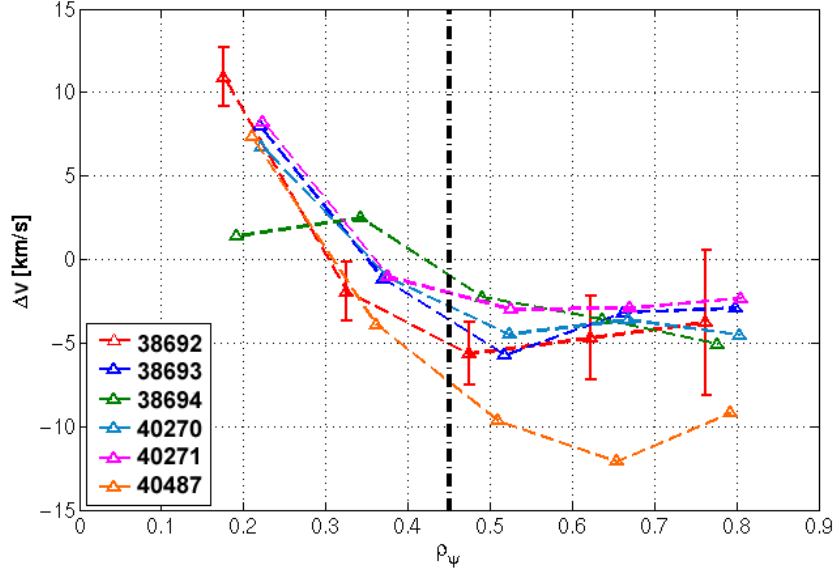
Figure 4.19: Comparison of the difference $\Delta v = v_{post-crash} - v_{pre-crash}$ between the first rotation profile following the sawtooth crash and the best estimation of the profile just before the crash for several discharges.

showing a strong co-current acceleration with the rest of the plasma slightly accelerated in the counter-current direction. Error bars are shown indicating estimations of typical fitting uncertainties. The determination of the radial electric profiles for these plasmas show a similar behavior to Fig.C.4, with a central outward E_r generated just after the crash.

In order to interpret the origin of the observed fast co-current acceleration in the plasma core and to distinguish between a sawtooth driven torque or a momentum redistribution, the total angular momentum L_{tot} was estimated for discharge #40271 and those illustrated in Fig.4.19, using the measured impurity profiles. The total angular momentum L_{tot} was derived from the relation:

$$L_{tot} = \int_{\mathtt{Vol}} n_i \cdot m_C \cdot \omega_\varphi \, \mathtt{dVol} \qquad (4.1)$$

where m_C is the atomic carbon mass, $\omega_\varphi = v_\varphi/(2\pi R)$ is the toroidal angular frequency with R the radius of the CXRS acquisition, n_i the carbon density and $\mathtt{dVol}$ is an element of the plasma volume $\mathtt{Vol}$, calculated using the LIUQE metrics.

In Fig.4.20.a L_{tot} is plotted as a function of the ST phase for discharge #40271. For

the same discharge, the angular momentum averaged on theta (i.e. surface average) as a function of the radial position (ρ_ψ) and the ST phase is illustrated in Fig.4.20.b. From these figures the momentum appears to be approximately conserved during the
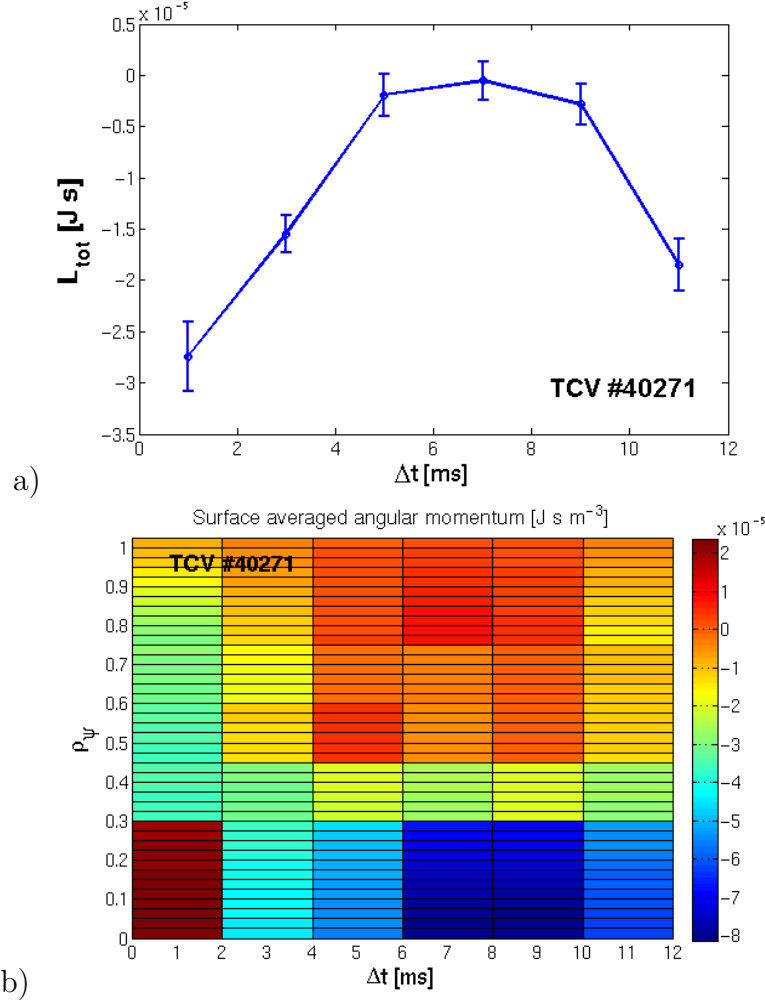
Figure 4.20: a) Total angular momentum as a function of the ST phase and b) surface average (on theta) angular momentum calculated as a function of ρ_ψ and ST phase for shot #40271. The error bars shown in a) are calculated using a Monte Carlo procedure described in appendix A of [51].

ST crash to within 80-90% (i.e. between the "just before" and "just after" values). We recall the missing measurement in the time interval 2-3ms between the last "just before the crash" measurement and the crash itself, which may, in part, explain this difference. Inside the q=1 surface ($\rho_\psi \cong 0.35 - 0.4$) a co-torque is visible (in red), together with indications of recoil outside the mixing radius (in yellow-orange). The effect of ST seems not simply to provide a fast momentum transport at the ST crash but, somehow, to pinch plasma momentum in the co-current direction with the outer plasma recoiling in the opposite direction. The available data quality is unable to discern whether the momentum is conserved to better than 80-90% (similar results

have been also obtained for the other considered discharges discussed in Fig.4.19). Although an extra torque accompanying the ST crash is not excluded, this work does not require such a torque to explain the experimental observations.

From the ST cycle resolved rotation profiles shown in Fig.4.17, the rotation profiles averaged over various ST phases were calculated in Fig.4.21. By averaging more profiles (and active spectra), i.e. by increasing the acquisition time interval, the central co-current kick is clearly reduced with the outer region showing a tendency to shift towards smaller cnt-current values. If this approach is justified, we would assume that, outside the mixing radius, the last averaged rotation profile (i.e. $\Delta t = 14ms$), would approach the initial (pre-crash) profile (in blue). Unfortunately, no quality measurements are available for this last time interval. If we try to extrapolate some information from
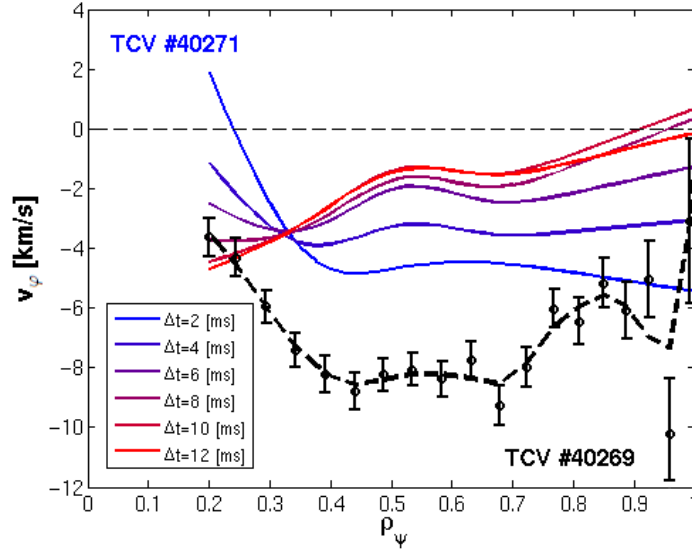
Figure 4.21: Total angular momentum as a function of the ST phase ($\Delta t = [2, 12]ms$ after the ST crash) calculated for shot #40271. Discharge #40269 with similar plasma characteristics, together with a CXRS standard average acquisition, is also plotted.

Fig.4.21, the first two fast averaged profiles ($\Delta t = [2, 4]ms$, in blue and dark blue), suggest that the co-current kick may be stronger for discharges with a shorter ST period (destabilized ST), leading to a higher negative core gradient (as suggested in Fig.C.2 and Fig.4.9). Less ST crashes over a given time interval (eg: for long stabilized ST), may result in a lower average co-kick in the core. This question could be partially resolved by performing similar experiments for plasmas with a range of ST periods. In any case the $|\nabla v_\varphi|$ for the long stabilized ST (fast and average) and short destabilized ST remain similar and we do not identify a different effect between short or long ST period. Even for stabilized ST, the effect of reconnection (and the related mixing) on the momentum does not appear to be significantly modified.

4.3.4 Open issues and most recent rotation profiles

The reduced CXRS spatial resolution used for obtaining the results discussed in Sec.4.3.3 implies that only one spatial chord monitors the plasma core. Because of the limited beam/plasma luminosity of the CXRS system it was not possible, with the Xcam cameras, to have usable data with an increased chord number inside the sawtooth inversion radius. A certain amount of doubt in the possible interpretation of the previous results remains since only the central observation chord, for the profile immediately following the sawtooth crash, showed a strong discontinuity. Nevertheless, all the diagnosed discharges have shown a similar effect that can not be ascribed to instrumental uncertainty, but a more detailed profile would be helpful. Conversely, we have noted that these results are consistent with the data obtained in Sec.4.2.

The new (Andor EMCCD) cameras that can measure the entire set of 40 chords with 512 pixels of spectral range using an integration time of 2ms (already discussed in Sec.3.2.1), should permit better coverage of the plasma core region and measure whether this co-current acceleration is completely physical or partially ascribable to measurement uncertainty. Preliminary rotation profiles obtained with the Andor cameras during 2011-2012 appear to confirm the results reported in this thesis (see Fig.4.22), but camera trigger issues were problematic. In many of the new measurements, some additional (and random) triggering of the cameras was observed that compromised the CXRS acquisition timing and, consequently, the conditional average sampling applicability. Several techniques were examined to coronet the random trigger problem (impedance and electrical termination of the trigger cable,...), but a reliable solution was only developed in 2013, at the time of writing.
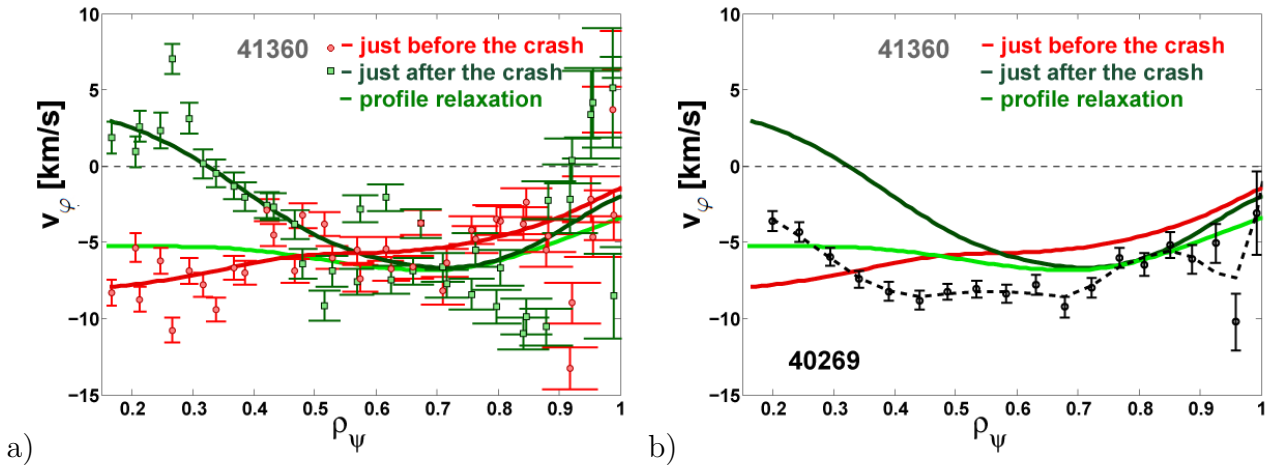
Figure 4.22: a) First profiles and b) fit of toroidal rotation taken every 2ms following the ST average crash of shot #41360 using the new Andor cameras. The entire set of 40 chords is acquired with 512 pixels of spectral range using an integration time of 2ms. Only the data for the intervals [-2,0]ms, [0,2]ms, [10,12]ms are fully plotted together with the corresponding fit profiles. b) The toroidal rotation profiles for shot #40269, averaged on several sawtooth, have also been added (in black, see also Fig.4.9).

For completeness a recent discharge (#41360) with correct CXRS triggers is shown in

Fig.4.22.a with the toroidal rotation profiles taken after the ST crash. The co-current "kick" in the core is, again, observed at the sawtooth crash (in dark green) with a higher resolution, together with a following slower relaxation outside $\rho_\psi = 0.5 \cong \rho_{inv}$ towards the initial pre-crash profile. Note that the profile just before and after the crash largely superpose within uncertainties (in red and light green). Indeed, for this discharge, the last profile acquired during the sawtooth, occurs less than 1ms before the sawtooth crash. This preliminary result, (which was outside the time window of this thesis), confirms the interpretation obtained with the legacy Xcam cameras adding significantly higher radial resolution in the plasma core (8 central chords instead of one).

For comparison, the toroidal rotation profile for shot #40269, averaged on several sawteeth and analyzed in Sec.4.2.2, is also shown (in black) in Fig.4.22.b. As observed for discharge #40271, inside ρ_{inv}, the averaged profile has a central rotation gradient similar to the "just after the crash" profile (in dark green), while the outer part approaches the "just before the crash" profiles (green and red) indication of a plasma recoil.

4.4 Discussion

This study has shown that MHD events, like the ST crash, have a strong effect on rotation profile and momentum transport and will need to be taken into account in order to build a complete model of momentum transport.

The main ST effect on momentum is not simply a rotation profile flattening, as might be conjectured from their effect on electron temperature and density (consistent with a ST reconnection model).

The measured averaged rotation profiles show that ST activity restricts the maximum attainable $|v_{\varphi,max}|$ and that in the plasma core, inside the q=1 surface, the rotations are clipped and often present a small co-current contribution or "bulge". ST are identified as the cause of the $1/I_p$ scaling observed in TCV limited L-mode plasmas. Without this clipping, the near constant rotation profile gradient in the plasma edge would result in a core rotation that was close to independent of the plasma current (as conjectured in [102]).

The experimental measurements performed during a ST cycle support the result that the ST crash results in a rapid and strong effect on the rotation and momentum profiles. Indeed, at the sawtooth crash, the core rotation profile shows a strong co-current acceleration, whereas the rest of the plasma outside the mixing radius recoils in the opposite direction. The calculation of the total angular momentum show that the momentum appears roughly conserved during the ST phase. Inside the q=1 surface, a co-torque is present at the ST crash, but there are also signs of plasma recoil in the opposite direction outside the mixing radius. A similar effect of the central toroidal rotation acceleration was observed recently in MST [103]. This result does not necessarily remove a more indirect effect on the average momentum transport caused by the strong change in the plasma parameters following the ST crash. These measurements

show that while the perpendicular momentum flux generated by plasma turbulence may act on longer timescales, the momentum fluxes "generated" at the ST crash are much prompter.

During the recent experiments performed at the time of writing, the new visible camera, installed on TCV to reconstruct the plasma boundary [104], showed rapid change at the boundary after each ST crash. Although this is only conjecture, it may result from the plasma recoil reaching up to the edge during each ST cycle, but could also be interpreted as the presence of a momentum source near the edge.

Indeed, as discussed in the introduction, since the boundary conditions seem to play an important role in providing a residual stress based rotation "source" this effect merits further experimentation for the discussed plasmas.

In a preliminary theoretical study on TCV, the redistribution of momentum due to magnetic reconnection and the acceleration induced by toroidal electric field developed during a reconnection event were investigated with ASTRA [105] simulations and both processes appeared to play a role in explaining this strong co-current acceleration [20]. The recent rotation, density and momentum measurements should help to provide some insight into these assumptions, but further theoretical and experimental work is needed to obtain a coherent picture.

4.5   Conclusion and outlook

In this chapter we have investigated the effect of MHD perturbative events, in particular the ST instability, on rotation profiles and momentum transport. Using the upgraded CXRS diagnostic we recovered the $1/I_p$ scaling observed in Ohmic limited L-mode plasmas, with increased accuracy and, for the first time, with simultaneous core and edge coverage. Using profiles averaged over many ST, a co-current feature inside the q=1 surface was resolved up to the ST mixing radius. We then employed ECH and co-CD near the q=1 surface to stabilize the ST to a duration where several CXRS spectra were possible during a ST cycle. A longer ST is needed in order to leverage the improved CXRS time resolution (2ms) to study the rotation as a function of the ST phase. We have observed that the momentum transport is roughly conserved across the strong acceleration that follows the ST crash. The ST affects momentum as if generating a fast central torque at the ST crash that is partially or completely compensated by the plasma recoil outside the mixing radius. Although a supplementary torque accompanying the ST crash (of unknown sign) is not excluded, this work does not require such a torque to explain the experimental observations to within the experimental uncertainties.

The work presented in this thesis has already been enhanced with the introduction of faster and more sensitive EMCCD detectors but a preliminary analysis recovers the main observations and conclusions described herein. In particular, improvements in ST stabilization control and wall-clock synchronization are decreasing both the statistical experimental error bars and the timing uncertainties. This is hoped to result in measurements that can measure the rotation profiles even closer to the ST crash time.

Although in this work the local $|\nabla v_\varphi|$ for the long stabilized ST and short destabilized ST remained similar, we were not able to completely discard a direct effect of the ST stabilization on the rotation itself. We recall that in [106], in order to reduce the ST effect, it is possible to destabilize them by reducing the quiescent time between crashes. Conversely, ST with long quiescent time have larger collapse radius and are more likely couple to modes at other rational surfaces, which may lead to further confinement degradation. TCV has recently reported [95] that sufficiently long ST (up to 80ms) lead to an increase in the ST-generated seed island widths that may destabilize NTM modes. This is modeled to result in a change in the current density and, thus the q profiles, towards more stable profiles at 3/2, 2/1 flux surfaces. The larger seed island eventually prevails and leads to an overall more NTM-susceptible plasma.

This clearly demonstrates that stabilizing the ST period does indeed change the effect of the ST crash. To estimate in what way the ST stabilization procedure may affect the ST crash and inter-crash behavior, we suggest in the future to systematically measure the rotation profiles with the new Andor cameras as a function of the ST phase for a range of ST periods from the shortest resolvable to the longest attainable that do not result in a full plasma current disruption. Any change in the momentum transport behavior as a function of ST period may help understand both the increased NTM sensitivity and/or the momentum pinch described in this thesis.

Such experiments would also provide more accurate measurements of the total angular momentum for a large range of ST cycles and allow to test whether full momentum conservation or an external torque may exist. Again, the possibility that an MHD mode may couple, either directly or through inter-mode coupling, to the vessel in such a way as to provide an overall torque has not been excluded.

Following this work, similar experiments of the ST effect on rotation profiles are also planned on other machines, such as AUG and/or Alcator C-Mod, both as a scientific proof of reproducibility and to gain information from other available diagnostic arrays. In order to identify the role of the auxiliary heating (ECRH for TCV) on the ST characteristics and rotation profiles it would be also interesting to repeat such measurements with different heating schemes such as NBH (on TCV and AUG) or ICRH (Alcator C-Mod).

This work was concentrated on only one specific MHD instability, which was expected to have the clearest effect on rotation profiles and whose cyclic nature made it amenable to conditional resampling analysis. Further experiments in the presence of other MHD modes or other fast events like ELMs on the impurity profiles are suggested in order to challenge the present momentum models' validity. Initially, they could focus on rotation profiles that measure the average transport effect over many mode periods such at the average ST profile measurements that stimulated the faster acquisition reported in this thesis. Preliminary studies [96] showed that the presence of strong 3/2 and 2/1 MHD modes can lead to a measurable effect on the rotation profiles such as rotation braking in the plasma mid-radius region or rotation reversal in the core. Conversely, a detailed study of ELMs on TCV using the CXRS diagnostic (by applying a similar "ELM crash trigger technique"), may be able to discern an effect on the coupling between edge flows and the confined plasma.

Chapter 5

Rotation studies in electron internal transport barriers on TCV

5.1 Introduction to internal transport barriers and motivation of this study

5.1.1 Internal transport barriers main characteristics

The first Internal Transport Barriers (ITB) were discovered in the mid-nineties on TFTR at Princeton [107]. They were an improved operational regime that showed a strong enhancement in confinement. The term *Transport Barrier* describes the presence of an obstacle to the ambient transport, leading to a localized region of reduced radial plasma transport. The H-mode, discovered in 1982 [18], is characterized by a transport barrier that occurs at the edge of the plasma and results in an overall improvement of the energy confinement by a factor of about 2. The plasmas performance with enhanced confinement is quantified by the H-factor, the ratio of the measured to the relevant scaling law estimation of the global energy confinement. Ion and electron ITBs are characterized by strong gradients of the temperature and density profiles that instead occur around the plasma mid-radius (i.e. *Internal*). Although a smaller volume is enclosed by ITBs, H-like-factors are found as high as those of the H-mode obtained with an L-mode, and higher still together with an H-mode configuration. The combination of high performance with strong gradients and the associated bootstrap current I_{BS} (that provides inductive-less plasma current, [14]) has resulted in intensive study of these advanced scenarios on several tokamaks. ITBs have been obtained experimentally in many devices such as JET [108, 109], JT-60U [110, 111], DIII-D [112, 113], AUG [114, 115], Tore Supra [116, 117] and TCV [118, 119, 120, 121]. Barriers in both ion and electron channels are being considered for possible steady-state operational solution for future fusion reactors like ITER [122]. However, problems with MHD stability at high β_n [123], impurity accumulation in the plasma core and the

---

[1]The normalised beta or Troyon coefficient is defined as $\beta_n = \beta[\%]a[m]B_\varphi[T]/I_p[MA]$, where $\beta = 2\mu_0 \langle p \rangle /B_0^2$ using the volume averaged pressure and the vacuum field value at the geometric

control of the barrier evolution in a burning plasma, pose challenges requiring advances in control techniques. Ions and/or electrons can be heated depending on the auxiliary power used, i.e. ion or electron cyclotron resonant heating (ICRH and ECRH), lower-hybrid heating (LHH) or neutral beam heating (NBH), that can lead to barriers in the ion and/or electron transport channel.

5.1.2 Theory and experiments on the formation and sustainment of ITBs and motivation of this chapter

Despite many theoretical and experimental studies aimed at elucidating the physics of ITBs, the physics involved in the formation and sustainment of ITBs remains unclear. A threshold power appears necessary to generate a barrier, but there is also sensitivity to the q profile and magnetic shear [2], to the power profile and heating scheme (ICRH, ECRH or NBH) and to the plasma rotation profile that in turn is affected by external input momentum [19].

In certain types of ITBs, such as those generated on DIII-D, TFTR, JET and ASDEX Upgrade, the $E \times B$ shearing rate is considered principally responsible in their formation. A significant background $E \times B$ shearing rate is thought to stabilize plasma instabilities leading to a reduction or even suppression of turbulence (see Sec.5.6). Many simulations and experiments performed for these machines probe this conclusion [124, 125, 126, 127].

Conversely, the primary cause for ITB formation and sustainment is sometimes considered the product of negative magnetic shear resulting from a non monotonic q profile. Even with this assumption many questions arise concerning whether the improved confinement is related to the proximity of the minimum q_{min} to low order rational q values [110, 128], the existence of a zero magnetic shear value at the plasma mid-plane [11, 129, 130] or the presence of negative magnetic shear inside q_{min} [19].

At the start of this thesis TCV considered the key ingredient for electron internal transport barrier (eITBs) formation and sustainment as the degree of reverse shear and, in contradiction to other machines, that $E \times B$ shearing rate does not play a significant role. Previous TCV experiments showed that electron core confinement in eITBs was determined essentially by the q profile and the consequent magnetic shear [11, 129]. Gyrokinetic simulations, of these barriers, have confirmed these observations [131, 132, 133]. These studies did not, however, consider any changes in the impurity temperature, density and toroidal or poloidal rotation profiles.

This chapter presents the first measurements of the formation and sustainment of eITBs, with simultaneous measurements of the toroidal and poloidal rotation profiles, on TCV. The CXRS diagnostic measured the intrinsic impurity profiles during the stationary pre-barrier and sustainment phases within a single discharge. From the

---

center R_0. The β value is a decisive quantity for the stability in magnetic confinement devices. Since in a tokamak $B_\theta << B_\varphi$, we have $\beta \approx \beta_\varphi = \beta_t$ where only the toroidal field B_φ is used. Respectively, for the poloidal $\beta_\theta = \beta_p$ the B_θ field is used.

[2]The magnetic shear s is the radial change rate of the safety factor q, which measures the twist of the helical magnetic field lines: $s = (\rho/q)dq/d\rho$.

rotation profiles, the radial electric field and $E \times B$ shearing rate ($\omega'_{E\times B}$) were derived experimentally across the whole plasma radius. Two main scenarios were investigated: a central barrier (ICEC,[120]) and a co-CD off-axis eITB ([11]). The $\omega'_{E\times B}$ shearing rate is then compared to the growth rate of the most unstable mode on TCV's eITBs for both cases. This constitutes the first direct experimental confirmation that, on TCV, the $E \times B$ shearing rate does not play an essential role in eITB barrier formation and sustainment.

Initially, the goal was to measure the $E \times B$ shearing rate in the same eITB scenarios studied in [120, 130, 134, 135, 136] as a function of confinement improvement and probe any link to the safety factor q. A particularity of TCV is a highly elongated vacuum vessel, with ECH X2 launchers installed at the top and mid-plane positions. Unfortunately, most previous experiments were performed above the midplane, typically at Z=21cm whereas the DNBI diagnostic resides at the midplane, Z=0cm. A large part of the experimental work was taken by the development of eITB TCV scenarios at this vertical position to obtain T_c, n_c, v_φ and v_θ measurements.

The equations and two different methods used during this thesis to determine the radial electric field and the $E \times B$ shearing rate are discussed in Sec.5.2. The first method is based on the force balance equation written with the explicit toroidal and poloidal rotation. The second, also based on the force balance equation, is expressed using the recent indirect determination of the poloidal rotation that exploits the toroidal rotation asymmetry [51]. An experimental validation of this method is shown and some analysis issues discussed in Appendix D.

This Chapter proceeds as follows: previous eITBs experiments are presented in Sec.5.3, with the discussion of the confinement improvement and reverse magnetic shear. Two types of eITBs have been studied with co-CD off-axis and cnt-CD on-axis. In Sec.5.4 and Sec.5.5 we first show how these scenarios have been reproduced at Z=0cm and confirm that similar improved confinement was obtained. The effect of the total and central injected power and MHD activity on the rotation profiles and barrier strength for the central barrier are investigated in Sec.5.4. In Sec.5.5, the effect of inductive current perturbations dI_{OH}/dt for the co-CD off-axis eITBs is presented, together with a summary of the experimental measurements. For completeness, in Appendix D.2, the effect of a global oscillation in both scenarios is discussed. Sec.5.6 presents a comparison between the experimental results and gyrokinetic simulations. The measured $E \times B$ shearing rates are compared with the growth rate of the most unstable mode for these discharges (TEM) to determine the importance of the $E \times B$ shear flows on TCV. Additionally, in Sec.5.7 the experimental impurity ion profiles for both scenarios are discussed and compared with the results of a quasi-linear model describing the particle transport on TCV eITBs [137, 138]. Some discrepancies are observed, suggesting a future revision of the model. Finally, a conclusion summarizing the main results (Sec.5.8) will close this chapter.

5.2 Radial electric field (E_r) determination

To determine experimentally the $E \times B$ shearing rate, the radial electric field is calculated from the impurity ion profiles. This theoretical section presents the equations, and the related techniques, used during this thesis to determine the radial electric field. The first uses the force balance equation written with explicit toroidal and poloidal rotation, which is the most frequently used method in the fusion community to derive E_r experimentally. The second, also based on the force balance equation, is expressed using the recent method of indirect determination of the poloidal rotation, which exploits toroidal rotation asymmetry [51].

5.2.1 E_r from "standard" force balance equation

The standard method for obtaining the radial electric field in fusion plasmas is to derive it through the radial ion force balance equation. This commences with the momentum balance equation (also referred as the fluid equation of motion) that can be written for each plasma species separately [49]. For a considered species α, this equation is given by [3, 139]:

$$m_\alpha n_\alpha \frac{d\mathbf{v}_\alpha}{dt} = n_\alpha q_\alpha \left(\mathbf{E} + \mathbf{v}_\alpha \times \mathbf{B}\right) - \nabla \cdot \mathbf{P}_\alpha + \mathbf{R}_\alpha \tag{5.1}$$

$$m_\alpha n_\alpha \left(\frac{\partial \mathbf{v}_\alpha}{\partial t} + (\mathbf{v}_\alpha \cdot \nabla)\mathbf{v}_\alpha\right) = n_\alpha q_\alpha \left(\mathbf{E} + \mathbf{v}_\alpha \times \mathbf{B}\right) - \nabla \cdot \mathbf{P}_\alpha + \mathbf{R}_\alpha$$

where $n_\alpha = \int f_\alpha d^3 v$ is the number density (i.e. the total number of α particles inside the volume V) and $f_\alpha(\mathbf{x}, \mathbf{v}, t)$ is the distribution function for the species α. The fluid velocity for the considered species α, is given by $\mathbf{v}_\alpha = \int \mathbf{v} f_\alpha d^3 v$, $q_\alpha = Z_\alpha e$ is the species charge and $\mathbf{P}_\alpha$ is the pressure tensor for the species α. The term $\mathbf{R}_\alpha$ is the momentum transfer due to collisions between different species (friction).

For a steady-state plasma, $\partial/\partial t = 0$. The $(\mathbf{v}_\alpha \cdot \nabla)\mathbf{v}_\alpha$ term, representing the inertial forces, is finite for finite rotation. If the rotation is subsonic, this term becomes small compared to the other terms and is often neglected. As carbon is the main impurity on TCV (α=C=i), we derive the radial electric field for the carbon species [3]:

$$E_r = \frac{\nabla p_i}{n_i Z_i e} + v_{\varphi,i} B_\theta - v_{\theta,i} B_\varphi \tag{5.2}$$

where the contributions from friction and any sources or sinks have been neglected. Furthermore, any off-diagonal terms in the pressure tensor have been ignored and the impurity ion velocity distribution f is assumed Maxwellian. The three terms that compose E_r are the diamagnetic term $\nabla p_i / n_i Z_i e$, where p_i is the considered carbon pressure and $Z_i = 6$, the poloidal $v_{\theta,i} B_\varphi$ and toroidal $v_{\varphi,i} B_\theta$ contributions. The equation shows that, to lowest order, the Lorentz force $\mathbf{F} = Z_i e n_i \left(\mathbf{E} + \mathbf{v}_i \times \mathbf{B}\right)$ is balanced by the pressure force. From this equation we can see the importance

of accurate measurements of the toroidal rotation profiles on both HFS and LFS, the poloidal rotation, together with the toroidal and poloidal magnetic fields. The magnetic fields are obtained from the magnetic probes and the LIUQE code, while the impurity rotations, temperature and density profiles are obtained from the three CXRS diagnostic systems. In this chapter we will simplify the notation of the measured carbon toroidal and poloidal rotations as v_φ (or v_t) and v_θ (or v_{pol}).

5.2.2 E_r from indirect measurement of poloidal rotation

A new method to measure the radial electric field is presented, again from the force balance equation, but exploiting an indirect measurement of the poloidal rotation and the two related flux functions $\hat{u}_\sigma(\psi)$ and $\hat{\omega}_\sigma(\psi)$. E_r is thus derived without directly measuring v_θ (or v_{pol}) using the CXRS diagnostic. The derivation of v_{pol} from the toroidal rotation asymmetry has been recently demonstrated and published on TCV and DIII-D [51, 140]. This method shows that, for divergence free flows, the difference between the toroidal rotation frequency $f_t = v_t/R$ at the HFS and LFS locations on the same flux surface is proportional to the poloidal rotation:

$$\Delta f_t = f_{HFS} - f_{LFS} \approx \frac{4q}{R_0} v_{pol} \tag{5.3}$$

where q is the safety factor, R_0 the location of the magnetic axis and v_{pol} the poloidal rotation at the LFS. This indirect measurement provides more accurate estimates of the poloidal rotation compared with the direct spectroscopic measure given by the CXRS diagnostic that suffers from relatively large experimental uncertainties. The Doppler shifts associated with the toroidal rotation are often much larger than the total measurement uncertainties, whereas these uncertainties often dominate the direct poloidal velocity measurement. This technique assumes that the ion temperature is a flux function as is the electrostatic potential (to first-order). The ion density usually is also considered a flux function, but for particular plasma cases (like strong eITBs) there may be a poloidal angular dependence. As a consequence, the first-order fluid velocity is assumed to lie entirely on flux surfaces and can be expressed as the sum of a toroidal rigid body component and a component parallel to the magnetic field (see Sec.5.2.2). To date, the method has only been applied to Ohmic and a few EC heated L-mode TCV plasmas to compare the profiles to neoclassical predictions [51]. In the next paragraphs we summarize the derivation of the E_r profiles based on this technique that was applied to the central barrier and eITB study.

Tokamak coordinate conventions

To calculate a local radial electric field, it is essential to have a coherent sign conversion for all toroidal and poloidal components (magnetic fields, rotations,...). Many conventions are used in the various TCV codes that can lead to confusion and errors. The tokamak COordinate COnventionS (COCOS), proposed in [141], can be used to define the specific direction of increasing toroidal and poloidal angles, the sign and

normalization of the poloidal flux, and is used here.

In the next subsection we briefly resume the derivation of the radial electric field using the indirect measurement of the poloidal rotation, expressed in the COCOS formalism. The calculation was performed using the coordinate COCOS=17 (for the LIUQE and psitbx codes), with the toroidal angle $\varphi > 0$ cnt-clockwise from the top, the poloidal angle $\theta > 0$ clockwise from the front ($\theta = 0$ at the top of a vertical line) and a decreasing poloidal flux ψ (see Fig.5.1).
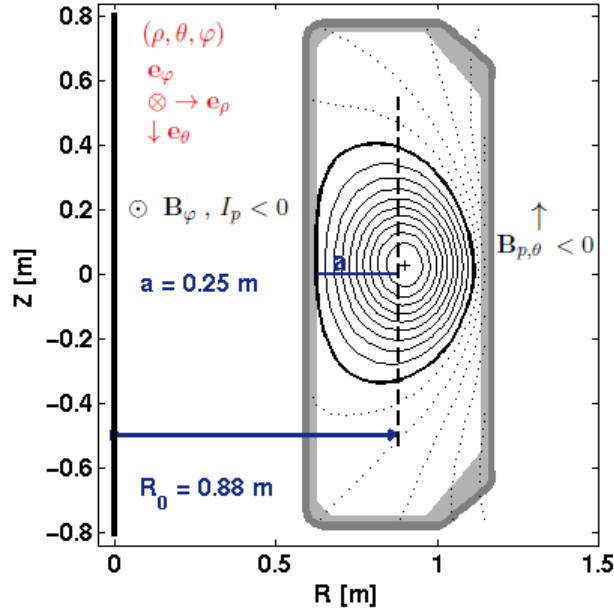
Figure 5.1: Schematic of the plasma current and magnetic fields directions obtained for the eITBs study using the chosen TCV Coordinate Conventions (COCOS=17).

Poloidal and toroidal rotation indirect measurement: the $\hat{u}(\psi)$, $\hat{\omega}(\psi)$, $K(\psi)$ and $\hat{\Omega}(\psi)$ flux functions

As shown in the appendix of [51] and [142], for the considered species (in this case the carbon impurity), the rotation so as its toroidal and poloidal components may be written in function of the two flux functions $\hat{u}_\sigma(\psi)$, $\hat{\omega}_\sigma(\psi)$:

$$\mathbf{v}_\sigma = \hat{u}_\sigma(\psi)\mathbf{B} + R\hat{\omega}_\sigma(\psi)\mathbf{e}_\varphi \tag{5.4}$$

$$v_{\sigma\varphi} = R\hat{\omega}_\sigma(\psi) + \hat{u}_\sigma(\psi)B_\varphi \tag{5.5}$$

$$v_{\sigma pol} = \hat{u}_\sigma(\psi)B_{pol} = \sigma_{\rho\theta\varphi}\sigma_{I_p}\hat{u}_\sigma(\psi)\widetilde{B}_{pol} \tag{5.6}$$

where $\widetilde{B}_{pol} = |B_{pol}|$ is the poloidal magnetic field and $B_\varphi = F/R$ the toroidal magnetic field. Taking the radial HFS and LFS positions R_H and R_L on the same flux surface and supposing impurity density symmetry, we define:

$$\hat{u}(\psi) = \frac{v_{\varphi,H}/R_H - v_{\varphi,L}/R_L}{R_L^2 - R_H^2}\frac{R_L^2 R_H^2}{F} \tag{5.7}$$

$$\hat{\omega}(\psi) = \frac{v_{\varphi,H}R_H - v_{\varphi,L}R_L}{R_L^2 - R_H^2} = \frac{v_{\varphi,L/H}}{R_{L/H}} - \hat{u}_{L/H}\frac{B_{\varphi,L/H}}{R_{L/H}} \tag{5.8}$$

where $v_{\varphi,H}$ and $v_{\varphi,L}$ are the toroidal rotations measured on the same flux surface respectively on the HFS and LFS. $\hat{u}(\psi)$ and $\hat{\omega}(\psi)$ are obtained experimentally. In the absence of poloidal rotation $v_{\sigma pol} = \hat{u}_\sigma = 0$, each plasma surface rotates toroidally as a rigid body at a rotation frequency $f_t = v_{\sigma\varphi}/R = \hat{\omega}_\sigma(\psi)$, while, with a finite $v_{\sigma pol}$ an additional contribution from the $\hat{u}_\sigma$ term modifies this frequency.

When the impurity asymmetry can not be neglected, (as for the investigated co-CD off-axis eITBs), $n_\sigma(\psi)$, $\hat{u}_\sigma(\psi)$ and $\hat{\omega}_\sigma(\psi)$ are no longer flux functions (they also depend on poloidal angle θ) and we must define two further flux functions $K_\sigma(\psi)$ and $\hat{\Omega}_\sigma(\psi)$ [51]:

$$K_\sigma(\psi) = n_\sigma(\psi,\theta)\hat{u}_\sigma(\psi,\theta) \tag{5.9}$$

$$\hat{\omega}_\sigma(\psi,\theta) = \sigma_{B_p}(2\pi)^{e_{B_p}}\left[\hat{\Omega}_\sigma(\psi) - \frac{T_\sigma(\psi)}{n_\sigma(\psi,\theta)Ze}\frac{\partial n_\sigma(\psi,\theta)}{\partial\psi}\right] \tag{5.10}$$

$$\hat{\Omega}_\sigma(\psi) = -\frac{\partial\Phi}{\partial\psi} - \frac{1}{Ze}\frac{dT_\sigma(\psi)}{d\psi} \tag{5.11}$$

where σ_{B_p} is the sign of B_p, $e_{B_p} = 1/0$ whether the poloidal flux ψ is divided by 2π or not and Φ is the electrostatic potential (assumed a flux function to first order). Using Eq.5.5, $K(\psi)$ and $\hat{\Omega}(\psi)$ may then be rewritten for the two positions R_L and R_H:

$$K(\psi) = \frac{1}{F}\left(\frac{v_{\varphi,H}}{R_H} - \frac{v_{\varphi,L}}{R_L} - \sigma_{B_p}(2\pi)^{e_{B_p}}\frac{T}{Ze}\frac{\partial ln(n_H/n_L)}{\partial\psi}\right) \times \left(\frac{n_L n_H R_L^2 R_H^2}{n_L R_L^2 - n_H R_H^2}\right) \tag{5.12}$$

$$\hat{\Omega}(\psi) = \frac{n_L v_{\varphi,L}R_L - n_H v_{\varphi,H}R_H + \sigma_{B_p}(2\pi)^{e_{B_p}}\frac{T}{Ze}\left(R_L^2\frac{\partial n_L}{\partial\psi} - R_H^2\frac{\partial n_H}{\partial\psi}\right)}{\sigma_{B_p}(2\pi)^{e_{B_p}}\left(n_L R_L^2 - n_H R_H^2\right)} \tag{5.13}$$

When $n_L = n_H$, we note that Eq.5.12 leads back to Eq.5.7 and Eqs.5.13, 5.10 to Eq.5.8. The main plasma parameters measured in the central barrier and eITBs sessions were with negative plasma current and magnetic field $I_p, B_0, B_{pol} < 0$ ($\sigma_{B_p} = -1$ and $e_{B_p} = 1$ defined by the COCOS index), with $\hat{\omega} > 0$ and $\hat{u} > 0$. For the central barrier, the resulting toroidal rotation was positive ($v_\varphi > 0$) and the poloidal rotation negative ($v_{pol} < 0$). The contributions can be plotted as vectors, as in Fig.5.2. We note that the total rotation is obtained as $\mathbf{v} = \mathbf{v}_\parallel + \mathbf{v}_\perp$, but it is also given by the sum of its projections on the magnetic field $\hat{u}\mathbf{B}$ and the toroidal rigid-body contribution $R\hat{\omega}\mathbf{e}_\varphi$ (see Eq.5.4). The red vector in Fig.5.2 shows that $v_\parallel - \hat{u}B$ is the flow speed parallel to the magnetic field required to cancel the poloidal component of the perpendicular flow $v_\perp$ (diamagnetic flow), in order to make the net poloidal flow $\hat{u}$ vanish.
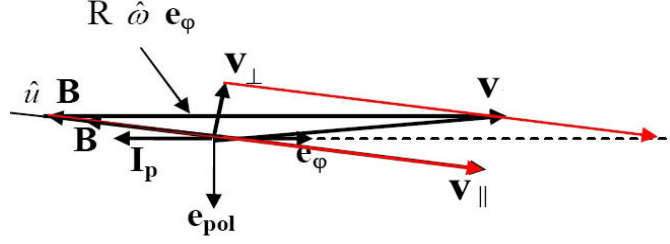
Figure 5.2: Contributions to the rotation vector $\mathbf{v}$ for a TCV central barrier: $I_p, B_0, B_{pol} < 0$, $\hat{\omega}, \hat{u} > 0$, $v_\varphi > 0$ and $v_{pol} < 0$ using COCOS=17 (at z=zaxis,LFS). The rotation can be obtained by summing $\mathbf{v} = \mathbf{v}_\parallel + \mathbf{v}_\perp$ or $\mathbf{v} = \hat{u}\mathbf{B} + R\hat{\omega}\mathbf{e}_\varphi$.

Radial electric field derivation

The relation of the radial electric field can be written as:

$$\mathbf{E} = \frac{1}{n_\sigma Ze}\nabla p_\sigma - \mathbf{v}_\sigma \times \mathbf{B} = \frac{1}{n_\sigma Ze}\nabla p_\sigma - R\hat{\omega}_\sigma\mathbf{e}_\varphi \times \mathbf{B} \qquad (5.14)$$

We immediately observe that only the rigid body portion of the toroidal rotation $\hat{\omega}_\sigma$ contributes to E_r and not the $\hat{u}\mathbf{B}$ term. The component of the radial electric field perpendicular to the flux surface is:

$$\frac{\mathbf{E}\cdot\nabla\psi}{|\nabla\psi|} = \left[\frac{1}{n_\sigma Ze}\frac{dp_\sigma(\psi)}{d\psi} + \hat{\omega}_\sigma(\psi)\frac{\sigma_{B_p}}{(2\pi)^{e_{B_p}}}\right](2\pi)^{e_{B_p}}R\widetilde{B}_{pol} \qquad (5.15)$$

where $\widetilde{B}_{pol} > 0$ as defined in Eq.5.6. We note that $sign(\nabla\psi)$ can be positive or negative depending on the chosen convention and on the plasma current direction. In order to have the radial electric field related to an outward direction, one needs to use the same transformation as in Eq.(24) of [141], so that:

$$E_r = \left[\frac{(2\pi)^{e_{B_p}}}{n_\sigma Ze}\frac{dp_\sigma}{d|\psi - \psi_{axis}|} + \hat{\omega}_\sigma(\psi)\sigma_{I_p}\right]R\widetilde{B}_{pol} \qquad (5.16)$$

where $d\psi = \sigma_{B_p}\sigma_{I_p}d|\psi - \psi_{axis}|$. The radial electric field is finally derived after replacing $\hat{\omega}_\sigma$ with Eqs.5.8 or 5.10 and 5.13 and using the impurity profiles from the CXRS, mapped on the same flux surface, to calculate the poloidal rotation, $\hat{\omega}_\sigma$, $\hat{u}_\sigma$ and ∇p_σ. It is important to note that E_r is proportional to the ∇p_σ and $\hat{\omega}_\sigma$ terms. The ∇p_σ term always leads to an inward radial electric field contribution (p_σ typically decreasing with minor radius), while $\sigma_{I_p}\hat{\omega}_\sigma$ can be additive or not. In most of the previously described barriers, the ∇p_σ contribution is considerably smaller than $\hat{\omega}_\sigma$ that usually dominates the E_r profile (see Fig.D.4). When ∇p_σ and v_{pol} are small and an inward $E_r < 0$ is expected, we observe $sign(\hat{\omega}_\sigma) = -\sigma_{I_p}$ and the $R\hat{\omega}_\sigma$ contribution to v_φ is in the counter-current direction. Note that, typically, $R\hat{\omega}_\sigma$ and $\hat{u}_\sigma B_\varphi$ have opposite signs, which can lead to counter-current v_φ on the LFS region (where the $R\hat{\omega}_\sigma$ dominates since R is larger) and to co-current v_φ on the HFS (where $\hat{u}_\sigma F/R$ dominates since $F/R = B_\varphi$ is larger). This explains the asymmetry of the toroidal rotation profiles

observed for the OH target and the central barrier, where, on the external flux surfaces, the plasma rotates in the opposite direction at the HFS and LFS (see Fig.D.1.b and Fig.D.2). This is explained by a finite $v_{\sigma pol}$ in the electron diamagnetic direction that generates an opposite contribution $\hat{u}_\sigma B_\varphi$ summed to the main $R\hat{\omega}_\sigma$ toroidal flow. Since $\widetilde{B}_{pol}$ is zero on the magnetic axis, it can be deduced that at $\rho_\psi = 0$:

$$E_r(\rho_\psi = 0) = 0. \tag{5.17}$$

To conclude this section, we recall that the main uncertainties on the indirect v_{pol} and E_r determination considered in this study come from uncertainties in the Doppler shift rotation measurements (spectral fit, wavelength calibration and background subtraction), the magnetic field reconstruction and the mapping of the HFS and LFS profiles to the flux surfaces. As an example, to estimate the uncertainties due to the $R_{H,L}$ mapping, a radial deviation of 5mm (2% of TCV minor radius) was applied to the equilibrium reconstruction position. All the described uncertainties were taken into account in the calculation of the error bars shown in this chapter. Further details on the validation of both methods applied to one TCV central barrier can be found in Appendix D.1.

5.2.3   ExB shearing rate determination

With the radial electric field from Sec.5.2.1 or 5.2.2, the $E \times B$ shearing rate may now be determined. The expression of the $E \times B$ shearing rate used throughout this study is given by [143]:

$$\omega'_{E \times B} = \frac{r}{q_s B_0} \frac{d}{dr}\left(\frac{q_s E_r}{r}\right) \tag{5.18}$$

where r is the minor radius, q_s the safety factor, B_0 the magnetic field on-axis and E_r the radial electric field previously defined. The minor radius is defined as $r = (R_{max} - R_{min})/2$ of the flux surface at $Z = Z_{axis}$.

5.3   eITBs at Z=21cm on TCV

In past years, TCV has formed eITBs using the flexible ECRH system in discharges with inductive current (driven by the Ohmic transformer) [120], or fully non-inductive scenarios [135, 136]. TCV demonstrated strong alignment between the barrier and the bootstrap current (see Sec.1.7.3) in a fully non-inductive stationary eITB. The plasma was fully sustained by a high bootstrap fraction together with a EC current drive component (see Sec.1.7.2) in order to create a hollow or flat current profile [118, 119]. The importance of the magnetic shear s shape in both the formation and performance of eITBs is observed on TCV [130, 144]. It was concluded that a reversed shear profile (a flat profile is already beneficial) plays a key role in eITB formation [11, 129]. TCV's eITBs are characterized by a high temperature ratio $T_e/T_i \approx 20 - 35$ (strong decoupling between ions and electrons), $\beta_{pol} > 2$, low density and may be created

without a fast current ramp or any direct momentum input (as is mostly used in other tokamaks).

The improvement in energy confinement over the Ohmic TCV L-mode is commonly parametrized by $H_{RLW} = \tau_{Ee}/\tau_{RLW}$, where τ_{Ee} is the electron energy confinement time and τ_{RLW} the time predicted by the Rebut -Lallia -Watkins scaling [145]. τ_{RLW} is an excellent predictor of TCV Ohmic L-mode electron confinement (and for many other dominantly electron-heated devices like Tore Supra). Another method is, of course, to measure the temperature scale length $|R/L_{Te}|$. It is usually near 10 for Ohmic and EC heated discharges as seen on many tokamaks [146]. With eITBs it can reach values of 45 (see Fig.3.8 in [30]), indicating a clear local barrier for heat transport.

On TCV, a direct control of the current profile is not available, and eITB control is achieved by continuously adjusting external actuators to vary the q profile [11, 129] together with interpretative transport simulations that model the evolution of the current profile [130, 134]. The Ohmic and bootstrap contributions are derived from the electron density and temperatures from the Thomson diagnostic, while the ECCD component is derived from Fokker-Planck codes like CQL3D [147] or LUKE [148].

As commented in Sec.1.7.2, the ECCD contributions are essential to obtain the hollow plasma current density profile needed to develop an eITB on TCV. So far two main strategies to create this current profile shape have been applied on TCV. By injecting a central counter-CD component at moderate I_p a central barrier can be developed, whilst by injecting a co-CD off-axis contribution at low I_p wider and stronger eITBs can be obtained. Hereafter, these two scenarios will be referred as *central barrier* and *co-CD off-axis eITB*.

To facilitate the comparison between the eITB targets developed during this thesis at Z=0cm and those previously studied on TCV, scenarios with internal barriers positioned at Z=21cm, studied on TCV, are now described.

5.3.1 Central barrier (ICEC)

A central barrier is obtained by injecting cnt-CD on-axis in order to compensate the central co-Ohmic current density (see Sec.1.7.1). The cnt-CD component partially cancels this OH contribution that tends to shrink the hollow current profile region. Co-CD off-axis power can also be added in order to better stabilize the barrier by broadening slightly the temperature and current density profiles.

The confinement improvement related to a central barrier can be observed when studying the effect of different central heating schemes. When applying 1.35MW of central cnt-CD to weakly elongated plasmas ($I_p = 170kA$, $\delta = 0.2$, $K = 1.2$), an evident increase in T_e and in the electron confinement time τ_{Ee} is obtained, compared to plasmas with the same power amount of central ECH or co-CD. This was shown in Fig.5.3 and 5.4.a (taken from [134]), where the electron temperature profiles as a function of the vertical position z and $\rho_V = \sqrt{V/V_a}$ were plotted. Cnt-CD heating produces almost double central T_e value compared with the ECH and co-CD on-axis heating. The deviation between the temperature profiles and the associated ∇T_e occurs in the region inside $\rho_V \cong 0.3$ (see Fig.5.4.a). In Fig.5.3 we see that the T_e profiles for all three

cases well superpose up to 2.5keV, whilst in the core region a clear temperature rise up to almost 10keV is attained for the cnt-CD heating. This corresponds to a central temperature barrier with a width of $\sim 15cm$. The higher electron temperature profile results from a confinement improvement with τ_{Ee} increasing from 3ms to 4ms for the cnt-CD heating [134]. A factor $H_{RLW} > 2$ is observed for the cnt-CD case, confirming the confinement enhancement. We recall that for L-mode conditions on TCV, a factor $H_{RLW} = 1$ is obtained for Ohmic plasmas, while $H_{RLW} = 2$ for EC heated plasmas [149]. PRETOR simulations were performed using the experimental results of these
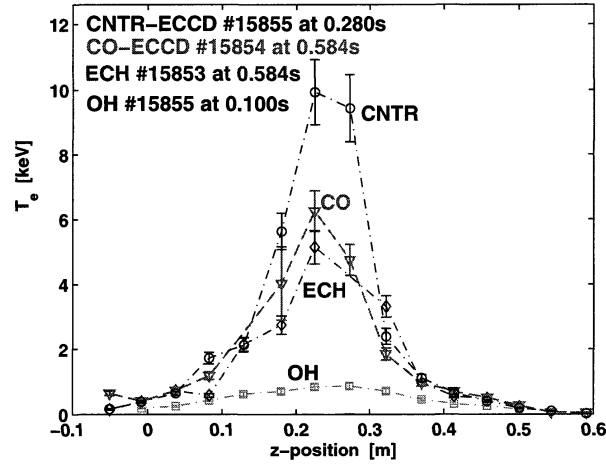
Figure 5.3: Electron temperature profiles obtained with central deposition of 1.35MW of only ECH (#15853), co-CD (#15854) and cnt-CD (#15855). A corresponding Ohmic profile is also plotted for comparison (from [134]).

discharges with the three different heating schemes. The simulated electron temperature profiles are plotted in Fig.5.4.a and the corresponding safety factor profiles in Fig.5.4.b. The q profile for the cnt-CD case is reversed in the core region with values
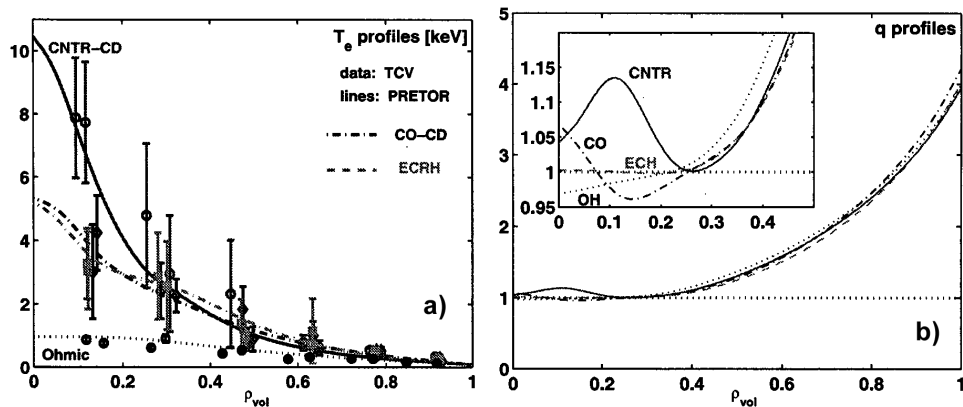
Figure 5.4: PRETOR simulations for the three different heating schemes with cnt-CD (#15855), co-CD (#15854) and ECH (#15853) on-axis, and for Ohmic heating (#15855). a) Experimental measurements (symbols with errorbars) and simulated temperatures profiles (lines). b) corresponding q profiles from [134].

above unity, consistent with the absence of sawtooth activity. For the co-CD case, the q profile may be slightly reversed in the very center but monotonically below 1 otherwise. It is also monotonic for the ECH case, crossing the q=1 surface and leading to some sawtooth activity in the core. These simulations indicated that a centrally reversed q profile is related to a confinement improvement. This correlation is more evident for the strong co-CD off-axis eITBs (see Fig.5.7.a), that present larger and more reversed shear regions for stronger barriers (and $q_{min} > 2$).

The discharges described above (#15853, #15854 and #15855) show that with only 1.35MW of central cnt-CD it is already possible to produce a central barrier. Nevertheless, applying only cnt-CD on-axis was not usually observed to suffice for a stable configuration with a long period of improved confinement. Therefore, some co-CD or ECH off-axis power is often added to stabilize the central barrier. A well localized co-CD or ECH off-axis power contribution can broaden the temperature profile and consequently the current density and reversed q profiles. Similar discharges to #15855 with additional ECH off-axis were exhaustively discussed in [120] and Sec.4.6.2-4.6.5 of [134]. The corresponding safety factor profiles illustrate a quite similar reversed profile in the core region inside $\rho_v \cong 0.3$. A reduction of the transport coefficient χ_e in the plasma center is also observed (see Fig.4.38 of [134]), confirming a confinement enhancement inside the barrier. R/L_{Te} values up to more than 20 are obtained in this case.

5.3.2 co-CD off-axis eITB

Besides central barriers, fully non-inductive scenarios featuring strong eITBs have been studied on TCV [11, 118, 119, 129, 130, 135, 136, 144].

In contrast to the strong ITBs formed on many machines employing early NBH heating and a fast current ramp to retard the current penetration, in TCV we start from an Ohmic discharge with the current peaked on-axis and then make a transition to a fully non-inductively driven discharge with the help of co-CD off-axis and central heating (or a combination of cnt-CD on-axis and co-CD off-axis).

The I_p, T_e and H_{RLW} time traces for an eITB scenario (#25956) are illustrated in Fig.1 of [130]. The corresponding TCV poloidal cross section with the plasma boundary and beam positions, together with the deposited power and driven currents are also shown in Fig.5.5. Starting from a stationary low current Ohmic plasma, an eITB target (#25956) is formed by replacing the inductive current, (OH ramp switched off), with co-CD off-axis heating (900kW from cluster A at 0.4s, in green and red). The confinement starts to improve with the bootstrap current build up. The current in the transformer coils I_{OH} is kept constant, leading to a $V_{loop} = 0$. Successively, at 0.85s 450kW of on-axis ECH (from cluster B, in lilac) is added to strengthen the barrier (for a total of 1.35MW injected power). The bootstrap current becomes largest off-axis and grows as a result of the increased temperature (and density) gradient from the additional heating that improves the confinement by further decreasing the magnetic shear.

A dI_{OH}/dt scan was performed for this eITB target to study the effect of inductive
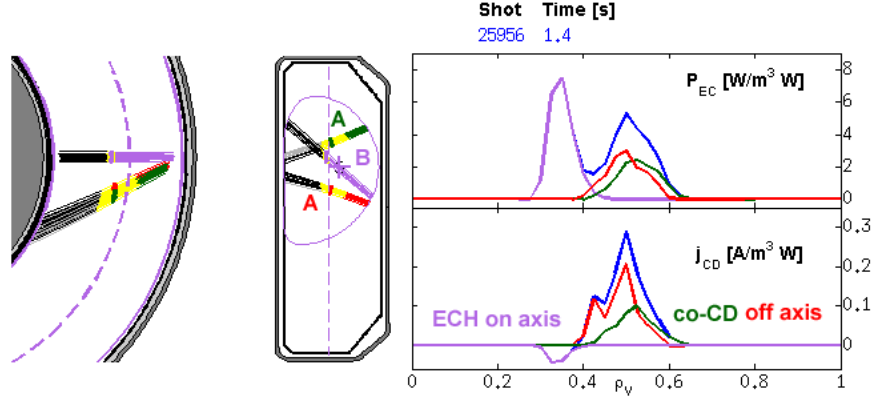
Figure 5.5: Power and ECCD current density deposition scheme reconstructed with TORAY for an eITB scenario #25956 at 1.4s. Two beams are injected co-CD off-axis (red + green, cluster A) and one beam is injected in ECH on-axis (lilac, cluster B) for a total of 1.35MW. N.B: $\rho_v = \sqrt{V/V_a}$ is the normalized volume coordinate.

current perturbations on the barrier strength. Confinement properties are thus modified at constant input power by changing only the central q profile. From 1.4s to the end of the pulse, a null $dI_{OH}/dt = 0$, a negative $dI_{OH}/dt = -500A/s$ or a positive $dI_{OH}/dt = +500A/s$ ramp were imposed in #25956 and two similar discharges. A stationary I_{OH} ($dI_{OH}/dt = 0$), corresponds to $V_{loop} = 0$ and drives no inductive current $j_{OH} = 0$ (#25956). A small positive ramp (co-OH), like $dI_{OH}/dt = 500A/s$ generates $V_{loop} = +30mV$ and $j_{OH} > 0$, increasing the total I_p and reducing the barrier strength (#25957). Conversely, a negative ramp, $dI_{OH}/dt = -500A/s$ corresponding to $V_{loop} = -30mV$, improves the barrier confinement (#25953). The effects of these three dI_{OH}/dt values on the electron temperature and density profiles are plotted in Fig.5.6.a-b. A peaked T_e profile with a steep ∇T_e value at $\rho_V \cong 0.4$ is visible for
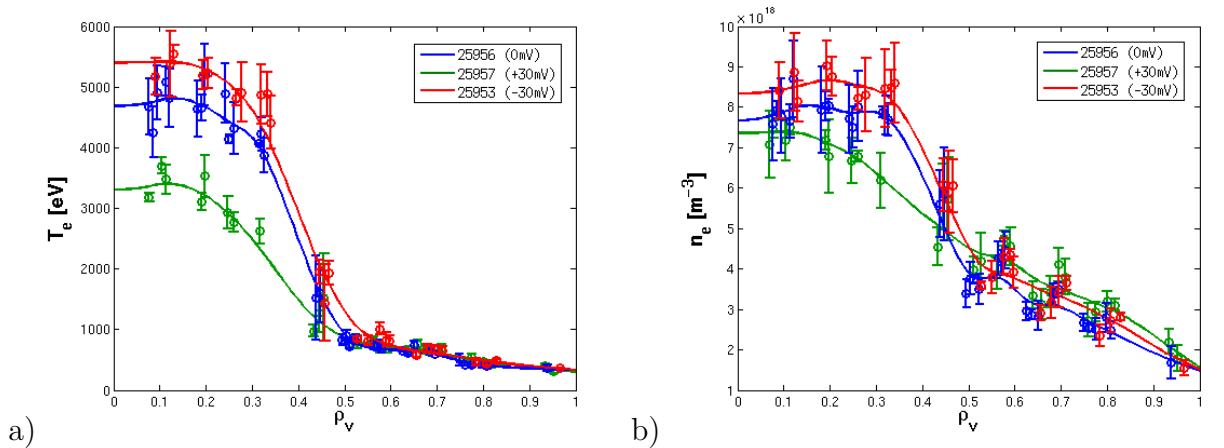
Figure 5.6: Electron a) temperature and b) density for shots #25956, #25957 and #25953 at [1.9,2.2]s as a function of $\rho_V = \sqrt{V/V_a}$.

both #25956 and #25957 discharges with $dI_{OH}/dt \leq 0$, indicating the presence of an

internal barrier. The negative dI_{OH}/dt ramp reinforces the existing barrier and simultaneously broadens and increases the T_e profiles (#25957 in red), while the positive dI_{OH}/dt ramp (#25953 in green) results in a reduced T_e profile and a weakened barrier (further details in [11]). The temperature and pressure broadening correspond to a larger plasma volume contained within the barrier with a commensurate confinement improvement ($H_{RLW} > 3$ identifying these eITBs). The presence of a density barrier inside $\rho_V \cong 0.4$ is visible for the $dI_{OH}/dt \leq 0$ cases. Compared with the central barrier case (Sec.5.3.1), this eITB target presents much larger T_e gradients values, together with a density barrier. In this case R/L_{Te} up to 45 can be obtained [30, 137].

The experiments in [11] demonstrated the fundamental role of the plasma current density tailoring as the main mechanism regulating the strength of a barrier on TCV. Steady state modeling of the total current density profile for the scenarios described above were performed in [130, 150] using the CQL3D [147] and ASTRA [105] codes. These simulations evaluated the effect of such perturbations on the degree of shear reversal. The results are summarized in Fig.5.7 taken from [130], where the q profiles obtained for discharges #25956, #25957 and #25953 are plotted together with similar stronger eITBs (produced with 2.25MW). Fig.5.7.a shows that the q profiles are
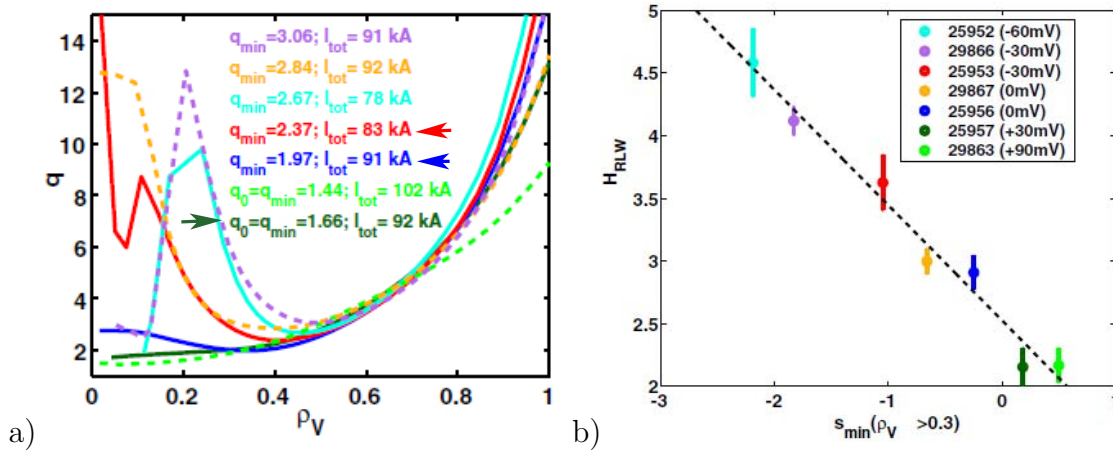
Figure 5.7: a) Safety factor profiles of discharges #25956, #25957, #25953 and #25952 (1.35MW) and of similar stronger eITBs (2.25MW) obtained for a dI_{OH}/dt scan. The obtained q_{min} varies between 1.97 and 3.06. The plasma current are also indicated. b) H_{RLW} as a function of the minimum value of the reconstructed magnetic shear outside $\rho_V \cong 0.3$. The linear growth indicates a smooth confinement improvement (taken from [130]).

reversed for the $dI_{OH}/dt \leq 0$ cases (in red and blue). More precisely, the negative j_{OH} contribution makes the total current density profile significantly hollow, leading to a more reversed q profile characterized by a higher q_{min} value. The depth of the magnetic shear s reversal increases by a factor 2 (see Fig.4 in [130]). In contrast, the addition of a positively peaked inductive current density leads to a monotonic q profile (in green). Recall that, for these scenarios, the total plasma current is mainly sustained by the ECCD and bootstrap components (50-80%) and the total current diffusion time into the plasma is in the 100-200ms range. The strongest barriers are characterized by steeper T_e gradients that increase the bootstrap off-axis contribution and make the j

profile more hollow. The simulated profiles suggested that the presence of an eITB is related to the existence of a $s \leq 0$ region and that the confinement improvement is lost for a monotonic q profile.

In Fig.5.7.b, the corresponding H_{RLW} are plotted as a function of the minimum value of the magnetic shear (outside $\rho_V \cong 0.3$). The confinement improvement increases gradually with the negative magnetic shear. The linear growth between these parameters indicates a smooth transition to improved confinement. As expected, with a negative I_{OH} perturbation the H_{RLW} factor increases from 2.8 to 3.7 (blue and red). For positive value of s_{min}, usually no barriers (or only weak) are obtained with $H_{RLW} = 2-2.5$, consistent with $H_{RLW} = 2$ observed for central heated plasmas. This correlation is used to estimate the minimum magnetic shear value as a function of the calculated H_{RLW} and supports the use of the H_{RLW} in the description of TCV's internal barriers. Further details on these experimental discharges and simulations may be found in [11, 150].

5.4 Central barrier (ICEC) at Z=0cm on TCV

In the next two sections, the two eITB targets studied in this thesis are described and compared with the discharges presented in Sec.5.3. Their main characteristics and the time evolution of the principal physics parameters are presented. As seen in Sec.5.3.1, the simplest way to check for a central eITB is to compare co-CD, ECH and cnt-CD cases, using profiles at constant input power but different q profiles. For off-axis barriers, Sec.5.3.2, the simplest technique is to add an Ohmic perturbation that modifies the central q profile, and hence the barrier strength, at constant input power.

For each of these scenarios, the effect of a few other plasma parameters on the toroidal and poloidal rotation, the radial electric field E_r and the $E \times B$ shearing rate are discussed.

In particular, the effect of the total and central injected power and of the MHD activity is investigated for the central barrier scenario. All the E_r and $E \times B$ shearing rate profiles shown in this section were determined using the indirect method discussed in Sec.5.2.

5.4.1 Effect of different CD components on central confinement

In Fig.5.8 and Fig.5.9 a typical scenario of a central barrier studied during this work, and similar to what was presented in Sec.5.3.1, is shown.

Starting from a stationary Ohmic plasma at 125kA, a power of 900kW cnt-CD on-axis (at $\rho_\psi = 0.2$) is injected at 0.5s from cluster B, together with 450kW of co-CD off-axis (at $\rho_\psi = 0.4$), to strengthen and stabilize the barrier, for a total of 1350kW initial injected power (see Fig.5.9.a). A power scan was performed with values of 450kW, 300kW and 200kW (for each launcher) at, respectively, 0.5s, 1.1s and 1.5s (Fig.5.8.b).
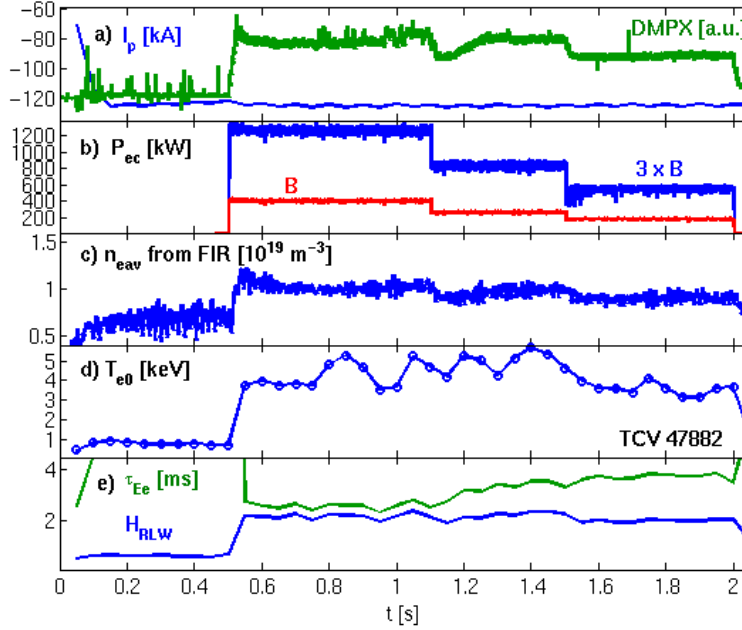
Figure 5.8: Main traces for a typical central barrier scenario #47882.

As discussed previously, this scenario relies on a strong OH current contribution, partially compensated by the cnt-CD component, and has a total plasma current of around 125kA. The co-CD off-axis power can be lower relative to the co-CD off-axis eITB target, since it is mainly used to broaden the temperature and current profile and not to fully sustain the plasma. From the FIR measurements, the line averaged plasma density for this scenario is about $n_{e,av} = 0.9 - 1.1 \times 10^{19} m^{-3}$ (Fig.5.8.c) with temperatures evolving up to 5.5keV.

In order to compare this developed scenario at Z=0cm with the central barriers described in Sec.5.3.1, a similar central power scan, based on discharge #47882, was performed. Figures 5.10.a-b show the electron temperature and density profiles obtained for three discharges obtained by applying 250kW of co-CD off-axis heating and 550kW of cnt-CD (#47882, in blue), co-CD (#47881, in green) or ECH (#47879, in red) on-axis heating for a total of 800kW (see Fig.5.9.b, and the power phase between 1.1s-1.5s in Fig.5.8.b). The Ohmic (OH) phase of shot #47882 is shown for comparison.

Fig.5.10.a shows that the cnt-CD heating produces a well peaked central T_e profile (inside $\rho_\psi = 0.35$), compared with the ECH and co-CD heatings, with albeit only a slightly modified electron density (slightly smaller for the cnt-CD heating, Fig.5.10.b). As observed in Fig.5.4.a, the ECH heating engenders a slightly smaller T_e profile than the co-CD case. This increase in the T_e profile is related to a confinement improvement with τ_{Ee} around 2-3.5ms and $H_{RLW} = 2.4$ (Fig.5.8.e). From Fig.5.11, an R/L_{Te} value up to 22 is obtained for the cnt-CD case, and smaller for the other two heating schemes (up to 18), consistent with [134]. The electron temperature and density profiles as a

Shot	Time [s]	P [%]	I [A/W]	P_N^4	P_N^5	P_N^6
47882	0.75	97.2	3.17e-02	98.4%	99.9%	93.4%

Shot	Time [s]	P [%]	I [A/W]
47882	0.75	97.2	3.17e-02
47881	0.75	98.2	-3.17e-02
47879	0.75	98.1	7.31e-04
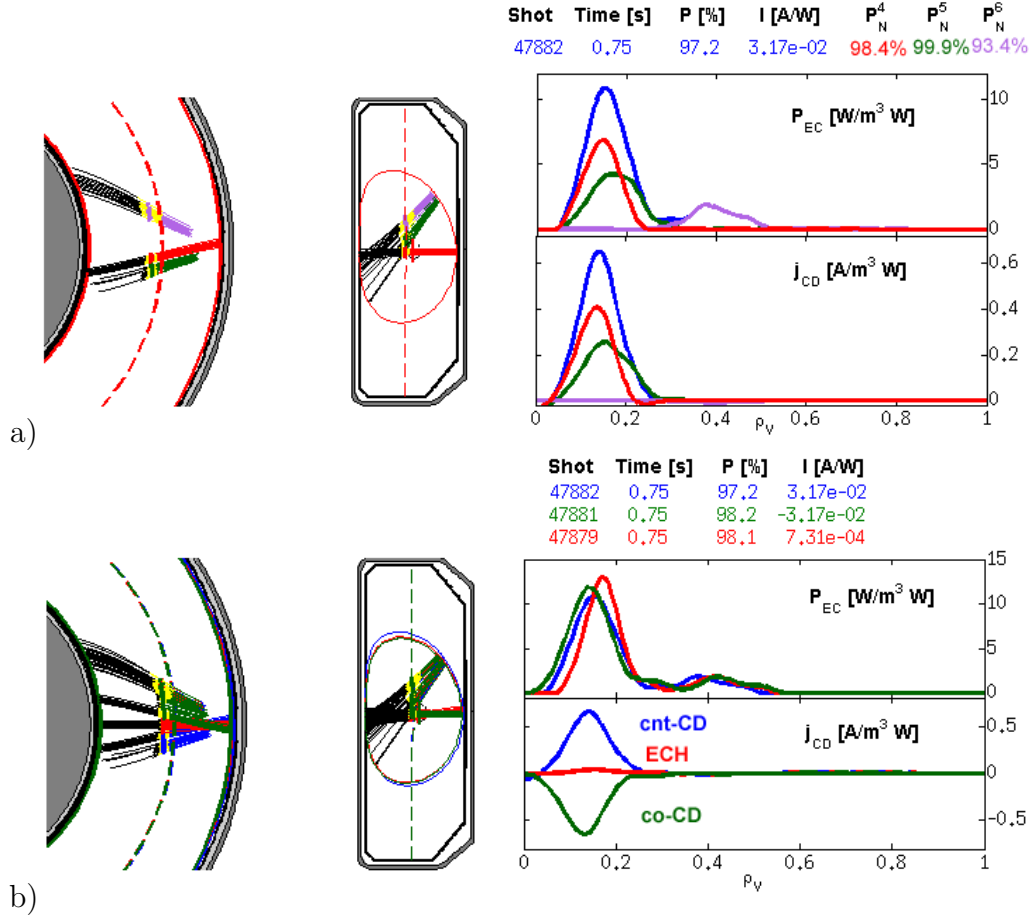
Figure 5.9: a) Power and ECCD current density deposition scheme reconstructed with TORAY for a central barrier scenario (#47882). Two beams are injected cnt-CD on-axis (red + green, cluster B) and one beam is injected in co-CD off-axis (lilac, cluster B). The percentage of absorbed power for each beam is indicated with the corresponding color. b) Total power and ECCD current density deposition for the three different heating schemes: cnt-CD (#47882, in blue), co-CD (#47881, in green) or ECH (#47879, in red) applied on-axis.

function of the vertical position in Fig.5.12 show the development of a central barrier. The T_e profiles for the three cases perfectly superpose up to 2.9keV, whilst in the core region the temperature increases up to 5.5keV for the cnt-CD heating. A barrier for the heat transport of $\Delta z = 15cm$ width is present in the cnt-CD case, whereas no barrier is observed for the density.

The central barrier (positioned at $\rho_\psi \cong 0.3$) is clearly weaker and of smaller volume compared to the co-CD off-axis eITBs (positioned at $\rho_\psi \cong 0.45$). This can explain why H_{RLW} is only slightly larger than two. As expected, the Ohmic phase is characterized by $H_{RLW} \cong 1$, confirming the validity of RLW scaling for these TCV plasmas (see Fig.5.10.a).

These three discharges well reproduce the results of the targets described in Sec.5.3.1. The safety factor profiles corresponding to these three different heatings are therefore assumed to be highly similar to those illustrated in Fig.5.4.b, showing a reversed q

Figure 5.10: Electron a) temperature and b) density for shots #47882 (500kW cnt-CD), #47881 (500kW co-CD), #47879 (500kW ECH) and OH (in cyan) cases (the total injected power attains 800kW). In a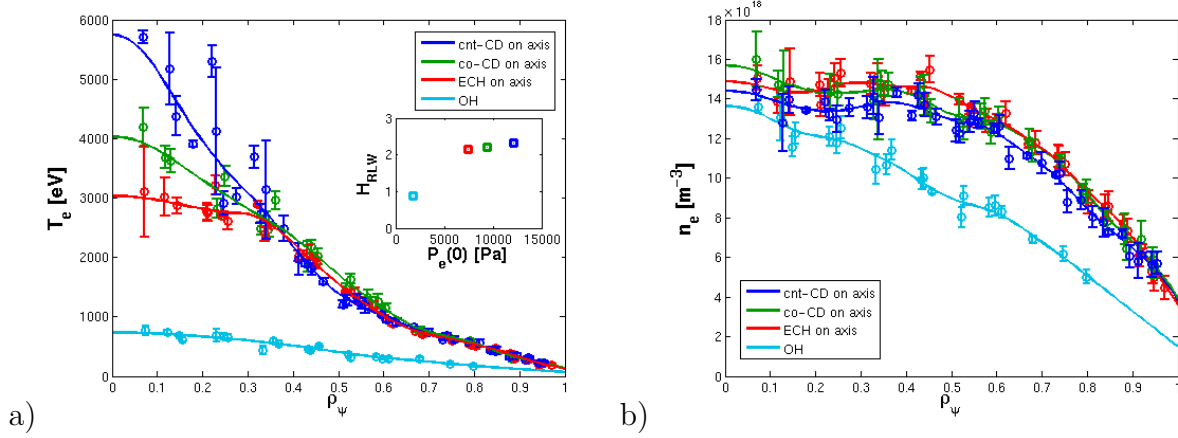) the H_{RLW} is also plotted as a function of the central electron pressure. As expected the Ohmic phase is characterized by $H_{RLW} \cong 1$, confirming the validity of the RLW scaling.

profile for the cnt-CD case. The new targets have, nevertheless, lower central T_e values, due to the reduced central injected power. This difference may eventually lead to less reversed q profiles in the center, but they still feature similar trends.

Figures 5.13 show the related p_e, toroidal rotation, radial electric field and $E \times B$ shearing rate profiles for this same scan. The toroidal rotation v_φ is in the cnt-current direction for all heating schemes (see Fig.5.13.b plotted as a function of ρ_ψ or Fig.E.2 as a function of the coordinate R). The v_φ profile for the cnt-CD case is more peaked in the core and doubled compared with the ECH case that develops a flat rotation profile. The ∇v_φ start to slightly diverge near $\rho_\psi = 0.7$ and then clearly "bifurcate" inside $\rho_\psi = 0.35 - 0.4$. In general, the ECH and co-CD heating engender a more similar effect on the plasma profiles. The poloidal rotation (see Fig.E.1) varies between -1 and -3km/s in the counter clockwise direction for the three cases. The derived radial electric field is inward at mid-radius ($E_r < 0$) and outward in the core (see Fig.5.13.d). It remains somewhat smaller for the cnt-CD heating, with a value of $E_r = -1.5kV/m$. For the cnt-CD case, the two contributions to E_r, $R\hat{\omega}_\sigma \tilde{B}_{pol}$ and the diamagnetic term, discussed in Sec.5.2.2, have been included in Fig.5.13.d and both contributions are of comparable importance. The position where ∇T_e mostly diverge (Fig.5.10.a), at $\rho_\psi = 0.35 - 0.4$, corresponds to the region where ∇v_φ also "bifurcates". Interesting, this region is close to the $E_r = 0$ location, but corresponds to a finite $E \times B$ shearing rate. Although p_e, v_φ and E_r profiles vary between the three heating schemes, the $E \times B$ shearing rates remain similar for all cases with values of around $|\omega'_{E \times B}| \cong 6 \times 10^4 s^{-1}$ (see Fig.5.13.c). The Ohmic phase (in cyan) shows that the v_φ profile is peaked up to 25 km/s and the E_r is larger in the inward direction (-3kV/m) along the plasma radius compared to all heated cases. The $E \times B$ shearing rate remains very small. Note that, for the entire chapter, in the name of graphical legibility, only a single set of error bars for each measured E_r and $E \times B$ shearing rate is plotted. Further details on the largest uncertainties, encountered in this study, may be found in Sec.5.2.2.
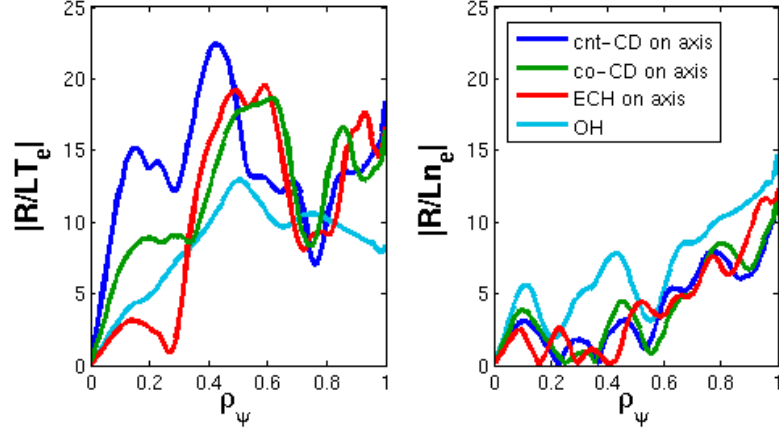
Figure 5.11: $|R/L_{Te}|$ and $|R/L_{ne}|$ profiles for cnt-CD (#47882, in blue), co-CD (#47881, in green), ECH (#47879, in red) and OH (in cyan).
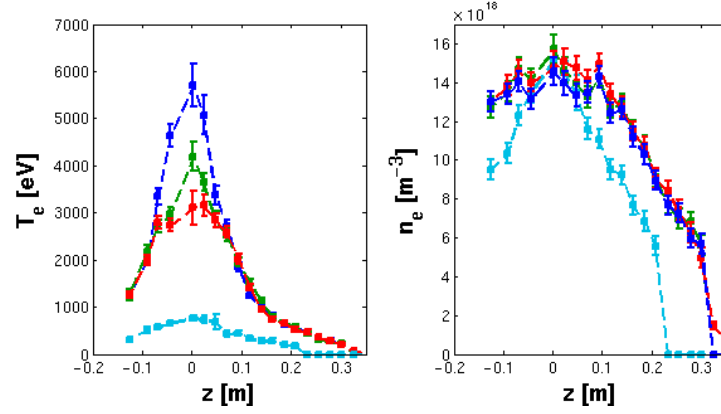
Figure 5.12: Electron temperature (left) and density (right) for the cnt-CD (#47882, in blue), co-CD (#47881, in green), ECH (#47879, in red) and OH (in cyan) cases as a function of the vertical position. A temperature barrier with $\Delta z = 15cm$ width can be observed for the cnt-CD heating.

For completeness, the corresponding carbon ion temperature and density profiles are reported in Appendix E (see Fig.E.3).

These results show that the cnt-CD heating yields the highest performance at constant input power. Despite the clear difference in the electron heat transport observed from the T_e and χ_e profiles, the $E \times B$ shearing rates remain similar, and does not appear to be the cause of the confinement improvement obtained with a central cnt-CD heating.

5.4.2 Effect of total ECH power on the central barrier

To better clarify the effect of the cnt-CD heating on the rotation profiles, a power scan was performed for a similar scenario to the central barrier presented in Sec.5.4.1. A snapshot of shot #45371 is illustrated in Fig.E.4 showing the time evolution and radial profiles of the main plasmas parameters. This snapshot plots the DMPX and FIR

Figure 5.13: a) Electron pressure and H_{RLW} factor b) impurity ion toroidal rotation c) $E \times B$ shearing rate and d) E_r profiles for Ohmic and three different central heating configurations: 500kW cnt-CD (#47882), co-CD (#47881) and ECH (#47879) applied on-axis. Only one set of error bar is plotted for each case. The two contributions of E_r, the $\hat{\omega}$ term and the diamagnetic term, have also been added in d) for the cnt-CD case, showing a comparable weight between these terms.

signals, the power traces, the MHD activity, the LIUQE reconstruction parameters, the radial T_e, n_e, T_i, n_i and v_i profiles. During this work these plots were used to rapidly discern interesting plasma phenomena. Similar snapshots are used during TCV daily operation as they provide rapid operational feedback on the performed discharges.

In Fig.5.14, Fig.5.15 and Fig.5.16, the profiles obtained for a scan of the total injected power during discharge #45371 are shown together with those of a similar Ohmic discharge (#45262). The profiles have been averaged for three power values at [0.9,1.1]s (1600kW, in blue see also Fig.E.4), [1.3,1.5]s (1100kW, in green) and [1.7,1.9]s (800kW, in red).

When depositing more power, the T_e profile increases and a central electron energy barrier is created ($H_{RLW} = 2.9$, Fig.5.16.a and Fig.5.14 in blue). An increase in the electron density is also observed, corresponding to higher p_e profiles. A barrier of 6keV in T_e with a $\Delta z = 17cm$ width is first created that deteriorates to 4keV after

a)
b)
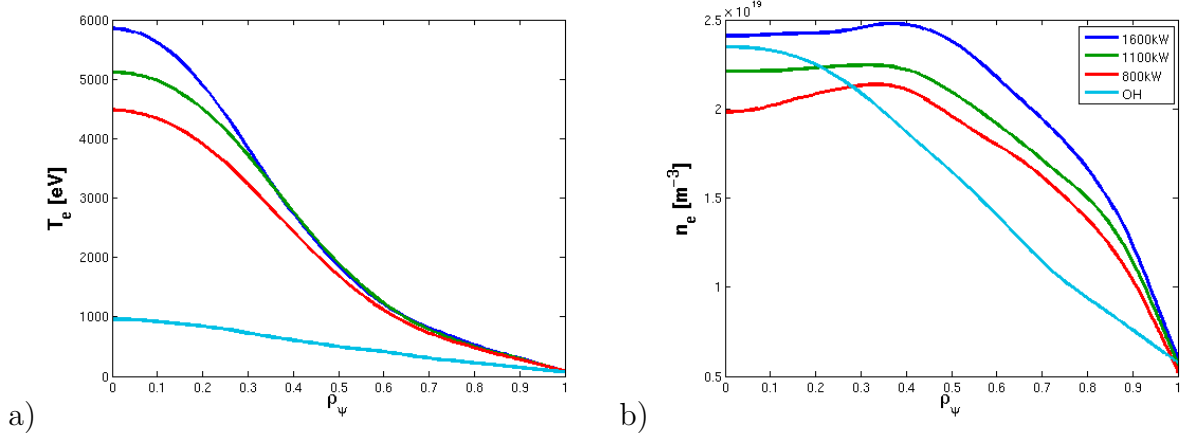
Figure 5.14: Electron a) temperature and b) density for shot #45371 and a similar Ohmic case #45262.
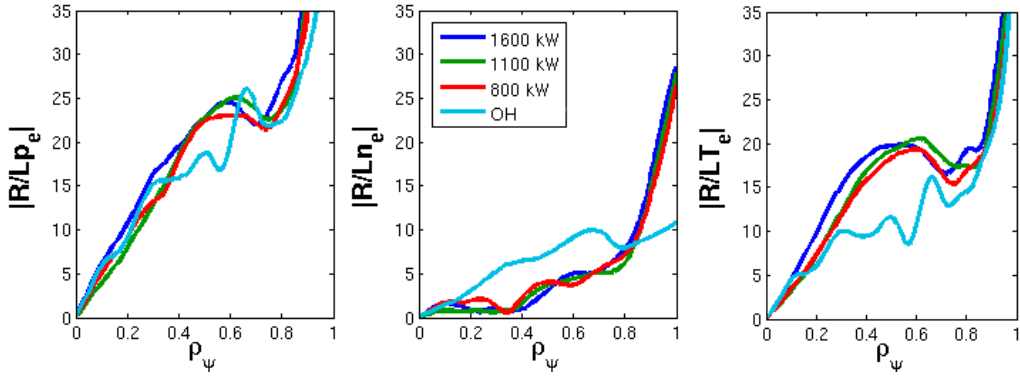
Figure 5.15: $|R/L_{pe}|$, $|R/L_{ne}|$ and $|R/L_{Te}|$ profiles for electrons (solid lines) of discharges #45371 and #45262 (OH).

the reduction of the total injected power (see Fig.E.5). The electron temperature and density scale length profiles plotted in Fig.5.15 show a peak of $|R/L_{Te}| \cong 20$ at $\rho_\psi = 0.45$ for the highest power case, while $|R/L_{ne}| \cong 5$. This $|R/L_{Te}|$ magnitude confirms the presence of a local barrier for heat transport and corresponds well to values obtained in [134].

The toroidal rotation profile is again in the cnt-Ip direction (see Fig.5.16.b plotted as a function of ρ_ψ or Fig.E.7.a as function of coordinate R) and becomes more peaked following the reduction of the total power, up to a value of $v_\varphi = 35 km/s$ for the OH case (in cyan). This is similar to that observed in [151] for H-modes plasmas, where the addition of ECH is seen to cause an increase in both momentum and ion heat transport, leading to a decrease of both the v_φ and T_i profiles (together with a change in the T_e/T_i coupling), as shown in Fig.5.16.b and Fig.5.33. An inboard-outboard v_φ asymmetry is well determined at all power values at LFS and HFS outer flux surfaces. In the HFS region the toroidal rotation changes direction at innermost ρ_ψ values. For the OH case, v_φ remains in the cnt-Ip direction up to $\rho_\psi = 0.85$, whereas in the HFS
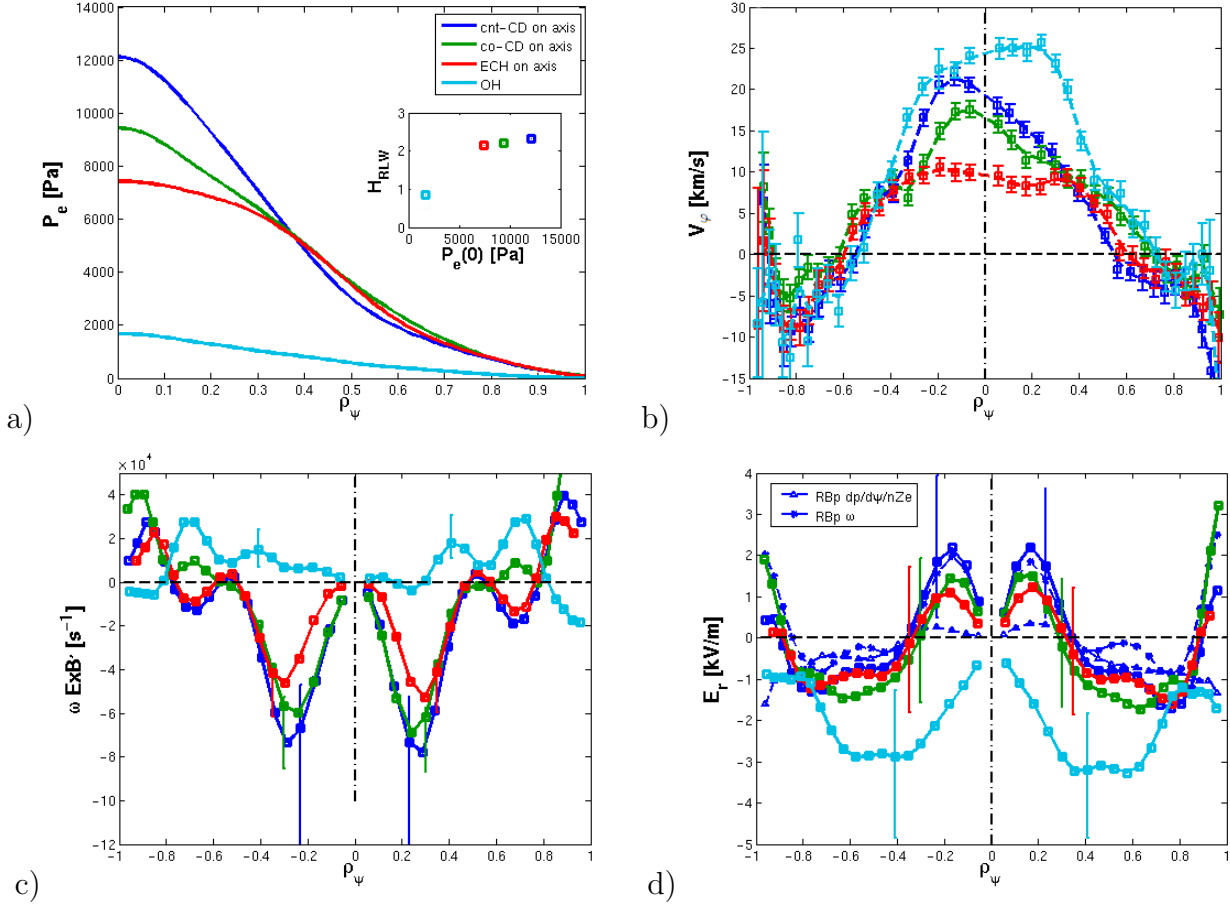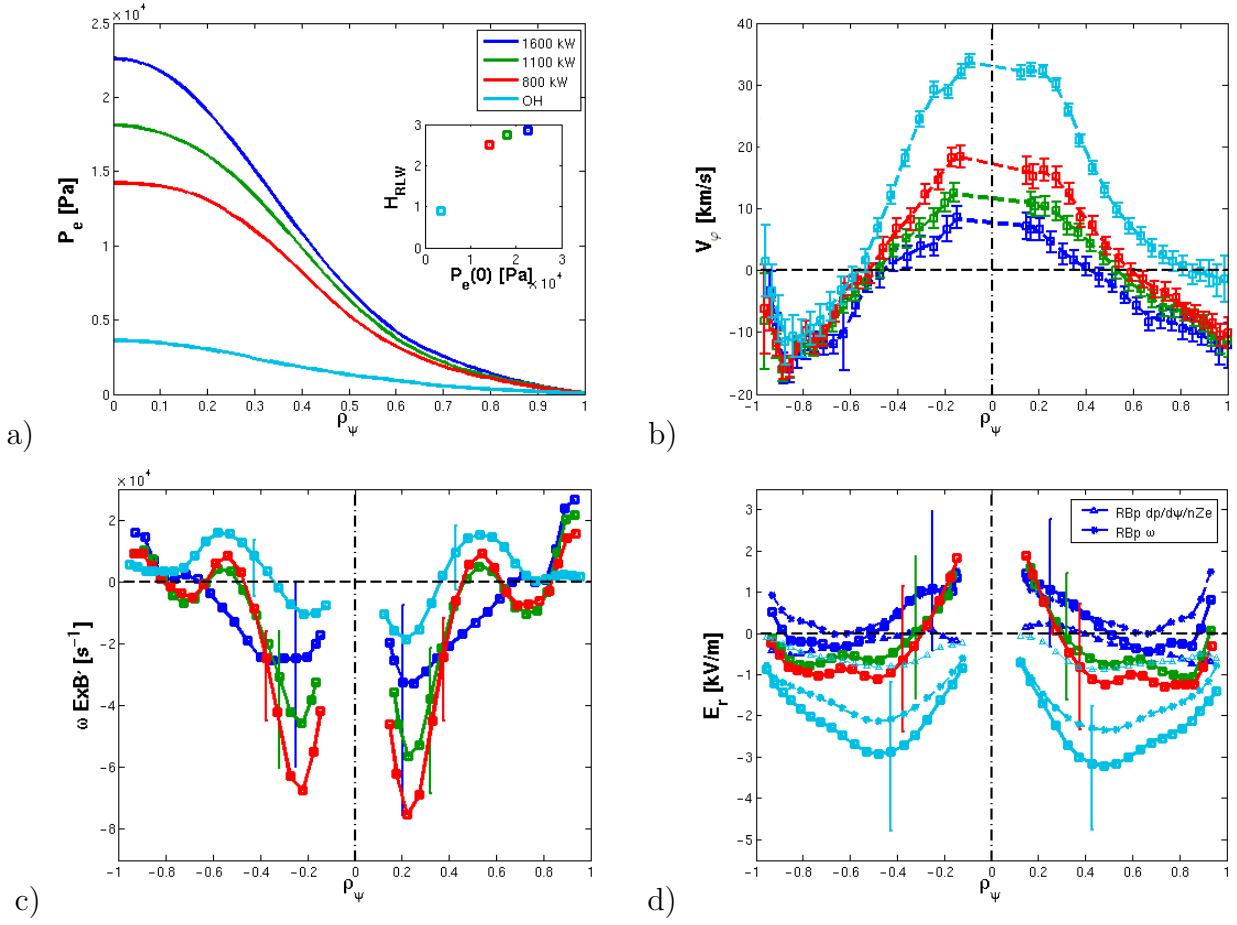
Figure 5.16: a) Electron pressure and H_{RLW} factor b) ion toroidal rotation c) $E \times B$ shearing rate and d) E_r profiles with 1600kW, 1100kW and 800kW of injected power (#45371) and a similar OH case (#45262).

region it reverses to a co-Ip direction outside $\rho_\psi = 0.5$. As is discussed in Sec.5.2.2 and Sec.D.1, this behavior is not compatible with a rigid body rotation approximation, It is explained by the presence of a finite v_{pol} in the electron diamagnetic direction ($v_{pol} \cong [-0.5, -3]km/s$ in the counter clockwise direction, see Fig.E.6). The radial electric field plotted in Fig.5.16.d (or Fig.E.7.b) is in the inward direction ($E_r < 0$) for all power values from $\rho_\psi > 0.2 - 0.3$. When reducing the ECH power, its absolute value increases in the inward direction. This is dominated by the $\hat{\omega} R \tilde{B}_{pol}$ term that increases in the plasma core and provides a strong contribution to radial electric field. Note that E_r tends to zero for $\rho_\psi = 0$, as expected (and necessary to maintain the assumptions made when interpreting the asymmetry as a poloidal velocity).

The $E \times B$ shearing rate in the plasma core varies between $|\omega'_{E \times B}| \cong 0.5 - 7 \times 10^4 s^{-1}$ for all ECH powered cases (Fig.5.16.c). As will be discussed in Sec.5.6, this value is an order smaller compared to the γ, predicted from linear gyrokinetic simulations, of TEM modes ($\gamma \propto 10^5 s^{-1}$) that are calculated to be the most unstable for TCV central barriers. These results are consistent with an assumed negligible effect of $\omega'_{E \times B}$ on

TEM stabilization and on the formation of TCV null-reverse shear barriers.

In Sec.5.7 the measured carbon temperature and density profiles of this power scan will be analyzed in more detail. The ion temperature profiles will be eventually compared with the results obtained with a quasilinear model proposed in [137, 138] for TCV eITBs.

5.4.3   Effect of MHD activity on the central barrier

During the development of the central barrier target, we often observed MHD activity that appeared responsible for a deterioration of the barrier or, sometimes, its complete suppression. In this section, a central barrier similar to shot #45371 was generated by adding progressively cnt-CD on-axis and co-CD off-axis at 0.9s for a total of 1400kW, as illustrated in Fig.E.10. After barrier formation at 1.2s, a 2/1 MHD mode at 7kHz has developed. The "fortuitous" failure of cluster B (i.e loss of about 900kW) at 1.5s strengthened the mode with the development of an additional harmonic.

In Fig.5.17, the profiles for shot #45273 are shown, averaged at the three time intervals [0.9,1.15]s (barrier formation, in blue, see also Fig.E.10), [1.2,1.5]s (with the MHD mode, in green) and [1.6,1.9]s (with the stronger mode, in red). The positions of the q=2 surface are illustrated at each time. From the T_e profiles (Fig.5.17.a), the development of MHD activity appears to destroy the barrier (from $H_{RLW} = 2.9$ to $H_{RLW} = 1.6 - 1.8$), and flatten the n_e profiles (Fig.E.11). This is also seen in Fig.5.18, where initially a barrier in T_e of 6keV with a $\Delta z = 18cm$ width is present that deteriorates after the development of the 2/1 mode and is destroyed by the stronger mode. The toroidal rotation profile, in the cnt-Ip direction with the central barrier (see Fig.5.17.b), is reversed to the co-Ip direction following the MHD activity. In the presence of the strong mode, there is a relaxation of the rotation towards the cnt-Ip direction (similar to an OH profile) followed by a rotation decrease in the plasma core. The $q = 2$ surface shifts outwards as the 2/1 mode is reinforced. More precisely, the location of the $q = 2$ surface (and that of the 2/1 mode) is situated immediately outside the region where the ∇v_φ changes sign and the toroidal rotation reversal occurs. This behavior is consistent with that observed in [96, 152], where a pronounced flattening and braking of the plasma rotation at the onset of the 2/1 tearing instability, in the neoclassical regime of TCV discharges, is observed. This global braking and rotation gradient sign reversal was taken to be associated with a neoclassical toroidal viscous torque [152]. The resulting radial electric field is directed inwards during the barrier ($E_r < 0$), but the MHD mode results in an E_r sign change in the core (see Fig.5.17.d). During the relaxation phase, the profile returns to an inward direction, again from cnt-Ip v_φ. Note that the $q = 2$ surface is situated near the minimum of the radial electric field. The $E \times B$ shearing rate is increased and strongly modified at the midradius with the MHD mode and varies between $|\omega'_{E \times B}| \cong 6 - 10 \times 10^4 s^{-1}$ (see Fig.5.17.c).

In conclusion we see clear evidence that MHD activity strongly affects the v_φ, E_r and $|\omega'_{E \times B}|$ profiles, in particular inside the mode's radial location.

Other interesting MHD activity effects, such as those related to a global plasma os-
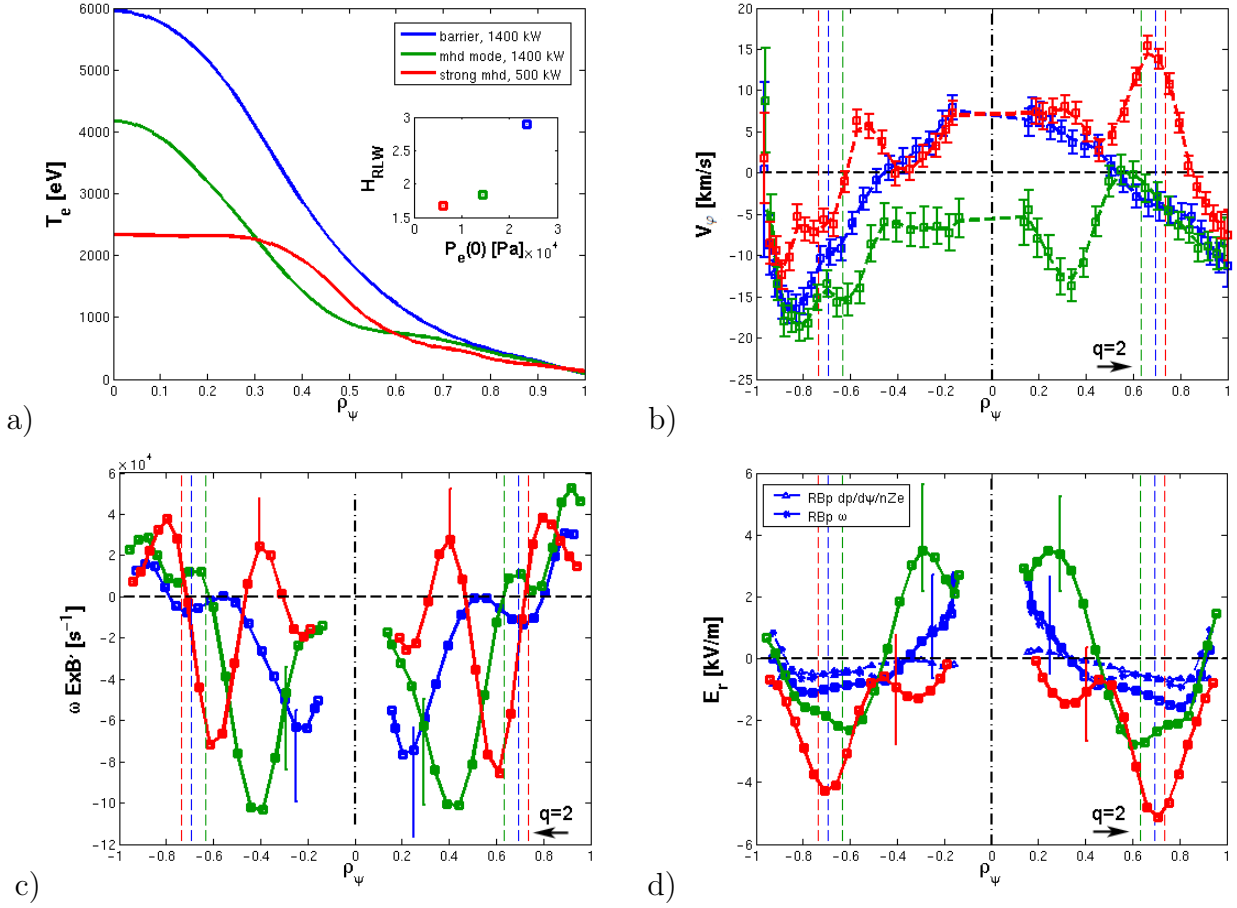
Figure 5.17: a) Electron temperature and H_{RLW} factor b) impurity ion toroidal rotation c) $E \times B$ shearing rate and d) E_r profiles for shot #45273. In dashed lines are indicated the positions of the q=2 surface at each time.
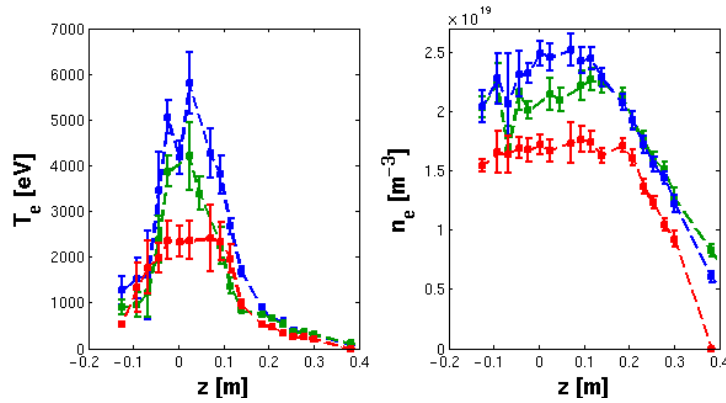

Figure 5.18: Electron temperature (left) and density (right) for discharge #45273.

cillation similar to [153, 154], also known as *oscillation regime* or *O-regime* [155], are discussed in App.D.2 for both the central and co-CD off-axis eITB. It is observed that these oscillations affect many plasma parameters such as the plasma current I_p, the loop voltage, the line averaged density $n_{e,av}$ and the plasma inductance l_i signals. The T_e and confinement factor H_{RLW} profiles are also clearly affected, indicating a cyclic deterioration of the barrier. A cyclic modification in the v_φ and E_r is also observed, but the time resolution of the CXRS and Thomson diagnostics were insufficient to illustrate clearly this change.

5.5 co-CD off-axis eITB at Z=0cm on TCV

This section focuses on the co-CD off-axis target and summarizes the results obtained in the study of the effect of a few parameters on the barrier strength and the toroidal and poloidal rotation, E_r and $E \times B$ shearing rate profiles. As observed in Sec.5.3.2, the simplest way to affect a co-CD off-axis barriers is to add an inductive perturbation from the OH coil, modifying the central q profile, and thus the barrier strength, at constant input power. The effect of inductive current perturbations dI_{OH}/dt, central injected power and MHD activity are now investigated for this scenario. To achieve these co-CD off-axis eITBs and the related scans, severely taxed the limits of the TCV device in terms of the available heating and of many diagnostics' limitations (DMPX, XTOMO and CXRS). Additional problems appeared during the analysis from inaccurate LIUQE equilibrium reconstructions that tended to exhibit convergence difficulties for plasmas with low I_p, large pressure gradients and reversed q profile (see Sec.5.7.4). Moreover, the presence of MHD activity, or non stationary targets, often partially or completely perturbed the CXRS profiles. To progress, a particularly onerous and detailed selection of the "*best*" profiles was performed as described in the following section.

5.5.1 Effect of dI_{OH}/dt scan in a co-CD off-axis eITB

In Fig.5.19 a typical co-CD off-axis eITB scenario used during this work, and similar to that presented in Sec.5.3.2, is shown. Similarly to discharge #25956, from a stationary low current Ohmic plasma, two co-CD off-axis gyrotrons, of 450kW each, are launched at 0.35s at $\rho_\psi = 0.4$ to sustain the total plasma current without creating a peaked current profile. After 150ms, two additional beams are added on-axis (one cnt-CD and one co-CD at $\rho_\psi = 0.2$) to strengthen the barrier, for a total of ∼1800kW injected power.

During the initial eITB target development experiments, strong MHD activity was observed for all discharges performed by applying ECH on-axis (such as the pulses studied in [150]), resulting in a less stationary barrier. For this reason, it was decided to choose the configuration of cnt-CD and co-CD on-axis, since a more central heating deposition can be achieved, giving stronger and more stable barriers.

Fig.5.20 shows a TCV poloidal cross section with the plasma boundary and beam positions. The plasma current decreases after 0.52s, following the OH current clamping by the real-time IOH control system (see Sec.2.4.4). Typically, a barrier forms around
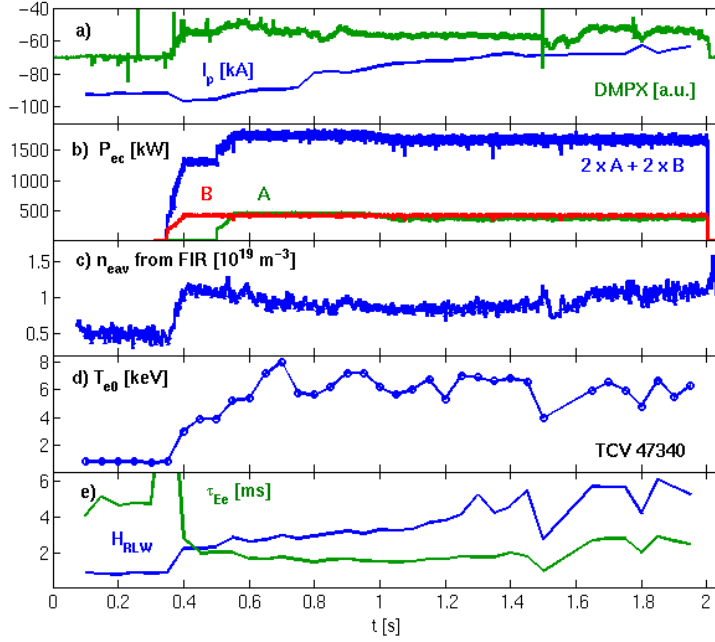
Figure 5.19: Main traces for a typical co-CD off-axis eITB scenario #47340 (strongest barrier obtained during this work). At 1.5s and 1.75s two barriers crashes are observed due to the development of infernal modes (ILMs, see [156]).

0.5s that further develops up to 0.8s at $\rho_\psi = 0.3 - 0.35$. At 1.1s, a negative IOH ramp, $dI_{OH}/dt = -250A/s$ (corresponding to $V_{loop} = -15mV$), was added in order strengthen the barrier. With this new contribution, I_p decreases further to a value of 60 kA (which is close to TCV's normal operational range). The time evolution of the various current contributions during the barrier formation and sustainment for discharge #47340 are shown in Fig.5.21. The total plasma current evolves from -90 kA at 0.6s ($I_p < 0$ means anticlockwise), given by summing $I_p = I_{CD}(-10kA) + I_{bs}(-50kA) + I_{OH}(-30kA)$, to -80 kA at 0.8s, given by $I_p = I_{CD}(-23kA) + I_{bs}(-60kA) + I_{OH}(+3kA)$, towards a final value of -65 kA at 1.9s, given by $I_p = I_{CD}(-10kA) + I_{bs}(-70kA) + I_{OH}(+15kA)$. We see an increase of the bootstrap contribution from 50%, to 75% to a final BS fraction close to 100% (full BS current drive). The OH current is decreased after 0.52s due by the IOH control system and at 1.1s it increases following the addition of the negative IOH ramp. The CD component, derived from $I_{CD}(t) = I_p(t) - I_{BS}(t) - I_{OH}(t)$, starts forming at 0.35s. From the FIR, the line averaged density for this scenario is about $n_{e,av} = 0.8 - 1.2 \times 10^{19}m^{-3}$, with electron temperatures up to 8keV. We recall that the plasma density must remain low to achieve sufficient off-axis CD.

In order to compare this developed scenario at Z=0cm (#47340), with the co-CD off-axis eITBs described in Sec.5.3.2, a similar dI_{OH}/dt scan has been performed.

Figures 5.22.a-b show four similar discharges in which, at 1.1s, a dI_{OH}/dt ramp is imposed using TCV's IOH control system (see Sec.2.4.4). The ramps were the following:
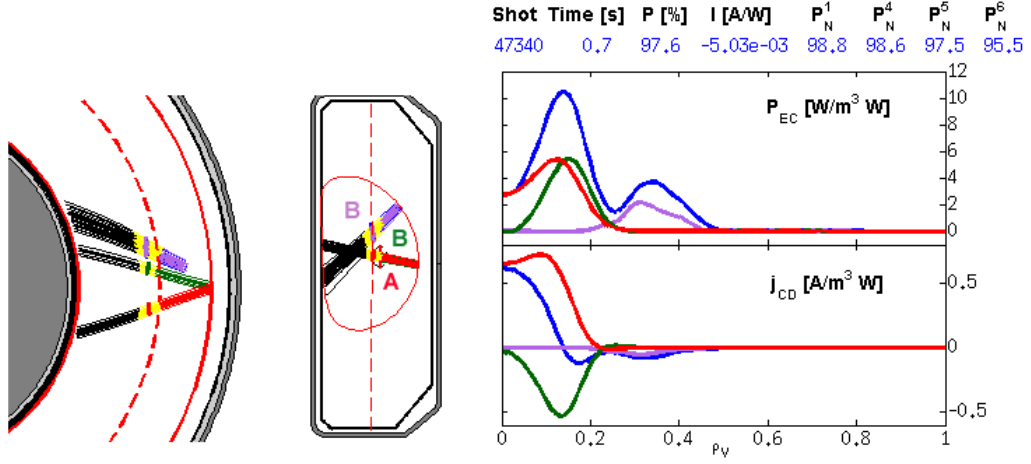
Figure 5.20: Power and ECCD current density deposition scheme reconstructed with TORAY for a co-CD off-axis eITB scenario (#47340). Two beams are injected on-axis: one cnt-CD and one co-CD (red cluster A + green cluster B) and two beams are injected in co-CD off-axis (lilac cluster B). The addition of a co-CD on-axis beam allows to partly compensate the large cnt-CD contribution and to obtain a strong stationary barrier.
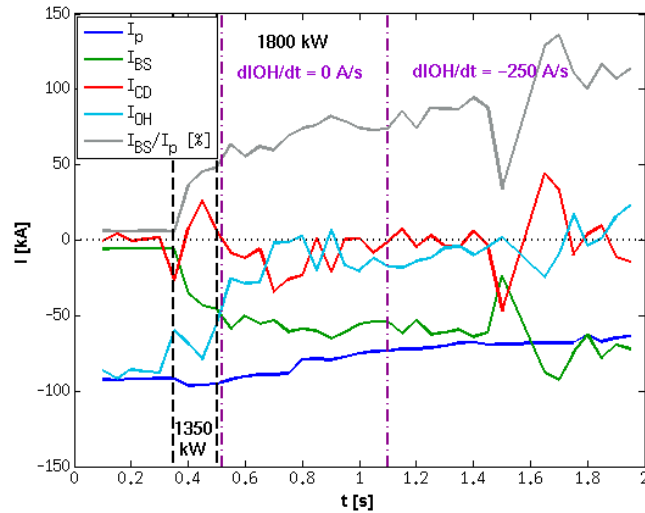
Figure 5.21: Evolution of the plasma current components for a typical central barrier scenario #47340. The CD component is simply derived from $I_{CD} = I_p - I_{bs} - I_{OH}$. The black vertical lines correspond to the various power regions, while the violet ones illustrate the values set with the IOH control system.
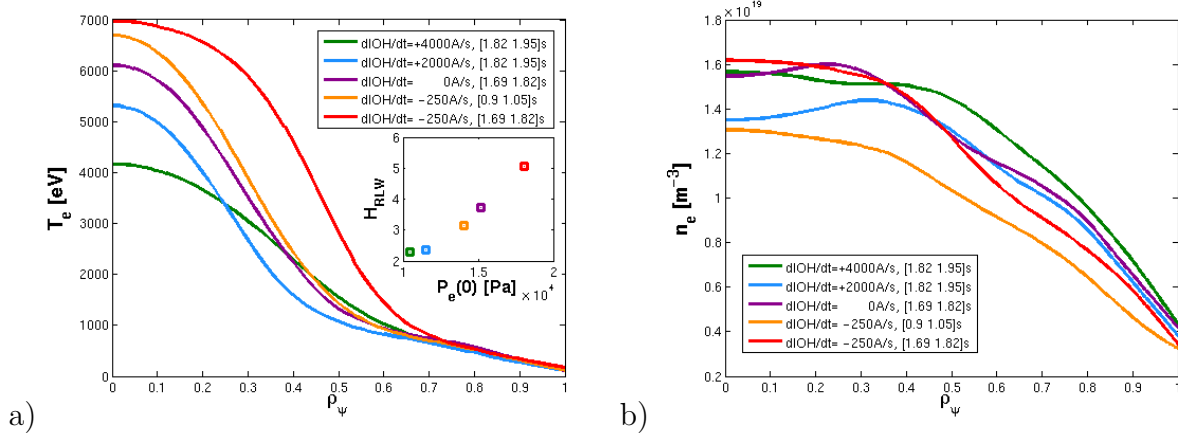
Figure 5.22: Electron a) temperature and b) density for shots #47345 ($dI_{OH}/dt = +4000A/s$), 47341 ($dI_{OH}/dt = +2000A/s$), 47351 ($dI_{OH}/dt = 0A/s$) and 47340 ($dI_{OH}/dt = -250A/s$).

$dI_{OH}/dt = +4000A/s$ (#47345, corresponding to $V_{loop} = +240mV$, see Fig.5.23.e) , $dI_{OH}/dt = +2000A/s$ (#47341), $dI_{OH}/dt = 0A/s$ (#47351) and $dI_{OH}/dt = -250A/s$ (#47340). The time evolution of $T_e(0)$, H_{RLW}, I_p, I_{OH} and V_{loop} of the four discharges are also plotted in Fig.5.23.

From Fig.5.22.a, a positive dI_{OH}/dt ramp (i.e co-OH) resulted in reduced T_e profiles and a weakened barrier (#47345 and #47341 in green and blue), consistent with [11]. Conversely, a negative dI_{OH}/dt ramp reinforces the existing barrier and simultaneously broadens and increases the T_e and p_e profiles (#47340 in orange and red). The pressure broadening corresponds to a larger plasma volume contained within the barrier, i.e. a confinement improvement, confirmed by $\tau_{Ee} = 4ms$ and H_{RLW} that increases from 3.2 to 5.4 in shot #47340. The electron temperature and density scale length profiles plotted in Fig.5.24 show a peak of $|R/L_{Te}| \cong 45$ at $\rho_\psi = 0.5$ for the strongest barrier #47340, while $|R/L_{ne}| \cong 12$. These values are indicative of a strong internal barrier for heat and particle transport and are consistent with values obtained in [30]. The barrier width is illustrated in Fig.5.25, where the electron temperature and density profiles are plotted as a function of the vertical position. A barrier in n_e and T_e of 7keV with a $\Delta z = 23cm$ width (in red) is obtained at the end of the discharge, and corresponds to the strongest barrier achieved during the entire study. The effect of the sign and magnitude of dI_{OH}/dt on the barrier strength is clearly demonstrated in Fig.5.23.a-b, where the central $T_e(0)$ and H_{RLW} increase, remain constant, or decrease, as soon as a negative, null or positive inductive perturbation is applied at 1.1s, respectively.

These discharges well reproduce those discussed in Sec.5.3.2, with even stronger temperature barriers resulting from higher power core deposition. Fig.5.22.a and Fig.5.26.a show how the confinement improvement, characterized by H_{RLW}, increases smoothly with more negative I_{OH} perturbations that lead to higher $p_e(0)$ values, in agreement with [11, 150]. From Fig.5.7, a q profile for discharge #47340 similar to #25952 (in cyan) can be deduced, corresponding to a minimum negative magnetic shear of around -3 (for $H_{RLW} = 5.4$).

The toroidal rotation v_φ is in the co-current direction for all ramp values (see Fig.5.26.b
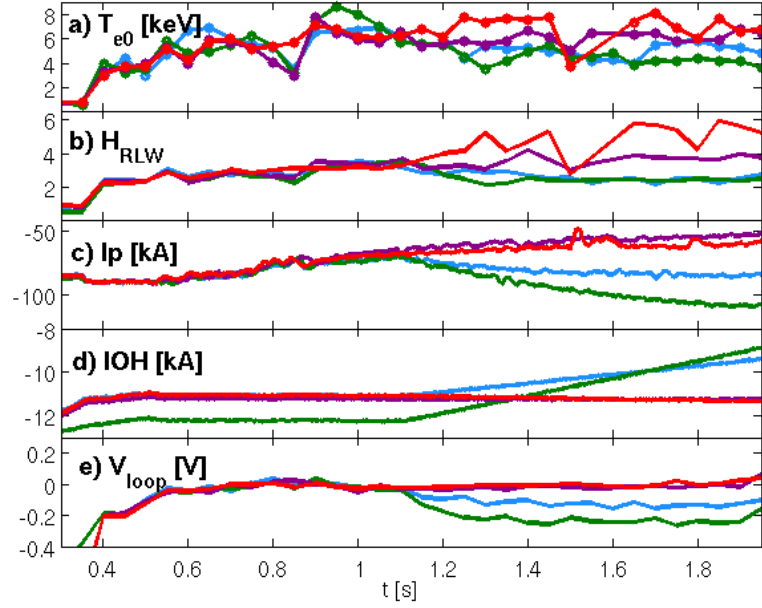
Figure 5.23: a) $T_e(0)$, b) Hrlw, c) I_p, d) I_{OH} and e) V_{loop} for discharges with $dI_{OH}/dt = +4000A/s$ (#47345, in green) , $dI_{OH}/dt = +2000A/s$ (#47341, in blue), $dI_{OH}/dt = 0A/s$ (#47351, in violet) and $dI_{OH}/dt = -250A/s$ (#47340, in red). Notice that TCV notation is $sign(V_{loop}) = -sign(dI_{OH}/dt)$.

plotted as a function of ρ_ψ or Fig.E.13 as a function of the coordinate R). v_φ taken just after the barrier formation ([0.9, 1.05s]) has a central value around -15km/s. For plotting simplicity, only the initial v_φ profile for shot #47340 is shown, similar profiles were obtained in all the discharges. For the negative and "null" ramps, the v_φ profiles do not evolve significantly, remaining similar to the initial barrier profile (in orange). For the positive ramp ($dI_{OH}/dt = +2000A/s$ and $+4000A/s$), i.e. for much weaker barriers, the rotation is shifted towards smaller co-current values and broadens in the LFS region. For these cases the v_φ profiles show a partial reversal that may again be ascribed to the MHD activity. The high rotation values (from -20 to -40km/s), measured at the LCFS with these co-CD off-axis eITBs, are unusual compared to the regular TCV rotation profiles of L-mode plasmas and even central barriers. Nonetheless, we recall that these plasma are highly "compressed", especially in the LFS region, so the LCFS shifts inwards with 6-8cm remaining to the TCV wall, where v_φ reduces to much smaller values. The poloidal rotation (see Fig.E.12) varies between -0.5 and -4km/s in the counter clockwise direction outside $\rho_\psi > 0.4$ for the four discharges. The resulting radial electric field changes between inward and outward values in the core, depending on the n_i and v_φ profiles (the change mainly corresponds to the partial rotation reversal ascribed to MHD), approaches zero at the mid-radius ($\rho_\psi = 0.6$), and is directed outward for $\rho_\psi > 0.7$ (see Fig.5.26.d). The $E \times B$ shearing rate varies in the central region between $|\omega'_{E \times B}| \cong 0.5 - 7 \times 10^4 s^{-1}$ (see Fig.5.26.c).
The discharges with MHD activity oscillate more strongly (green and cyan), while
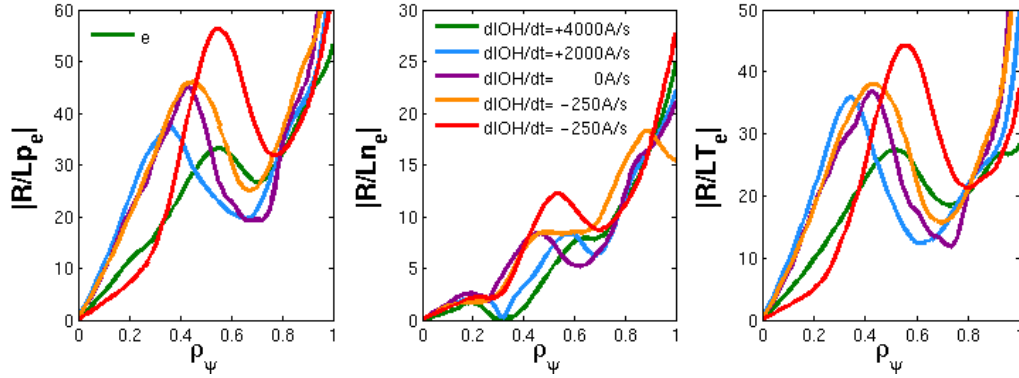
Figure 5.24: $|R/L_{pe}|$, $|R/L_{ne}|$ and $|R/L_{Te}|$ profiles for electrons (solid lines) of discharges #47345, 47341, 47351 and 47340.
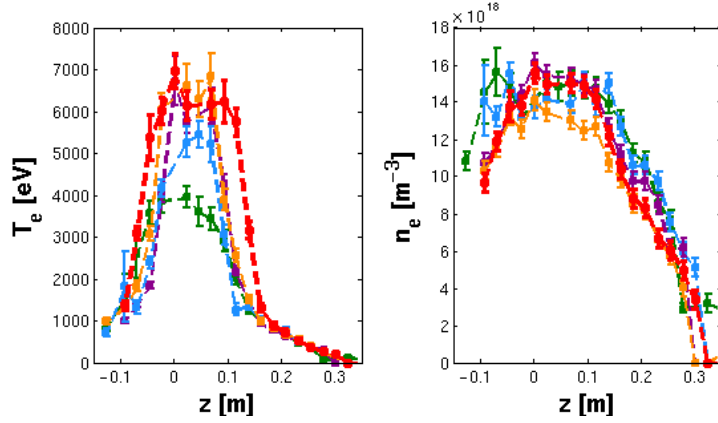
Figure 5.25: Electron temperature (left) and density (right) for discharges #47345 ($dI_{OH}/dt = +4000A/s$), 47341 ($dI_{OH}/dt = +2000A/s$), 47351 ($dI_{OH}/dt = 0A/s$) and 47340 ($dI_{OH}/dt = -250A/s$) as a function of the vertical position Z.

those with stable barriers (violet, orange, red), vary more slowly along the midplane. However we see that $|\omega'_{E \times B}|$ values are similar irrespective of the degree of confinement improvement. Similar to the central barrier target, these values remain one order of magnitude smaller compared to the γ of TEM modes ($\gamma \propto 10^5 s^{-1}$), predicted by linear gyrokinetic simulations that are the dominant modes in TCV co-CD off-axis eITBs (see Sec.5.6 for more details). These results are, again, consistent with a negligible effect of $\omega'_{E \times B}$ on TEM stabilization and on the formation of TCV reverse shear barriers.

As mentioned previously, discharges performed with the same amount of central ECH power, compared to central co-CD and cnt-CD, generate barriers with comparable strength. The change of the central heating modifies T_{eo} as expected, but these eITBs have a similar $|\omega'_{E \times B}|$. By applying ECH near $\rho_\psi \cong 0.25$, stronger MHD activity is observed that generates a less stationary barrier. Therefore the cnt- and co-CD heating solutions are easier to examine. Further details on the effect of different total and central power in a co-CD off-axis eITB are given in App.D.3.

As observed in Fig.5.23 for shot #47340 (in red), when a large negative IOH ramp
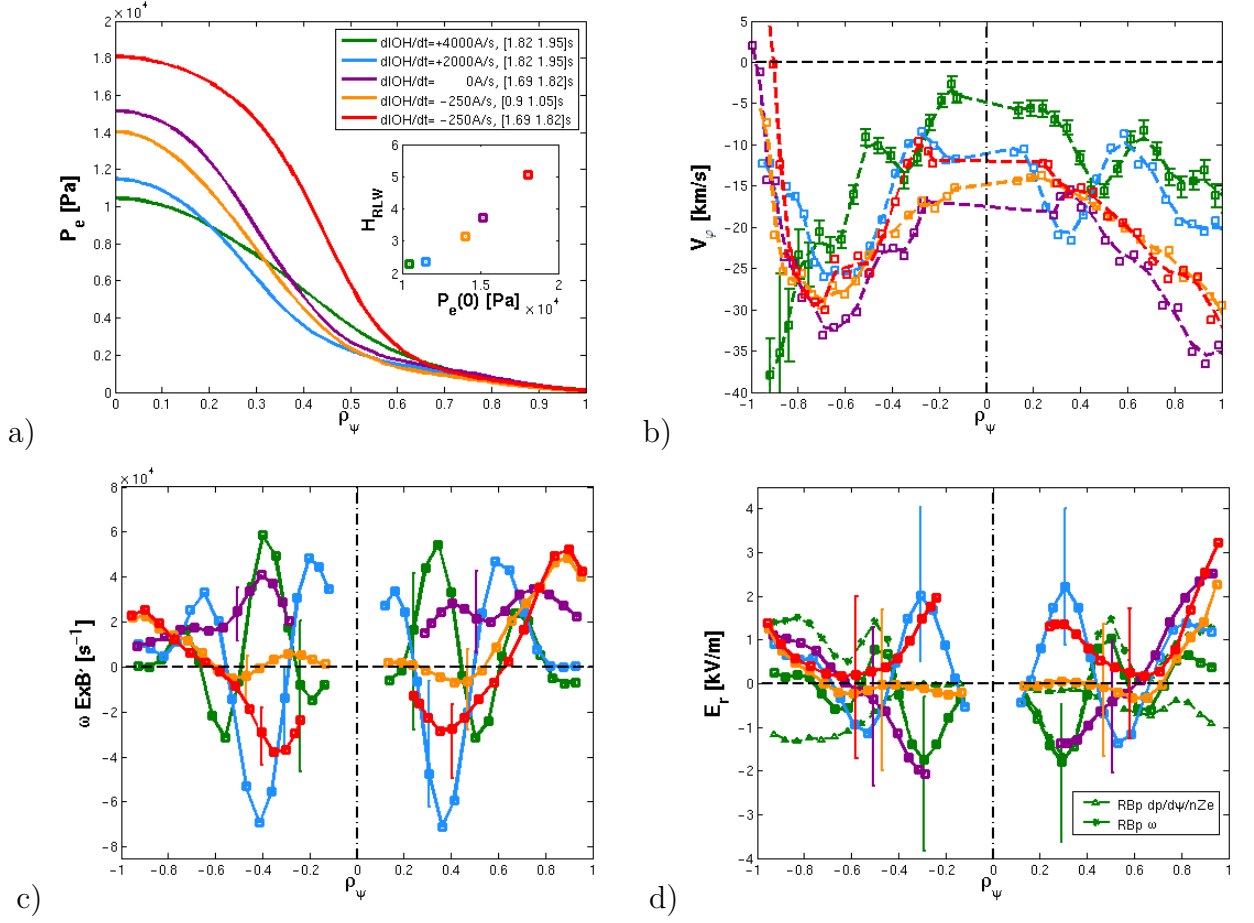
Figure 5.26: a) Electron pressure and H_{RLW} factor b) ion toroidal rotation c) $E \times B$ shearing rate and d) E_r profiles for shots with $dI_{OH}/dt = +4000A/s$ (#47345) , $dI_{OH}/dt = +2000A/s$ (#47341), $dI_{OH}/dt = 0A/s$ (#47351) and $dI_{OH}/dt = -250A/s$ (#47340). For these discharges 900kW of cnt + co-CD on-axis and 900kW of co-CD off-axis are applied, giving a total of 1800kW injected power.

(cnt-OH) is applied, the barrier becomes too strong and approaches the ideal infernal mode stability limit. An infernal mode crash sometimes results that can partly, or completely, destroy the barrier [156]. Note that the first partial disruption at 1.5s reduces the confinement and stabilizes the mode until 1.75s (see Fig.5.19.a), when the barrier has completely recovered after which the mode is again destabilized by another minor crash. This example demonstrates how a discharge, even with a very strong barrier, is able to recover after an internal crash. In a similar shot, with a larger negative IOH ramp ($dI_{OH}/dt = -500A/s$) where the ideal mode was already destabilized at 1.4s, the barrier was completely destroyed and a major plasma disruption followed. During the development of a strong co-CD off-axis eITB target, an interesting global plasma oscillation, similar to that discussed in App.D.2.1, appeared during some discharges that lasted until a disruption. These effects of MHD activity are further discussed in in App.D.2.2.

In Sec.5.7 the measured carbon temperature and density profiles will be analyzed in more detail. Together with the related electron profiles, the ion temperature profiles will be compared with the results obtained with a quasilinear model proposed in [137, 138] for TCV eITBs.

5.5.2 Summary of experimental $E \times B$ shearing rates for both internal barrier scenarios

To summarize Sec.5.4 and Sec.5.5, the experimental $E \times B$ shearing rates measured at the maximum $|R/L_{Te}|$ of the LFS region for the central barriers, the strong co-CD off-axis eITBs, and corresponding OH shots were plotted as a function of the confinement factor H_{RLW} in Fig.5.27. We recall that $H_{RLW} > 2 - 2.5$ and $|R/L_{Te}| > 10$ are the best indicators of eITBs (see Sec.5.3). It can be observed that the $E \times B$ shearing

Figure 5.27: Experimental $E \times B$ shearing rates of the LFS region measured at the maximum $|R/L_{Te}|$ position (taken between $0.2 < \rho_\psi < 0.7$) for the central barriers (in green), the strong co-CD off-axis eITBs (in red) and the corresponding OH (in cyan) scenarios as a function of the confinement factor H_{RLW}. The shot number of some important discharges discussed in these sections are highlighted beside the corresponding $E \times B$ shearing rate.

rate ranges between $|\omega'_{E \times B}| \cong 0.3 - 7 \times 10^4 s^{-1}$ and that no evident increase of $\omega'_{E \times B}$ as a function of H_{RLW} is obtained. The $E \times B$ shearing rates vary little between the OH shots and strongest barriers. Some central barrier cases present stronger negative shear flow values due to a stronger core asymmetry of the toroidal rotation and of E_r (#45273, #47882), or to larger MHD oscillations (#47341). An analogous behavior is also obtained for the $E \times B$ shearing rates measured at the HFS region. In order to compare two "global" quantities, the maximum $\omega'_{E \times B}$ values measured in the range $0.2 < \rho_\psi < 0.7$ were also determined, and show a similar behavior as a function of H_{RLW} to Fig.5.27.

For the same discharges discussed in Fig.5.27, the $E \times B$ shearing rates were plotted as
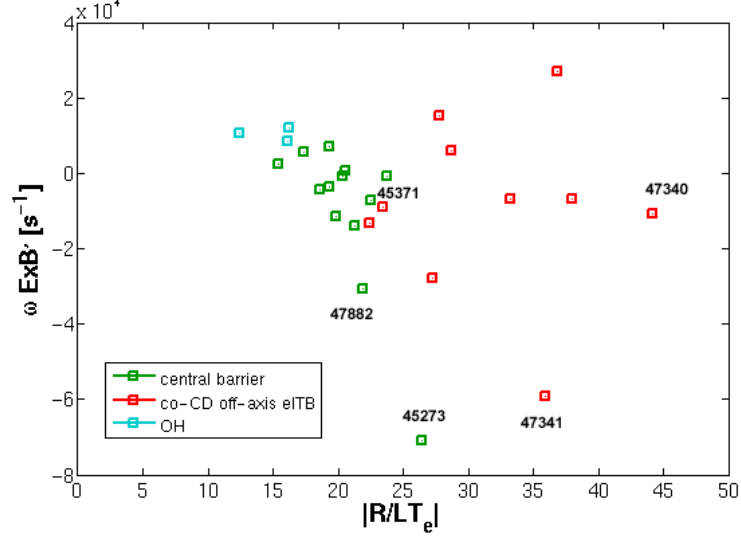
Figure 5.28: Experimental $E \times B$ shearing rates of the LFS region measured at the maximum $|R/L_{Te}|$ position for the central barriers (in green), the strong co-CD off-axis eITBs (in red) and the corresponding OH (in cyan) scenarios as a function of the maximum $|R/L_{Te}|$ (taken between $0.2 < \rho_\psi < 0.7$). The shot number of some important discharges discussed in these sections are highlighted beside the corresponding $E \times B$ shearing rate.
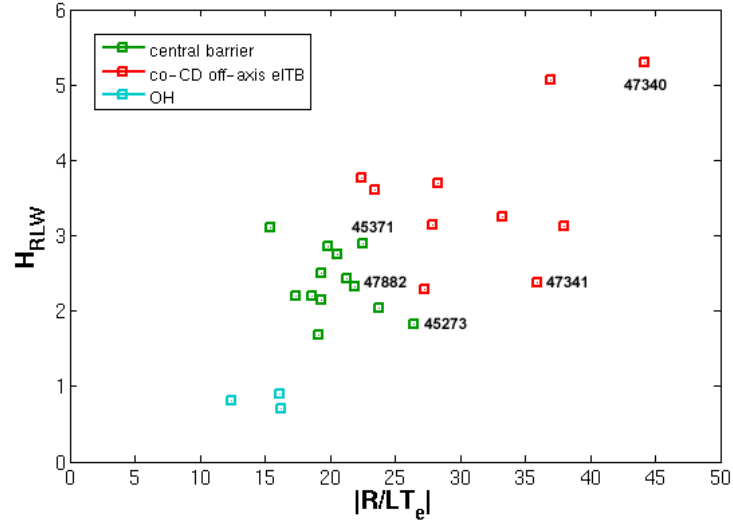

Figure 5.29: Confinement factor H_{RLW} as a function of the maximum $|R/L_{Te}|$ for the central barriers (in green), the strong co-CD off-axis eITBs (in red) and the corresponding OH (in cyan) scenarios.

a function of the maximum $|R/L_{Te}|$ in Fig.5.28. As observed for the H_{RLW} parameter, the $E \times B$ shearing rate does not vary significantly with higher $|R/L_{Te}|$ values (and therefore with stronger barriers).

To confirm the dominant correlation between H_{RLW} and $|R/L_{Te}|$, Fig.5.29 shows H_{RLW} against the maximum $|R/L_{Te}|$ for the same cases as in Fig.5.27 and Fig.5.28. A clear correlation is seen, in confirmation of the discussion in Sec.5.3.

For completeness, the LFS radial electric field E_r and $v_{E \times B}$ taken at the maximum $|R/L_{Te}|$ are also plotted as a function of the maximum $|R/L_{Te}|$ in Fig.E.15 and Fig.E.16.

These plots prove strong experimental confirmation of the TCV understanding that the $E \times B$ shearing rate plays a negligible role in the formation of internal barriers on TCV that should be contrasted with Fig.5.7.b (Fig.16 of [130]) showing a correlation of H_{RLW} with negative shear.

5.6 Experimental $E \times B$ shearing rates compared with gyrokinetic simulations

In the two previous sections, Sec.5.4 and Sec.5.5, the experimental $E \times B$ shearing rates have been calculated for both scenarios and summarized in Sec.5.5.2. To interpret the effective role of the $E \times B$ shear flows ($|\omega'_{E \times B}|$) on the barrier formation on TCV, we used the linear theory approach and the standard assumption: $|\omega'_{E \times B}| \geq \gamma$ for shearing rate stabilization, where γ is the growth rate of the most unstable mode. For comparison with the shearing rate, we now determine the most unstable modes for these plasmas with eITBs and calculate their growth rates.

We recall that anomalous transport, driven by temperature gradient modes in tokamaks, is characterized by three types of microinstabilities: long to medium wavelength ($k_\theta \rho_i \approx 0.1-1$, with the poloidal wave number k_θ and ion gyro radius ρ_i), ion temperature gradient (ITG) mode and trapped electron mode (TEM) and the short wavelength ($k_\theta \rho_i \geq 1$) electron temperature gradient (ETG) modes. These modes are responsible for the thermal ion and thermal electron heat conduction and particle transport, at least inside $\rho \cong 0.7$. Many plasma parameters can influence the stability of these modes. Amongst the most important we find the $E \times B$ shearing rate, q, magnetic shear, Shafranov shift and T_e/T_i.[3]

Although ineffective on the small spatial scales of ETG modes, the $E \times B$ shearing rate, has, in many tokamaks, been found to be the main stabilizing process of plasma turbulence driven by ITG mode and therefore is considered the mostly responsible for ITB formation [124, 125, 126, 127]. Using the linear theory approach, for sufficiently large sheared flows, the turbulent ITG and TEM modes can be completely stabilized. Non linear simulations appear to indicate a smaller effect on TEM [157, 158]. Never-

---

[3]The stabilization of electrostatic instabilities constitutes an interesting issue not only for ITBs, but also in the edge and scrape off layer regions. In Appendix A, a critical neutral gas pressure is shown to play an important role in the stabilization of the interchange instability in simple magnetized tori (SMT).

theless, turbulence is often taken to be suppressed if the shearing rate $\omega'_{E \times B}$ exceeds the maximum linear growth rate γ^{lin}_{max} of the dominant or most unstable mode (ITG or TEM) [159, 160]. In non-linear simulations, a qualitative similar result is obtained, at least for ITGs.

5.6.1 Gyrokinetic simulations and observations about the role of q profile and $E \times B$ shearing rate on TCV

Previous linear simulations of TCV non-inductive eITBs using the global gyrokinetic code LORB5 [161] and the GLF23 [162] transport model, demonstrated stabilization of TEM modes (the most unstable electrostatic instabilities in these discharges) in the presence of negative magnetic shear and Shafranov shift [131]. With a hollow current density profile, i.e. a non monotonic q profile, TEM modes located near q_{min} present a smaller growth rate and a reduced radial extent. As a consequence, larger $k_\perp$ are observed leading to considerably smaller mixing length estimate $\gamma/k_\perp^2$ of the thermal diffusion coefficient. This suggests that a reversed shear configuration could provide the mode stabilization inside $\rho(q_{min})$ sufficient to explain the presence of eITBs on TCV [131].

These assumptions were further investigated using the quasi-linear CQL3D Fokker-Planck code [147] and the ASTRA transport code [105]. The simulated profiles confirmed that the presence of an eITB is related to the existence of a null or negative magnetic shear region in the plasma, regardless of the heating and current drive scheme used [130] (see also Sec.5.3.2). No evidence was found for the presence of preferred low-order rational q_{min} favoring the eITB triggering. The confinement improvement occurs rather as a smooth (but rapid) transition as the magnetic shear becomes increasingly reversed [129, 130].

Further gyrokinetic simulations with the global version of the GENE code [158] were performed using a TCV eITB discharge previously studied in [130]. The dominant electron heat flux in these eITBs is recovered and most transport contributions were attributed to TEM modes, as already found in previous linear global simulations [131] and non-linear local simulations [132]. Moreover, it was suggested that high-k transport contributions driven by ETG modes may not be negligible for these discharges [133].

In these TCV reverse shear eITBs, preliminary measurements did not indicate the presence of a strong $E \times B$ shear flows, which suggested a negligible effect of the background $E \times B$ shearing rate on eITB formation (opposite to that reported on other devices [125, 126]). No systematic measurements of the impurity profiles and of the $E \times B$ shearing rates were available to confront these results, until the work performed during this thesis.

5.6.2 Comparison between experimental $E \times B$ shearing rate and simulated γ of TEM modes

Using the local (flux-tube) version of the gyrokinetic GENE code [163], linear simulations were performed for the TCV eITBs discharges presented in Sec.5.4 and Sec.5.5, to determine the γ_{max} of the dominant instability and compare with the measured $E \times B$ shearing rate. The simulations considered two species (deuterium and electrons) and used the electron profiles from the Thomson diagnostic (Fig.5.30.a) and the carbon ion profiles from the CXRS diagnostic (Fig.5.30.b, discussed in Secs.5.4.2 and 5.5.1). Note that the deuterium and carbon ions are taken to have identical tem-
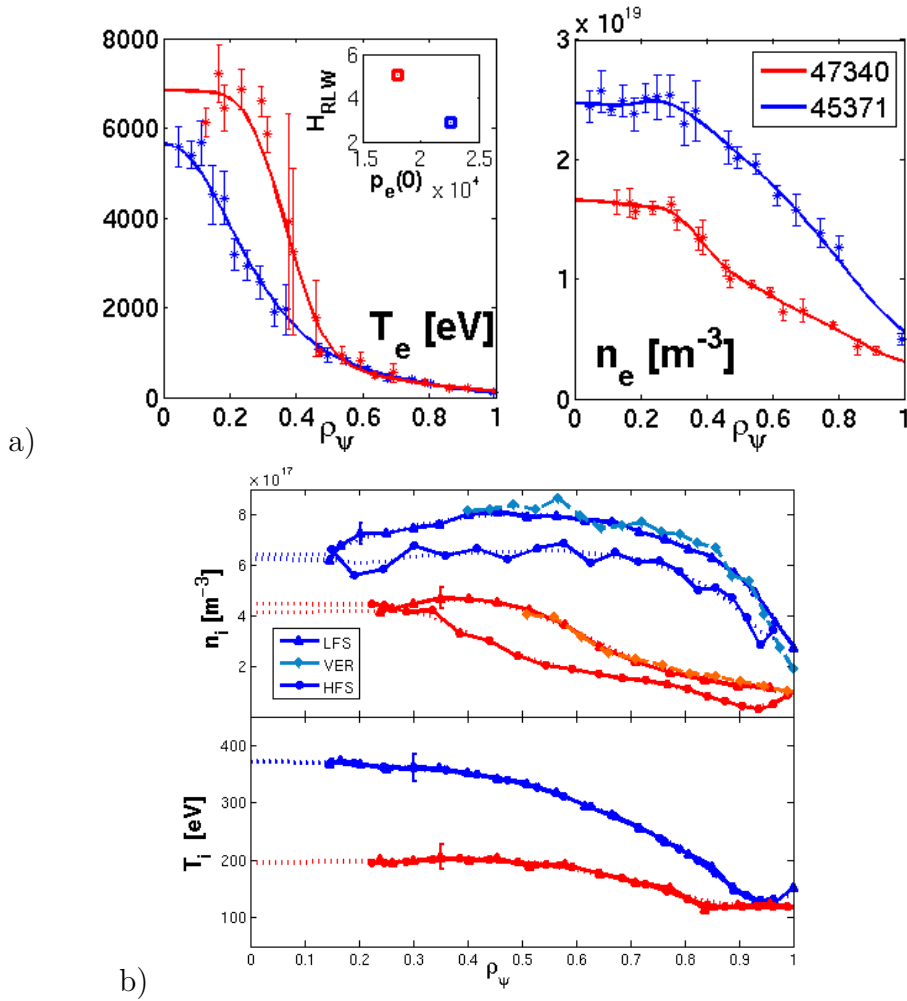

Figure 5.30: a) Electron temperature, H_{RLW} (left) and density (right) for discharges #47340 (strongest co-CD off-axis eITB) and #45371 (strongest central barrier). The points correspond to the raw Thomson measurements evaluated on ρ_ψ and the lines to the fitted profiles (usually plotted in the main chapter figures). b) Carbon ion density and temperature profiles for the same discharges.

perature $T_D = T_C = T_i$ and same ratio $R/L_{T_D} = R/L_{T_C} = R/L_{T_i}$. Additionally, we suppose $n_e = n_i$ [164]. Collisions were not taken into account for these linear simula-

tions (assumed negligible in eITBs). The growth rate (γ) and the real frequency (ω) are plotted as a function of $k_y\rho_i$ for different ρ_ψ positions, where $\rho_i = v_{th,i}/\Omega_i$ is the deuterium Larmor radius and y is the bi-normal coordinate in the GENE convention giving the corresponding wavenumber k_y [163][4]. For these simulations an almost flat, monotonic, q profile was used in order to see if the $E \times B$ shearing rate without q reversal could explain the confinement improvement. Fig.5.31 and Fig.5.32 show the growth
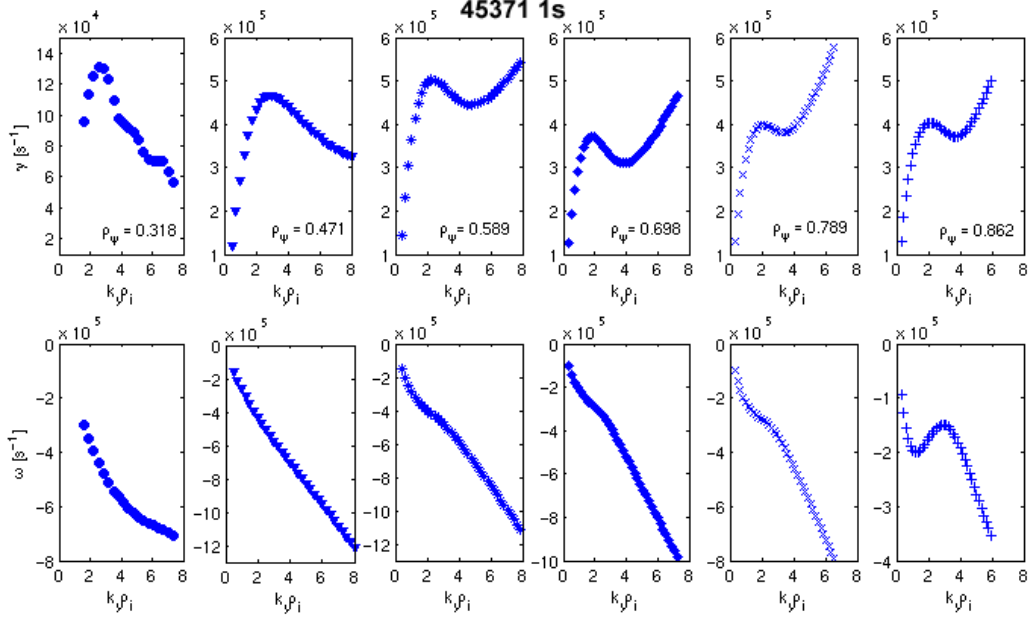

Figure 5.31: Growth rate (γ) and real frequency (ω) in function of $k_y\rho_i$ for various ρ_ψ predicted by a GENE simulation based on shot #45371.

rate (γ) and real frequency (ω) of the most unstable mode for discharges #45371 and #47340, corresponding to the strongest central barrier and co-CD off-axis barrier (see Fig.5.30.a). From the simulations we note that the real part of the frequency is always negative for both discharges ($|\omega| = 2 - 10 \times 10^5 s^{-1}$), so the modes propagate in the electron diamagnetic direction (GENE convention). This result confirms that the TEM mode is dominant. The growth rate of the most unstable TEM mode obtained for the central barrier case (Fig.5.31) varies between $\gamma = 1.5 - 5 \times 10^5 s^{-1}$. This is smaller in the core region ($\rho_\psi = 0.32$), maximum near the maximum ∇T_e position ($\rho_\psi = 0.4 - 0.55$) and slightly reduced outside the barrier. For the co-CD off-axis eITB case (Fig.5.32), the growth rate of the most unstable TEM mode is larger and ranging between $\gamma = 2.5 - 8 \times 10^5 s^{-1}$. Again it is smaller in the core ($\rho_\psi = 0.32$), maximum near the maximum ∇T_e position ($\rho_\psi = 0.4 - 0.55$) and then remains similar for larger ρ_ψ. In Sec.5.4.2 and Sec.5.5.1, the $E \times B$ shearing rate for both barriers were already calculated and discussed. A maximum $E \times B$ shearing rate between $|\omega'_{E \times B}| \cong 3 - 4 \times 10^4 s^{-1}$ was measured for the central barrier (see Fig.5.16.c) and for

---

[4]Note that for a circular plasma we can define $k_y = nq_s/r$, where n is the toroidal wavenumber and r the minor radius at the flux tube position.
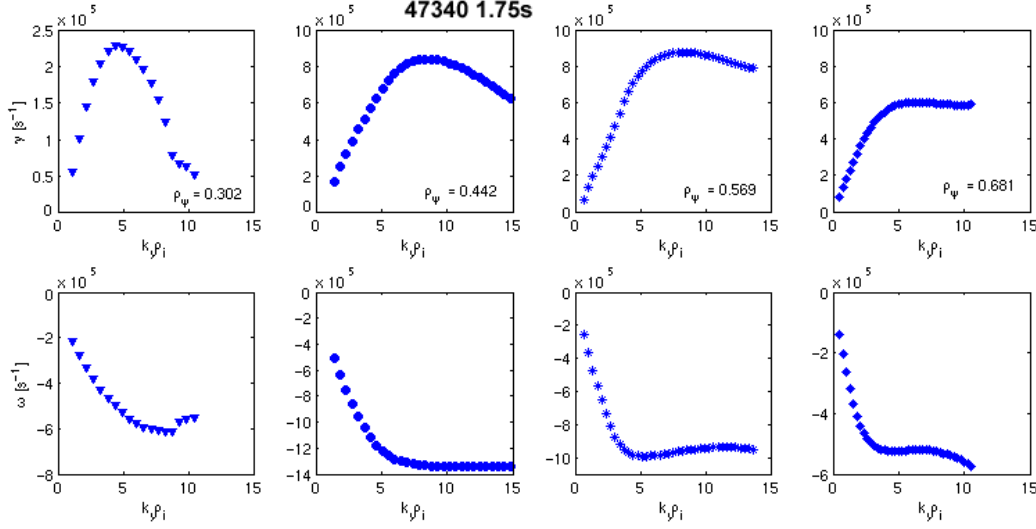
Figure 5.32: Growth rate (γ) and real frequency (ω) in function of $k_y\rho_i$ for various ρ_ψ predicted by a GENE simulation based on shot #47340.

the co-CD off-axis eITB an $|\omega'_{E\times B}| \cong 4 - 5 \times 10^4 s^{-1}$ was obtained (see Fig.5.26.c). Comparison of the measured $E \times B$ shearing rates with the predicted growth rates γ, immediately shows at least one order larger value of ($\gamma \propto 10^5 s^{-1}$) with respect to the measured $E \times B$ shearing rates $|\omega'_{E\times B}| \propto 10^4 s^{-1}$. Preliminary linear simulations based on the same discharges and considering three species (electrons, deuterium and carbon) were also performed. $T_D = T_C$ and $R/L_{T_D} = R/L_{T_C}$ were supposed and quasi-neutrality $n_D = n_e - 6n_C$ with $Z_{eff} \cong 2.4$. The results did not show any clear difference compared with the two species simulations for TEM modes, but the ETG became stabilized with the addition of the third species [164], as observed in [132].

For completeness, the effective collisionality $\nu_{eff} = \nu_{ei}/\omega_{De}$ that compares the electron ion collision frequency ν_{ei} with the curvature drift frequency ω_{De}, was estimated using the approximation $\nu_{eff} = 0.1Rn_eZ_{eff}/T_e^2$ [165]. We obtained $\nu_{eff} \cong 0.015 - 0.025$ for both discharges in the core and $\nu_{eff} > 0.1$ for $\rho_\psi > 0.4 - 0.5$ (i.e. outside the barrier). This suggests that the stabilizing effect of collisions on TEM modes is not particularly relevant in these eITBs.

These results confirm the previous preliminary $E \times B$ shear flows measurements and the assumption that the $E \times B$ shearing rate has an unperceivable effect on the formation of TCV eITBs, like the discharges presented in this chapter. This work supports the main role of the q profile shape for the electron heating and shows that even a slightly reversed q profile seems sufficient to form an eITB on TCV and to stabilize the dominant TEM mode. Global simulations on the same discharges are likely to give even smaller growth rates and the reversed shear can reduce the growth rates by one order of magnitude. Therefore $|\omega'_{E\times B}|$ could play a subsidiary role, but this is out of the scope of this work.

5.7 Experimental impurity ion profiles in eITBs

In parallel to the $E \times B$ shearing rate study, based on the toroidal and poloidal rotation CXRS measurements, the impurity ions temperature and density profiles were determined. This was also motivated by previous results obtained with a quasi-linear model applied to TCV eITBs [137, 138, 166]. In the latter work, it was shown that the large R/L_{ne} values observed in eITBs were related to large R/L_{Te} values, and could be better explained with significant R/L_{Ti} values. Therefore, we want to analyze the T_i profiles in eITBs. Below are summarized the impurity profiles measured for the discharges presented in Sec.5.4.2 and Sec.5.5.1.

5.7.1 Impurity temperature and density profiles in a central barrier (total power scan)

In Fig.5.33 the impurity ion density and temperature profiles for the discharge discussed in Sec.5.4.2 (total power scan), obtained at the HFS (circle) and LFS (triangle) are plotted. For a central barrier scenario, the carbon density profiles remain rela-
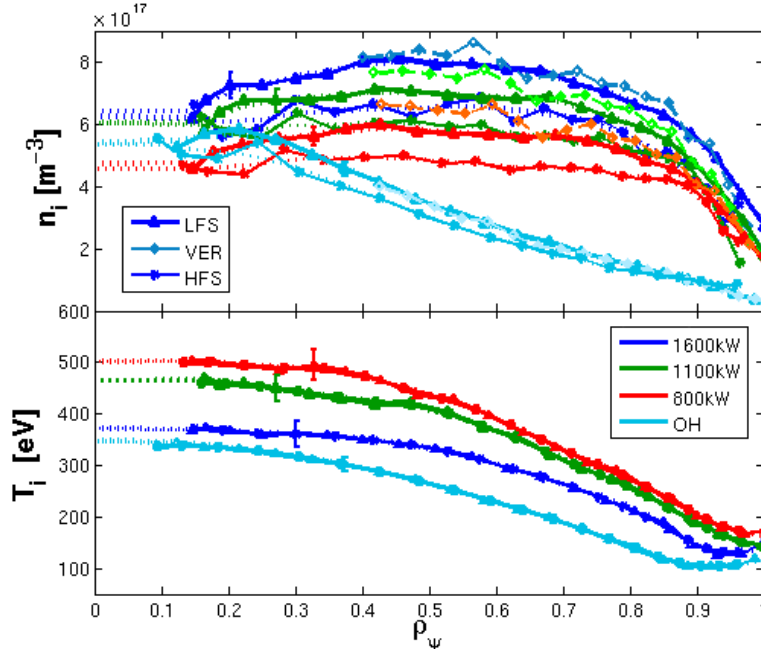

Figure 5.33: Carbon ion density (top) and temperature (bottom) for shot #45371 and a similar OH case #45262 (same color convention as Fig.5.16). In the top plot, the THFS, TLFS and VER (PLFS) profiles are plotted all together. The good superposition between LFS and VER measurements shows the high precision of the various CXRS systems data. A set of error bars has been added for each profile.

tively symmetric. This can be verified together with the magnetic reconstruction (see Fig.E.4 for shot #45371), where the plasma is close to a symmetric shape. The ion temperature profile used for the E_r calculation during the entire chapter is a fitted average profile of both the HFS and LFS profiles. The original CXRS profiles obtained

from both systems are plotted in Fig.E.9 of Appendix E. We see that the temperature profiles well superpose within the error bars, an essential requirement, since the E_r determination from the indirect measurement of poloidal rotation (see Sec.5.2.2) is valid only if the ion temperature is a flux function. For this reason we have preferred to work with an average ion temperature profile that introduce small uncertainties. Calculations with the raw profiles result in minor modifications of the results (see instead Sec.5.7.4 for the strong eITBs). For the carbon density profiles, a small asymmetry between the HFS and LFS is, nevertheless, detected. The LFS density is 10-20% higher than the HFS density, corresponding to an impurity accumulation in the LFS region with a θ dependence on n_i. This accumulation is confirmed by the VER profiles (diamond) that well superpose the LFS data. Although only small differences are observed in the central barrier target, all E_r calculations for this scenario and the co-CD off-axis eITB were performed including an account of the measured density asymmetry (Eq.5.12). In Sec.5.7.3 we will see that, in stronger eITBs, this difference can become much larger around the mid-radius. From Figs.5.14 and 5.33 we see that a total power increase causes an enhancement in the electron temperature and density together with the carbon density profiles, whereas the entire ion temperature profile is reduced. As commented in Sec.5.4.2, this effect could be explained by an enhanced ion heat transport following the addition of ECH, leading to a drop of the T_i profiles [151]. The Ohmic case has a peaked impurity ion density profile and the lowest temperature values (typical of a low current Ohmic L-mode discharge).

The ion temperature profile does not display an ion barrier, but a profile similar to the usual L-mode T_i profiles, with the maximum gradient ∇T_i located at around $\rho_\psi = 0.8 - 0.85$. The $T_e(0)/T_i(0)$ ratio in the core attains 15 and ~ 10 at $\rho_\psi = 0.4$, due to the elevated electron temperature and a lower T_i value obtained with this improved confinement (see Figs.5.30.a-b). The carbon ion density profile is mainly flat and ∇n_i slowly increases outside $\rho_\psi = 0.7$. These observations suggest that the ion channel is only slightly modified during the electron central barrier formation. This could result from ion-electron collisions (the principal ion heating mechanism on TCV) being insufficient to heat the ions for an ion temperature transport barrier to manifest itself, or, of course, that there is, in fact, no associated ion confinement improvement.

The $|R/L_{ni}|$, $|R/L_{Ti}|$ and $|R/L_{pi}|$ profiles for ions were calculated for these discharges and are plotted in Fig.E.8 for comparison with the electron profiles. For the barrier in shot #45371, $|R/L_{Ti}| \cong 10$ at $\rho_\psi = 0.85$. The $|R/L_{ni}|$ profiles for the three powers are considerably smaller, with a local maximum value of $|R/L_{ni}| = 1 - 2$ at $\rho_\psi = 0.65$ for shot #45371. The Ohmic case (in cyan) attains a larger value of $|R/L_{ni}| \cong 10$. Comparison of the electron and ion profiles in Figs.E.8, 5.14 and 5.33, places the maximum gradients in T_e and n_e (and the related electron scalelength) at the mid radius, well inside those of the ions, suggesting a different behavior of the electron and ion channels during the central barrier formation.

5.7.2 Impurity temperature and density profiles in a co-CD off-axis eITB (dI_{OH}/dt scan)

In Fig.5.34, the impurity ion temperature and density profiles for the four discharges studied in Sec.5.5.1 are plotted. The highest n_i and T_i are obtained for the weakest barrier #47345 (in green), whereas the lowest profiles are obtained for the strongest barrier #47340 (in red). Note that, for these co-CD off-axis eITBs, a very clear HFS and LFS carbon impurity asymmetry is observed.
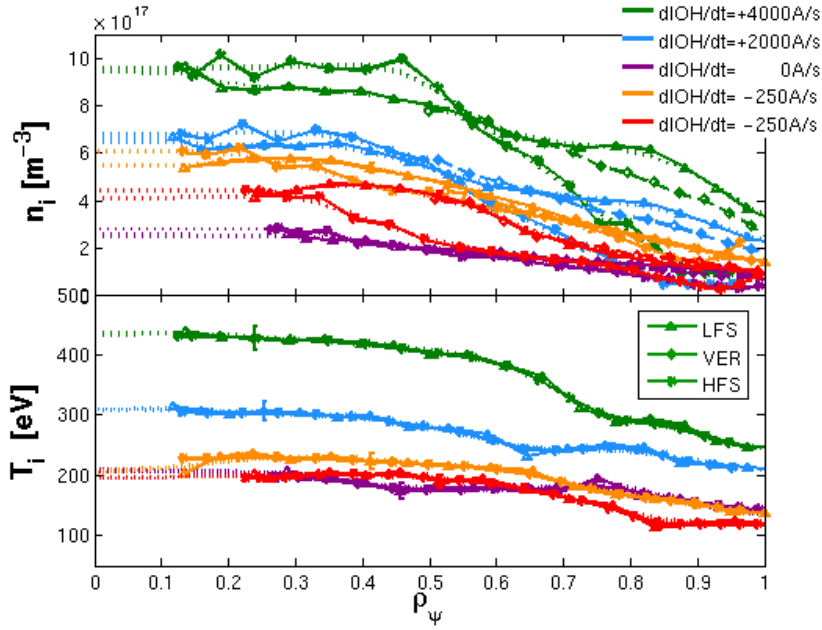

Figure 5.34: Carbon ion density (top) and temperature (bottom) for shots #47345 ($dI_{OH}/dt = +4000A/s$, in green), 47341 ($dI_{OH}/dt = +2000A/s$, in azure), 47351 ($dI_{OH}/dt = 0A/s$, in violet) and 47340 ($dI_{OH}/dt = -250A/s$, in orange and red, same color convention as Fig.5.26). In the top plot the HFS, LFS and VER (PLFS) profiles are plotted all together. The good superposition between LFS and VER measurements shows the high precision of the various CXRS systems data. A set of error bar has been added for each profile.

As for the central barrier, (#45371 in Sec.5.7.1), the ion temperature profile for #47340 (in red) does not display an ion barrier, but presents a profile similar to the L-mode cases with the maximum gradient ∇T_i located further outboard around $\rho_\psi = 0.7$. $T_e(0)/T_i(0)$ in the core attains 35 (considerably higher than the central barrier case ~15), confirming the strong central T_e value (and low T_i) attained and the related confinement improvement (see Figs.5.30.a-b). Like the ion temperature, the carbon ion density profile displays no barrier and the local maximum ∇n_i is located at $\rho_\psi = 0.65$. As noted previously in Sec.5.4.2, these observations suggest that the ion channel is only slightly modified during the electron central barrier formation and that ion-electron collisions do not sufficiently heat the ions to observe a ion transport barrier. High ion confinement may exist, but no significant ∇T_i is observed. Nevertheless, the intense electron heating applied in these discharges increases the ion-electron decoupling re-

ducing the ion-electron collisions and does not significantly modify $|R/L_{Ti}|$.

The $|R/L_{ni}|$, $|R/L_{Ti}|$ and $|R/L_{pi}|$ profiles for ions were calculated for these discharges (see Fig.E.14 compared with the electron profiles). For the strongest barrier #47340, $|R/L_{Ti}| \cong 8$ and $|R/L_{ni}| \cong 15$ at $\rho_\psi = 0.7 - 0.75$ are obtained. From Fig.E.14 we see that the maximum gradients in T_e and n_e (and the peaks of the related electron scalelength) are measured at the mid-radius (near $\rho_\psi \cong 0.5 - 0.55$), while for the ions these are displaced much farther outwards. These values demonstrate no observed ion barrier in these discharges.

Comparing the strongest barriers achieved for both targets (#45371 and #47340), we see that the impurity temperature profiles are substantially lower for the co-CD off-axis eITB, with central temperature of 200eV compared to 380eV (see Fig.5.30.b). This is due to the lower electron density characterizing the strong eITB target that reduces coupling and heat exchange between electrons and impurity ions. Even the carbon density profiles appear reduced for the eITB and present a more peaked shape compared to the central barrier target.

5.7.3 Impurity ion density poloidal asymmetry issue

As mentioned above, in the strong eITBs discharges, we often observe a clear asymmetry between the HFS and LFS carbon density profiles (usually $n_{C,H}/n_{C,L} \cong 0.5 - 0.7$) compared to the central barrier cases ($1 < n_{C,H}/n_{C,L} < 0.85$). The carbon density is higher at the LFS around the mid-radius region. This poloidal asymmetry corresponds to a dependence on θ that cannot be neglected for the co-CD off-axis eITBs cases. As presented in Sec.5.2.2 and App.D.1, we account for this density asymmetry in the calculation of the radial electric field.

Only preliminary attempts to explain this mid-radius density asymmetry, such as the effect of the centrifugal force, were attempted at the time of writing. The centrifugal force was estimated, by approximately comparing the carbon velocity against the thermal velocity (i.e. the ratio between the kinetic energy and the thermal energy: $m_C v_C^2/(2T_C)$). Centrifugal effects are considered important when these velocities have comparable weight (i.e. nearly equal). From the impurity values measured for strong eITBs, a ratio of 0.2-0.5 was obtained, suggesting only a modest effect of the centrifugal force, insufficient to explain the asymmetry. The existence of a link between the flow structure and the density asymmetry was recently proposed [167], and a complete 2D impurity density map was measured on TCV late in 2013, (and thus outside the scope of this thesis) to better quantify this asymmetry in a search for a physical explanation.

5.7.4 Impurity ion temperature asymmetric profiles issue

As previously outlined in Sec.5.5 and 5.7.1, for the strongest eITBs, T_i measurements using CXRS showed a problematic asymmetry ($\Delta\rho_\psi \cong 0.15$) between the HFS and LFS profiles, opposed to a flux function, as supposed in the theory. In many shots, the T_i HFS profiles were up to 10-20% higher than the LFS measurements. At first, this difference was supposed to derive mainly from the CXRS uncertainties associ-

ated with the different spectrometers installed for the THFS and TLFS systems (see Fig.3.2) and also to the strong barriers, which were less stable and presented many MHD phenomena, increasing the measurement uncertainties. To assess the spectrometers differences, the fibers of the THFS system were exchanges with the PLFS-VER spectrometer. Discharges performed with this configuration showed an unchanged asymmetry in T_i and, possibly, even slightly accentuated, since the data quality was improved by using both SPEX750Mi spectrometers for the TLFS and THFS systems. Additionally, an accurate appraisal at the various CXRS uncertainties, mainly due to the fitting of the spectra with the instrumental function (Doppler shift, FWHM,..), did not show a specific increase for these discharges. This discounted any explanation resulting from uncertainties, caused by the CXRS optical path or the related analysis. Our attention turned to the LIUQE equilibrium reconstruction. The code was seen to converge with increasing difficulty for plasmas with low I_p and reversed q profile. Comparison of the positions of the magnetic axis R_{axis} obtained from the LIUQE reconstruction and estimated from the maximum SXR emissivity from the XTOMO diagnostic, showed a spatial disagreement in the radial and vertical position of a few cm for many eITBs discharges. In the vertical direction, the two Z_{axis} can vary by 1-2cm, while, in the radial direction, the LIUQE reconstruction often appeared to overestimate R_{axis} by 1cm or more. A clear example of this problem is shown in Fig.5.35 for shot #47340 at 1.75s, where a shift of [dR,dZ]=[-3cm,-1cm] is observed between the GTI (general tomographic inversion with soft X-rays, in this case with the XTOMO data) and LIUQE reconstructions.
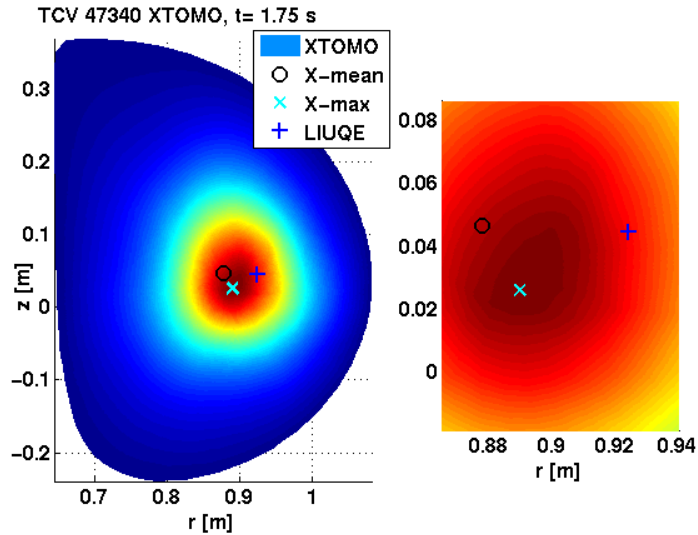

Figure 5.35: Magnetic axis position obtained from the LIUQE reconstruction (blue cross) and the maximum SXR emissivity measured with the XTOMO diagnostic (cyan cross) for shot #47340. A radial and vertical shift of a few cm ([dR,dZ]=[-3cm,-1cm]) is clearly visible.

Since upgrading LIUQE's reconstructions was not possible within this thesis's mandate, the effect of a magnetic axis shift on the CXRS profiles was tested, by simply adding a shift of equal magnitude to the LIUQE reconstruction (without changing
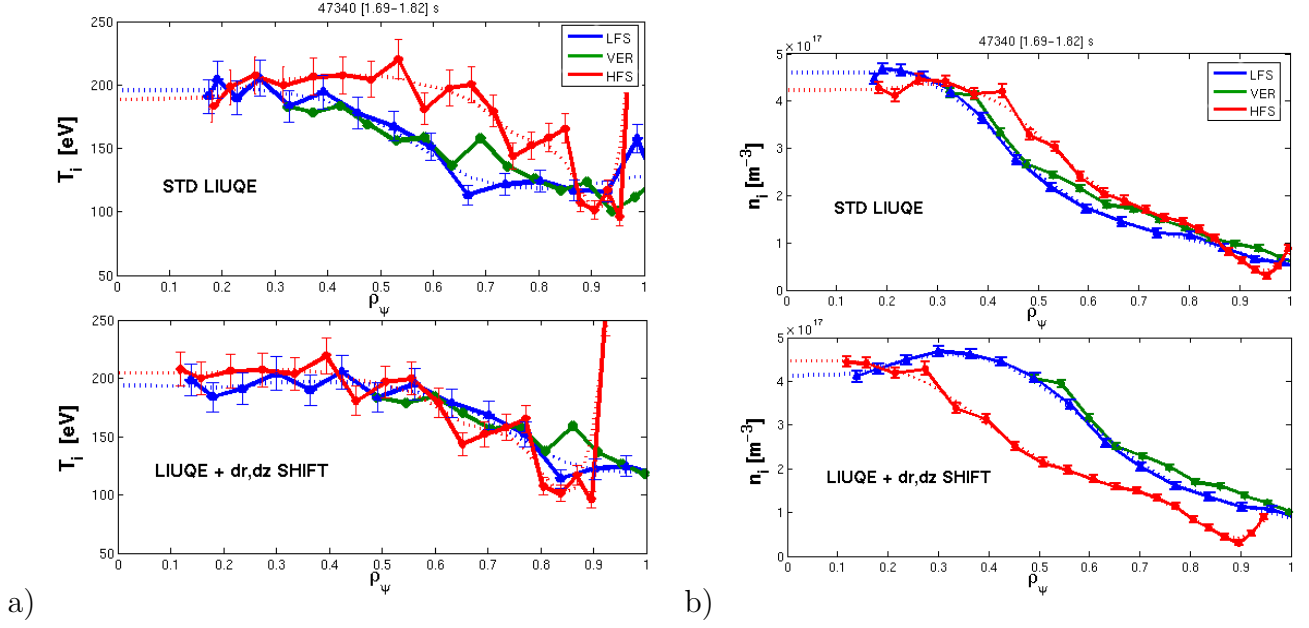
Figure 5.36: Comparison between the T_i and n_i profiles obtained from a standard LIUQE reconstruction and by simply imposing a shift [dR,dZ]=[-3cm,-1cm] equal to the XTOMO magnetic axis position to the same reconstruction. This shift allows to obtain a clear superposition of the LFS and HFS T_i profiles and a correct n_i asymmetry (higher in the LFS region).
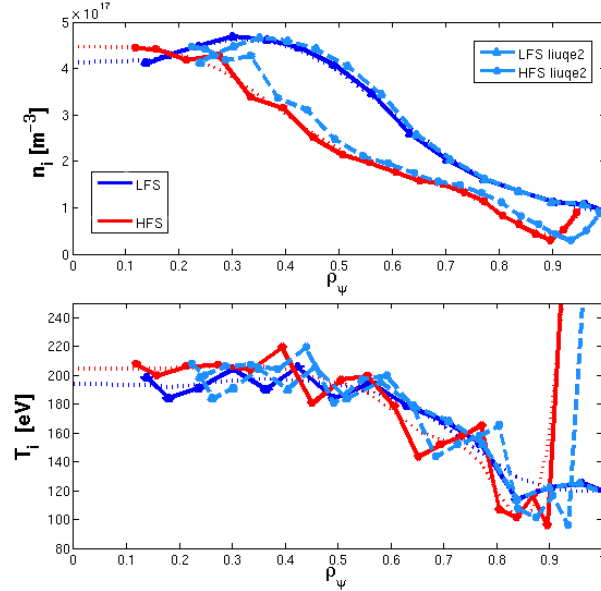

Figure 5.37: Comparison between the T_i and n_i profiles obtained from the previous standard LIUQE reconstruction with the shift [dR,dZ]=[-3cm,-1cm] and a LIUQE2 run taking into account the electron pressure profile. Notice that with the LIUQE2 version it is possible to mainly correct the shift and the imprecise magnetic equilibrium of the standard run.

the equilibrium shape). The CXRS analyses, including profile evaluation, were then recalculated. The T_i and n_i profiles obtained with and without the LIUQE shift are plotted in Fig.5.36. With this correction, the T_i profiles of the HFS (red), LFS (blue) and VER (green) system now well superpose. The n_i profiles change significantly with the LFS density higher than the HFS profile, as already observed for the central barrier targets (see Sec.5.7.1). A correction of a few centimeters in the determination of R_{axis}, in the direction implied by another diagnostic, was able to explain the difference ($\Delta\rho_\psi \cong 0.15$) observed in the ion temperature profiles.

Such a vertical shift implies that all CXRS profiles are entirely shifted inwards or outwards and may be easily corrected, but a radial shift implies a more complicated problem in solving the Grad-Shafranov equation in the LIUQE code. This issue is still being studied and a method to include the XTOMO data in a future LIUQE version is being implemented, together with research into understanding the possible causes of this deviation. As this will not be completed before the end of this thesis, an other acceptable solution was sought. We tried to improve the magnetic reconstruction by rerunning LIUQE with the best available fitted electron pressure profile using different basis functions. With this method, we were sometimes able to correct the R_{axis} position and the plasma shape and finally the CXRS profiles (see Fig.5.37 in cyan for shot #47340). An adequate superposition of the HFS and LFS T_i profiles was used to judge this process. A final average between these profiles is then performed and compared with the VER T_i and $T_i(0)$ (from the NPA diagnostic) profiles. Although this is, clearly, not an optimal solution, it was deemed to be the best available at the time of writing and it was used for the analysis of the strong co-CD off-axis eITB target. In the future, it is hoped that improvements of the LIUQE reconstruction for strong eITBs, will also include basis functions that correctly account for strong pressure gradients and reversed q profiles.

5.7.5 Comparison between the experimental impurity ion and electron profiles with a quasi-linear model applied to eITBs

In Secs.5.7.1, 5.7.2 and Secs.5.4.2, 5.5.1, the impurity ion/electron temperature and density profiles were measured and discussed for the strongest central barrier and co-CD off-axis eITB.

In a previous study, a quasilinear model was proposed using the gyrokinetic GS2 code [168] to assess the particle transport in eITBs and L-mode plasmas [137, 138, 166]. This model was also used to interpret the density peaking in the core of TCV H-mode plasmas [169]. Based on previous eITBs discharges, the study shows the existence of an inward pinch that couples electron density and temperature gradients inside the barrier. A ratio of $|R/L_{ne}|/|R/L_{Te}| = 0.4 - 0.5$ was obtained [137]. To explain this ratio and observe its effect on particle transport, a local ratio between ion and electron temperature gradients of $|R/L_{Ti}|/|R/L_{Te}| = 0.3 - 0.5$ is required at the barrier location (i.e local max $|R/L_{Te}|$) [137, 138]. Since the previous investigations lacked impurity temperature and density measurements, we compared the profiles measured

during this work with the proposed model.

Secs.5.7.1 and 5.7.2 already noted that, for both targets, the positions of the maximum ∇T_e and ∇n_e are located well inside the maximum of ∇T_i and ∇n_i. The local $|R/L_{Ti}|/|R/L_{Te}|$ was calculated at the location of maximum ∇T_e ($\rho_\psi \cong 0.5$). For the central barrier, a $|R/L_{Ti}|/|R/L_{Te}| \cong 0.24$ is obtained, with $T_e/T_i \cong 8.5 - 9$, while for co-CD off-axis eITB $|R/L_{Ti}|/|R/L_{Te}| \cong 0.12$ with $T_e/T_i \cong 18 - 19$. The obtained $|R/L_{Ti}|/|R/L_{Te}|$ ratios are both lower than 0.25, which is smaller than predicted by the quasi-linear model. By comparing the electron profiles for the same location, a $|R/L_{ne}|/|R/L_{Te}| \cong 0.25$ is obtained for the central barrier and $|R/L_{ne}|/|R/L_{Te}| \cong 0.27$ for the co-CD off-axis eITB, again lower than expected [137]. The results in this work display some discrepancies between the measured profiles and the theory at the maximum barrier gradients.

[169] successfully used the same model applied to TCV H-modes to explain the density peaking at $\rho_\psi = 0.6 - 0.8$ with a $|R/L_{Ti}|/|R/L_{Te}| = 0.4 - 0.5$ ratio. We therefore investigated the region around the maximum ∇T_i ($\rho_\psi \cong 0.8$) and calculated the local $|R/L_{Ti}|/|R/L_{Te}|$ to probe any difference in behavior outside the electron barrier position. For the central barrier, $|R/L_{Ti}|/|R/L_{Te}| \cong 0.45 - 0.55$ is obtained at $\rho_\psi = 0.75 - 0.9$, while for the co-CD off-axis eITB a $|R/L_{Ti}|/|R/L_{Te}| \cong 0.25 - 0.4$ is obtained at $\rho_\psi = 0.75 - 0.9$. At this location, a $|R/L_{ne}|/|R/L_{Te}| \cong 0.3 - 0.4$ is obtained for the central barrier and $|R/L_{ne}|/|R/L_{Te}| \cong 0.5 - 0.6$ for the co-CD off-axis eITB. These results are, indeed, more encouraging indicating that the model may be applied to the maximum ∇T_i region outside the electron barrier. For the studied TCV H-modes, an important interplay between the ITG mode and TEM mode was observed, whilst for eITBs, TEM modes dominate the entire plasma. The co-existence of different modes can have a strong influence on the $|R/L_{ne}|/|R/L_{Te}|$ ratio and non-linear effects should also be taken into account [169].

From these new measurements, including ion profiles, it is suggested that the quasi-linear model proposed in [137, 138] should be revisited for eITBs. As proposed in [137], the effect of the ETG instability may now be also included in the model. In the future, experiments could be performed with the neutral beam heating system, to be installed on TCV in 2015. The NBH will establish whether any ions barriers are observed on TCV by applying direct ion heating.

5.8 Summary and conclusions

In this chapter, a detailed study about the formation and sustainment of TCV eITBs, including toroidal and poloidal rotation profiles (v_φ and v_{pol}) has been reported. For the first time on TCV eITBs, the CXRS diagnostic has provided the impurity profiles required to systematically derive the radial electric field and $E \times B$ shearing rate ($\omega'_{E \times B}$) across the whole plasma radius.

The formation of ITBs is an important issue that has been studied for several years on many machines. In contrast to other devices, the key ingredient for eITB formation and sustainment on TCV is the degree of reverse shear, and the $E \times B$ shearing rate

was theoretically determined to not to play a significant role. The negligible role of the $E \times B$ shearing rate was experimentally confirmed in this work.

The equations and the two different methods used during this work to determine E_r and the $E \times B$ shearing rate were presented in Sec.5.2. Both use the force balance equation with the poloidal rotation either measured directly or indirectly determined from toroidal rotation asymmetry. This method allows the derivation of E_r without requiring a measured v_{pol} from the CXRS diagnostic. Toroidal and poloidal rotations and the radial electric field may be derived inside the LCFS using the two flux functions $\hat{u}_\sigma(\psi)$ and $\hat{\omega}_\sigma(\psi)$, assuming that the ion temperature is also a flux function. E_r was found proportional to the ∇p_σ and $\hat{\omega}_\sigma$ terms. The ∇p_σ term always leads to an inward radial electric field contribution (since p_σ typically decreases with minor radius), while the $\sigma_{I_p} \hat{\omega}_\sigma$ term can be additive or not.

A central barrier (ICEC) and a co-CD off-axis eITB target, centered at Z=0cm in order to maximize the CXRS coverage, similar to previously studied scenarios at Z=21cm, were developed for this work by applying cnt-CD on-axis and co-CD off-axis. Strong co-CD off-axis eITBs have been obtained with H_{RLW} factors up to 5.4 (compare to 2.9 for the central barriers) and large $|R/L_{Te}|$ up to 45, indicating a strong confinement improvement. A barrier in $T_e = 7keV$ and n_e with a 23cm width was achieved in this work.

To better understand the barrier formation and sustainment, the effect on the barrier strength and on the rotation profiles of the central and total power, Ohmic current perturbations and MHD activity was investigated for both targets (Secs.5.4 and 5.5). It was observed that, as expected, the barrier strength increases with cnt-CD applied on-axis, higher total power and negative inductive current (I_{OH}) perturbations. Particularly, the addition of a negative dI_{OH}/dt ramp reinforces the barrier and simultaneously broadens and increases the T_e profile.

Toroidal rotation profiles, measured for the central barrier cases, presented a central peaked cnt-current profile (up to 20km/s), and ∇v_φ increased with the barrier strength, while the poloidal rotation was mainly in the electron diamagnetic direction. The resulting radial electrical fields were mainly in the inward direction ($E_r = -[0.5, 3]kV/m$) and the measured $E \times B$ shearing rates were $|\omega'_{E \times B}| \propto 10^4 s^{-1}$, slightly changing in presence of a barrier.

The presence of MHD activity strongly affected the constancy of the co-CD off-axis eITBs, leading often to rotation and E_r reversal. For strong co-CD off-axis eITBs, v_φ was mainly in the co-current direction with a central value of -15km/s. For weaker barriers, the rotation profile was observed to shift towards smaller co-current values or even reverse towards cnt-current values. This effect remains unclear, but may be linked to some modifications in the edge conditions. Similarly to the central barrier cases, the $E \times B$ shearing rates in the central region remained of the order of $10^4 s^{-1}$. We found no special dependence between the experimental $\omega'_{E \times B}$ and H_{RLW} or the maximum $|R/L_{Te}|$, confirming that on TCV, the barrier improvement is not linked to higher $|\omega'_{E \times B}|$ values.

The experimental $E \times B$ shearing rates were then compared, in Sec.5.6, with the growth rate of the most unstable mode for these discharges (TEM) obtained with the GENE

code, in order to determine the importance of the $E \times B$ shear flows on TCV. The estimated growth rate is always one order of magnitude larger than the measured $E \times B$ shearing rates, confirming that the $E \times B$ shearing is not the cause of the formation of eITBs on TCV. This result supports the main role of the q profile in TCV eITB formation, proposed in previous studies [129, 130, 131].

In Sec.5.7, the impurity ion temperature and density profiles were observed to decrease with stronger barriers, and additionally, a still unexplained n_i poloidal asymmetry was noted for the co-CD off-axis eITBs. For the strongest barrier, we obtained a maximum of $|R/L_{Te}| \cong 45$ and $|R/L_{ne}| \cong 12$ at $\rho_\psi \cong 0.5 - 0.55$, while $|R/L_{Ti}| \cong 5$ and $|R/L_{ni}| \cong 7$ at the same location. This result confirms the presence of an electron barrier and shows that no ion barrier can be observed for these discharges, since no significant change between L-mode or eITB carbon temperature and density profiles is seen.

The comparison between the experimental ion temperature profiles and the results obtained with a quasi-linear model applied to TCV eITBs showed some discrepancies. The $|R/L_{Ti}|/|R/L_{Te}|$ ratios measured at the barrier position are considerably lower than expected from the model, and no ion barrier is observed in these discharges. Nevertheless, it was found that the same model may be applicable in the external region near the maximum ∇T_i. From the new presented measurements, including ion profiles, it is suggested that this quasi-linear model should be revisited for eITBs.

In conclusion, the theoretical study of this work shows that the toroidal and poloidal rotation can not be considered as flux functions. To perform relevant rotation studies, it is therefore required to measure the $v_\varphi(R)$ and $v_{pol}(R)$ (or $v_{\varphi\,L,H}(\psi)$ and $v_{pol\,L,H}(\psi)$) profiles across the whole plasma radius (i.e. for both HFS and LFS), as it is now possible on TCV. The indirect method used to determine the poloidal rotation, shows that the rotation profiles should be preferably analyzed using the two flux functions $\hat{u}_\sigma(\psi)$ and $\hat{\omega}_\sigma(\psi)$. Further studies are to be performed to better interpret the meaning of both terms, particularly $\hat{\omega}_\sigma(\psi)$, that plays a dominant role in the calculation of the radial electric field. Additionally, future studies should focus on the importance of the derivative $\nabla\hat{\omega}_\sigma(\psi)$, included in the $E \times B$ shearing rate term, that was not directly investigated in this work.

Additional NBH heating, to be installed on TCV in 2015, will allow to directly heat the ion channel and therefore increase the ion temperature. The effect of such heating on TCV ITBs should be investigated with the help of CXRS measurements, to establish the presence of any ion barrier on TCV. For these new iITBs, the question will again arise as to whether their formation can be explained with the only presence of a reverse q profile or possibly by additional significant effect from the $E \times B$ shearing rate. Based on the studies in this thesis, NBH heating will permit a new series of experiments and modeling studies related to TCV internal transport barriers that may help resolve the different conclusions of eITB formation between machines.

Chapter 6

Conclusions and outlook

This thesis has presented experimental studies of rotation and impurity profiles performed in the TCV tokamak. Effort was expended to better understand the formation of electron internal transport barriers on TCV and on the role of MHD activity, particularly the sawtooth instability, on momentum transport. The work is based essentially on measurements from a CXRS diagnostic. The upgraded CXRS-DNBI system of TCV permits high time and space resolved measurements of the ion density, temperature and group velocity from the spectroscopic analysis of the CVI emission line. The non perturbative nature of this CXRS diagnostic was combined with the unique capabilities of TCV in terms of plasma shaping and heating by electron cyclotron waves that were exploited, (and pushed to their limits), in order to develop pertinent scenarios.

The three main topics treated during this thesis, i.e. the CXRS diagnostic, the effect of sawtooth instability on rotation profiles and momentum transport, and the investigation of the eITBs formation using rotation measurements, have been already largely summarized at the end of each chapter, therefore, here, we focus on the main contributions of this work.

This thesis led to an important improvement and automation of the CXRS diagnostic. The present day CXRS2013 diagnostic covers the entire TCV radial midplane with up to 80 measurement locations (for the extended double slit configuration) with a time resolution ranging from 2-30ms. This capability was leveraged in the investigation of more complex scenarios featuring fast events, such as low density eITBs and the sawtooth instabilities. The diagnostic together, with the RT-trigger system, are now equipped to investigate standard L-mode and improved scenarios, in ever more challenging ways.

For the first time, a comparison between rotation profiles measured over several sawtooth events and across a "canonical" sawtooth cycle have been undertaken to identify the effect of the various ST phases on the rotation profile, and thus momentum transport. This study showed that sawteeth crashes, have, in particular, a strong and rapid effect on rotation profiles, particularly in the core region. The obtained averaged rotation profiles show that ST restrict the maximum attainable $|v_{\varphi,max}|$ and that, in the plasma core, inside the q=1 surface, the rotation profiles are flattened and almost

always display a small co-current contribution. It is this effect that results in the $1/I_p$ scaling observed in TCV limited L-mode plasmas. The co-current core contribution was identified to be related to the ST crash, whilst, during the quiescent ramp of the sawtooth period, a plasma recoil outside the mixing radius is observed. A high degree of momentum conservation, up to 80-90%, was measured, suggesting that a supplementary torque accompanying the ST crash is not required to explain the experimental observations (although, conversely, it can not be completely excluded and will be the subject of further experiments). This study has demonstrated the importance of including fast perturbative effect such as MHD modes in momentum transport models to build a complete picture, since these are likely to generate strong and fast 3D evolving fluxes inside the plasma. In essence, the presumptions at the start of the work were verified: MHD events such as ST that are well known to strongly affect particle and energy transport can also strongly affect momentum transport and should not be neglected in the development of operational scenarios.

Additionally, this thesis contributed in better elucidating the formation and characteristics of TCV eITB scenarios. Extensive work on eITBs allowed systematic measurement of the radial electric field and the $E \times B$ shearing rate in eITBs. Toroidal and poloidal rotations were, for the first time on TCV, measured in eITBs. Despite the complexity of these scenarios and the consequent reduced CXRS data quality, it was possible to measure that, on TCV, the $E \times B$ shearing rate's effect on the formation of eITBs is negligible. This result supports previous theoretical studies that concluded that the reversed shear profile was mainly responsible for the eITB formation. Amongst a large variety of theories and experiments performed on several devices, this result is in contrast to the observations on larger devices that concluded that for ITBs with $T_i > T_e$ produced by NBH or ICRH, the shear flows play an important role.

Some of the questions posed in this work remain, as is often the case, incomplete, and some suggestions that will use the future high power NBH and diagnostic upgrades have been included in the chapter discussions.

From the diagnostic point of view, the CXRS still has room for improvement, in particular concerning the THFS and PLFS systems. The installation of an Andor camera on the THFS system and a complete optical analysis of its spectroscopic performance may allow a further increase in sensitivity. The combination of the updated THFS and TLFS could then be re-applied to the "between sawtooth" measurements by simultaneously triggering both systems. In the future, this trigger technique may be also exploited to study the ELM relaxations in H-mode, using the H_α signal from TCV photodiodes as a reference (instead of the soft X-rays). To perform such experiments, a strong effort is required to develop stationary H-mode target plasmas at Z=0cm for complete CXRS plasma coverage. As observed during this thesis, the poloidal rotation measurements present larger uncertainties that are comparable to the effective poloidal rotation values of few km/s. The derivation of poloidal rotation from the asymmetry of the toroidal rotations has allowed during this thesis to circumvent this problem and obtain profiles with much smaller uncertainties. Nevertheless, to further study the edge poloidal rotation, a more precise optical system with higher photon efficacy and

higher radial resolution is still required.

To explain the central co-current kick and momentum recoil observed during the ST study, a model should be applied (and possibly developed), that accounts for the redistribution of toroidal momentum inside the sawtooth mixing radius and the development of a strong toroidal electric field. Further experiments are also suggested in order to identify the effect of ST stabilization and further probe the conservation of the momentum flux across strong MHD events.

Finally, with the new NBH installed on TCV in 2015, it will be interesting to pursue the behavior of ITBs with neutral beam assistance. It will be then possible to directly heat the ion channel and probe the presence of a possible ion transport barrier, to be compared with the revisited quasi-linear model predicting the electron and impurity transport on TCV eITBs. For these new iITBs, the question will again arise as to whether their formation can be explained with the only presence of a reverse q profile or with an additional significant effect from the $E \times B$ shearing rate that will then become relevant.

Appendix A

Observation of a critical pressure gradient for the stabilization of interchange modes in TORPEX plasmas

A.1 Preamble

The subject presented in this chapter was performed during the first year of this thesis on the TORPEX basic plasma device in Lausanne. Even though the topic is not completely related with the main work performed later on TCV, the author believes that it is important to include it in the report, as a complementary contribution in the characterization of pressure driven instabilities in simple magnetized tori.

A.1.1 Introduction

In simple magnetized tori (SMT), global interchange modes characterized by $k_\parallel \simeq 0$ (flute-like) can be destabilized by pressure gradients in the unfavorable curvature region, where ∇B and ∇p are collinear. Linear theories developed for Z-pinch [2, 170] and magnetic dipole [171, 172] configurations have shown that plasma compressibility can stabilize the interchange mode even in the presence of a finite pressure gradient. The aim of this chapter is to determine whether a critical pressure gradient for interchange instabilities exists in the SMT device TORPEX [173] and to experimentally quantify its value. In TORPEX, a vertical magnetic field B_z is superposed to a toroidal field B_φ, creating helical field lines with both ends terminating on the torus vessel (see Fig.A.1). TORPEX is particularly well suited for the quest of a critical pressure gradient. Its flexibility, together with the high spatial and time resolved set of diagnostics, has led to the characterization of linear and non-linear properties for low frequency electrostatic instabilities [173, 174, 175] and of the associated transport [176, 177]. The existence of a threshold gradient driving the interchange instability observed in certain TORPEX plasmas is experimentally demonstrated during a scan in the neutral

gas pressure p_n. Around a critical neutral concentration $p_{n,crit}$, a small increase of the latter causes a profile broadening and a reduction in the fluctuation amplitude. The pressure profile is flattened locally, stabilizing the interchange mode observed at lower p_n. The value of the critical pressure gradient measured experimentally is in agreement with the theoretical prediction [178].

A.2 Theoretical background

For the SMT configuration, we consider a linearized system for the plasma density n, the electron temperature T_e and the plasma potential ϕ, based on the 2D Braginskii drift-reduced equations in the limit $\beta = 2\mu_0 \overline{n}\,\overline{T}_e / B^2 \ll 1$, $T_i \ll T_e$ and $k_\parallel = 0$ ([170, 179]). Drift wave terms are neglected since our study concentrates on interchange modes. We denote each quantity as the sum of a stationary and a fluctuating part: $f = \overline{f} + \widetilde{f}$. The equations are written in a coordinate system parallel to the magnetic field lines, where x is the radial direction and y the direction perpendicular to x and the magnetic field line. Assuming no stationary flows ($\overline{\phi} = 0$) and including an ion-neutral collision term, the linearized equations for the fluctuating quantities $\widetilde{n}$, $\widetilde{\phi}$, $\widetilde{T}_e$ can be deduced from the model in [180]. At the radial position R, the linear system is given by:

$$\frac{\partial \widetilde{n}}{\partial t} = -\frac{1}{B}\frac{\partial \widetilde{\phi}}{\partial y}\frac{\partial \overline{n}}{\partial x} + \frac{2}{eRB}\left(\overline{n}\frac{\partial \widetilde{T}_e}{\partial y} + \overline{T}_e\frac{\partial \widetilde{n}}{\partial y} - e\overline{n}\frac{\partial \widetilde{\phi}}{\partial y}\right) + \frac{\omega_\sigma}{\overline{T}_e}\left[\overline{T}_e\widetilde{n} + \left(\Lambda + \frac{1}{2}\right)\widetilde{T}_e - e\widetilde{\phi}\right] \tag{A.1}$$

$$\frac{\partial \nabla^2 \widetilde{\phi}}{\partial t} = -\nu_{in}\nabla^2\widetilde{\phi} + \frac{2B}{m_i R}\left(\frac{\overline{T}_e}{\overline{n}}\frac{\partial \widetilde{n}}{\partial y} + \frac{\partial \widetilde{T}_e}{\partial y}\right) - \frac{\omega_\sigma}{\overline{T}_e}\frac{\Omega_i^2}{e}\left(\Lambda\widetilde{T}_e - e\widetilde{\phi}\right) \tag{A.2}$$

$$\frac{\partial \widetilde{T}_e}{\partial t} = -\frac{1}{B}\frac{\partial \widetilde{\phi}}{\partial y}\frac{\partial \overline{T}_e}{\partial x} + \frac{4}{3eRB}\left(\frac{7}{2}\overline{T}_e\frac{\partial \widetilde{T}_e}{\partial y} + \frac{\overline{T}_e^2}{\overline{n}}\frac{\partial \widetilde{n}}{\partial y} - e\overline{T}_e\frac{\partial \widetilde{\phi}}{\partial y}\right)$$
$$-\frac{2}{3}\omega_\sigma\left[\left(1.71\Lambda + \frac{3}{2}\right)\widetilde{T}_e - 1.71e\widetilde{\phi}\right] \tag{A.3}$$

In Eq. A.2 the ion-neutral collision frequency $\nu_{in} \simeq n_n\sigma_{ion}v_{thi} = \frac{p_n}{T_{amb}}\sigma^{mt}v_{thi}$, with p_n as the neutral background pressure is introduced, T_{amb} the neutral gas temperature and σ^{mt} the momentum transfer cross section [181]. The electron-neutral collision term can be neglected compared to ν_{in} because of the mass ratio m_e/m_i. In the linearized system the terms related to the interaction of the plasma with the vessel are those proportional to $\omega_\sigma = \frac{\sigma}{R}\sqrt{\frac{T_e}{m_i}}$, with $\sigma = \frac{\Delta}{2\pi L_v} = \frac{B_z}{B_\varphi}\frac{R}{L_v}$, $\Delta = 2\pi R\frac{B_z}{B_\varphi}$ and the SMT height L_v. The term Λ defines the Coulomb logarithm $\Lambda = \log\sqrt{m_i/(2\pi m_e)}$ and Ω_i corresponds to the ion-cyclotron frequency. Each fluctuating quantity can be written in the form: $\widetilde{f} = \widetilde{f}\exp(\gamma t + ik_y y)$, where $\gamma = -i\omega$ and the real part $\Re(\gamma)$ is the growth rate. The mode is driven unstable when $\Re(\gamma) > 0$. Moreover, we consider a

local approximation, i.e. that the perturbations do not depend on x.

A dispersion relation for interchange modes, including the ion-neutral collision term ν_{in} is derived from the linearized system (Eq. A.1 - Eq. A.3):

$$b_{00}\nu_{in} + b_0 + (b_1 + b_2\nu_{in})\gamma + (b_2 + b_3\nu_{in})\gamma^2 + b_3\gamma^3 = 0 \tag{A.4}$$

with $b_{00} = \frac{20}{3}\omega_d^2 k_y^2 \rho_s^2$, $b_0 = \frac{20}{3}i\omega_d^2(2\omega_d + \omega_*)$, $b_1 = \frac{20}{3}\left(k_y^2\rho_s^2 - 1\right)\omega_d^2 - 2(\eta + 1)\omega_*\omega_d$, $b_2 = \frac{20}{3}i\omega_d k_y^2\rho_s^2$, $b_3 = -k_y^2\rho_s^2$ and where $\omega_d = k_y\rho_s c_s/R$ is the curvature frequency, $\omega_* = k_y\rho_s c_s/L_n$ the diamagnetic frequency, $\eta = L_n/L_T$, with $L_n = \overline{n}/(d\overline{n}/dx)$ and $L_T = \overline{T_e}/(d\overline{T_e}/dx)$. The ω_σ term can be neglected in Eq. A.4, since for the experimental scenarios considered here $\omega_\sigma \ll \omega_d$, ω_* and ν_{in}. A similar dispersion relation, but neglecting the ion-neutral collision term, has been derived in [170].

Assuming $k_y\rho_s \ll 1$ (scaling $\gamma \sim c_s/R$), Eq. A.4 reduces to:

$$\left[k_y^2\rho_s^2\gamma^2 + \nu_{in}k_y^2\rho_s^2\gamma + \left(\frac{20}{3}\omega_d^2 + 2(\eta + 1)\omega_*\omega_d\right)\right]\gamma = 0 \tag{A.5}$$

The trivial solution $\gamma = 0$ has no interest. A root of Eq. A.5 with positive real part only exists if the third term in the square brackets is negative. Thus, the condition for instability reads:

$$\frac{20}{3}\omega_d^2 + 2(\eta + 1)\omega_*\omega_d < 0 \tag{A.6}$$

This condition does not depend on ν_{in}: the ion-neutral collisions do not affect the value of the critical normalized pressure gradient $L_p = \overline{p}_e/(d\overline{p}_e/dx)$ for interchange instabilities. Introducing $L_p^{-1} = (\eta + 1)L_n^{-1}$ in Eq. A.6 we get a stability condition. Interchange modes are stable if

$$L_p^{-1} > L_{p,crit}^{-1} = -\frac{10}{3R} \tag{A.7}$$

With R = 1 m for the TORPEX device, we get $L_{p,crit}^{-1} \cong -3.3$ m^{-1}. An interchange mode cannot be driven unstable on the HFS since L_p is always positive in that region. On the LFS, interchange modes are driven unstable if $L_p^{-1} < L_{p,crit}^{-1}$. One has to note that a constant $E \times B$ flow, not included in the Eqs. A.1-A.3, would not affect the threshold value we found. The interchange mode frequency in the laboratory frame is essentially given by the $E \times B$ drift velocity ($\omega_I \cong \omega_{E\times B} = k_\perp v_{E\times B}$). Therefore, a change in the $E \times B$ flow profile will locally affect the measured mode frequency. Moreover, shear flows are not considered in this analysis, even though they could affect the instability threshold. Note also that using a non local approximation and/or considering also drift modes, it could be shown that collisions can change the pressure radial profile [182, 183].

To address the question of the existence of a critical pressure gradient experimentally, one needs to find a way to efficiently decrease the pressure gradient until interchange modes are stabilized. If a critical gradient is observed, its value can be compared with the prediction of the linear theory.

A.3 Experimental setup and standard plasmas

The experiments are performed in the simple magnetized toroidal device TORPEX (major radius $R = 1$ m and minor radius $a = 0.2$ m, see Fig.A.1). Helical magnetic field lines are obtained by superposing a vertical magnetic field $B_z \cong 1.3$ mT to a dominant toroidal magnetic field $B_\varphi \cong 80$ mT, which can be slightly varied in order to maintain the plasma at the center of the poloidal section. Plasmas of different gases (H_2, He, Ne, Ar, Kr,...) can be produced and sustained by continuous injection of microwaves in the range of Electron Cyclotron (EC) frequencies (2.45 GHz). As RF power is an efficient tool to control the density profile [184], a low power magnetron ($P_{RF} \leq 1.2$ kW) is used in order to produce low density and weakly turbulent plasmas, as needed for these specific experiments. We focus on Neon plasmas, for which we expect stronger collisional effects than for lighter ions. The neutral gas pressure can be varied between 2×10^{-5} mbar and 2×10^{-3} mbar. Measurements are taken with the two-dimensional 86 Langmuir probes (LP) fixed array HEXTIP (with a 3.5 cm pin separation, see Fig.A.1.b) and [185]), the 8-tip LP movable array SLP and an 8 tip array fixed near the vessel walls on the Low Field Side (LFS). The LP can be operated in the ion saturation current regime ($V_{bias} = -40$V) or in the swept mode needed to extract the time averaged profiles. The time averaged 2D density profile
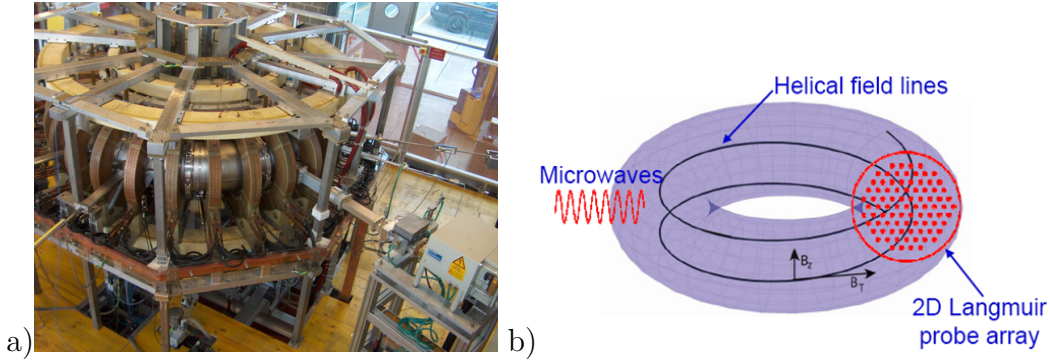
Figure A.1: a) The TORPEX device and the magnetron injecting the EC waves to heat its plasma. b) Schema of the open helical magnetic field lines and of the HEXTIP probe.

of a typical plasma, measured with HEXTIP is shown in Fig.A.2.a. The neutral pressure is $p_n = 7.6 \times 10^{-4}$ mbar with $P_{RF} \cong 120$ W, $B_z \cong 1.3$ mT and $B_\varphi \cong 80$ mT. The density profile is directly derived from measurements of the ion saturation current, assuming a constant temperature of 5 eV. The plasma is centered around $r = -2$ cm ($n_{e,max} \simeq 3.7 \times 10^{16}$ m^{-3}) and is elongated in the vertical direction (slab-like). A coherent mode with $f \cong 7.5$ kHz is detected at $r = 3.5$ cm and $z = 0$ cm (Fig.A.2.c). The 2D profile of the rms of $\tilde{n}_e$ calculated in the range $\Delta f = [3.4, 12]$ kHz and normalized over the entire spectrum [175] shows that this mode is observed for all z in the region $0 \leq r \leq 10$ cm on the LFS (Fig.A.2.b).

To identify the electrostatic instability observed in this plasma, the dispersion relation of the wave is evaluated across and along the magnetic field from the wavenumber-frequency power spectrum $P(k_z, \omega)$ computed for density fluctuations using a two
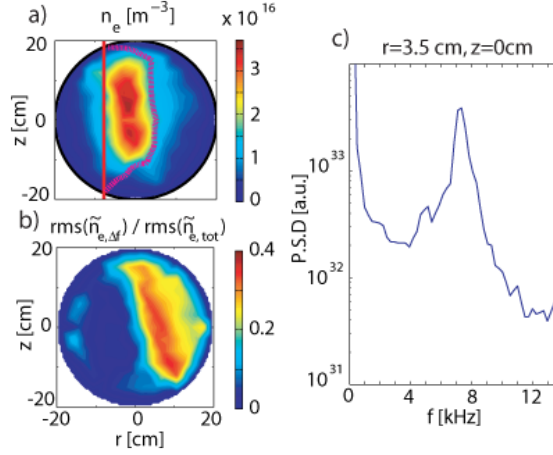
Figure A.2: 2D time averaged profiles of a) the electron density n_e b) the rms of the electron density $\tilde{n}_e$ in the range $\Delta f = [3.4, 12]$ kHz normalized over the entire spectrum; c) Power spectral density for I_{sat} measured at $r = 3.5$ cm.
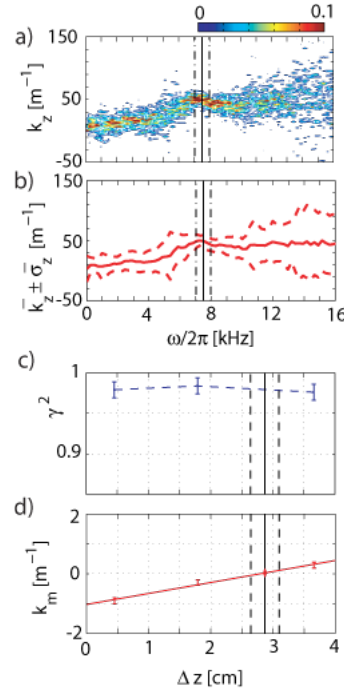

Figure A.3: Statistical dispersion relation reconstructed for the mode detected on I_{sat} measured at $r = 7$ cm and $z = 0$ cm. a) Conditional wavenumber-frequency spectrum $p(k_z|\omega)$; b) First (red line) and second moment (red dotted line) of the spectral density in the wavenumber space $\bar{k}_z(\omega) \pm \bar{\sigma}_{k_z}(\omega)$. The black lines correspond to the mode frequency $\omega_0/2\pi \pm \Delta\omega_0/2\pi$; c) Spectral coherence and d) Wavenumber measured at the frequency of the mode and as a function of the vertical separation between the tips ($k_\parallel = k_m(z_{opt})$). The error bars associated to k_m correspond to the spectral width of the spectrum $P(k_m)$ measured for each couple of tips, whereas the black lines define $z_{opt} \pm \Delta z_{opt}$.
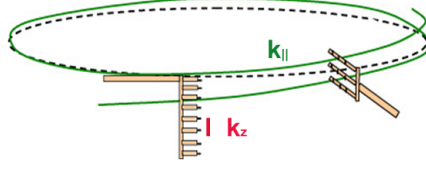
Figure A.4: Schematic of the Langmuir Probes used to estimate, with a two point correlation technique, the vertical k_z and parallel $k_\parallel$ wavenumbers of the investigated mode. The parallel wavenumber is obtained by measuring the phase shift between two toroidally separated ($\Delta\varphi = \pi/2$) probes and positioned as precisely as possible on the same magnetic field line (in green). The vertical wavenumber is derived from the conditional wavenumber-frequency spectrum $p(k_z|\omega)$ evaluated at $r = 7$ cm with two probes separated in the vertical direction by a distance $\Delta z = 1.34$ cm (in red).

point correlation technique [186, 187]. In TORPEX, this technique has been used to identify instabilities in Hydrogen plasmas [175]. We apply it here to characterize Neon plasmas. Indeed, changing the mass ratio m_e/m_i and the plasma resistivity might affect the properties of drift waves. So, it is essential to verify that the investigated plasmas are still in an interchange dominated regime. To apply this method, the distance between the two Langmuir probes measuring $\tilde{I}_{sat}$ has to be much smaller than the correlation length. The conditional wavenumber-frequency spectrum $p(k_z|\omega) = \frac{P(k_z,\omega)}{\sum_{k_z} P(k_z,\omega)}$ is evaluated at $r = 7$ cm with two probes separated in the vertical direction by a distance $\Delta z = 1.34$ cm (Fig.A.3.a and Fig.A.4). Figure A.3.b shows the mean value $\overline{k}_z(\omega)$ and the variance $\overline{\sigma}_{k_z}(\omega)$ of the spectral density in the wavenumber space. The vertical wavenumber k_z associated with the frequency of the mode 7.5 ± 0.6 kHz is about $k_z = (50.4 \pm 7.4)m^{-1}$. This corresponds to a wavelength $\lambda_z \simeq 12.5$ cm, which is approximatively equal to the vertical displacement of the magnetic field lines after one toroidal turn at this radial location ($\Delta \simeq 11.5$ cm for $R = 1.07$ m). The mode phase velocity $v_{ph} = \frac{\sum_{k_z,\omega} \frac{\omega}{k_z} P(k_z,\omega)}{\sum_{k_z,\omega} P(k_z,\omega)}$ is estimated to be $v_{ph} = (920 \pm 73)$ m/s, which is in good agreement with the $E \times B$ drift velocity (not shown). The estimated vertical wavelength and the phase velocity are indicators that the observed instability is an interchange mode. To complete the mode identification, one needs to estimate the parallel wavenumber. This is done by measuring the phase shift between two toroidally separated ($\Delta\varphi = \pi/2$) probes and positioned as precisely as possible on the same magnetic field line (see Fig.A.4). The details of this procedure are given in [175, 188, 189]. Figures A.3.c-d summarize the measurements of the parallel wavenumber at $r = 7$ cm. The high level of the spectral coherence estimated at the mode frequency confirms the quality of our measurements (Fig.A.3.c). Figure A.3.d shows the linear relation between the measured wavenumber and the corresponding vertical distance separating the tips. For the optimal vertical separation defined as $z_{opt} = R\Delta\varphi\frac{B_z}{B_\varphi}$, a linear fit gives $k_\parallel = (0.02 \pm 0.09)$ m^{-1}, which corresponds to a flute mode within experimental errors. We conclude that the coherent fluctuations observed at 7.5 kHz correspond to an interchange mode. The theoretical prediction developed in the previous section can thus be tested in this case.

A.4 Experimental evidence of a critical pressure gradient

Starting from the plasma conditions described in App.A.3, we perform a neutral gas pressure scan between $p_n = 0.8 \times 10^{-3}$ mbar and $p_n = 2.8 \times 10^{-3}$ mbar ($P_{RF} \cong 120$ W). Figure A.5.a shows the density radial profiles taken at the position $z = 0$ cm (from HEXTIP) for various neutral pressures values. It is clearly visible that for neutral pressures lower than $p_{n,crit} = 1.8 \times 10^{-3}$ mbar the density profile depends weakly on p_n, except that it is shifted to the LFS. As soon as this neutral pressure value is exceeded, an increase in the plasma density is observed, together with a broadening of the profile. For larger neutral gas concentrations, the profile shape remains constant although the total density decreases, which might be due to a less efficient ionization process or to an increase in the plasma losses. This change occurs rather abruptly as the pressure is incremented by 5% around $p_n = 1.8 \times 10^{-3}$ mbar, as is evident in the rms of $\tilde{n}_e$ calculated in the range $\Delta f = [3.4, 8]$ kHz and normalised over the entire spectrum (Fig.A.5.b). Below $p_{n,crit}$, the frequency of the strong interchange mode decreases with the neutral pressure from 7.5 kHz to 4.8 kHz (Fig.A.5.c). This is due to a local reduction of the $E \times B$ drift velocity. At the neutral pressure $p_{n,crit}$ associated with the increase in the electron density n_e, the interchange mode abruptly disappears.
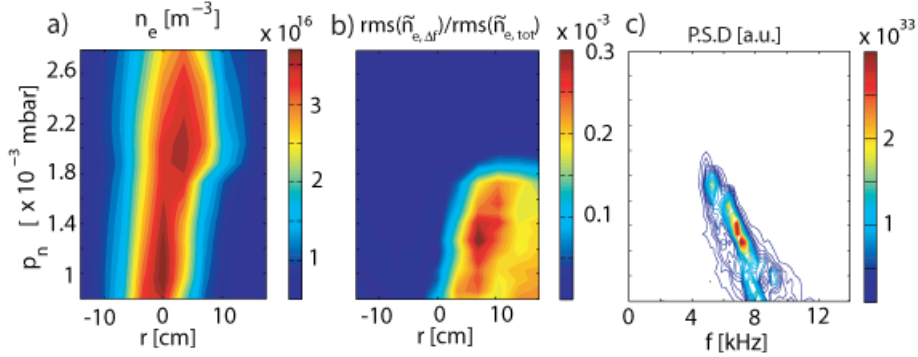
Figure A.5: Radial profiles taken at $z = 0$ cm of a) the electron density n_e b) the normalized rms of $\tilde{n}_e$ in the range $\Delta f = [3.4, 8]$ kHz for different neutral gas pressures; c) Frequency spectrum measured at $R - R_{n_{max}} = 7$ cm and $z = 0$ cm for different neutral gas pressures.

This transition is relatively robust, since it can occur at a different critical neutral gas pressure for different RF power levels and/or vertical magnetic field values, and it has also been observed in Argon plasmas. The following trend is observed: the critical neutral gas pressure increases with B_z and diminishes when the RF power is incremented as shown in Fig.A.6. For similar B_z and P_{RF}, the transition occurs at lower neutral gas pressures in Argon compared to the Neon case.

To better characterize the transition, two plasmas discharges produced with $P_{RF} \cong$ 300 W have been investigated in detail. In this case, $p_{n,crit} = 1.3 \times 10^{-3}$ mbar. The first plasma is produced using a neutral pressure just below the critical value ($p_n = 1.2 \times 10^{-3}$ mbar), the other with a pressure just above ($p_n = 1.4 \times 10^{-3}$ mbar).
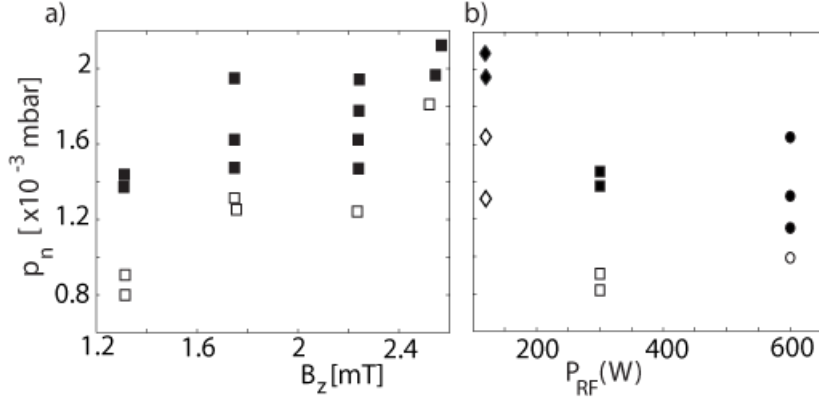
Figure A.6: Neon plasmas below (open symbols) and above (filled symbols) the transition for different neutral gas pressures as a function a) of the vertical magnetic field ($P_{rf} = 300$ W) and b) of the RF power ($B_z = 1.3$ mT). For the P_{rf} scan, the toroidal magnetic field was varied in order to keep the plasma at the center of the poloidal section: $B_\varphi = \{72 \ (\circ); \ 76 \ (\square); \ 80 \ (\diamond)\}$ mT.

The corresponding time averaged density profiles shown in Fig.A.7.a-b confirm the abrupt increase of the plasma density on the Low Field Side. As a consequence of such increment, the Upper Hybrid resonance layer is shifted by a few centimeters towards the LFS (represented by the pink dotted line in Fig.A.7.a-b) while the level of absorbed microwave power does not change significantly. We remind that in the TORPEX device most of the plasma is generated at the UH resonance layer, where the power absorption is much higher than at the EC layer, once the ionization is initiated [184]. We cannot exclude that the broadening of the density profile is due to a change in the ionization source, which may be subject for future work. The broadening of the density profile is also visible on the cut at z=0 cm shown in Fig.A.7.c. It is worth noting that the profile does not change significantly on the High Field Side. The profile broadening is associated with the reduction of the normalized density gradient L_n^{-1} in the region $6 \leq r \leq 13$ cm (Fig.A.7.d). As a consequence, the level of fluctuations is reduced by up to a factor of ten, as shown in Fig.A.7.e.

Time averaged 2D profiles of the density n_e, the electron temperature T_e and the plasma potential V_p have been reconstructed using the 8-tip movable LP array on a shot-to-shot basis. Typical values are $n_{e,max} \cong 9 \times 10^{16} m^{-3}$, $T_{e,max} \cong 6$ eV and $V_{pl,max} \cong 18$ V (Fig.A.8.a-b). Figure A.8.c presents the radial profile of the plasma pressure $p_e = n_e T_e$ taken at $z = 0$ cm. Similarly to the density profile, a strong flattening in the region $5 \leq r \leq 15$ cm is observed for the higher pressure, while the profile does not change on the HFS. We can therefore exclude any artifact due to the assumption of constant temperature for the I_{sat} measurements. In quantitative terms, the normalized pressure gradient $\left|L_p^{-1}\right|$ is reduced by a factor of four at $r = 11$ cm (from $\left|L_p^{-1}\right| = 13$ m^{-1} to $\left|L_p^{-1}\right| = 3$ m^{-1}, see Fig.A.8.d. Note that the latter value is close to the $\left|L_{p,crit}^{-1}\right|$ found in Eq. A.7. Together with the time averaged profiles, the properties of the fluctuations are strongly affected by a small increase in the neutral concentration. In particular, the coherent features of the fluctuations spectrum dis-
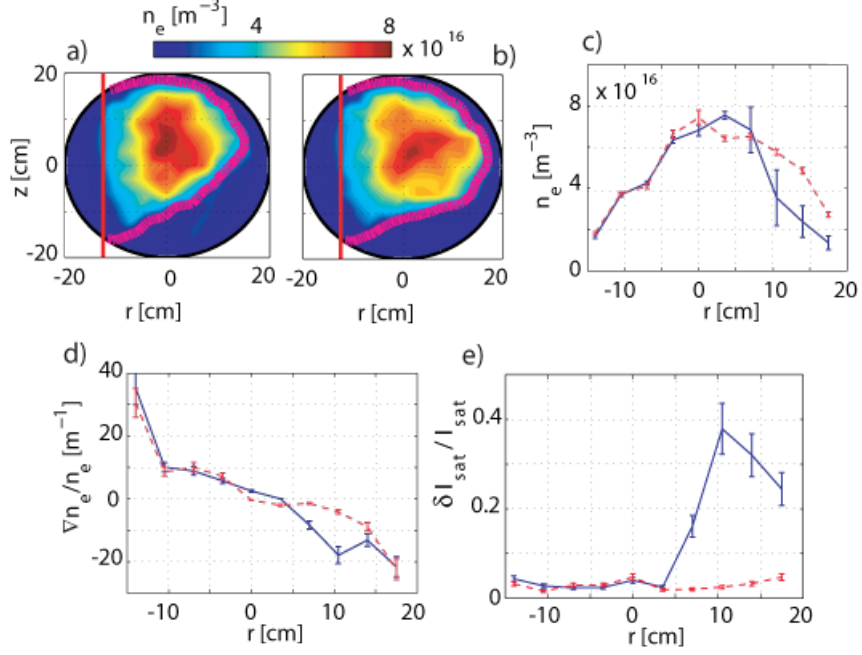
Figure A.7: 2D time averaged profile of the density measured with HEXTIP for a) $p_n = 1.2 \times 10^{-3}$ mbar and b) $p_n = 1.4 \times 10^{-3}$ mbar. The red and the pink dot lines correspond to the EC (at $R - R_o = -12.5$ cm) and UH resonance layers, respectively. Radial profiles measured at $z = 0$ cm c) of the density, d) of the normalized density gradient and e) of the ratio $\delta I_{sat}/I_{sat}$ for the low pressure (solid, blue) and for the high pressure (dashed, red) cases. The error bars correspond to the standard deviation of the time varying quantities.
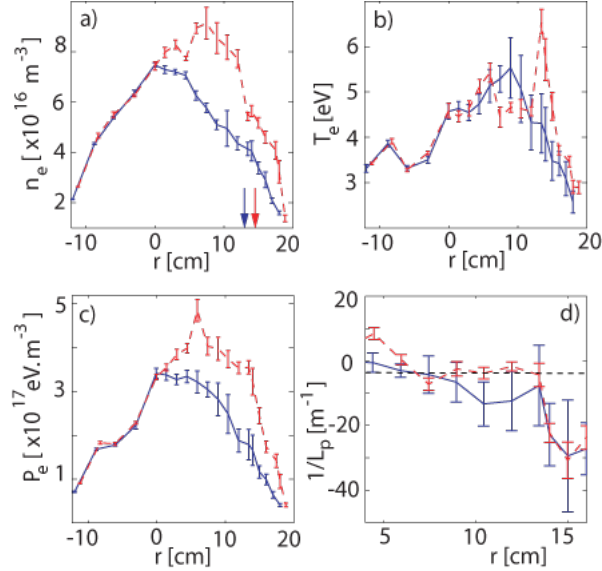
Figure A.8: Radial profile of a) the plasma density, b) the electron temperature, c) the plasma pressure p_e and d) the normalized pressure gradient $L_p^{-1} = \nabla p_e/p_e$ for $p_n = 1.2 \times 10^{-3}$ mbar (solid, blue) and $p_n = 1.4 \times 10^{-3}$ mbar (dashed, red). The black dashed line represents the critical value associated to the mode stabilization found in App.A.2 (see Eq. A.7). The error bars are given by the quality of the I-V characteristics fit. In subplot a) the arrows represent the UH resonance location for both cases.
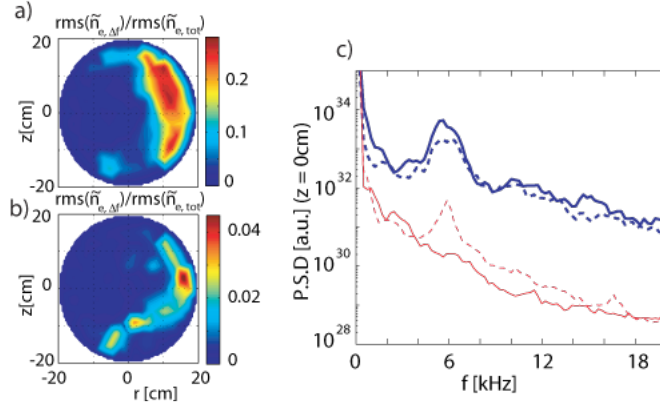
Figure A.9: 2D profile of the rms $\tilde{n}_e$ in the range $\Delta f = [3.4, 8]$ kHz normalized over the entire spectrum for a) $p_n = 1.2 \times 10^{-3}$ mbar and b) $p_n = 1.4 \times 10^{-3}$ mbar and c) Power spectral densities for I_{sat} measured at $r = 10.5$ cm (solid) and $r = 14$ cm (dashed) for the lower pressure (blue) and the higher pressure (red).

play an abrupt change. The rms of $\tilde{n}_e$ in the range $\Delta f = [3.4, 8]$ kHz normalized over the entire spectrum has been estimated for both neutral gas pressures and over the entire plasma cross section (Fig.A.9). As expected, for the higher pressure a strong reduction of the fluctuations amplitude is observed. Moreover, the spatial extent of the fluctuations, which are concentrated only at the very edge in the LFS region, is reduced. The power spectral densities estimated at $r = 10.5$ cm and $r = 14$ cm ($z = 0$ cm) reveal the interchange mode at 5.8 kHz for the lower pressure. When the critical neutral gas pressure is exceeded, the mode at r=10.5 cm is not detected anymore. A peak is still visible at $r = 14$ cm with a 6.4 ± 0.3 kHz frequency, but with an amplitude reduced by two orders of magnitude (Fig.A.9).

It is important to note that the mode detected after the transition maintains its interchange character, as verified on the basis of the dispersion relation for $k_z(\omega)$. Its phase velocity is qualitatively in good agreement with the $E \times B$ drift velocity.

A.5   Concluding remarks

In this work, we have investigated the interchange mode linear stability in Neon plasmas. The instability grows on top of profiles resulting from a non-trivial combination of several ingredients: a broadened source profile, a $E \times B$ drift velocity with both radial and vertical components, parallel losses with a more complicated pattern than in the slab-like configuration, diffusive radial transport due to the high level of neutrals and finally interchange dynamics. In this work, we did not address the role of the interchange mode as a transport mechanism to establish the plasma profiles.

We have shown that interchange modes can be stabilized in simple magnetized TORPEX plasmas. If a critical neutral gas pressure $p_{n,crit}$ is exceeded, it is possible to locally ($10 \leq r \leq 14$ cm) reduce the pressure gradient below a threshold value. Around the critical $p_{n,crit}$, depending on the RF power and on the applied magnetic fields B_z and B_φ, an increase by only $\sim 5\%$ of the neutral gas pressure is sufficient to trigger these

strong changes in the pressure profile. The observations indicate a bifurcation rather than a smooth transition, suggestive of a critical phenomenon. The experimental critical normalized pressure gradient $L_{p,crit}^{-1}$ needed to stabilize the interchange instability is in a good agreement with the linear threshold estimated in this paper.

The exact role of neutral gas pressure in the mechanism leading to this transition is not easily identifiable and will be the subject of future work. In addition, we note that a recent study on a magnetic dipole device has shown a similar effect of the neutral gas pressure on the low-frequency instabilities [190].

After the transition, the pressure gradient closer to the edge is almost unchanged and still sufficient to drive the interchange mode. Nevertheless, in this region ($r > 13$ cm), the level of fluctuations is reduced by two orders of magnitude. Among several mechanisms that could cause this reduction, the $E \times B$ velocity shear might play a significant role, as predicted by nonlinear theory and simulations [191]. Preliminary measurements show that, after the transition, the $E \times B$ velocity shear is increased by a factor of three in the narrow region where the interchange mode is still observed but saturated at much lower amplitude. This increase leads to a ratio $\frac{\gamma}{\partial v_{E \times B}/\partial r}$ smaller than unity. Recent numerical simulations [180] predict that a transition between a low confinement regime and a high confinement regime for 2D interchange-dominated simple magnetized plasmas occurs for a ratio close to 0.5. Further comparisons with nonlinear simulations are suggested for the future.

Appendix B

Estimation and measurement of the CXRS diagnostic photon transmission

B.1 Photon collection estimation, CXRS optical path and system efficiency

When building and exploiting a CXRS diagnostic it is important to identify the signal losses of the system in order to estimate its efficiency. It is then possible to identify ways of improving the signal quality and increase the final photon flux collected by the CCD. This section describes the entire CXRS optical path covered by the photons emitted from the CX reactions taking place in a TCV plasma up to the CXRS cameras, passing through the plasma, lenses, optical fibers and spectrometers. By taking into account the real instrument parameters, the various system losses have been estimated. This calculation is performed for a central observation chord of the TLFS CXRS system.

As described in Sec.3.1.3, the CXRS 2011-2013 diagnostic consists of three observational systems covering the plasma core and edge: the toroidal low field side and high field side (TLFS and THFS), and the poloidal low field side (PLFS-VER), see Fig.3.1. Each system comprises similar optical elements, shown in Fig.B.1 for the TLFS and THFS cases, that are the following:

- two beral mirrors (inside TCV, see Sec.3.2.2), the observation window (vacuum interface) and one focusing lens that collects the light emitted by the CX reactions between the carbon ions and the H^0 of the DNBI

- 40 optical fibers arranged in pairs (double slit configuration) transmitting the collected signal to the spectrometers

- a Czerny-Turner spectrometer resolving spectroscopically the observed CVI line
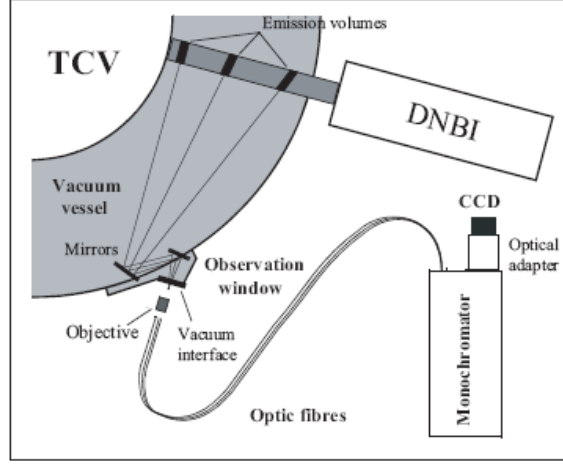
Figure B.1: Schematic of the main elements of the CXRS toroidal diagnostics.

- a reducer maximizing the image area observed by the multi-channel detection system constituted by a back illuminated e2v CCD97 detector with EM gain (Andor cameras, see Sec.3.2.1)

In the following section, the losses for each of the listed elements will be discussed in order to derive the total efficiency. In parallel, an estimation of the photons emitted during a discharge on TCV and arriving at the cameras will be derived and compared with the measured photons signal.

B.1.1 Initial emitted photons quantity in TCV: beam current, attenuation cross-sections and etendue

The photon quantity emitted during a typical Ohmic limited L-mode plasma on TCV is estimated in this paragraph. The discharge #42422, characterized by a stationary phase with $I_p = 350kA$, line averaged density from FIR $n_{e,av} = 2.3 \times 10^{19} m^{-3}$, $\kappa_a = 1.44$ and $\delta_a = 0.15$ is studied at 1.02s.

DNBI

In this shot, the DNBI (see [46, 20] for more details) injects 50.3 keV-H^0 atoms in 20 ms bursts with a total power of $P_B = 80kW$. The investigated CX reactions occur between the C^{6+} ions and neutrals H^0, which generate CVI line emission (n=8→7) at λ =529.059 nm. The photons emission for each observation volume can be determined from the beam current density distribution along the beam injection path. A beam attenuation code written for TCV DNBI [46, 67] is used to derive the line integrated beam current density along each observation chord (also named as DCD on TCV, i.e. diagnostic-chord-description) for each DNBI pulse. We have considered the central observation chord #10 corresponding to the region of interest #10 of the CCD (i.e at ρ_ψ=0.57).

The main parameters used to determine the initial photons emission are as follows:

B.1. Photon collection estimation, CXRS optical path and system efficiency

- Beam energy components and injected power: $E_{B0} = 50.3 keV$, $P_B = 80 kW$ (injection upper power limit)

- Beam ion current: $I_{DNB} = 2.85A$, of which 1.22A corresponds to the equivalent current of the full energy beam fraction $H^0(E_0)$ (neutralization efficiency: $\kappa_{E_0} = 52\%$, beam radius in the plasma: $r_B \cong 3.8cm$)

- Experimental beam composition in H^0: $[E_0, E_0/2, E_0/3, E_0/18]$=[61, 8, 26, 5]%

- Attenuation cross sections obtained for $E_{B0} = 50.3 keV$ and $T_e = 1000 eV$:

    - $\sigma_{Di} = 1.42 \times 10^{-20} m^2$: H^0 ionization by collisions with bulk ions (D or H), $E_B >> T_i$ (see Sec.2.2.1 of [192])

    - $\sigma_{ei} = 8.07 \times 10^{-21} m^2$: ionization by collisions with electrons (see Sec.2.1.5 of [193])

    - $\sigma_{cxC} = 1.83 \times 10^{-19} m^2$: CX collisions with carbon ions (source ELPRO code database, see [194])

    - $\sigma_{cxD} = 9.38 \times 10^{-21} m^2$: CX collisions with bulk ions, $E_B >> T_i$ (see Sec.2.2.1 of [192])

- Plasma parameters: $n_e = 2.78 \times 10^{19} m^{-3}$, $n_C/n_e = 0.05$, $n_D = (Z - Z_{eff})/(Z - 1)n_e \cong 0.7 n_e$ with $Z_{eff} = 2.5$ and $Z = 6$

- CX reaction: $r_{cx87} = 1.5 \times 10^{-14} m^3 s^{-1}$ excitation rate for $n = 8 \rightarrow 7$ transition of C^{6+} (at $E_{B0} = 50.3 keV$)

- CXRS-DNBI crossing points: $r_{CX,sv} = 0.38cm$ radius of the sampling volume determined experimentally from the chords alignment verification, see Sec.3.3.1, and confirmed by optics calculations (see App.B.1.1)

From the attenuation code, the beam current density integral along the DCD for the H^0 full energy component E_0 is determined: $J_{sB}^{E_0} = \int J_{nB}^{E_0} dl \approx 14.17 A/m$. Additionally, the beam current densities in the plasma $J_{plasma}^{E_0}$ and in the vacuum $J_{vac}^{E_0}$ are given by $J_{plasma}^{E_0} \approx 248.11 A/m^2$ and $J_{vac}^{E_0} \approx 270.17 A/m^2$. Note that the presented beam density currents consider only the H^0 neutrals fraction with E_0 energy, which represents only the 61% of the total beam current. The effective CXRS chords path in the beam is obtained by dividing $J_{sB}^{E_0}/J_{plasma}^{E_0} = L_{CX,sv} \approx 5.7cm$.

The beam attenuation inside the plasma is derived from the attenuation coefficient α, which is obtained from the species densities (e,D,C) and the previously listed cross-sections:

$$exp\left(-\int \alpha dl\right) = \qquad \text{(B.1)}$$

$$= exp\left(-\int (n_e\sigma_{ei} + n_D\sigma_{Di} + n_D\sigma_{cxD} + n_C\sigma_{cxC})dl\right) =$$

$$= exp\left(-\int n_e(\sigma_{ei} + 0.7\sigma_{Di} + 0.7\sigma_{cxD} + 0.05\sigma_{cxC})dl\right) \cong 0.83$$

where $\Delta l = 14cm$ is the distance covered by the beam between TCV outer vessel and the studied chord.

The maximal density of full energy beam neutrals is finally obtained:

$$n_B^{E_0} = \frac{J_{plasma}^{E_0}}{ev_0} \approx 4.97 \times 10^{14} m^{-3} \tag{B.2}$$

where $v_0 = \sqrt{2E_0[J]/m_H[kg]} \cong 3.12 \times 10^6 m/s$ is the velocity of the beam for the E_0 component.

Theoretical initial photon emission in TCV

The theoretical volumetric photon emission from the plasma is finally obtained as:

$$E_\Phi = \Phi_{0\,CXRS,t,V} = n_B^{E_0} n_C r_{cx87} = 1.04 \times 10^{19} ph\ s^{-1} m^{-3} \tag{B.3}$$

where the fully ionized carbon density is $n_C = 1.39 \times 10^{18} m^{-3}$.

Etendue

To determine the photon flux theoretically collected by a single fiber, the etendue of the sampling volume $\Omega_{sv} A_{sv}$ and of the optical fiber $\Omega_{fo} A_{fo}$ are considered. The etendue is a property of light in optical systems that characterizes how the light is "spread out" in area and solid angle. The etendue is preserved, i.e. a perfect optical system produces an image with the same etendue as the source (for more details see [195]).

To determine the etendue, the main characteristics of the optical fibers and the lens placed in front of them are required. These are listed as follows:

- air refractive index: $n_{air} = 1.00027717$

- optical fiber Numerical Aperture[1]: $NA_{fo} = 0.12$ (equivalent to a $f/\#_{fo} = 4.17$ aperture)

- optical fiber radius: $r_{fo} = 318\mu m$

- distance between sampling volume and lens core in front of the fibers: $S_1 = 1.29m$

- lens focal length: $F_{lens} = 0.1m$

Further characteristics of the lens and the optical fibers will be discussed in App.B.1.2 and App.B.1.3.

Using the thin lens equation, the distance between the lens and the optical fiber can be obtained as $d_{ol} = F_{lens} \cdot S_1/(S_1 - F_{lens}) \cong 10.8cm$. The magnification is $M =$

---

[1]The Numerical Aperture is defined as $NA = n \cdot sin(\theta)$, where n is the refractive index of the medium and θ is the half-angle of the light cone. A relation exists between NA and the $f/\#$ aperture, which is given by: $f/\# = 1/(2NA)$.

$F_{lens}/(F_{lens} - d_{ol}) = -11.9$ [2], which is equal to $M = (F_{lens} - S_1)/F_{lens}$ [195]. The sampling volume size (i.e. the radius of the light spot) becomes $r_{CX,sv} = abs(M \cdot r_{fo}) \cong 3.8mm$ (confirmed experimentally during the system alignment), which gives the area of the base of the sampling volume $A_{sv} = \pi \cdot r_{sv}^2 \cong 4.5 \times 10^{-5} m^2$.

From geometrical optics calculations with thin lenses, a relation for the magnification can be derived $|M| = NA_{input}/NA_{output} = d_{image}/d_{object}$, where d_{image} and d_{object} are the distances between the lens and the image or object respectively. Using this relation, the Numerical Aperture of the sampling volume is obtained $NA_{sv} = NA_{fo}/abs(M) = 0.01$. We may now calculate the acceptance angle θ_{sv} and the solid angle Ω_{sv} of the sampling volume:

$$\theta_{sv} = asin(NA_{sv}/n_{air}) = 0.01 rad \tag{B.4}$$

$$\Omega_{sv} = (NA_{sv}/n_{air})^2 \cdot \pi = 3.19 \times 10^{-4} sr \tag{B.5}$$

Note that Ω_{sv} is derived from $\Omega_{sv} = \pi \cdot sin^2(\theta_{sv})$, since the projected surface is required to calculate the projected solid angle (i.e. when considering a half sphere the projected solid angle is π and the total solid angle is 2π).

Finally, the etendue for the sampling volume is determined:

$$Etendue_{sv} = \Omega_{sv}A_{sv} = 1.436 \times 10^{-8} sr\ m^2 \tag{B.6}$$

By comparing the etendue of the sampling volume with the etendue of the fiber optic $Etendue_{fo} = \Omega_{fo}A_{fo} = NA_{fo}^2 \cdot \pi^2 r_{fo}^2 \cong 1.437 \times 10^{-8} sr\ m^2$, we see that they are identical. This result conforms to the preservation of the etendue.

Theoretical photon flux collected by a fiber

From the previously determined initial photon emission and the sampling volume etendue, the photon flux collected per unit time by a single fiber (emitted by the selected sampling volume) is calculated from:

$$\Phi_{0\ CXRS,t} = \frac{E_{\Phi}}{4\pi} \cdot \Omega_{sv}A_{sv} \cdot L_{CX,sv} \cong 6.77 \times 10^8 ph\ s^{-1} \tag{B.7}$$

where the photon emission per unit time and volume E_{Φ} has been divided by the total angle 4π and multiplied by the etendue $\Omega_{sv}A_{sv}$ and the sampling volume length $L_{CX,sv}$ (i.e the effective CXRS chord path in the beam). The total emission is multiplied by the solid angle ratio $\Omega_{sv}/(4\pi)$ and the considered sampling volume.

Notice, that so far, $\Phi_{0\ CXRS,t}$ has been calculated without taking into account any losses from the in-vessel mirrors, vacuum window and the lenses. These elements are discussed in more detail in App.B.1.2. The initial collected photon quantity will be reduced following passage through the CXRS optical system (see next paragraphs).

---

[2]Note that for real images M<0, and the image is inverted.

B.1.2 Optical elements in TCV and at the observation window

Two beral mirrors are placed inside the vessel in order to reflect the collected light outside the observation window, which is focused by the lens placed in front of the fibers. The main characteristics for the quartz window (hublot) and mirrors are $\phi_{hu} = 60mm$ (diameter) and $e_{hu} = 10mm$ (thickness) with a reflectance coefficient of $R_{hu} = 3\%$ and $R_{mir\,Beral} = 91\%$ at each surface. The lens, partly discussed in App.B.1.1, is characterized by $\phi_{lens} = 48mm$ (diameter), $e_{lens} = 8.5mm$ (thickness) and $F_{lens} = 100mm$ and has a reflectance coefficient of $R_{lens} = 2.5\%$ at each surface. Since the calculation is performed for a central line of sight, there is no vignetting, i.e all the incoming light is collected by the lens, for these four elements.

The transmission coefficient of the photons to the fiber entrance is thus given by:

$$\epsilon_{mir-hu-lens} = R_{mir\,Beral}^2 \cdot (1 - R_{hu})^2 \cdot (1 - R_{lens})^2 \cong 74\% \qquad (B.8)$$

The photons collected by a single fiber per unit time $\Phi_{0\,CXRS,t}$, calculated in App.B.1.1 by neglecting in-vessel optical losses, should be corrected with this transmission coefficient.

B.1.3 Optical fibers

The 40 optical fibers are placed at the lens focal point in order to collect the maximum photons number. As already discussed in App.B.1.1, the fibers have a diameter of $\phi_{fo} = 636\mu m$ and a Numerical Aperture of $NA_{fo} = 0.12$. They are $L = 20m$ long with an attenuation of 10 dB/km causing a loss of $R_{fo_{att}} = 4.5\%$. At the fiber entrance and exit, a photons reflectance of $R_{fo_{in/out}} = 4\%$ should be taken into account.

The transmission coefficient in the fibers is therefore given by:

$$\epsilon_{fo} = (1 - R_{fo_{in/out}})^2 \cdot (1 - R_{fo_{att}}) \cong 88\% \qquad (B.9)$$

B.1.4 Entrance slit and spectrometer

Directly in front of the fibers a slit is placed with an $ES_w = 0.22mm$ width and $ES_h = 14mm$ height. The fibers bundle is then placed at the entrance of the monochromator. The Czerny-Turner spectrometer SPEX750Mi has a $f/\#_{spex} = 7.5$ aperture at first order (i.e $NA_{spex} = 0.0667$) and 0.75m focal length. It is composed of two square mirrors and a holographic 2400 l/mm grating of $\phi_{mir\,1} = 90mm$, $\phi_{mir\,2} = 102mm$ and $\phi_{grat} = 96mm$ sides. The reflectance coefficients for these elements are respectively: $R_{mir\,spex} = 90\%$ and $R_{grat} = 60\%$ (in first order). The main components described in this section are illustrated in Fig.B.2.

Two main losses have to be considered at the entrance slit (see [35], Appendix III). The first loss takes into account the apertures of the fibers and spectrometer, the latter being bigger and therefore limiting the light collected by the fibers. The photons
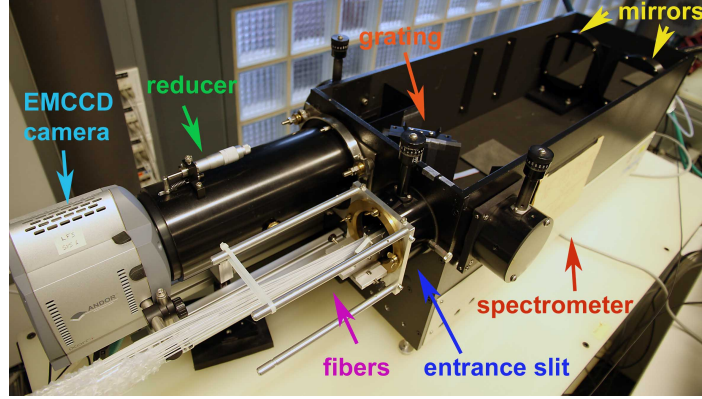
B.1. Photon collection estimation, CXRS optical path and system efficiency

Figure B.2: Main optical components of the CXRS LFS system.

number is reduced by:

$$\eta_1 = \left(\frac{1}{f^2/\#_{fo}} - \frac{1}{f^2/\#_{spex}} \right) \cdot f^2/\#_{fo} = \left(NA_{fo}^2 - NA_{spex}^2 \right)/NA_{fo}^2 \cong 69\% \quad \text{(B.10)}$$

Another method to deduce and interpret the above calculated η_1 loss comes from directly comparing the reduced dimension of the spectrometer first mirror with respect to the fiber aperture. The cone of light from the fibers exceeds the mirror surface area, therefore the collected light is only that included in a pyramid volume having the mirror surface as a basis. The cone radius $R_{cone\,fo}$ can be obtained by determining the fiber aperture angle θ_{fo}:

$$NA_{fo} = sin\theta_{fo} \ \Rightarrow \ \theta_{fo} \cong 0.12 rad \quad \text{(B.11)}$$

$$R_{cone\,fo} = \frac{f/\#_{spex}}{10} \cdot tan\theta_{fo} \cong 9.07 \times 10^{-2} m \quad \text{(B.12)}$$

The cone and the pyramid volumes are obtained as:

$$V_{cone\,fo} = \frac{R_{cone\,fo}^2 \cdot f/\#_{spex} \cdot \pi}{3 \cdot 10} \cong 6.5 \times 10^{-3} m^3 \quad \text{(B.13)}$$

$$V_{mir\,fo} = \frac{\phi_{mir\,1}^2 \cdot f/\#_{spex}}{3. \cdot 10} \cong 2 \times 10^{-3} m^3 \quad \text{(B.14)}$$

Supposing an homogeneous photons distribution (see App.B.1.9), the fraction of collected photons on the first mirror is:

$$\epsilon_{spex\,mir} = V_{mir\,fo}/V_{cone\,fo} \cong 31\% \quad \text{(B.15)}$$

We clearly see that the fraction $\epsilon_{spex\,mir}$ well corresponds to the $(1 - \eta_1)$ obtained previously and that the $f/\#$ of a spectrometer is defined by the size if its first mirror. To partially reduce the light cone volume (and the consequent loss), when purchasing the new fibers, the model with the smallest numerical aperture NA_{fo} available was chosen.

The second loss is due to the entrance slit width being smaller than the fiber diameter. Therefore the illuminated area $S_{ES} = ES_w \cdot \phi_{fo}$ is smaller compared to the fiber surface $S_{fo} = \frac{\phi_{fo}^2}{4}\pi$ and the loss is given by the surfaces difference:

$$\eta_2 = \frac{(S_{fo} - S_{ES})}{S_{fo}} \cong 56\% \tag{B.16}$$

A third loss of a 2-5% should also be considered when the optical fiber and the entrance slit are separated by a small distance ($d_{os} = 0.1 - 0.2mm$). Since, on the CXRS diagnostic, the fibers are directly attached and fixed to the slit and that no fiber separation has been observed during any recent manipulation, this third loss can be ignored in this calculation.

Therefore, the total fraction of photons entering the spectrometer is only:

$$\epsilon_{ES} = (1 - \eta_1) \cdot (1 - \eta_2) \cong 14\% \tag{B.17}$$

The effective entrance and exit apertures of the spectrometer are determined by considering the effective grating surface seen by the two mirrors, which is different due to the grating inclination. Using $\alpha = 47°$ and $\beta = 33°$ as the incident and diffraction angles on the grating surface (obtained from spectrometer measurements), it is possible to first derive the surface overlap between the projected area of the first mirror on the grating surface, and then successively compare the determined "overlap surface" to the projected area of the second mirror. In this way, the effective illuminated surface inside the spectrometer is determined, which finally gives the transmitted photon efficiency from the entrance to the exit of the spectrometer.

The calculation is performed for only one fourth of each element surface (mirrors and grating), supposing that the central origin of the grating corresponds to the central origin of both mirrors (placed at the same height and same central axis). This assumption is valid for symmetrical optical objects (rectangles or circles), since each total surface is obtained by simply multiplying x4 the selected surface, but the final surface ratio will remain the same. The projected width and height of the first mirror on the grating are therefore obtained as:

$$x_{pr1} = \frac{\phi_{mir\,1}}{2cos(\alpha)} \cong 6.6cm \qquad\qquad y_{pr1} = \frac{\phi_{mir\,1}}{2} \cong 4.5cm \tag{B.18}$$

These dimensions are compared with the grating sides:

$$x_g = \frac{\phi_{grat}}{2} \cong 4.8cm \qquad\qquad y_g = \frac{\phi_{grat}}{2} \cong 4.8cm \tag{B.19}$$

to derive the overlap area, which is calculated by taking the smallest values in x and y. From the initial projected area $A_{input} = x_{pr1} \cdot y_{pr1} \cong 30cm^2$ we obtain an overlap area of $A_{overl1} = x_{overl1} \cdot y_{overl1} = x_g \cdot y_{pr1} \cong 22cm^2$ between the first mirror and the grating. A clear reduction between the two illuminated surfaces is already observed:

$$\epsilon_{m1g} = \frac{A_{overl1}}{A_{input}} \cong 73\% \tag{B.20}$$

The projected width and height of the second mirror on the grating are also calculated:

$$x_{pr2} = \frac{\phi_{mir\,2}}{2cos(\beta)} \cong 6.1cm \qquad\qquad y_{pr2} = \frac{\phi_{mir\,2}}{2} \cong 5.1cm \qquad (B.21)$$

These dimensions are again compared with the overlap surface sides x_{overl1} and y_{overl1} and the final overlap area of $A_{overl2} = x_{overl2} \cdot y_{overl2} = x_g \cdot y_{pr1} \cong 22cm^2$ between the grating and the second mirror is obtained. $A_{overl1} = A_{overl2}$, which indicates that no losses are observed between these two last elements ($\epsilon_{m2g} = 100\%$).

The final transmission inside the spectrometer is therefore given by:

$$\epsilon_{grat} = \epsilon_{m1g} \cdot \epsilon_{m2g} \cong 73\% \qquad (B.22)$$

As a complementary study, we have tried to deduce the effective entrance $f/\#_{spex\,in}$ and exit $f/\#_{spex\,out}$ apertures of the spectrometer. To determine the $f/\#$ of a spectrometer with a rectangular grating, it is first necessary to calculate an "equivalent diameter", D_{in}, as seen from the entrance slit and D_{out}, as seen from the exit slit. This is achieved by equating the projected area of the grating to that of a circular disc and then calculating the diameter D_{in} or D_{out} (see [196] and [35], Appendix I). This calculation supposes a perfect overlap between the various element surfaces and that the $f/\#$ is actually defined by a cone of light with $2\theta_{spex}$ as acceptance angle. The projected area of the grating from the entrance slit and the projected area of the grating from the exit slit are given by:

$$A_{in} = \phi_{grat} \cdot \phi_{grat} cos\alpha \qquad\qquad A_{out} = \phi_{grat} \cdot \phi_{grat} cos\beta \qquad (B.23)$$

From these relations the "equivalent diameters" D_{in} and D_{out} are deduced:

$$D_{in} = 2\sqrt{\frac{\phi_{grat}^2 cos\alpha}{\pi}} \cong 8.9cm \qquad (B.24)$$

$$D_{out} = 2\sqrt{\frac{\phi_{grat}^2 cos\beta}{\pi}} \cong 9.9cm \qquad (B.25)$$

The entrance $f/\#_{spex\,in}$ and exit $f/\#_{spex\,out}$ apertures can finally be obtained:

$$f/\#_{spex\,in} = \frac{r_{spex}}{D_{in}} \cong 7.56 \qquad (B.26)$$

$$f/\#_{spex\,out} = \frac{r_{spex}}{D_{out}} \cong 8.38 \qquad (B.27)$$

where $r_{spex} = f/\#_{spex}/10$ is the spectrometer focal length in meters.

Note that the effective apertures of the spectrometer are larger than the theoretical value ($f/\#_{spex} = 7.5$).

Finally, the transmitted photons at the exit of the spectrometer is therefore:

$$\epsilon_{ES+spex} = (1 - \eta_1) \cdot (1 - \eta_2) \cdot R_{mir\,spex} \cdot \epsilon_{grat} \cdot R_{grat} \cdot R_{mir\,spex} \cong 4.8\% \qquad (B.28)$$

B.1.5 Reducer and CXRS camera

To increase the size of the image observed by the CCD, a set of four lenses is placed at the spectrometer exit in front of the camera. The reflectivities of these lenses are $R_{lens\,red\,1} = 0.3\%$ (first three) and $R_{lens\,red\,2} = 1.3\%$ (for the final one).
The transmission of the reducer is given by:

$$\epsilon_{reducer} = (1 - R_{lens\,red\,1})^6 \cdot (1 - R_{lens\,red\,2})^2 = 95.7\% \tag{B.29}$$

The camera has a quantum efficiency of $Q_{eff} = 98\%$ and a CCD sensitivity of $PA_{e,counts} = 22.5 e^- per\ A/D\ cnt$ for a 5 MHz readout at 14 bit with a PreAmplifier gain of $\times 2.4$ and EM amplifier.

B.1.6 TLFS system total efficiency and final theoretical photon collected quantity

Taking into account all transmission and loss coefficients, the total efficiency ϵ_{tot} of the CXRS system can be measured by multiplying the main optical elements efficiencies $\epsilon_{mir-hu-lens}$, ϵ_{fo} and $\epsilon_{reducer}$ with the one at the spectrometer entrance and interior $\epsilon_{ES+spex}$:

$$\epsilon_{tot\,TLFS} = \epsilon_{mir-hu-lens} \cdot \epsilon_{fo} \cdot \epsilon_{ES+spex} \cdot \epsilon_{reducer} \cong 3\% \tag{B.30}$$

The estimated photons collected by the CCD for the channel/fiber N.10 per unit time are therefore:

$$\Phi_{CCD,t} = \Phi_{0\,CXRS,t} \cdot \epsilon_{tot} \cong 2.03 \times 10^7 ph\ s^{-1} \tag{B.31}$$

which in a typical $dt = 20ms$ CXRS acquisition time gives:

$$\Phi_{CCD} = \Phi_{CCD,t} \cdot dt \cong 4.06 \times 10^5 ph \tag{B.32}$$

as the number of collected photons by the considered central fiber.
By multiplying with the quantum efficiency Q_{eff}, the corresponding photoelectron count generated in the region of interest of the CCD are $3.98 \times 10^5 e^-$. A final division by the CCD sensitivity $PA_{e,counts}$ gives the number of measured counts per time interval ($\sim 17685 cnts$).

B.1.7 THFS and PLFS-VER systems efficiencies

The optical system of the THFS is almost the same as the TLFS apart for the spectrometer. The spectrometer is a Czerny-Turner spectrometer ACTON AM-506 with a $f/\#_{spex} = 5.5$ aperture at first order and a 0.66m focal length, comprising two rectangular mirrors and a grating of $h_{mir\,1,2} = 118mm$, $L_{mir\,1,2} = 138mm$ and $h_{grat} = 120mm$, $L_{grat} = 140mm$ sides. The measured incident and diffraction angles

are $\alpha = 48.4°$ and $\beta = 28.4°$. The reflectance coefficients for these elements are respectively: $R_{mir\,spex} = 90\%$ and $R_{grat} = 70\%$.

The PLFS system uses the same spectrometer as the TLFS but with different mirrors and grating shapes and sizes: $\phi_{mir\,1} = 90mm$ (circle), $\phi_{mir\,2} = 102mm$ (square) and $\phi_{grat} = 110mm$. The measured incident and diffraction angles are the same as the TLFS system. In addition, no mirrors are installed inside the TCV vessel, but one mirror with an Alu layer is placed just outside the observation window to direct the plasma light towards the focussing lens ($R_{mir\,Alu} = 90\%$).

The total efficiency obtained for both cases results to be:

$$\epsilon_{tot\,PLFS} = \epsilon_{mir-hu-lens} \cdot \epsilon_{fo} \cdot \epsilon_{ES+spex} \cdot \epsilon_{reducer} = \cong 67\% \cdot 88\% \cdot 6\% \cdot 95.7\% \cong 3.3\%$$

$$\epsilon_{tot\,THFS} = \epsilon_{mir-hu-lens} \cdot \epsilon_{fo} \cdot \epsilon_{ES+spex} \cdot \epsilon_{reducer} \cong 74\% \cdot 88\% \cdot 9\% \cdot 95.7\% \cong 6\%$$

The efficiency of the PLFS system is a little higher than the TLFS system, mainly due to a slightly higher transmission inside the spectrometer. Taking into account the optical elements parameters, the THFS system should have a better efficiency than the TLFS from its larger mirror surfaces. However, an incorrect curvature radius of the first mirror and a coma effect do not optimally focus the image, which imposed the use of a mask placed in front of the second mirror to improve the data quality (see Sec.3.2.3). Hence this surface mask should be included in the calculation of the transmission inside the spectrometer.

B.1.8 Measured photons by CCD cameras and comparison with the theoretical value

To compare with the real efficiency of the system, the flux of measured photons for the same discharge has been calculated. From the counts measured by the CCD cameras and the quantum efficiency and the camera set up parameters (EMCCD gain and PreAmplifier gain), it is possible to deduce the number of acquired photons. By subtracting the passive signal before and after the beam pulse from the spectra acquired during the beam, the active signal is deduced for the specific discharge (for more details see Sec.3.4). The total number of photons detected by the CCD camera in a $dt = 20ms$ pulse is therefore $\Phi_{CCD,exp} \cong 9.29 \times 10^4 ph$. After dividing this value by the CXRS acquisition time, the total number of photons per unit time is obtained:

$$\Phi_{CCD,exp,t} = \frac{\Phi_{CCD,exp}}{dt} \cong 4.65 \times 10^6 ph\,s^{-1} \tag{B.33}$$

Using the sampling volume of the selected fiber $V_{CX,sv} = \pi \cdot r_{CX,sv}^2 \cdot L_{CX,sv} \cong 2.6 \times 10^{-6} m^{-3}$ and multiplying by $4\pi/\Omega_{sv}$, the volumetric photon emission detected from the plasma is derived:

$$\Phi_{CCD,exp,t,V} = \Phi_{CCD,exp,t}/V_{CX,sv} \cong 7.05 \times 10^{16} ph\,s^{-1} m^{-3} \tag{B.34}$$

When, dividing this value with the total efficiency $\epsilon_{tot\,TLFS}$ calculated previously, we recover an experimental initial photon emission $\Phi_{CCD,exp,t,V} \cong 2.35 \times 10^{18} ph\,s^{-1} m^{-3}$.

The comparison between the measured collected photons per unit time $\Phi_{CCD,exp,t}$ and the theoretically estimated collected photons per unit time $\Phi_{CCD,t}$, shows a system efficiency of 0.7% instead of the estimated 3%. The measured value is considerably lower than that estimated (x4.3 lower).

The same theoretical and experimental calculation was repeated for the central fiber #30 of the second slit and again similar results obtained (i.e. an experimental system efficiency of 0.65%). Even more external fibers show this discrepancy.

This reduced measured quantity supposes the presence of some additional losses that are not taken into account in the calculation (inside TCV or in the optical elements), some uncertainties in the determination of the initial photons emission with the beam attenuation code, the choice of some incorrect assumptions or maybe even some incoherences with the real instruments characteristics. A brief discussion about some assumptions considered in this calculation and some possible "source of errors" is given in the next section.

B.1.9 Discussion about the main losses, the considered approximations and ideas to improve the system efficiency

As noted in the previous sections, the comparison between the measured and estimated collected photons shows a clear x4 loss, indicating a reduced effective system efficiency compared to that expected.

We recall that, in these calculations, we have not considered any photons diffusion outside the corresponding sampling volumes due to dust on the optical elements, neither wear of the various elements nor bubbles in the lens, which may all influence the photon collection.

In addition, the fibers are supposed to have approximatively the same losses, but the external fibers tend to have larger losses, due to a shift in the position of the cone of collected light created at the spectrometer entrance, which is larger than the diameter of the first spectrometer mirror. Furthermore, the photon intensity at the fiber exit has a Gaussian distribution (higher density in the core), whereas for simplicity in this calculation a homogeneous distribution was used. This approximation results in an important uncertainty in the calculation. Indeed, for a Gaussian distribution we may suppose that the photons emission is contained within a light cone with a basis diameter shaped like a $\pm 3\sigma$ interval (σ is the standard deviation) containing almost the 99% of all photons. From the first mirror size and the $f/\#_{spex}$ aperture, the covered interval results to be about $[1, 1.5]\sigma$, which implies that between 68%-86% of the total photons amount may actually be collected by the first mirror. This is clearly much higher than when considering an homogeneous distribution like supposed in this calculation (31%, TLFS case). Therefore, the loss fractions due to the first mirror size η_1 and $1 - \epsilon_{m1g}$ may be even lower than what calculated previously. In order to have a more precise measure, the knowledge of the photons Gaussian distribution width σ, obtained experimentally, is required.

The beam attenuation code should also be carefully revisited in particular the deter-

mination of the effective beam width and divergence and the various cross-sections, which eventually define the sampling volume length and the final beam current attenuation.

An annoying optical effect, that may influence also the determination of the sampling volume for the external chords, can be seen in Fig.3.10.a. The more external light spots at both edges are larger and have an elliptical shape instead of a circular shape. This aberration is due to the errors of the lens shape that impairs the focus light illuminating the edge of the lens. A solution may consist in installing a larger lens or two distinct lenses, but the restricted space near the observation window will make this problematic. This effect is not critical for the impurity profiles determination and the calculated errorbars increase by just 2-3%.

The main estimated losses are observed at the entrance slit, where almost 86% of the total photons are lost. To reduce this, a spectrometer with larger mirrors should be used (i.e. with smaller $f/\#_{spex}$ aperture) to provide a larger surface collecting the incoming light. From the above calculation, together with a larger first mirror a sufficiently larger grating would also be required. Other solutions may imply an enlargement of the illuminated slit surface or the purchase of new fibers with smaller NA.

Despite the discrepancy between prediction and experiment, the total efficiency of the CXRS diagnostic is very low and ranges between 0.7-3.3% (TLFS and PLFS). This value is still sufficient to obtain enough signal to measure the rotation, temperature and density profiles in many TCV plasmas scenarios, but requires the use of high sensitivity and time resolving cameras. The purchase of two EMCCD cameras allowed an increase in the exploitation of the CXRS diagnostic by better converting the final photons signal to electrons and by measuring faster events when collecting fewer photons. As the low intensity of the beam limits the initial photon flux and cannot be modified, it is preferable to find some other techniques permitting to reduce the losses incurred along the optical path.

To verify that the main losses are at the entrance slit of the spectrometer and to determine any further loss of the CXRS system, an experimental verification/calibration is strongly suggested. Some ideas were proposed during this work but were not performed because of intense TCV operation, high CXRS diagnostic presence requested, missing equipment, etc. and a lack of time. One proposed idea is to place a calibrated integrating sphere (see Sec.3.3.2) or a green laser (with a λ near the investigated line) inside TCV, then in front of each fiber and successively at the entrance slit. By using a sensitive photodiode, usually used for the Thomson diagnostic, it would be thus possible to verify the mirror and the lens efficiency and track the collected/emitted light at the entrance/exit of the fiber and at the entrance/exit of the spectrometer. The optical path from the mirrors, through the fibers and to the cameras may thus be experimentally checked step by step. To obtain a more exact estimation of the real photon flux emitted inside TCV, it is required to recheck the beam penetration and divergence inside the plasma and the various considered cross-sections. Despite the several repetitions of the above calculations, the presence of an algebraic error may also partly or completely explain this discrepancy.

The TCV upgrade opening planned for 2014 may finally allow the execution of a complete measurement of the photons transmission through the various optical elements of the CXRS and explain the observed discrepancy.

Appendix C

Complements to Chap.4: toroidal rotation and momentum transport studies related to sawteeth events

C.1 Toroidal rotation averaged over several sawtooth periods in limited L-mode plasmas

C.1.1 B_φ/I_p modification in Ohmic plasmas

Starting from a scenario similar to discharge #41386 studied in Sec.4.2.1, three discharges with different values of B_φ and I_p were performed, with the same B_φ/I_p ratio to maintain the $q = 1$ surface position. The toroidal rotation and electron pressure profiles for the B_φ/I_p values -1.44T/-342kA (#48959), -1.19T/-282kA (#48954) and -1.11T/-263kA (#48956) are plotted in Fig.C.1.a. For all cases, the toroidal rotation profile is co-current directed in the core ($v_\varphi \cong 1 - 4km/s$), and cnt-current for $\rho_\psi > 0.5$. The main ∇v_φ is slightly modified for discharges #48954 and #48956, but agree within the measurement error bars with discharge #48959. The inner local gradient at $\rho_\psi = 0.5$ is highly similar for all three cases. As expected, similarly to the high plasmas current cases, the carbon density profiles shown in Fig.C.1.b are flat. The $T_i(0)$ values for these discharges vary between 240-380eV. This example shows that when the B_φ/I_p ratio (and therefore also $q = 1$) is kept constant, the toroidal rotation profile is not affected, although I_p is modified.

C.1.2 Effect of ECH and co-CD applied near the q=1 surface

To highlight the similarity between the rotation profiles in Ohmic and EC heated plasmas for high I_p values, discharge #40269 (B_φ/I_p = -1.18T/+288kA) is plotted in Fig.C.2, together with the entire I_p scan presented in Sec.4.2.1.
Clearly, the v_φ profile for the discharge with ECH + co-ECCD near q=1 (in black) lies between the OH discharges with comparable plasma currents (-279kA in grey and -301kA in green). The local $\nabla v_\varphi < 0$ feature inside $\rho_{q=1}$ is always present and appears
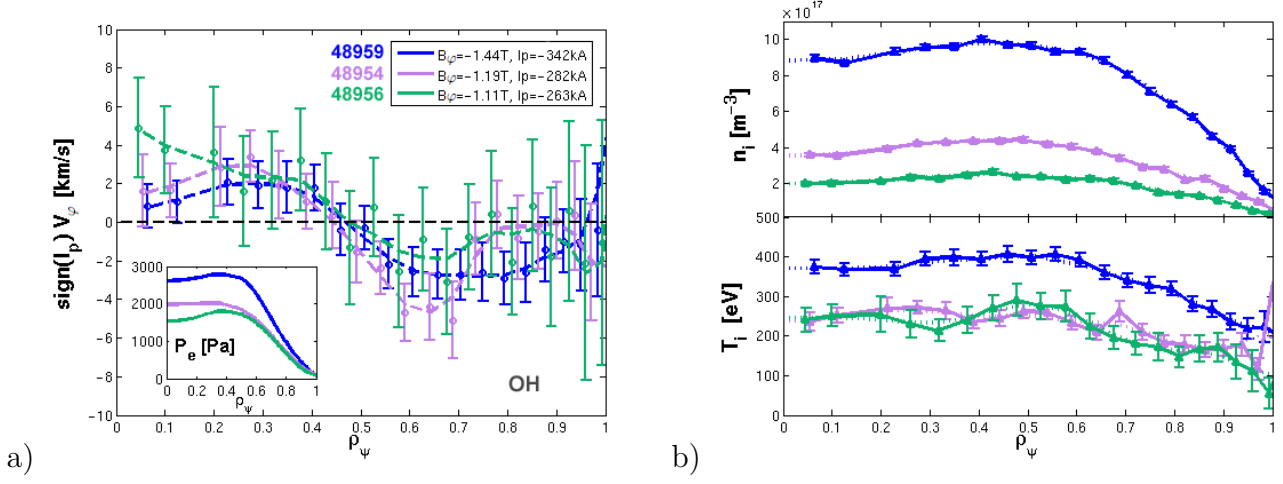
Figure C.1: a) Carbon toroidal rotation ($sign(I_p)v_\varphi$) and electron pressure, b) carbon density and temperature profiles in limited OH plasmas for three different B_φ/I_p pairs: -1.44T/-342kA (#48959), -1.19T/-282kA (#48954) and -1.11T/-263kA (#48956). Since the B_φ/I_p ratio is not modified, the position of the $q = 1$ surface remains constant.
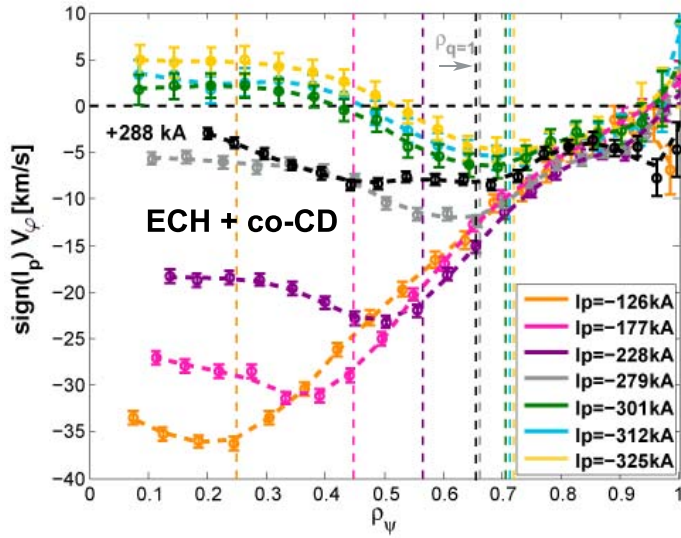
Figure C.2: Carbon toroidal rotation profiles for Ohmic and an ECH heated plasma with co-ECCD deposition near q=1. The plotted discharges are #40117/-126kA, #40118/-177kA, #40119/-228kA, #40130/-279kA, #41385/-301kA, #41388/-312kA, #41386/-325kA (Ohmic) and #40269/+288kA (EC heated, in black). Notice that the magnetic field used for the Ohmic shots was $B_\varphi = -1.44T$ and for the ECH discharge $B_\varphi = -1.18T$.

slightly larger for the ECH case. The small rotation difference of discharge #40269 is ascribed to a small variation in the B_φ/I_p ratio, the larger core plasma density and possible changes in the edge boundary conditions.

C.2 Toroidal rotation and momentum transport studies in between successive sawtooth crashes

C.2.1 E_r calculation during a ST cycle

From the impurity temperature, density and toroidal rotation profiles obtained with the fast acquisition configuration, the radial electric field between ST crashes in the same discharge employing the "standard" force balance equation (see Sec.5.2.1) can be estimated.

The poloidal rotation v_p (determined in Fig.C.3, noted as v_θ [1]), the toroidal and poloidal magnetic fields (B_t and B_p) were averaged on a 100ms time interval. This choice for v_p was made since, during the stationary phase, the profiles averaged on a few sawtooth periods at different times remain quite constant (see Fig.C.3) and the measurements with the fast acquisition are sparse. The poloidal rotation does not change significantly during the stationary phase, remaining around -2 km/s (directed counter clockwise) inside $\rho_\psi = 0.8$ and varying more strongly in the LCFS region (largely due to CXRS measurement uncertainties). The poloidal rotation is considerably smaller than the toroidal rotation, as it is strongly damped by magnetic pumping and friction with trapped particles, as predicted by neoclassical transport predictions and confirmed in previous works on TCV [20, 51].
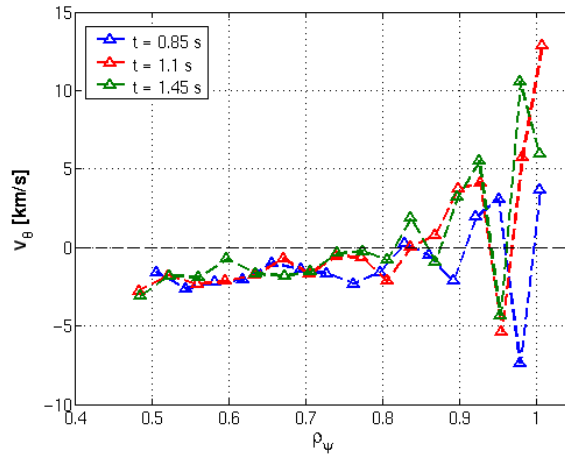
Figure C.3: Poloidal rotation v_θ measured at the CXRS central acquisition time 0.85s, 1.1s and 1.45s for shot #40271 ($v_\theta < 0$ is in the counter clockwise direction).

Note that a fast DNBI-CXRS poloidal rotation measurement with the present system

---

[1]Note that the coordinates θ, or simply p, indicate the poloidal direction (positive when directed clockwise).

is not feasible, because of the small poloidal rotation and the high statistical quality required to resolve such small values. A constant value is assumed for the toroidal and poloidal magnetic fields that only slightly vary on the timescale of 50-100ms. Clearly, an accurate reconstruction of the magnetic field just before and just after a crash (not available on TCV for such elevated time resolutions) would be necessary to confirm this assumption across the whole sawtooth cycle.

The radial electric profile measured at 1, 5 and 11ms after the ST crash (same time intervals as Fig.4.17 and Fig.4.18) via the impurity profiles is illustrated in Fig.C.4.a. The radial electric field shows a fast change in the plasma core inside the sawtooth
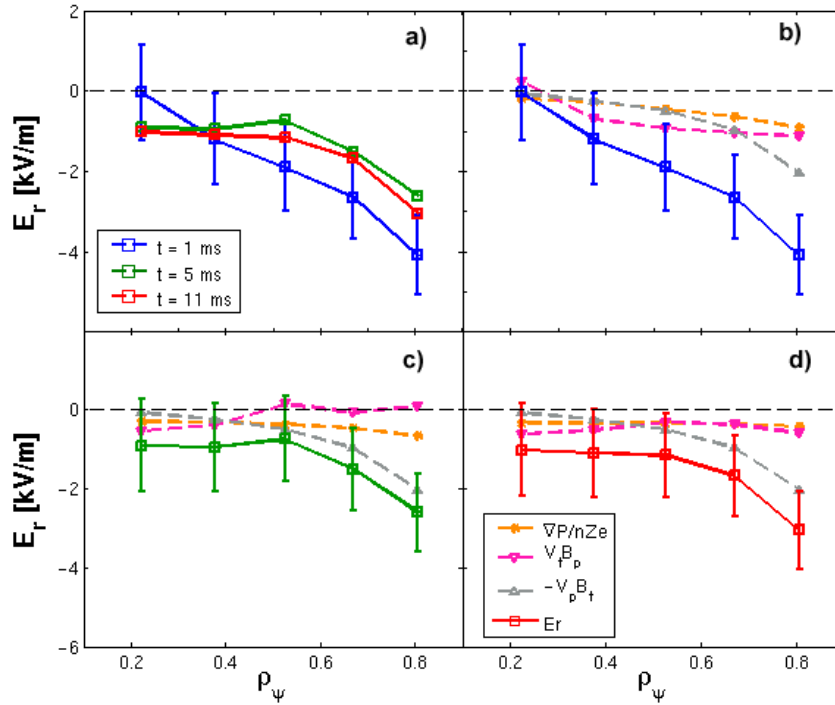
Figure C.4: a) Radial electric field measured at 1, 5 and 11ms after the ST crash for shot #40271. The error bars are plotted for $t_{ca} = 1ms$. The various E_r contributions are also shown in b), c) and d) for each time.

inversion radius. Before the crash, E_r is in the inward direction ($E_r < 0$) and then immediately after the crash evolves towards an outward direction ($E_r \geq 0$). The profile then relaxes towards a constant inward central value of $E_r = -1kV/m$. The contributions to E_r are plotted in Fig.C.4.b-d. The term that most strongly determines the E_r profile in the core is $v_\varphi B_p$ (in magenta). At $t_{ca} = 1ms$, just after the ST crash, this term is positive in the core (since v_φ is in the co-Ip direction) and negative outside ρ_{inv}, whereas at $t_{ca} = 5ms$, it is negative in the core (since v_φ relaxes to a cnt-Ip direction) and positive outside ρ_{inv}. The diamagnetic term $\nabla p_i/n_i Ze$ (in orange) is small in the core at $t_{ca} = 1ms$ and only slightly larger outside $\rho_\psi > 0.5$. As explained above, the $v_p B_t$ term (in grey) is assumed constant over the whole time interval and vanishes at

$\rho_\psi = 0$ (since $v_p(0) = 0$). This example illustrates that, after a ST crash, the acceleration in the toroidal direction is accompanied by a modification, (even reversal), of the radial electric field. This implies a reduction, or reversal, of the $E \times B$ drift velocity that is directed downward for the impurity ions just before the crash (with an inward $E_r < 0$).

Appendix D

Additional discussions for the investigated central barriers and co-CD off-axis eITBs

D.1 Comparison between direct measured v_φ, v_{pol} and indirect calculated u_φ, u_{pol} rotations: validation of the indirect method

To validate the indirect method used to determine the poloidal rotation (see Sec.5.2.2), a comparison between the measured v_φ,v_{pol} and calculated u_φ,u_{pol} rotation profiles was performed[1]. Fig.D.1.a shows the $\hat{\omega}_\sigma$ and $\hat{u}_\sigma$ profiles taken for the highest (in blue) and lowest (in red) power phase of the central barrier #47287 (repetition of discharge #45371, discussed in Sec.5.4.2 and 5.5.2). As will be discussed in Sec.5.7.1, a carbon density asymmetry is observed between the LFS and HFS CXRS profiles for both scenarios (generally stronger for the off-axis eITB). Therefore, these calculations are performed, accounting for this density asymmetry. From Eq.5.9 and Eq.5.12, we assume $K(\Psi)$ to be a flux function and not directly the $\hat{u}_\sigma$ term. The superposition of the LFS and HFS $\hat{u}_\sigma$ and $\hat{\omega}_\sigma$ profiles (within the errorbars) shows that the carbon density asymmetry is not significant for this discharge that features a central barrier (both terms may be simply considered as two flux functions). In the central plasma region, an incorrect determination of R_L and R_H position can lead to larger errors, since the denominator $n_L R_L^2 - n_H R_H^2$ (or $R_L^2 - R_H^2$ for a symmetric density) can approach zero.

The poloidal and toroidal rotation profiles for both LFS and HFS are also plotted for the same time intervals in Fig.D.1.b. As expected, the measured v_φ and calculated u_φ superpose well. The poloidal rotation v_{pol} and u_{pol} remain within the error bars that supports the use of the indirect method. The error bars of the poloidal rotation from the indirect calculation are considerably smaller than those from the direct mea-

---

[1]In order to better distinguish the measured and indirect rotation profiles in this section, v denotes the measured profiles and u the calculated profiles using the indirect method.
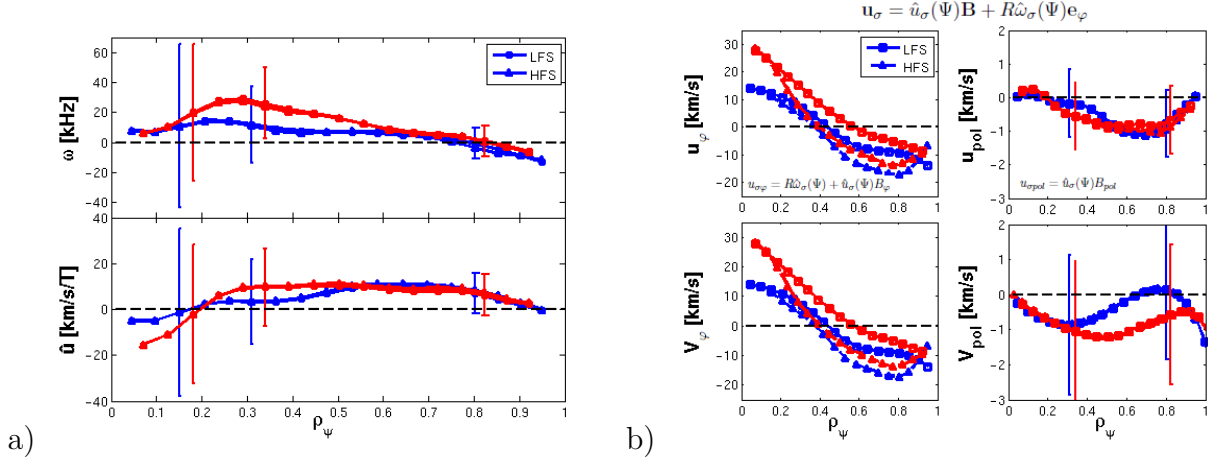
Figure D.1: a) Determination of $\hat{u}$ and $\hat{\omega}$ for shot #47287. The carbon density asymmetry is taken into account for this calculation (Eq.5.9 and Eq.5.12). The good superposition of the $\hat{u}$ and $\hat{\omega}$ LFS and HFS components shows a small effect from the carbon density asymmetry. Notice that the blue and red colors correspond to the highest and lowest power values shown in Fig.E.4 (for #45371). b) A good agreement between the measured v_{pol} and the indirect u_{pol} is observed and $v_\varphi = u_\varphi$ for shot #47287.

surement. In Fig.D.2, the toroidal rotation frequency $f_t = v_{\varphi L,H}/R_{L,H}$ is plotted for the same discharge. Due to the toroidal rotation HFS-LFS asymmetry, this frequency (and therefore v_φ) can have opposite signs for the external flux surfaces at the HFS and LFS that is not compatible with a rigid body rotation approximation. As already described in Sec.5.2.2, this can be explained with the presence of a finite v_{pol} in the electron diamagnetic direction. Neoclassical simulations performed with NEOART [52]
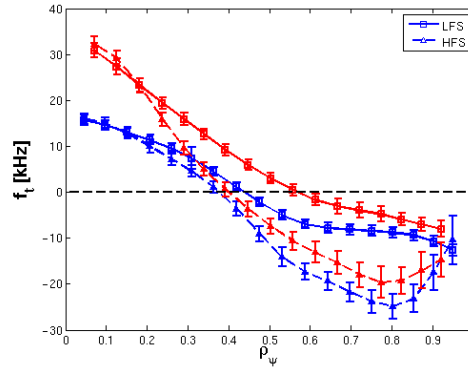
Figure D.2: Toroidal rotation frequency $f_t = v_{\varphi L,H}/R_{L,H}$ at the HFS and LFS, plotted in function of ρ_ψ for shot #47287. Due to the HFS-LFS asymmetry this frequency can have opposite signs for the external flux surfaces at the HFS and LFS ($\rho_\psi > 0.4$).

for similar central barriers (low collisionality regime) also showed reasonable quantitative agreement between the calculated u_{pol} and the predicted poloidal rotation (both in the electron diamagnetic drift direction) providing further evidence that the poloidal rotation is consistent with neoclassical transport [197].

A comparison between the radial electric field calculated from the force balance equation using the standard-direct (above) and indirect (below) methods is shown in Fig.D.3 for the same shot and LFS and HFS regions. The indirect E_r, was obtained by
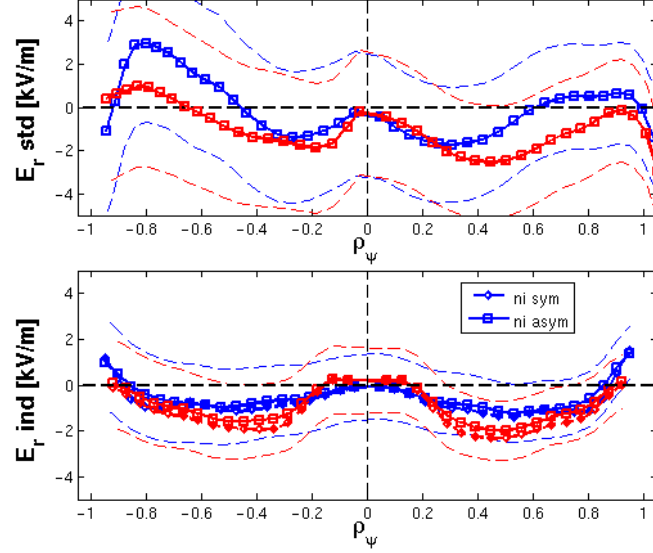
Figure D.3: Comparison between the radial electric field derived from the force balance equation using the standard formulation (above) or the indirect poloidal rotation method (below) for two time intervals of shot #47287. The indirect E_r was also obtained considering a symmetric or asymmetric ion density (see Eq.5.7 or Eq.5.12). Only a small difference is observed between these two cases since the plasma shape of a central barrier is mainly symmetric. The indirect E_r profiles lie well inside the error bars (dashed lines) of the standard E_r and it can be calculated only up to the LCFS due to the basis assumptions of the indirect method.

considering either a symmetric or asymmetric ion density profile (i.e. using Eq.5.7 or Eq.5.12). Only a small difference is observed between these cases, mainly as a central barrier features symmetric nested flux surfaces (see Fig.E.4). For stronger eITBs, this deviation may increase around the mid-radius, where an evident density asymmetry is measured (see Fig.5.34 and Fig.5.36.b). In addition, a comparison of the indirect u_{pol} obtained considering either a symmetric or asymmetric ion density, shows that the poloidal rotation derived for the density asymmetry case is systematically lower by about 0.3-1km/s, depending the eITB target. The indirect E_r profiles clearly remain well inside the error bars of the standard E_r profiles ($E_r < 0$ corresponds to an inward electric field). As explained previously, we note that the indirect E_r can be calculated only up to the LCFS since the indirect poloidal rotation method is only applicable on closed flux surfaces.

In Fig.D.4, the contributions to the radial electric field are shown for both methods. With the standard formulation, the $v_{pol}B_t$ term mainly influences the E_r shape in the core (since $v_{pol} = 0$ at $\rho_\psi = 0$), while the $v_\varphi B_{pol}$ term affects more the profile in the mid-radius region. Using the indirect u_{pol} method, the dominant term for the E_r profile is $R\hat{\omega}_\sigma \widetilde{B}_{pol}$, which indirectly again contains u_{pol} and u_φ.
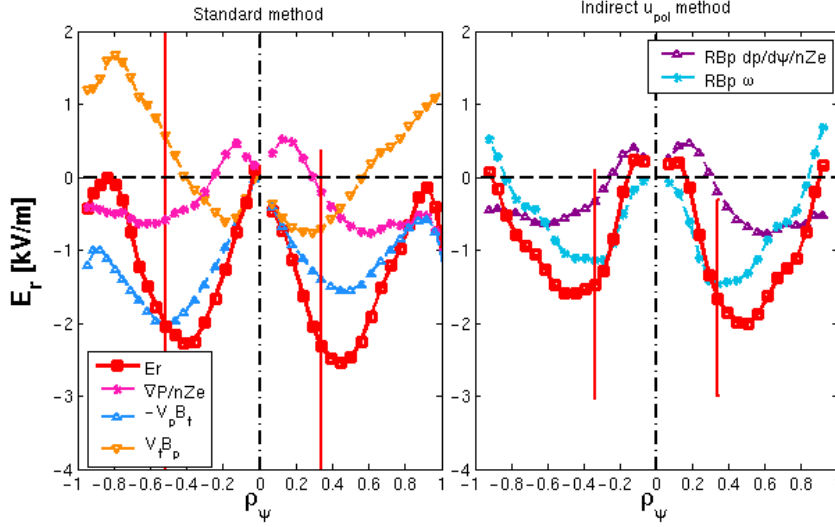
Figure D.4: Radial electric field contributions obtained from the force balance equation using the standard formulation (left) and the indirect poloidal rotation method (right) for the lower power phase of shot #47287 (in red). Only one set of error bars is plotted for the total E_r (in red, for more details on the considered uncertainties see Sec.5.2.2).

D.2   Effect of MHD activity on the central barrier and co-CD off-axis eITB scenarios

D.2.1   Oscillation-mode regime in a central barrier

During repetitions of the discharge presented in Sec.5.4.3, a global plasma oscillation similar to [153, 154] was observed to develop at the end of the power ramp-up phase. The main plasma parameters of shot #46080, featuring a global oscillation (in blue and dark green), and #46118 without the latter (in cyan and light green), are illustrated in Fig.D.5. At 1.4s, a crash is observed in the soft X-ray (SXR) signal (see Fig.D.5.a), followed by a sequence of regular oscillations with a cycle period of 20-30ms. These oscillations affect the plasma current I_p, the loop voltage and the line averaged density $n_{e,av}$ signals (see Fig.D.5.a,b and c), together with the plasma inductance l_i (jumping from 0.9 to 0.91). This particular regime has similarities to the *oscillation regime* or *O-regime* observed in Tore Supra [155]. These oscillations have a m/n=0/0 periodicity. They co-exist with MHD modes in TCV and are triggered by resistive or ideal (infernal) modes depending their proximity to the ideal stability limit. The presence of MHD modes in eITBs reduces the confinement and lowers the pressure and bootstrap current density. Near marginal stability, the modes can self-stabilize, following the modification of the p_e and q profiles. The discharge may recover confinement and re-build the barrier until the next mode is destabilized [154]. The dynamics of a magnetic island has an important role in the creation of this cycle, since it periodically grows and decays when destabilized by unfavorable q and p_e profiles. The H_{RLW} and T_e profiles of shot #46080 also show a periodic oscillation (with a small delay compared to the DMPX signal), indicating a cyclic deterioration of the barrier (Fig.D.5.d and
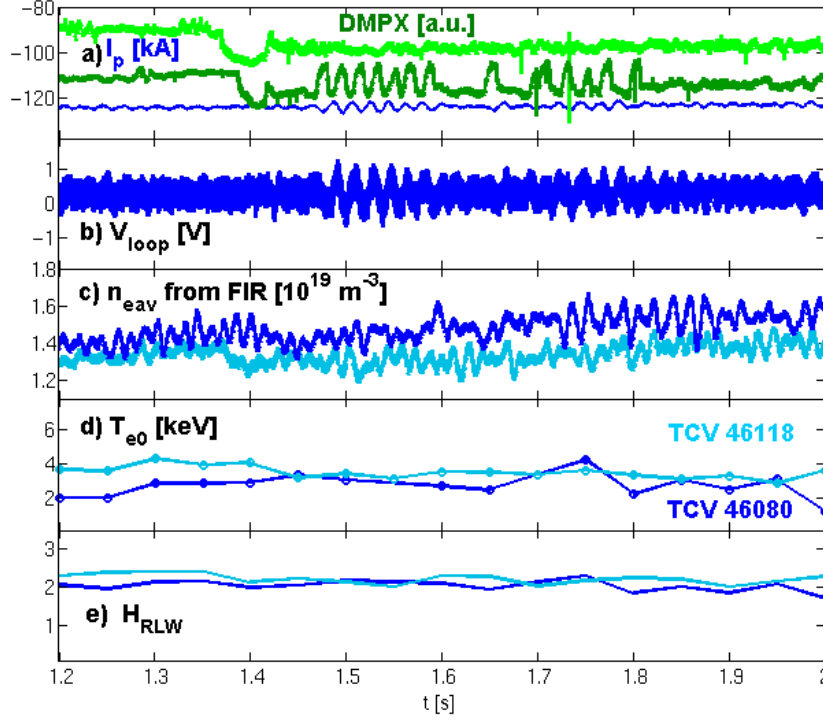
Figure D.5: Main parameters for shot #46080 (in blue and dark green). The oscillation mode affects many traces, mainly I_p, the SXR signal, V_{loop} and $n_{e,av}$. A comparison with shot #46118 (in cyan and light green), shifted downward by 1cm, shows that the O-mode has disappeared.

e). When the confinement recovers, after mode stabilization, an increase in the SXR signal is observed, as shown in Fig.D.6, from the contours of local SXR emissivity of the DMPX diagnostic. A rise of the SXR intensity is detected each time the barrier reforms with a radial extent up to $\rho_\psi = 0.35$ that corresponds to the location of the maximum ∇T_e of the barrier. Note that a vertical shift of only 1 cm (such as that in #46118) is sufficient to modify the heating deposition location and affect the pressure and q profiles. In this second discharge, no oscillations develop and confinement is constant. Previous studies showed that these global oscillations may manifest themselves as sinusoidal-like, when triggered by resistive MHD modes, or as fast "crash-like" disruptions, when triggered by ideal infernal modes [153, 156]. The MHD analysis performed for shot #46080 indicates the presence of a resistive 3/1 mode at 8.5kHz from 0.7s with a magnetic island width of 3-4cm that at 1.42s suddenly decreases in frequency to 5kHz and strengthens (see Fig.D.7.b, highlighted in cyan). This mode is clearly linked to a degradation of the barrier and triggers the global plasma oscillation. The effect of such plasma oscillations on the rotation and radial electric field profiles was studied using the CXRS standard acquisition. In Fig.D.8, the plasma parameter profiles for shot #46080 are shown during the power ramp up phase (blue and green) and between the O-mode phases. To better understand the time associated with each plotted profile, the acquisition intervals are separately highlighted in Fig.D.7.a. The
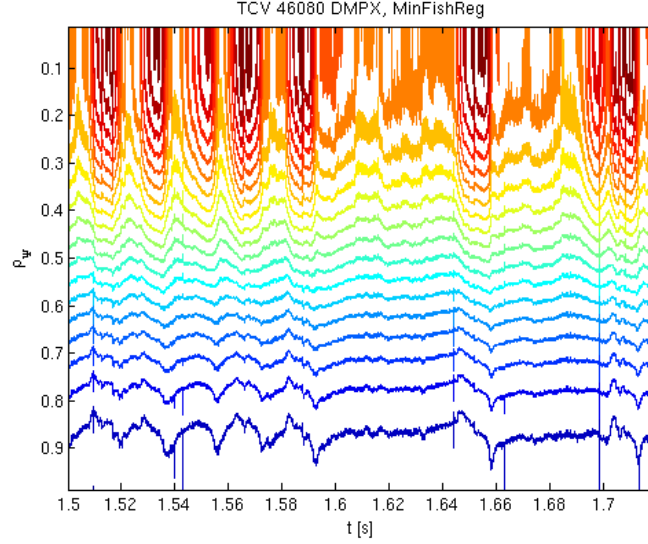
Figure D.6: Contours of local soft X-ray emissivity derived by Fisher inversion from the DMPX diagnostic showing the global oscillation and the related barrier phases (peaks in dark red) and the barrier deterioration phases (in orange and yellow) in shot #46080 at [1.5, 1.72]s.
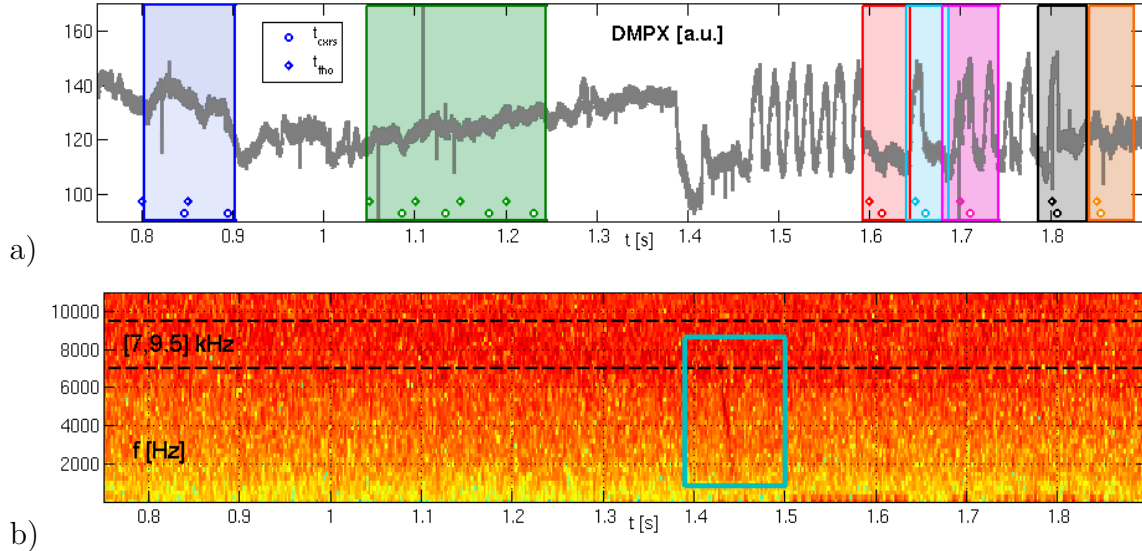
Figure D.7: a) DMPX signal with chosen time intervals for shot #46080. The Thomson (diamonds, above) and CXRS acquisition times (central ON pulse, circles, below) are also plotted. Notice that t_{tho} is usually slightly shifted compared to the t_{cxrs} times. b) Magnetic spectrogram of the discharge. A m/n=3/1 mode is visible at 8.5kHz, which at 1.4s rapidly decreases in frequency but get reinforced in amplitude (inside the square).
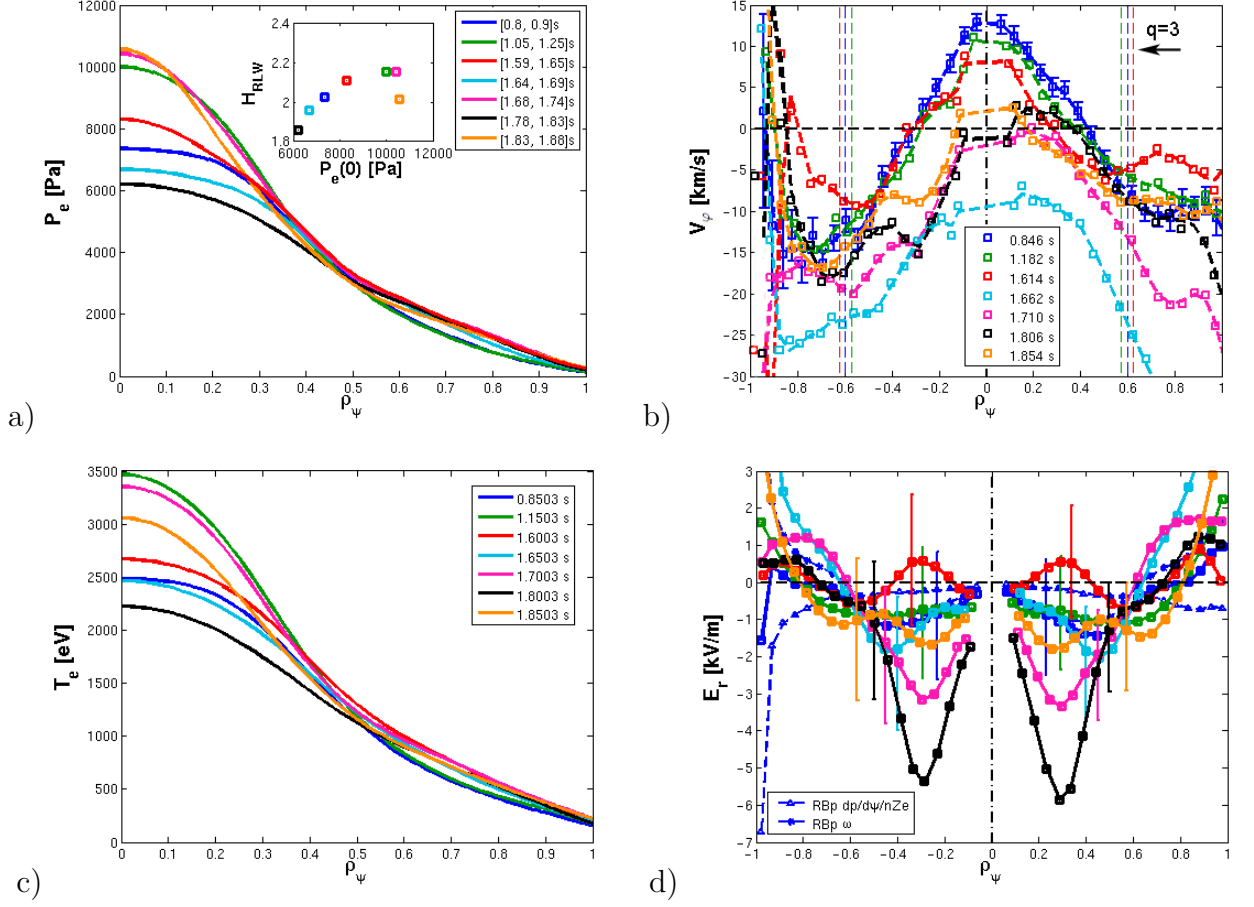
Figure D.8: a) Electron pressure and H_{RLW} factor b) ion toroidal rotation c) electron temperature and d) E_r profiles for shot #46080. The time resolution of the Thomson diagnostic is of 50ms, whereas for the CXRS diagnostic is $3 \times 16ms = 48ms$. In a) the legend shows the selected time intervals used for this study, while more precisely in b) the CXRS (middle ON phase) and in c) the Thomson acquisition times considered for each interval are indicated. In b) the locations of the $q = 3$ surface are plotted for the first three time intervals (it ranges between $\rho_\psi = [0.55, 0.65]$ during the entire shot).

barrier is formed at 1.1s (green) with $H_{RLW} = 2.2$ (see Fig.D.8.a) and $T_e(0) = 3.5keV$ (see Fig.D.8.c). As already observed in Sec.5.4.3, the toroidal rotation is peaked in the cnt-current direction in presence of the central barrier with $v_\varphi(0) = 10km/s$ (see Fig.D.8.b). When CXRS samples the top of an oscillation (black), v_φ is slightly shifted towards the co-current direction in the plasma core. The LFS rotation profile retains the shape of the initial profiles (blue and green) for $\rho_{\psi,LFS} > 0.3$, while for the LFS and HFS core region, it is flattened or reversed by the presence of the oscillation and MHD activity.

The position of the $q = 3$ surface is also plotted in Fig.D.8.b for the initial barrier formation phases with the 3/1 mode and for the first stationary phase between the O-mode. Since the q=3 surface remains between $\rho_\psi = 0.55 - 0.65$ during the entire discharge, we plotted the position for only these three time intervals. Inside the mode

location a slight change in ∇v_φ can be observed. When approaching the mode desta-bilization time, and during the degradation phase (black and cyan), v_φ increasingly move towards the co-current direction. During the stationary phases before or after the O-mode, characterized by a weak barrier (red and orange), v_φ recovers a shape similar to the initial profiles without the O-mode with $v_\varphi(0) = 3 - 8km/s$. The poloidal rotation for all these cases is directed counter clockwise with $v_{pol} \cong -2km/s$. The radial electric profiles shown in Fig.D.8.d, are mostly directed inwards with values in the range $E_r = [-3, -0.5]kV/m$. The carbon ion density and temperature profiles are plotted for completeness in Fig.E.17 and range between $n_i(0) = 5 - 8 \times 10^{17}m^{-3}$ and $T_i(0) = 200 - 370eV$.

The CXRS and Thomson acquisition times (see Fig.D.7.a, in circles or diamonds) are slightly displaced within each selected time interval. This results from different time resolutions of the two diagnostics: 48ms for the CXRS (i.e. 16ms of acquisition time and 24ms of background subtraction) and 50ms for the Thomson diagnostic. The T_e, p_e and v_φ profiles are calculated at different times separated by a few ms during the oscillation, which may explain, but only in part, some of the incoherences observed between these profiles, i.e for the magenta case T_e is measured at the top of the barrier while the rotation measurement is closer to the barrier crash, and for the black case T_e is taken before the recovery of the barrier while the rotation is measured during the re-established barrier. This time resolution is insufficient to accurately measure the electron and ion profiles in between these oscillations, since a cycle takes around 20-30ms whereas CXRS has only 50ms resolution. Nonetheless, each selected time interval contains one measurement from the Thomson and the CXRS diagnostics that provide some informations on the evolution of the rotation, T_e and n_e profiles at different times in the O-mode. We can already see that this O-regime, triggered by a resistive 3/1 mode, has a strong effect on the plasma confinement, and on the electron pressure and v_φ profiles.

In next Sec.D.2.2, a similar behavior is identified also for the co-CD off-axis eITB target. Since eITB are close to the ideal infernal mode limit, a small change in the q profile may easily trigger resistive modes (just like this described central barrier or in shot #46094), before reaching the ideal limit (attained with the strongest barrier #47340).

D.2.2 Oscillation-mode regime in a a co-CD off-axis eITB

During the development of a strong co-CD off-axis eITB target, a global plasma oscillation, similar to the one already discussed in Sec.D.2.1, appeared during some discharges that lasted until a final disruption. The main plasma parameters of shot #46094, featuring such a global oscillation (in blue and dark green), are illustrated in Fig.D.9. At 0.55s, after some initial short events (see the spikes on the SXR signal in Fig.D.9.a), a sequence of regular oscillations with a cycle period of around 150ms develops. These oscillations affect the plasma current I_p, the normalized internal inductance per unit length l_i and the line averaged plasma density $n_{e,av}$ signals (see Fig.D.9.a-c). As in Sec.D.2.1, these oscillations have a m/n=0/0 periodicity and, as
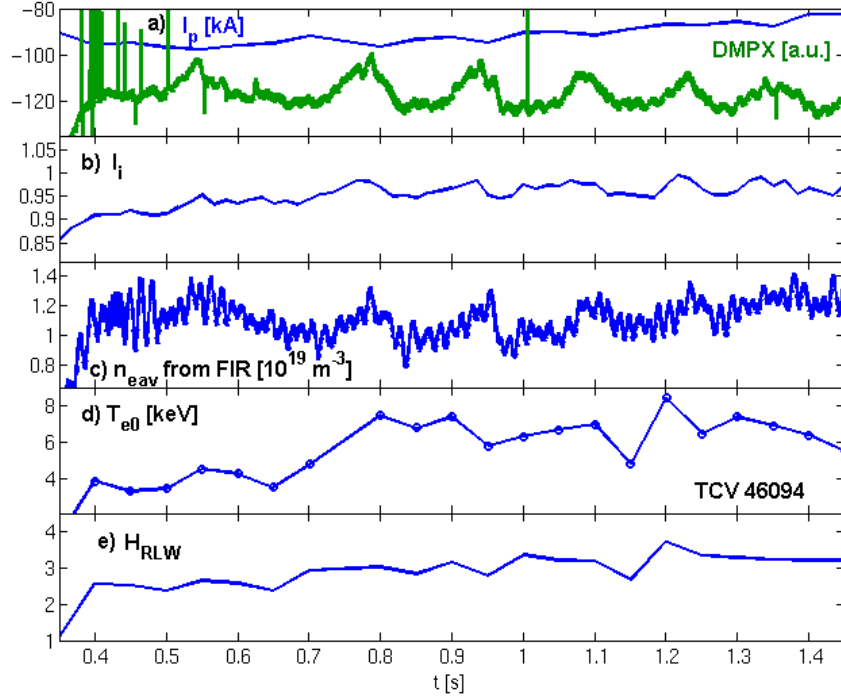
Figure D.9: Main parameters for shot #46094. The oscillation mode affects many traces, mainly I_p, the SXR signal, the normalized internal inductance per unit length l_i and $n_{e,av}$. The confinement is also influenced as shown by the oscillating $T_e(0)$ and H_{RLW} profiles.

previously observed on TCV [153, 154], can be triggered by resistive or ideal (infernal) modes [156] depending their proximity to the ideal stability limit. The presence of these MHD modes in the eITBs reduces the improved confinement and lowers the pressure and bootstrap current density. The H_{RLW} and T_e profiles of shot #46094 display such a periodic oscillation, and confirm a cyclic deterioration of the barrier (see Fig.D.9.d and e). When the confinement recovers, an increase in the SXR signal is measured, as shown in Fig.D.10, where the contours of local SXR emissivity of the DMPX diagnostic are plotted. A large increase in the SXR emission is detected at each barrier reformation with a radial extent up to $\rho_\psi = 0.4$, corresponding to the location of the maximum ∇T_e of the barrier. These global plasma oscillations have a clear sinusoidal-like oscillation that indicate a triggering by resistive MHD modes [153, 154]. MHD analysis performed on shot #46094 shows the presence of a resistive 3/1 mode of 8kHz starting at 0.58s with a magnetic island width of 6-7cm. At 0.67s the mode frequency increases to 15kHz, then decreases to 4kHz and then cyclically repeats. In the destabilization phase, the mode takes 20ms to decrease from 8kHz towards 4kHz and remains stable at this frequency for 50ms before the barrier recovers and the mode increases again in 30ms to 8kHz. During this sequence, the island width varies between 7cm to 4cm and then increases again during the barrier reinforcement. In the 50ms separating the two 8kHz periods, the mode oscillates up to 15kHz, but in this phase the signal is weak and some small crashes due to an ideal instability are observed
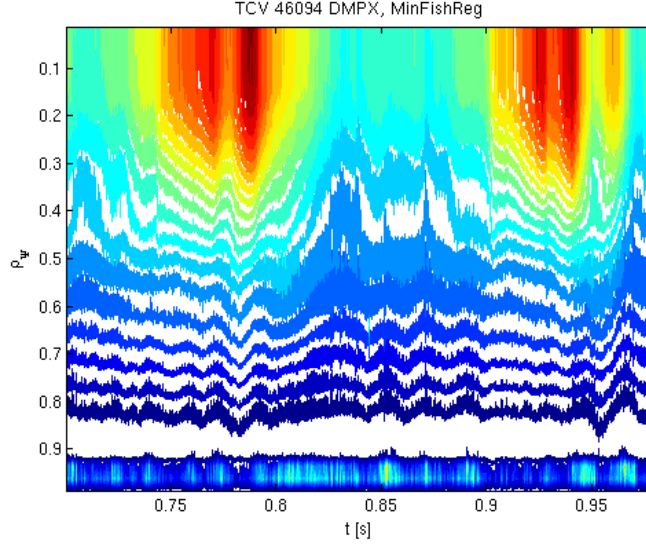
Figure D.10: Contours of local soft X-ray emissivity derived by Fisher inversion from the DMPX diagnostic showing the barrier phases (peaks in red) and the deterioration of the barrier (in blue and green) in shot #46094 at [0.7, 0.98]s. The radial extent of the peaks is up to $\rho_\psi = 0.4$, which corresponds to the location of the maximum ∇T_e of the barrier.

together with the global oscillation. The resistive MHD mode appears to be already destabilized by the small crashes occurring at high frequencies. The mode amplitude is much higher during the lower frequency phase (i.e. during the destabilization phase from 8 to 4kHz and the restabilization phase from 4 to 8kHz, see Fig.D.11.b). Moreover, some constant residual activity can be observed around 3kHz during the entire global oscillation. The effect of such plasma oscillations on the rotation and radial electric field profiles has been studied in this work using the CXRS LFS system with an acquisition time of $t_{acq} = 8ms$ (i.e. $t_{resolution} = 24ms$). In Fig.D.12 the profiles are shown for two oscillations of the O-mode observed in shot #46094. To better estimate the time associated to each plotted profile, the CXRS and Thomson central acquisition times are separately highlighted in Fig.D.11.a. All v_φ profiles during the O-mode are in the co-current direction with a central $v_\varphi \cong -[17, 24]km/s$. Some specific rotation modifications are present at times with and without the barrier (see Fig.D.12.b). At 0.7s, the electron temperature and pressure profiles (see Fig.D.12.a and c) are small indicating the presence of a weak barrier ($H_{RLW} = 2.8$, in cyan) and the toroidal rotation presents a bulge around $\rho_\psi = 0.5$. During the barrier reinforcement, between [0.73,0.77]s (in azure and green), the central toroidal rotation relaxes and decreases from -21km/s to -17km/s (in azure). With the limited time resolution of 50ms, the Thomson measurements are taken as constant for the second and third intervals (in azure and green). The crash observed at the top of the oscillation (0.77s, in green) immediately causes a co-current "kick" and the rotation slightly shifts towards larger co-current values. This behavior is accentuated during the destabilization phase and barrier deterioration ([0.79,0.83s], in violet), where v_φ clearly increases even further (in absolute value). Notice that an 18ms acquisition delay between the two diagnostics
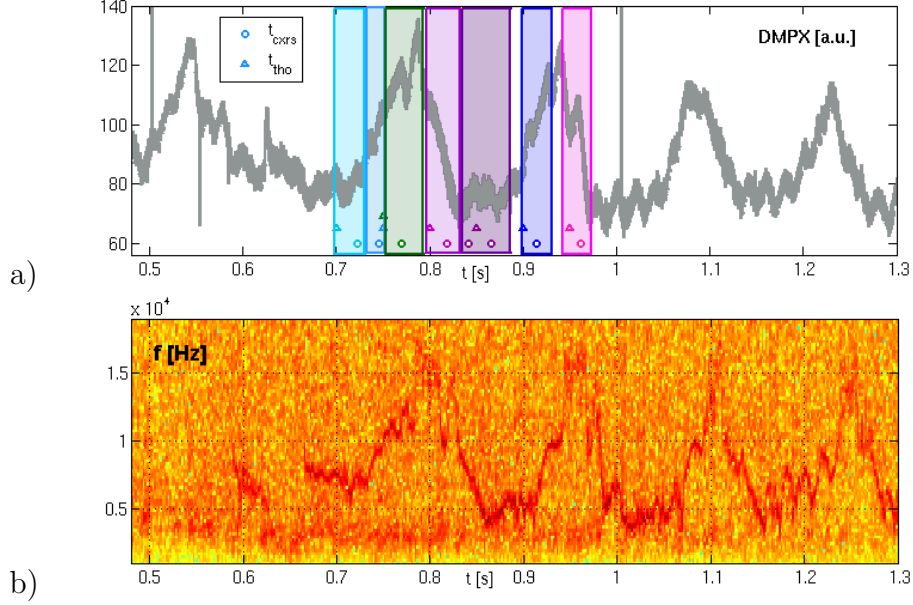
Figure D.11: a) DMPX signal with chosen time intervals for shot #46094. The Thomson (triangles, above) and CXRS acquisition times (central ON pulse, circles, below) are also plotted. Notice that t_{tho} is usually slightly shifted compared to the t_{cxrs} times. b) Magnetic spectrogram of the discharge. A m/n=3/1 mode is visible at 8kH from 0.58s, which successively triggers a global oscillation.

causes another discrepancy for this time interval. Indeed, the Thomson profiles are taken at the maximum barrier time ($H_{RLW} = 3.05$), while the CXRS measurements are taken at the end of the degradation phase. The toroidal rotation also remains at high co-current values during the "stable" phase ([0.83,0.88s], in dark violet) characterized by a weaker barrier ($H_{RLW} = 2.85$). When the barrier starts to reinforce again to $H_{RLW} = 3.15$ ([0.90,0.93s], in blue), v_φ relaxes and decreases from -35km/s to -25km/s at $\rho_\psi = 0.5$, similarly to that observed at [0.73,0.75]s (in azure). Finally, after the crash occurring at 0.95s, the barrier deteriorates and the rotation shifts again towards higher co-current values (in magenta). These results show the presence of a cyclic modification for the toroidal rotation profile, linked to the barrier evolution occurring during the discharge. The poloidal rotation for all these cases is directed counter clockwise, with $v_{pol} \cong -[1, 3]km/s$ for the stronger barriers and $v_{pol} \cong -[3, 5]km/s$ for the destabilized barriers (see Fig.E.18). The radial electric profiles in Fig.E.19, are directed inward for $\rho_\psi < 0.55$ with values ranging between $E_r = -[0.5, 6]kV/m$. For $\rho_\psi > 0.55$, the E_r of the destabilized barriers remain in the inward direction, whereas the stronger barriers present a small E_r directed outward. The $E \times B$ shearing rates vary between $|\omega'_{E \times B}| \cong 0.5 - 8 \times 10^4 s^{-1}$ (see Fig.D.12.d).

Finally, for completeness, the carbon ion density and temperature profiles are plotted in Fig.E.20 and range between $n_i(0) = 6 - 9.5 \times 10^{17} m^{-3}$ and $T_i(0) = 250 - 330eV$. These are slightly lower than for the stronger barrier cases, but the CXRS measurements, (in particular the background subtraction), are affected by the non stationarity of the discharge, which limits the deduced impurity profiles accuracy.
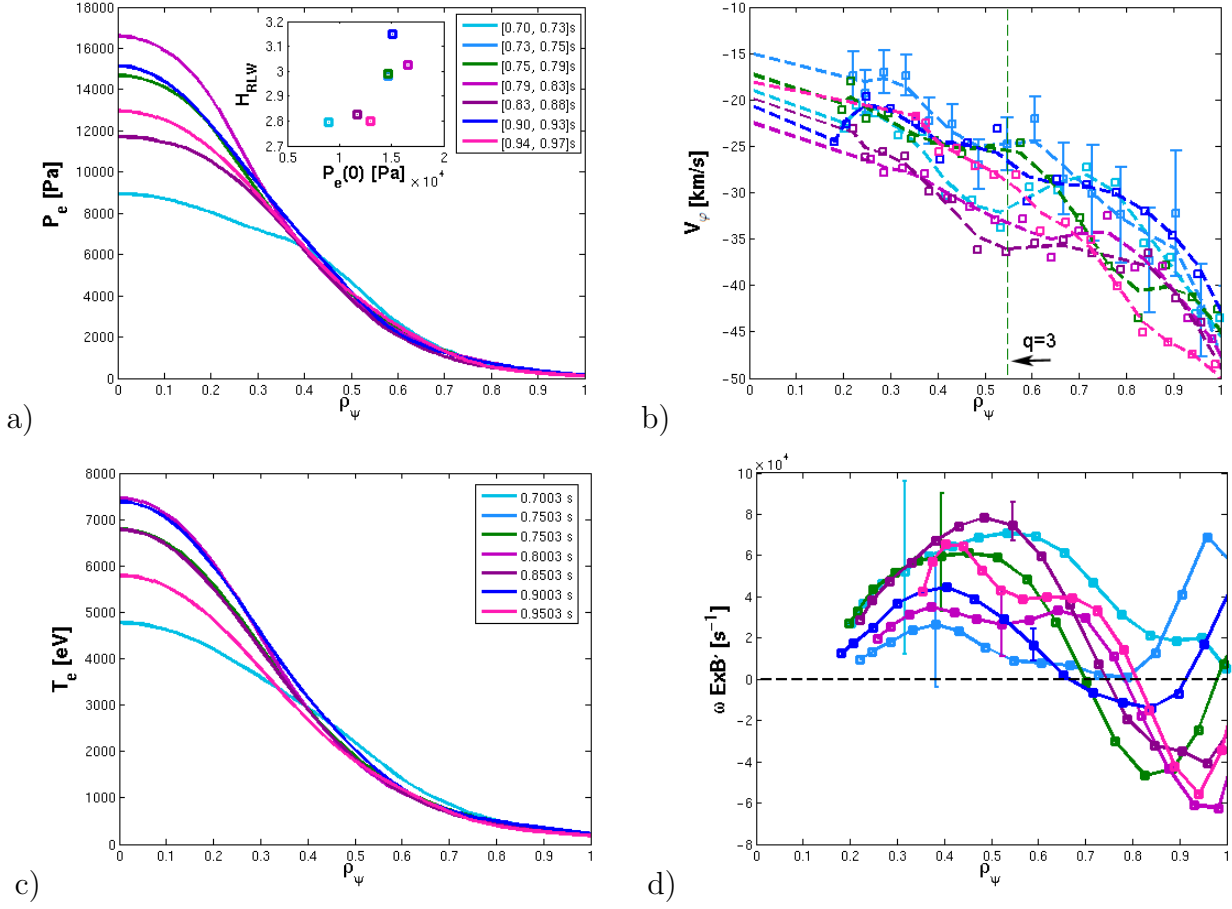
Figure D.12: a) Electron pressure and H_{RLW} factor b) impurity ion toroidal rotation c) electron temperature and d) $|\omega'_{E \times B}|$ profiles for shot #46094.

To conclude this section, we have observed that global oscillations, triggered by a resistive 3/1 mode, have a strong effect on the plasma confinement and the main plasma parameters. The v_φ profiles also react to the presence of this cyclic modification, clearly linked to the barrier evolution, during these discharges. Further discharges with increased time resolution of the Thomson and CXRS diagnostics may be used to better investigate this cyclic change in the rotation profiles and help identify the causality of link between the MHD mode presence, the barrier deterioration and the rotation modification.

D.3 Effect of total and central power in a co-CD off-axis eITB

To summarize the effect of the total and central heating on the rotation profiles and the eITB strength for the co-CD off-axis eITB scenario, we have compared three different heating schemes in Fig.D.13 and D.14. These discharges were created by applying

460kW or 900kW of co-CD off-axis, together with 900kW cnt+co-CD on-axis (1380kW in total, #47906), 900kW cnt+co-CD on-axis (1800kW in total, #47340), or 900kW of ECH on-axis (1800kW in total, #47418). An Ohmic discharge (#47865) with similar parameters as the barrier shots is also analyzed.

From Fig.D.14.a, the highest electron pressure profiles and strongest barriers are achieved by applying in total 1800kW, with 900kW of cnt-CD and co-CD on-axis (#47340, in red) or 900kW of only ECH on-axis (#47418, in lilac) to heat the center. By applying the same ECH power on-axis, a similar strong barrier is obtained with $H_{RLW} = 5.2$ (instead of $H_{RLW} = 5.4$ for #47340).

This is confirmed in Fig.D.13 and Fig.E.21, where the electron temperature and density profiles are plotted as a function of ρ_ψ and the vertical position. Both discharges, #47340 and #47418, present a barrier in n_e and T_e of 7keV with a width of $\Delta z = 23cm$ and respectively $\Delta z = 16cm$. The same central temperature $T_e(0)$ is obtained for both barriers, but the $T_e(\rho_\psi)$ and $T_e(z)$ profiles are narrower for the ECH case, indicative of a reduced plasma volume included inside the barrier. The barrier obtained with 1380kW (in orange) displays a narrower electron density and a temperature barrier of 5keV.

a)   b)
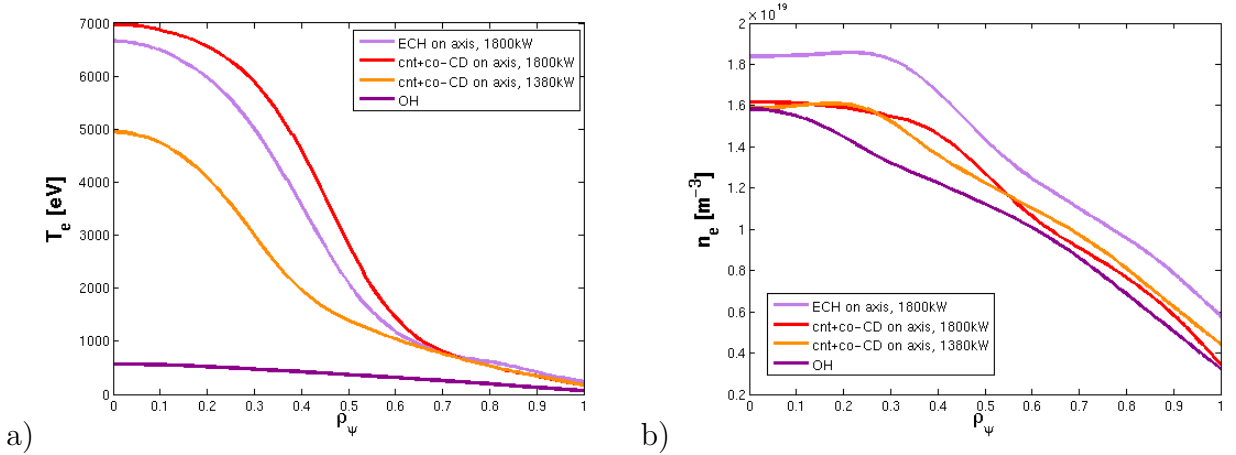
Figure D.13: Electron a) temperature and b) density for shots #47418 (900kW of co-CD off-axis and 900kW of ECH on-axis, in lilac), 47340 (900kW of co-CD off-axis and 900kW cnt+co-CD on-axis, in red), 47906 (460kW of co-CD off-axis and 900kW cnt+co-CD on-axis, in orange) and 47865 (OH, in violet).

The toroidal rotation v_φ obtained for both 1800kW cnt+co-CD and 1800kW ECH on-axis cases are in the co-current direction (see Fig.D.14.b) with central $v_\varphi = -[8, 12]km/s$. The v_φ profile for the ECH on-axis case (in lilac) is flatter at the LFS region and displays many oscillations at the HFS region. During this discharge, strong MHD activity is observed, which strongly affects the rotation profiles. During the initial eITB target development experiments, even stronger MHD activity was observed for all discharges performed by applying ECH on-axis that generated a less stationary barrier. For this reason, it was decided to choose the configuration of cnt+co-CD on-axis, since stronger and more stable barriers were formed.
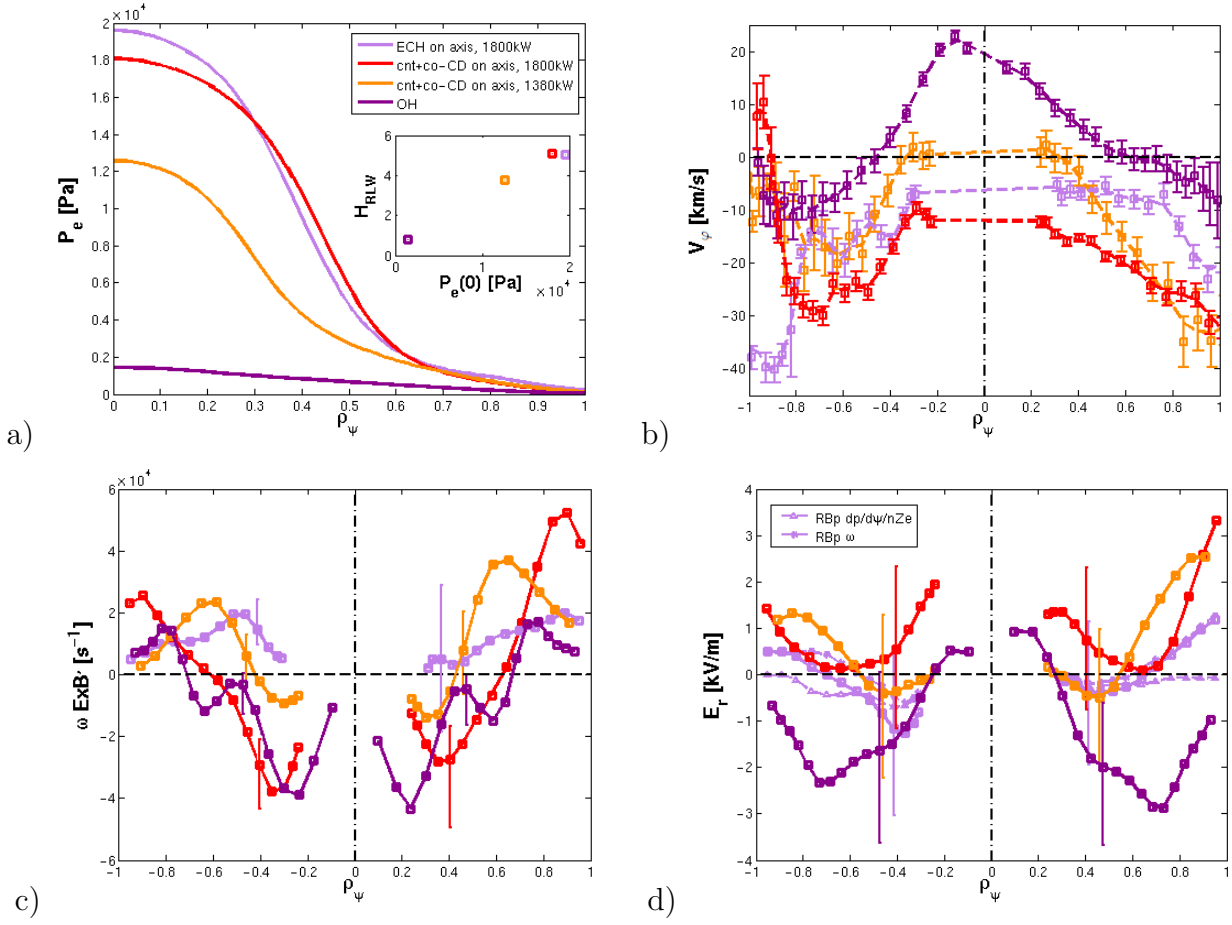
Figure D.14: a) Electron pressure and H_{RLW} factor b) impurity ion toroidal rotation c) $E \times B$ shearing rate and d) E_r profiles for comparable shots with $dI_{OH}/dt = [-500, -250]A/s$ with four different central or total injected power: ECH on-axis (1800kW in total, #47418), cnt + co-CD on-axis (1800kW in total, #47340), cnt + co-CD on-axis (1380kW in total, #47906) and the corresponding Ohmic discharge (#47865).

The v_φ rotation for the 1380kW cnt+co-CD case is mainly in the co-current direction, with a small core cnt-current rotation of 1-2km/s inside $\rho_\psi < 0.3$ (in orange). The Ohmic discharge (with no barrier) presents a peaked cnt-current v_φ profile up to 22km/s for $\rho_\psi < 0.5$ (in violet). For the 1380kW cnt+co-CD case, the main ∇v_φ gradient is larger compared to the #47340 case at the LFS region (around $\rho_\psi = 0.4$), but both gradients are almost equal in the HFS region for the same position. More generally, in the whole LFS region, the strongest ∇v_φ gradient seems more strongly affected by heating type and barrier strength, whereas, in the central HFS region ($\rho_\psi = 0.3 - 0.5$), ∇v_φ remains similar for all cases. Since for higher β, a larger Shafranov shift occurs (leading to more "compressed" flux surfaces), we have plotted the same profiles as a function of R in Fig.E.22. The larger difference in the ∇v_φ gradients at the LFS is again observed. The poloidal rotation varies between central clockwise and external counter clockwise direction for the four discharges (see Fig.E.23).
The Ohmic discharge presents a well defined inward E_r (see Fig.D.14.d), similar to

the Ohmic discharge #45262 with same parameters as the central barrier shots (see Fig.5.16.c). The other three EC heated discharges present a concave E_r profile, but are displaced towards smaller inward values in the core and are directed outwards for $\rho_\psi > 0.6$. The $E \times B$ shearing rate in the core region is larger for the Ohmic case and varies between $|\omega'_{E \times B}| \cong 0.5 - 5 \times 10^4 s^{-1}$ (see Fig.D.14.c). Nevertheless, for $\rho_\psi > 0.6$ it is larger for the cnt+co CD heated cases. For completeness, the carbon density and temperature profiles are also plotted in Fig.E.24 and range between $n_i(0) = 2 - 4.2 \times 10^{17} m^{-3}$ and $T_i(0) = 130 - 230 eV$.

To conclude, in this section we have again observed that a modification in the total and central heating has a clear effect on the barrier strength and rotation profiles. A higher total injected power of cnt and co-CD on-axis results in stronger and more stable barriers. Moreover, for similar eITB discharges, a reduction in the power (and therefore in the eITB strength), seems to decrease the toroidal rotation towards smaller central co-current values and can also lead to a core rotation reversal for weak barriers. This displacement may also be linked to a change in the edge conditions. Uncertainties in the CXRS measurements and the presence of MHD activity do not permit the extraction of a trend for the main ∇v_φ gradient values, but we can note that they appear to be more affected in the LFS region compared to the HFS region. In the future an investigation of the main terms composing v_φ, i.e. the flux functions $\hat{u}_\sigma(\psi)$ and $\hat{\omega}_\sigma(\psi)$ (see Sec.5.2.2) may help to better understand these observations.

Appendix E

Additional Figures for the investigated central barriers and co-CD off-axis eITBs

In this appendix are regrouped all the additional Figures essential for a better analysis of the discharges discussed in Chap.5. Mainly the electron/ion temperature and density profiles and the poloidal rotation profiles are shown here.

E.1 Central barrier (ICEC) scenario

E.1.1 Effect of different CD components on central confinement
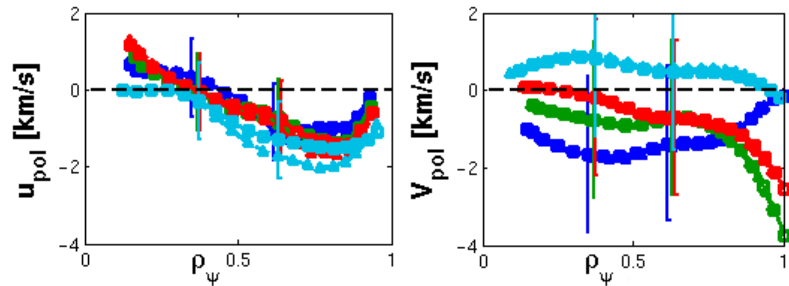
Figure E.1: Measured v_{pol} and calculated indirect u_{pol} for shots #47882 (500kW cnt-CD, in blue and OH in cyan), #47881 (500kW co-CD, in green) and #47879 (500kW ECH, in red).
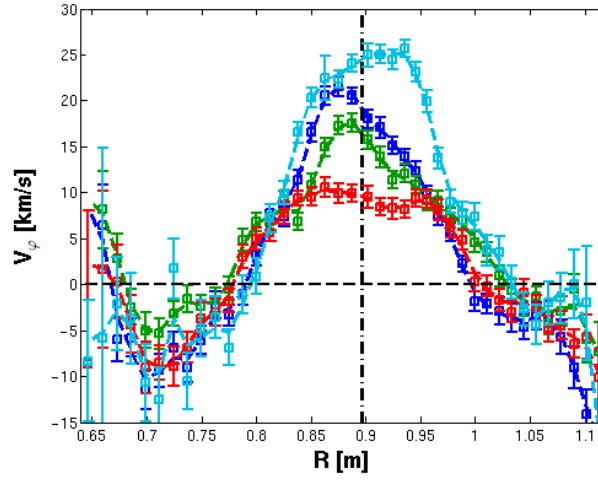
Figure E.2: v_φ as a function of R for shots #47882 (500kW cnt-CD, in blue and OH in cyan), #47881 (500kW co-CD, in green) and #47879 (500kW ECH, in red).
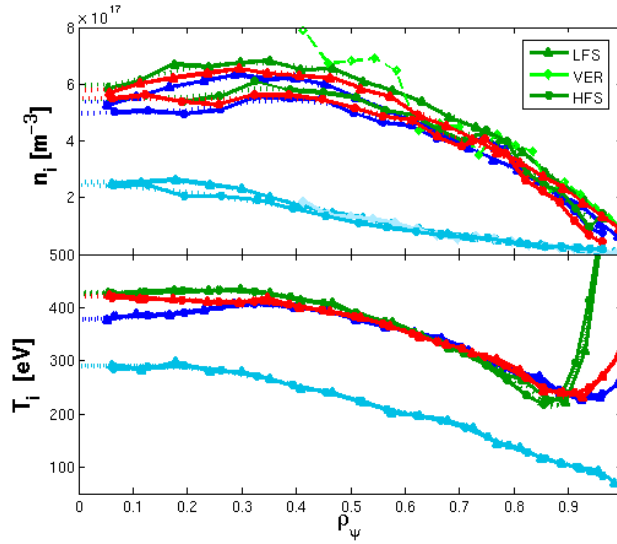
Figure E.3: Carbon ion density and temperature for shots #47882 (500kW cnt-CD, in blue and OH in cyan), #47881 (500kW co-CD, in green) and #47879 (500kW ECH, in red).

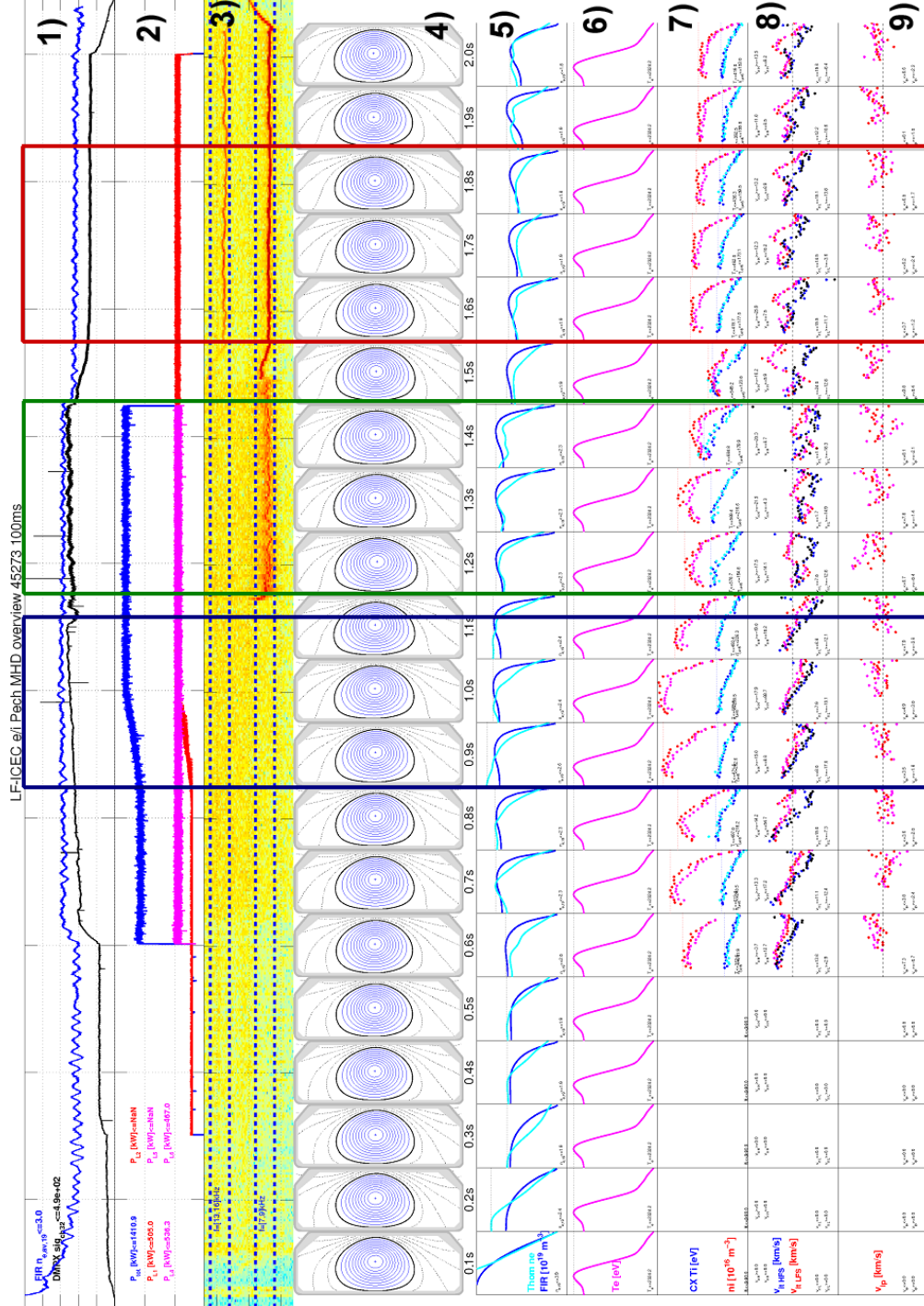## E.1.2 Effect of total ECH power on the central barrier
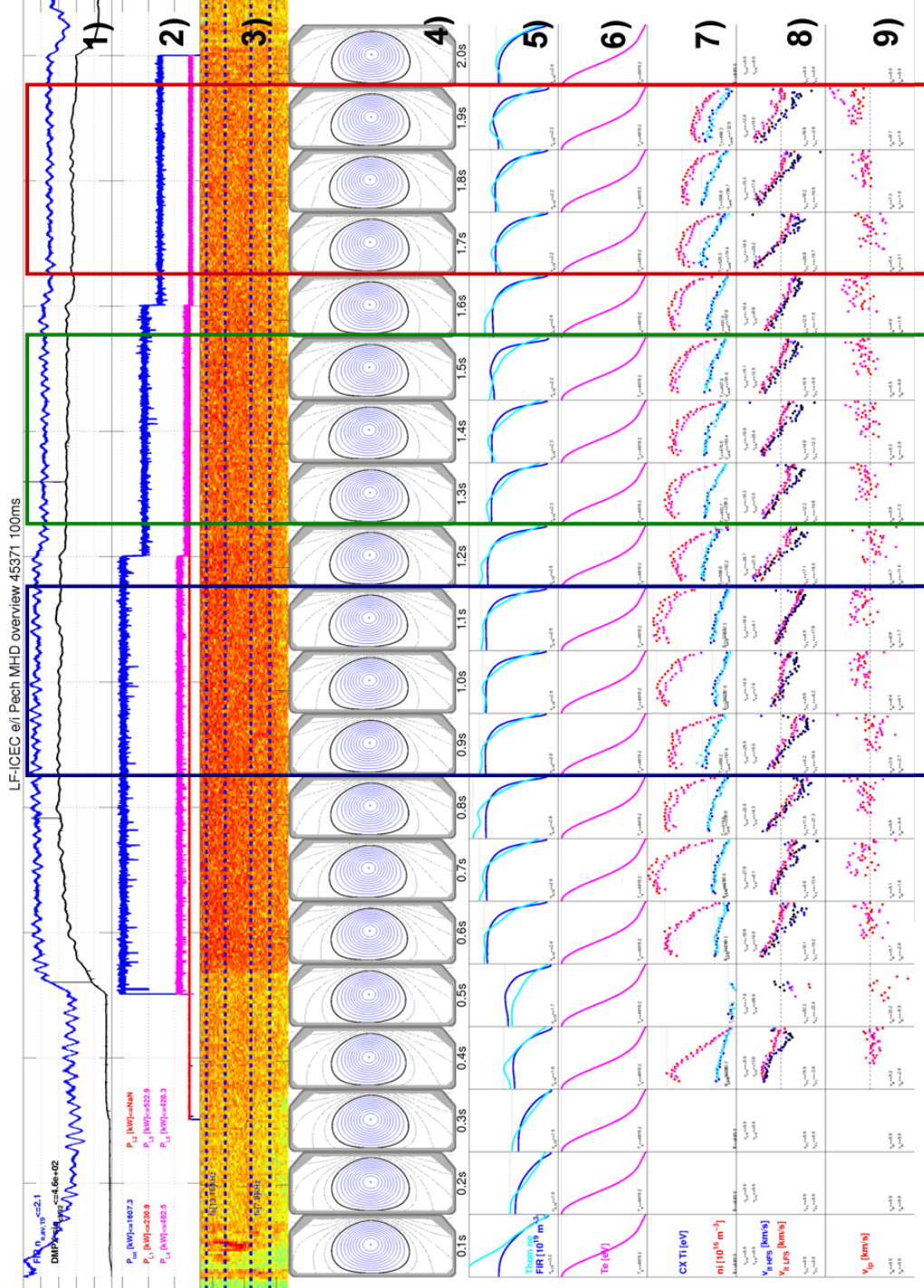
Figure E.4: Snapshot of the main traces for shot #45371. The parameters list for each line (from top to bottom) is the following: 1) DMPX (in black) and FIR (in blue) time evolution, 2) ECH power traces, 3) Magnetic spectrogram, 4) LIUQE reconstruction, 5) $n_e(\rho_\psi)$ from Thomson and FIR, 6) $T_e(\rho_\psi)$ from Thomson, 7) $T_i(\rho_\psi)$ (in blue-cyan) and $n_i(\rho_\psi)$ (in red-pink) from CXRS, 8) $v_\varphi(\rho_\psi)$ for HFS (in blue-black) and LFS (in red-pink) from CXRS, 9) $v_{pol}(\rho_\psi)$ from CXRS.
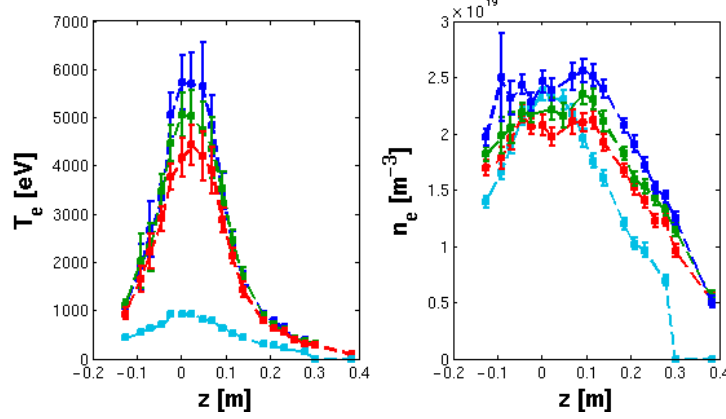
Figure E.5: Electron temperature (left) and density (right) for the three power values of shot #45371 (1600kW in blue, 1100kW in green, 800kW in red) and the OH discharge #45262 (in cyan, same color convention as Fig.5.16) as a function of the vertical position.
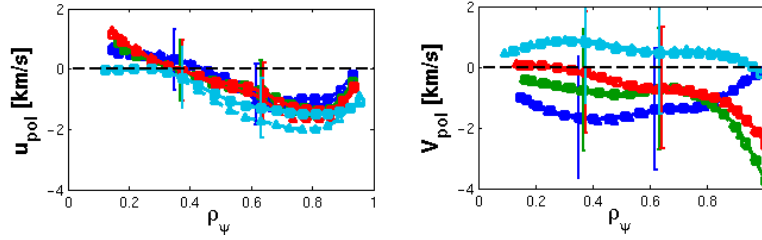
Figure E.6: Measured v_{pol} and calculated indirect u_{pol} for shot #45371 (1600kW in blue, 1100kW in green, 800kW in red) and a similar OH case #45262 (in cyan, same color convention as Fig.5.16).
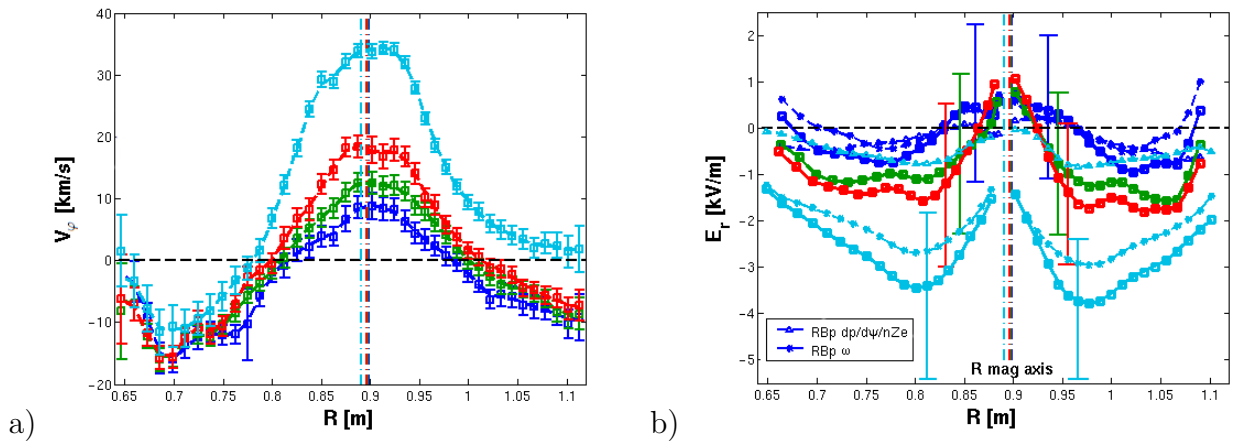
Figure E.7: a) v_{φ} and b) E_r as a function of R for shot #45371 (1600kW in blue, 1100kW in green, 800kW in red) and a similar OH case #45262 (in cyan). The positions of the magnetic axis are plotted for each time interval (dashed-dot line).
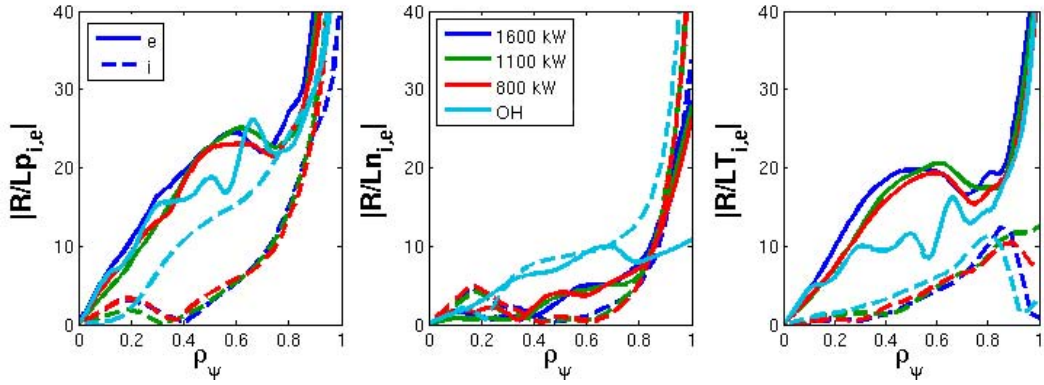
Figure E.8: $|R/L_{pi,e}|$, $|R/L_{ni,e}|$ and $|R/L_{Ti,e}|$ profiles for carbon ions (dashed line) and electrons (solid lines) of discharges #45371 and #45262 (OH).
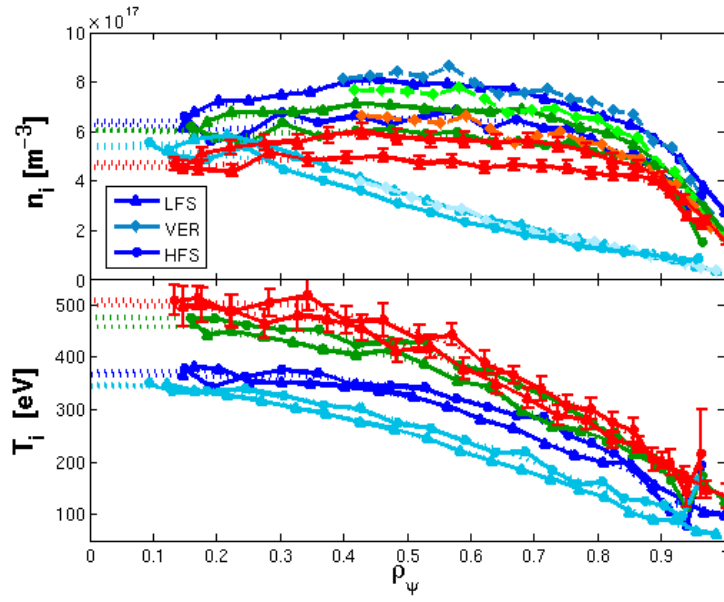
Figure E.9: Carbon ion density and temperature (LFS and HFS) for shot #45371 and a similar OH case #45262.

E.1.3 Effect of MHD activity on the central barrier

Figure E.10: Snapshot of the main traces for shot #45273. The parameters list for each line (from top to bottom) is the following: 1) DMPX (in black) and FIR (in blue) time evolution, 2) ECH power traces, 3) Magnetic spectrogram, 4) LIUQE reconstruction, 5) $n_e(\rho_\psi)$ from Thomson and FIR, 6) $T_e(\rho_\psi)$ from Thomson, 7) $T_i(\rho_\psi)$ (in blue-cyan) and $n_i(\rho_\psi)$ (in red-pink) from CXRS, 8) $v_\varphi(\rho_\psi)$ for HFS (in blue-black) and LFS (in red-pink) from CXRS, 9) $v_{pol}(\rho_\psi)$ from CXRS.
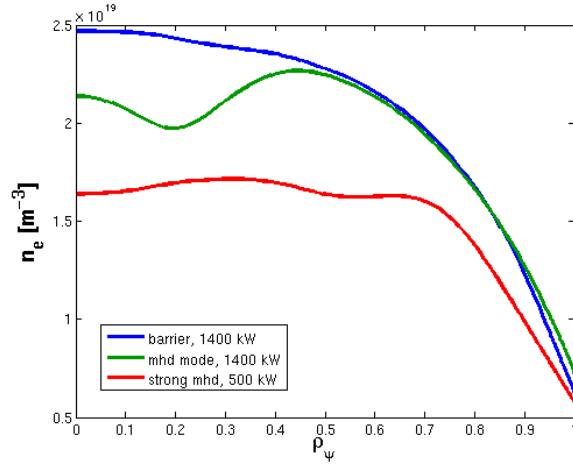
Figure E.11: Electron density fit for shot #45273.

E.2 co-CD off-axis eITB scenario

E.2.1 Effect of dI_{OH}/dt scan in a co-CD off-axis eITB
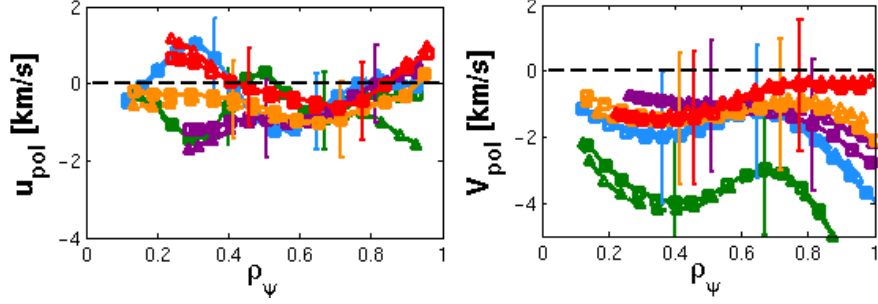
Figure E.12: Measured v_{pol} and calculated indirect u_{pol} for shots #47345 ($dI_{OH}/dt = +4000A/s$, in green), 47341 ($dI_{OH}/dt = +2000A/s$, in azure), 47351 ($dI_{OH}/dt = 0A/s$, in violet) and 47340 ($dI_{OH}/dt = -250A/s$, in orange and red).
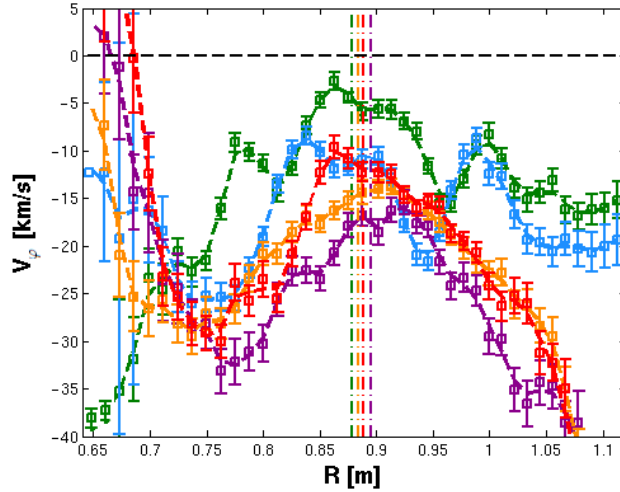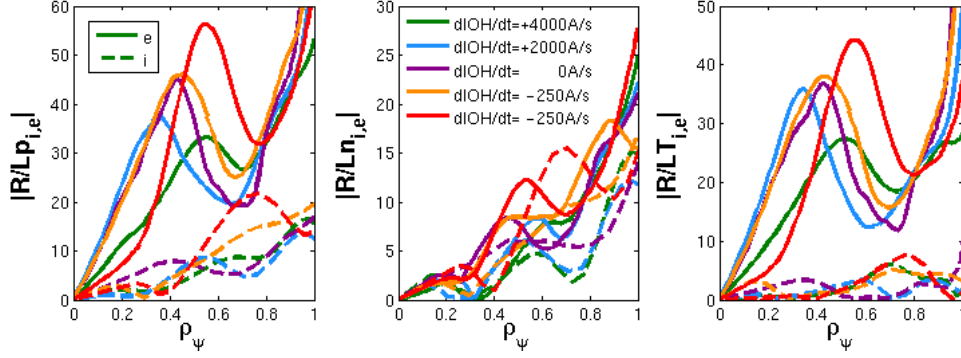

Figure E.13: v_{φ} as a function of R for shots #47345 ($dI_{OH}/dt = +4000A/s$, in green), 47341 ($dI_{OH}/dt = +2000A/s$, in azure), 47351 ($dI_{OH}/dt = 0A/s$, in violet) and 47340 ($dI_{OH}/dt = -250A/s$, in orange and red).

Figure E.14: $|R/L_{pi,e}|$, $|R/L_{ni,e}|$ and $|R/L_{Ti,e}|$ profiles for ions (dashed line) and electrons (solid lines) of discharges #47345 ($dI_{OH}/dt = +4000A/s$, in green), 47341 ($dI_{OH}/dt = +2000A/s$, in azure), 47351 ($dI_{OH}/dt = 0A/s$, in violet) and 47340 ($dI_{OH}/dt = -250A/s$, in orange and red)

E.2.2 Summary of experimental $E \times B$ shearing rates for both internal barrier scenarios
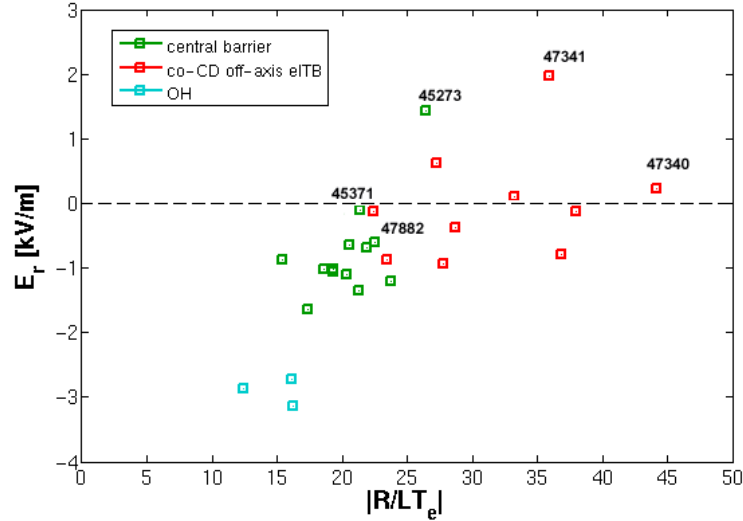

Figure E.15: Radial electric field E_r of the LFS region taken at the maximum $|R/L_{Te}|$ for the central barriers (in green), the strong co-CD off-axis eITBs (in red) and the corresponding OH (in cyan) scenarios as a function of the maximum $|R/L_{Te}|$. The shot number of some important discharges discussed in Secs.5.4 and 5.5 are highlighted beside the corresponding E_r values. The OH cases present a negative E_r (directed inwards), while for stronger barriers it increases towards smaller negative and positive near $E_r = 0$ values. Comparison of the two terms in the E_r profile, shows that the diamagnetic component remains similar for all discharges and is much smaller than the $\hat{\omega}$ term. A similar behavior is also observed for the E_r values measured at the HFS region.
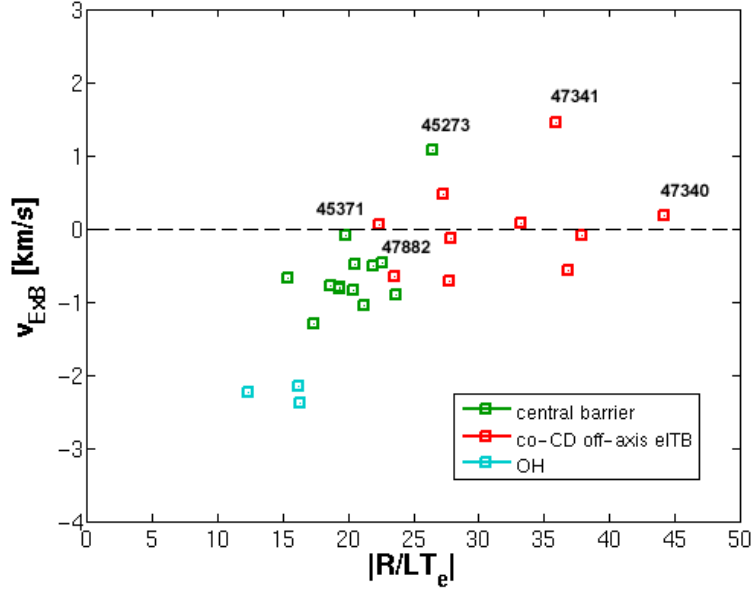
Figure E.16: $v_{E \times B}$ of the LFS region measured at the maximum $|R/L_{Te}|$ for the central barriers (in green), the strong co-CD off-axis eITBs (in red) and the corresponding OH (in cyan) scenarios as a function of the maximum $|R/L_{Te}|$. The shot number of some important discharges discussed in Secs.5.4 and 5.5 are highlighted beside the corresponding $v_{E \times B}$ values. The negative values correspond to a drift velocity in the counter clockwise direction.

E.3 Effect of MHD activity on the central barrier and co-CD off-axis eITB scenarios

E.3.1 Oscillation-mode regime in a central barrier
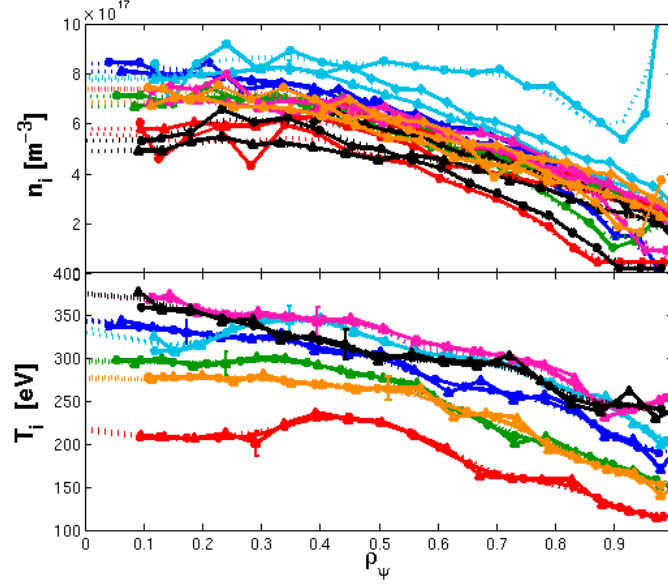
Figure E.17: Carbon ion density and temperature for shot #46080 (same color convention as Fig.D.8).

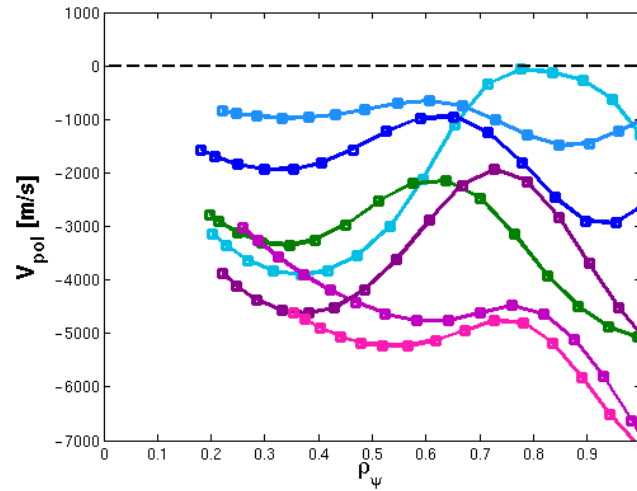## E.3.2 Oscillation-mode regime in a co-CD off-axis eITB

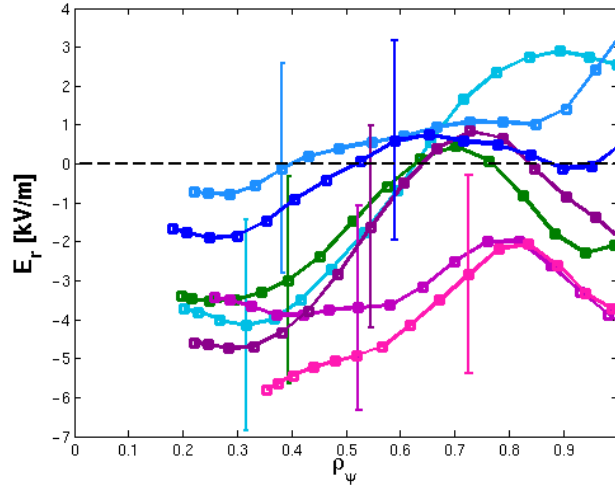**Figure E.18:** v_{pol} for shot #46094 (same color convention as Fig.D.12).

Figure E.19: E_r for shot #46094 (same color convention as Fig.D.12).
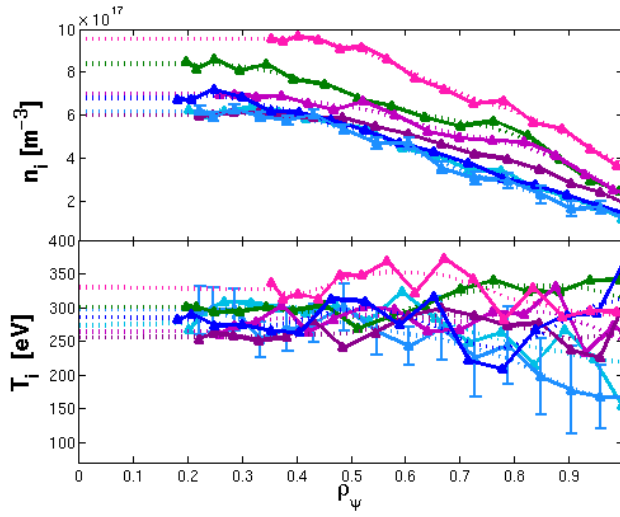

Figure E.20: Carbon ion density and temperature for shot #46094 (same color convention as Fig.D.12).

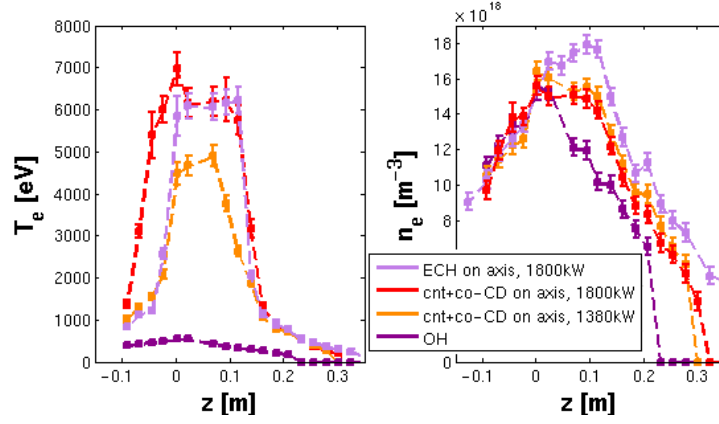# E.4 Effect of total and central power in a co-CD off-axis eITB

Figure E.21: Electron temperature (left) and density (right) for discharges #47418 (900kW of co-CD off-axis and 900kW of ECH on-axis, in lilac), 47340 (900kW of co-CD off-axis and 900kW cnt+co-CD on-axis, in red), 47906 (460kW of co-CD off-axis and 900kW cnt+co-CD on-axis, in orange) and 47865 (OH, in violet).
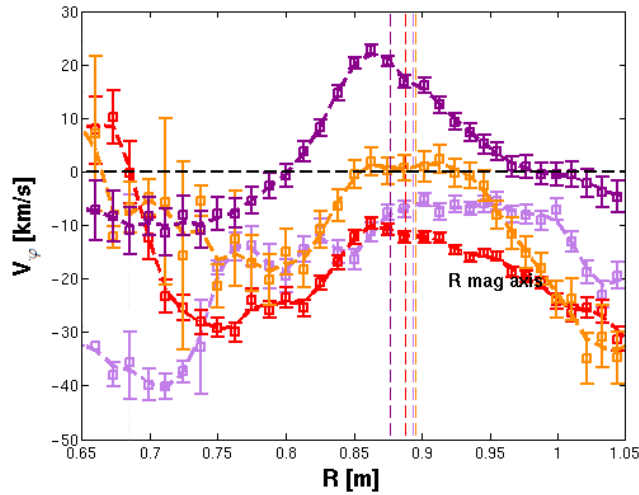

Figure E.22: v_φ as a function of R for shots #47418, 47340, 47906 and 47865 (same color convention as Fig.E.21). The vertical lines indicate the magnetic axis R_{mag} for each discharge.
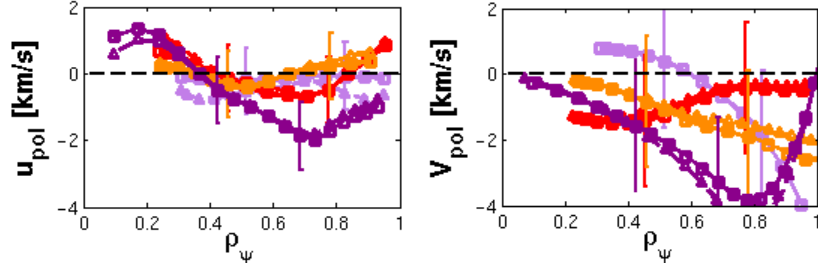
Figure E.23: Measured v_{pol} and calculated indirect u_{pol} for shots #47418, 47340, 47906 and 47865 (same color convention as Fig.E.21).
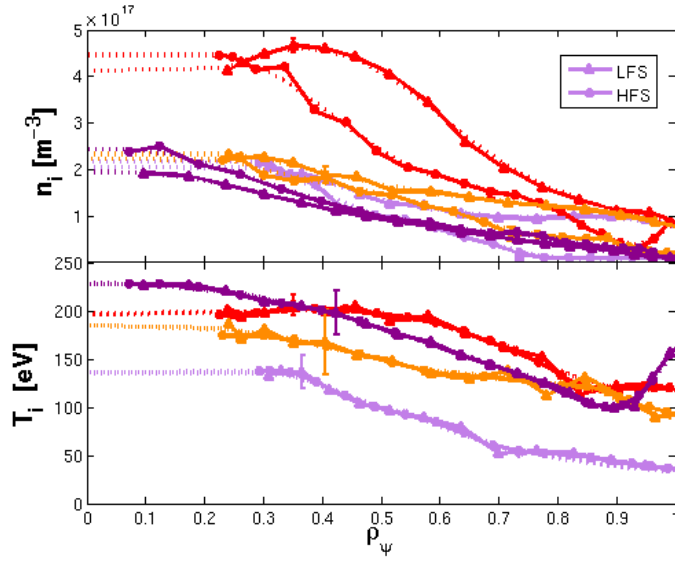

Figure E.24: Carbon ion density and temperature for shots #47418, 47340, 47906 and 47865 (same color convention as Fig.E.21).

Glossary

BS	Bootstrap (current)
CRPP	Centre de Recherches en Physique des Plasmas
CXRS	Charge eXchange Recombination Spectroscopy
DMPX	Duplex Multi-wire Proportional X-ray diagnostic
DNBI	Diagnostic Neutral Beam Injector
ECCD	Electron Cyclotron Current Drive
EC(R)H	Electron Cyclotron (Resonance) Heating
eITB	electron Internal Transport Barrier
ELM	Edge Localized Mode
FIR	Far InfraRed interferometer
HFS	High Field Side
H-mode	High confinement mode
ICRH	Ion Cyclotron Resonance Heating
IOH	Ohmic coil current control mode
ITER	"The Way" in Latin. International tokamak experiment under construction in Cadarache (France)
ITG	Ion Temperature Gradient
LCFS	Last Closed Flux Surface
LFS	Low Field Side
LIUQE	TCV offline equilibrium reconstruction code
MHD	MagnetoHydroDynamic
NBH	Neutral Beam Heating
NTM	Neoclassical Tearing Mode
OH	OHmic heating
PLFS	Poloidal Low Field Side CXRS system
RT	Real Time
SOL	Scrape Off Layer
ST	Sawtooth
TCV	Tokamak à Configuration Variable
TEM	Trapped Electron Mode
THFS	Toroidal High Field Side CXRS system
TLFS	Toroidal Low Field Side CXRS system

Bibliography

[1]   J. Wesson. *Tokamaks*. Clarendon Press Oxford, 2004.

[2]   J. P. Freidberg. *Ideal Magnetohydrodynamics*. Plenum Press, New York, 1987.

[3]   R. J. Goldston. *Introduction to plasma physics*. Institute of Physics Publishing, Bristol and Philadelphia, 1997.

[4]   F. Hofmann et al. "Experimental and Theoretical Stability Limits of Highly Elongated Tokamak Plasmas." In: *Phys. Rev. Lett.* 81 (14 1998), pp. 2918–2921. DOI: 10.1103/PhysRevLett.81.2918. URL: http://link.aps.org/doi/10.1103/PhysRevLett.81.2918.

[5]   A. D. Turnbull et al. "Current and beta limitations for the TCV tokamak." In: *Nuclear Fusion* 28.8 (1988), p. 1379. DOI: 10.1088/0029-5515/28/8/006. URL: http://stacks.iop.org/0029-5515/28/i=8/a=006.

[6]   Y. Camenen. "Étude du transport d'énergie thermique dans les plasmas du tokamak à configuration variable au moyen de chauffage électronique cyclotronique." PhD thesis. EPFL LAUSANNE, 2006. DOI: 10.5075/epfl-thesis-3618.

[7]   F. Troyon et al. "MHD-Limits to Plasma Confinement." In: *Plasma Physics and Controlled Fusion* 26.1A (1984), p. 209. DOI: 10.1088/0741-3335/26/1A/319. URL: http://stacks.iop.org/0741-3335/26/i=1A/a=319.

[8]   E. Lerche et al. "Optimizing ion-cyclotron resonance frequency heating for ITER: dedicated JET experiments." In: *Plasma Physics and Controlled Fusion* 53.12 (2011), p. 124019. DOI: 10.1088/0741-3335/53/12/124019. URL: http://stacks.iop.org/0741-3335/53/i=12/a=124019.

[9]   O. Sauter et al. "Steady-State Fully Noninductive Current Driven by Electron Cyclotron Waves in a Magnetically Confined Plasma." In: *Phys. Rev. Lett.* 84 (15 2000), pp. 3322–3325. DOI: 10.1103/PhysRevLett.84.3322. URL: http://link.aps.org/doi/10.1103/PhysRevLett.84.3322.

[10]   J. Jacquinot and G. T. Hoang. "Progress Toward Steady-State Operation on Tore Supra." In: *Plasma Science and Technology* 6.1 (2004), p. 2101. DOI: 10.1088/1009-0630/6/1/001. URL: http://stacks.iop.org/1009-0630/6/i=1/a=001.

[11]   O. Sauter et al. "Inductive Current Density Perturbations to Probe Electron Internal Transport Barriers in Tokamaks." In: *Phys. Rev. Lett.* 94 (10 2005), p. 105002. DOI: 10.1103/PhysRevLett.94.105002. URL: http://link.aps.org/doi/10.1103/PhysRevLett.94.105002.

[12] V. V. Alikaev and V. V. Parail. "Current drive by electron cyclotron waves." In: *Plasma Physics and Controlled Fusion* 33.13 (1991), p. 1639. DOI: 10.1088/0741-3335/33/13/011. URL: http://stacks.iop.org/0741-3335/33/i=13/a=011.

[13] R. Prater. "Heating and current drive by electron cyclotron waves." In: *Physics of Plasmas* 11.5 (2004), pp. 2349–2376. DOI: 10.1063/1.1690762. URL: http://link.aip.org/link/?PHP/11/2349/1.

[14] A. G. Peeters. "The bootstrap current and its consequences." In: *Plasma Physics and Controlled Fusion* 42.12B (2000), B231. DOI: 10.1088/0741-3335/42/12B/318. URL: http://stacks.iop.org/0741-3335/42/i=12B/a=318.

[15] M. C. Zarnstorff et al. "Bootstrap current in TFTR." In: *Phys. Rev. Lett.* 60 (13 1988), pp. 1306–1309. DOI: 10.1103/PhysRevLett.60.1306. URL: http://link.aps.org/doi/10.1103/PhysRevLett.60.1306.

[16] A. D. Turnbull et al. "Synergism between cross-section and profile shaping in beta optimization of tokamak equilibria with negative central shear." In: *Nuclear Fusion* 38.10 (1998), p. 1467. DOI: 10.1088/0029-5515/38/10/305. URL: http://stacks.iop.org/0029-5515/38/i=10/a=305.

[17] K. H. Burrell. "Tests of causality: Experimental evidence that sheared E x B flow alters turbulence and transport in tokamaks." In: *Physics of Plasmas* 6.12 (1999), pp. 4418–4435. DOI: 10.1063/1.873728. URL: http://link.aip.org/link/?PHP/6/4418/1.

[18] F. Wagner et al. "Regime of Improved Confinement and High Beta in Neutral-Beam-Heated Divertor Discharges of the ASDEX Tokamak." In: *Phys. Rev. Lett.* 49 (19 1982), pp. 1408–1412. DOI: 10.1103/PhysRevLett.49.1408. URL: http://link.aps.org/doi/10.1103/PhysRevLett.49.1408.

[19] R. C. Wolf et al. "Characterization of ion heat conduction in JET and ASDEX Upgrade plasmas with and without internal transport barriers." In: *Plasma Physics and Controlled Fusion* 45.9 (2003), p. 1757. DOI: 10.1088/0741-3335/45/9/313. URL: http://stacks.iop.org/0741-3335/45/i=9/a=313.

[20] A. Bortolon. "Plasma rotation and momentum transport studies in the TCV tokamak based on charge exchange spectroscopy measurements." PhD thesis. EPFL LAUSANNE, 2009. DOI: 10.5075/epfl-thesis-4569.

[21] A. Bortolon et al. "Observation of Spontaneous Toroidal Rotation Inversion in Ohmically Heated Tokamak Plasmas." In: *Phys. Rev. Lett.* 97 (23 2006), p. 235003. DOI: 10.1103/PhysRevLett.97.235003. URL: http://link.aps.org/doi/10.1103/PhysRevLett.97.235003.

[22] B. P. Duval et al. "Spontaneous L-mode plasma rotation scaling in the TCV tokamak." In: *Physics of Plasmas* 15.5 (2008), p. 056113. DOI: 10.1063/1.2841528. URL: http://link.aip.org/link/?PHP/15/056113/1.

[23] E. J. Doyle (Chair Transport Physics) et al. "Chapter 2: Plasma confinement and transport." In: *Nuclear Fusion* 47.6 (2007), S18. DOI: 10.1088/0029-5515/47/6/S02. URL: http://stacks.iop.org/0029-5515/47/i=6/a=S02.

[24] J.-M. Moret et al. "Magnetic measurements on the TCV Tokamak." In: *Review of Scientific Instruments* 69.6 (1998), pp. 2333–2348. DOI: 10.1063/1.1148940. URL: http://link.aip.org/link/?RSI/69/2333/1.

[25] J. Rossel. "Edge Localized Mode Control in TCV." PhD thesis. EPFL LAUSANNE, 2012. DOI: 10.5075/epfl-thesis-5311.

[26] J.-M. Moret, F. Buhlmann, and G. Tonetti. "Fast single loop diamagnetic measurements on the TCV tokamak." In: *Review of Scientific Instruments* 74.11 (2003), pp. 4634–4643. DOI: 10.1063/1.1614856. URL: http://link.aip.org/link/?RSI/74/4634/1.

[27] F. Hofmann and G. Tonetti. "Tokamak equilibrium reconstruction using Faraday rotation measurements." In: *Nuclear Fusion* 28.10 (1988), p. 1871. DOI: 10.1088/0029-5515/28/10/014. URL: http://stacks.iop.org/0029-5515/28/i=10/a=014.

[28] I. H. Hutchinson. *Principles of plasma diagnostic.* Cambridge University Press, 1992.

[29] S. Franke. "Application of Thomson scattering at 1.06 μm as a diagnostic for spatial profile measurements of electron temperature and density on the TCV tokamak." PhD thesis. EPFL LAUSANNE, 1997. DOI: 10.5075/epfl-thesis-1654.

[30] A. Pitzschke. "Pedestal characteristics and MHD stability of H-Mode plasmas in TCV." PhD thesis. EPFL LAUSANNE, 2011. DOI: 10.5075/epfl-thesis-4917.

[31] S. Barry. "The extension of the FIR Interferometer of TCV to a polarimeter and measurements of the Faraday rotation caused by the poloidal magnetic field." PhD thesis. EPFL LAUSANNE, 1999.

[32] V. S. Udintsev et al. "Recent Electron Cyclotron Emission Results on TCV." In: *Fusion Science and Technology* 52.2 (), pp. 161–168. URL: http://www.ans.org/pubs/journals/fst/a__1495.

[33] V. Vuille and L.Porte et al. "Investigation of turbulence and zonal flows for different shapes and scenarios in TCV using correlation ECE." In: *40th European Physical Society Conference on Plasma Physics* Poster P2.176.Espoo,Finland (2013).

[34] *Technology description YIG tuned filters.* URL: http://www.microlambdawireless.com/apppdfs/ytfdefinitions2.pdf.

[35] P. Bosshard. "Confinement ionique dans le tokamak TCV mesuré par spectroscopie d'échange de charge." PhD thesis. EPFL LAUSANNE, 2003. DOI: 10.5075/epfl-thesis-2723.

[36] C. Schlatter. "Turbulent ion heating in TCV tokamak plasmas." PhD thesis. EPFL LAUSANNE, 2009. DOI: 10.5075/epfl-thesis-4479.

[37] M. Mironov. *DOUBLE-TCV: Simulation of CX fluxes emitted by tokamak plasma.* Ioffe Physico-Technical Institute, St. Petersburg, Russian Federation, 2006.

[38] L. Curchod. "High density plasma heating in the Tokamak à Configuration Variable." PhD thesis. EPFL LAUSANNE, 2011. DOI: 10.5075/epfl-thesis-5012.

[39] I. Furno. "Fast transient transport phenomena measured by soft X-ray emission in TCV tokamak plasmas." PhD thesis. EPFL LAUSANNE, 2001.

[40] J. I. Paley et al. "From profile to sawtooth control: developing feedback control using ECRH/ECCD systems on the TCV tokamak." In: *Plasma Physics and Controlled Fusion* 51.12 (2009), p. 124041. DOI: 10.1088/0741-3335/51/12/124041. URL: http://stacks.iop.org/0741-3335/51/i=12/a=124041.

[41] J. I. Paley et al. "Architecture and commissioning of the TCV distributed feedback control system." In: *Real Time Conference (RT), 2010 17th IEEE-NPSS*. 2010, pp. 1–6. DOI: 10.1109/RTC.2010.5750487. URL: http://ieeexplore.ieee.org/stamp/stamp.jsp?tp=&arnumber=5750487&isnumber=5750311.

[42] F. Felici. "Real-Time Control of Tokamak Plasmas: from Control of Physics to Physics-Based Control." PhD thesis. EPFL LAUSANNE, 2011. DOI: 10.5075/epfl-thesis-5203.

[43] A. H. Kritz et al. In: *Proc. 3rd Varenna-Grenoble Int. Symposium on Heating in Toroidal Plasmas* II.Brussels (1982), p. 707.

[44] H. Lütjens, A. Bondeson, and O. Sauter. "The CHEASE code for toroidal MHD equilibria." In: *Computer Physics Communications* 97.3 (1996), pp. 219–260. DOI: http://dx.doi.org/10.1016/0010-4655(96)00046-X. URL: http://www.sciencedirect.com/science/article/pii/001046559600046X.

[45] R. J. Fonck, D. S. Darrow, and K. P. Jaehnig. "Determination of plasma-ion velocity distribution via charge-exchange recombination spectroscopy." In: *Phys. Rev. A* 29 (6 June 1984), pp. 3288–3309. DOI: 10.1103/PhysRevA.29.3288. URL: http://link.aps.org/doi/10.1103/PhysRevA.29.3288.

[46] A. N. Karpushov et al. "The diagnostic neutral beam injector with arc-discharge plasma source on the TCV Tokamak." In: *Fusion Engineering and Design* 94.2 (2009), pp. 993–997. DOI: 10.1016/j.fusengdes.2008.12.006. URL: http://www.sciencedirect.com/science/article/pii/S0920379608004626.

[47] A. Karpushov. In: *Private communication* (2013).

[48] Ch. Schlatter, B. P. Duval, and A. N. Karpushov. "Reconstruction of ion temperature profiles from single chord NPA measurements on the TCV tokamak." In: *Plasma Physics and Controlled Fusion* 48.12 (2006), p. 1765. DOI: 10.1088/0741-3335/48/12/006. URL: http://stacks.iop.org/0741-3335/48/i=12/a=006.

[49] Y. B. Kim, P. H. Diamond, and R. J. Groebner. "Neoclassical poloidal and toroidal rotation in tokamaks." In: *Physics of Fluids B: Plasma Physics (1989-1993)* 3.8 (1991), pp. 2050–2060. DOI: http://dx.doi.org/10.1063/1.859671. URL: http://scitation.aip.org/content/aip/journal/pofb/3/8/10.1063/1.859671.

[50] A. Scarabosio et al. "Toroidal plasma rotation in the TCV tokamak." In: *Plasma Physics and Controlled Fusion* 48.5 (2006), p. 663. DOI: 10.1088/0741-3335/48/5/012. URL: http://stacks.iop.org/0741-3335/48/i=5/a=012.

[51] A. Bortolon et al. "Indirect measurement of poloidal rotation using inboard-outboard asymmetry of toroidal rotation and comparison with neoclassical predictions." In: *Nuclear Fusion* 53.2 (2013), p. 023002. DOI: 10.1088/0029-5515/53/2/023002. URL: http://stacks.iop.org/0029-5515/53/i=2/a=023002.

[52] A. G. Peeters. "Reduced charge state equations that describe Pfirsch Schlüter impurity transport in tokamak plasma." In: *Physics of Plasmas* 7.1 (2000), pp. 268–275. DOI: 10.1063/1.873812. URL: http://link.aip.org/link/?PHP/7/268/1.

[53] B. A. Grierson et al. "Measurements of the deuterium ion toroidal rotation in the DIII-D tokamak and comparison to neoclassical theory)." In: *Physics of Plasmas* 19.5 (2012). DOI: http://dx.doi.org/10.1063/1.3694656. URL: http://scitation.aip.org/content/aip/journal/pop/19/5/10.1063/1.3694656.

[54] J. A. Boedo et al. "Poloidally and radially resolved parallel D+ velocity measurements in the DIII-D boundary and comparison to neoclassical computations." In: *Physics of Plasmas (1994-present)* 18.3 (2011). DOI: http://dx.doi.org/10.1063/1.3559492. URL: http://scitation.aip.org/content/aip/journal/pop/18/3/10.1063/1.3559492.

[55] R. E. Bell et al. "Comparison of poloidal velocity measurements to neoclassical theory on the National Spherical Torus Experimenta)." In: *Physics of Plasmas (1994-present)* 17.8 (2010). DOI: http://dx.doi.org/10.1063/1.3478571. URL: http://scitation.aip.org/content/aip/journal/pop/17/8/10.1063/1.3478571.

[56] A. R. Field et al. "Comparison of measured poloidal rotation in MAST spherical tokamak plasmas with neo-classical predictions." In: *Plasma Physics and Controlled Fusion* 51.10 (2009), p. 105002. DOI: 10.1088/0741-3335/51/10/105002. URL: http://stacks.iop.org/0741-3335/51/i=10/a=105002.

[57] E. Viezzer et al. "Investigation of passive edge emission in charge exchange spectra at the ASDEX Upgrade tokamak." In: *Plasma Physics and Controlled Fusion* 53.3 (2011), p. 035002. DOI: 10.1088/0741-3335/53/3/035002. URL: http://stacks.iop.org/0741-3335/53/i=3/a=035002.

[58] K. D. Marr et al. "Comparison of neoclassical predictions with measured flows and evaluation of a poloidal impurity density asymmetry." In: *Plasma Physics and Controlled Fusion* 52.5 (2010), p. 055010. DOI: 10.1088/0741-3335/52/5/055010. URL: http://stacks.iop.org/0741-3335/52/i=5/a=055010.

[59] R. E. Bell et al. "Poloidal Rotation in TFTR Reversed Shear Plasmas." In: *Phys. Rev. Lett.* 81 (7 1998), pp. 1429–1432. DOI: 10.1103/PhysRevLett.81.1429. URL: http://link.aps.org/doi/10.1103/PhysRevLett.81.1429.

[60] K. Crombé et al. "Poloidal Rotation Dynamics, Radial Electric Field, and Neoclassical Theory in the Jet Internal-Transport-Barrier Region." In: *Phys. Rev. Lett.* 95 (15 2005), p. 155003. DOI: 10.1103/PhysRevLett.95.155003. URL: http://link.aps.org/doi/10.1103/PhysRevLett.95.155003.

[61] W. M. Solomon et al. "Experimental test of the neoclassical theory of impurity poloidal rotation in tokamaksa)." In: *Physics of Plasmas (1994-present)* 13.5 (2006). DOI: http://dx.doi.org/10.1063/1.2180728. URL: http://scitation.aip.org/content/aip/journal/pop/13/5/10.1063/1.2180728.

[62] *iXon Ultra and iXon3.* URL: https://crpplocal.epfl.ch/wiki/images/e/e5/Andor_iXon3_EMCCD_Brochure.pdf.

[63] *Fundamentals of EMCCD Tutorial.* URL: http://www.emccd.com/.

[64] R. N. Tubbs. "Lucky Exposures: Diffraction Limited Astronomical Imaging Through the Atmosphere." PhD thesis. St Johns College Cambridge University, UK, 2003.

[65] T. P. Goodman et al. "Sawtooth Pacing by Real-Time Auxiliary Power Control in a Tokamak Plasma." In: *Phys. Rev. Lett.* 106 (24 2011), p. 245002. DOI: 10.1103/PhysRevLett.106.245002. URL: http://link.aps.org/doi/10.1103/PhysRevLett.106.245002.

[66] I. Titov and A. Karpushov. "New control algorithm for DNBI RT (real time) triggering." In: *CRRP Report, Private communication* (2011).

[67] A. N. Karpushov. "Charge exchange recombination spectroscopy measurement of ion temperature, rotation and impurity density profiles on the TCV tokamak." In: *Proc. 39th European Physical Society Conf. on Plasma Physics* (2012), P2.037.

[68] E. Viezzer et al. "High-resolution charge exchange measurements at ASDEX Upgrade." In: *Review of Scientific Instruments* 83.10 (2012). DOI: http://dx.doi.org/10.1063/1.4755810. URL: http://scitation.aip.org/content/aip/journal/rsi/83/10/10.1063/1.4755810.

[69] A. Karpushov et al. "Charge-eXchange Recombination Spectroscopy (CXRS) measurement on the TCV with fresh first wall (after boronisation)." In: *TCV scientific meeting, Private communication* (2012).

[70] W. M. Solomon et al. "Advances in understanding the generation and evolution of the toroidal rotation profile on DIII-D." In: *Nuclear Fusion* 49.8 (2009), p. 085005. DOI: 10.1088/0029-5515/49/8/085005. URL: http://stacks.iop.org/0029-5515/49/i=8/a=085005.

[71] J. S. deGrassie. "Tokamak rotation sources, transport and sinks." In: *Plasma Physics and Controlled Fusion* 51.12 (2009), p. 124047. DOI: 10.1088/0741-3335/51/12/124047. URL: http://stacks.iop.org/0741-3335/51/i=12/a=124047.

[72] J. S. deGrassie et al. "Intrinsic toroidal velocity near the edge of DIII-D H-mode plasmas." In: *Nuclear Fusion* 49.8 (2009), p. 085020. DOI: 10.1088/0029-5515/49/8/085020. URL: http://stacks.iop.org/0029-5515/49/i=8/a=085020.

[73] P. C. de Vries et al. "Scaling of rotation and momentum confinement in JET plasmas." In: *Nuclear Fusion* 48.6 (2008), p. 065006. DOI: 10.1088/0029-5515/48/6/065006. URL: http://stacks.iop.org/0029-5515/48/i=6/a=065006.

[74] B. P. Duval et al. "Bulk plasma rotation in the TCV tokamak in the absence of external momentum input." In: *Plasma Physics and Controlled Fusion* 49.12B (2007), B195. DOI: 10.1088/0741-3335/49/12B/S18. URL: http://stacks.iop.org/0741-3335/49/i=12B/a=S18.

[75] R. M. McDermott et al. "Core momentum and particle transport studies in the ASDEX Upgrade tokamak." In: *Plasma Physics and Controlled Fusion* 53.12 (2011), p. 124013. DOI: 10.1088/0741-3335/53/12/124013. URL: http://stacks.iop.org/0741-3335/53/i=12/a=124013.

[76] A. G. Peeters et al. "Overview of toroidal momentum transport." In: *Nuclear Fusion* 51.9 (2011), p. 094027. DOI: 10.1088/0029-5515/51/9/094027. URL: http://stacks.iop.org/0029-5515/51/i=9/a=094027.

[77] N. Mattor and P. H. Diamond. "Momentum and thermal transport in neutral beam heated tokamaks." In: *Physics of Fluids* 31.5 (1988), pp. 1180–1189. DOI: http://dx.doi.org/10.1063/1.866747. URL: http://scitation.aip.org/content/aip/journal/pof1/31/5/10.1063/1.866747.

[78] S. D. Scott et al. "Local measurements of correlated momentum and heat transport in the TFTR tokamak." In: *Phys. Rev. Lett.* 64 (5 1990), pp. 531–534. DOI: 10.1103/PhysRevLett.64.531. URL: http://link.aps.org/doi/10.1103/PhysRevLett.64.531.

[79] Y. Camenen et al. "Experimental Evidence of Momentum Transport Induced by an Up-Down Asymmetric Magnetic Equilibrium in Toroidal Plasmas." In: *Phys. Rev. Lett.* 105 (13 2010), p. 135003. DOI: 10.1103/PhysRevLett.105.135003. URL: http://link.aps.org/doi/10.1103/PhysRevLett.105.135003.

[80] F. J. Casson et al. "Anomalous parallel momentum transport due to ExB flow shear in a tokamak plasma." In: *Physics of Plasmas* 16.9 (2009). DOI: http://dx.doi.org/10.1063/1.3227650. URL: http://scitation.aip.org/content/aip/journal/pop/16/9/10.1063/1.3227650.

[81] C. J. McDevitt et al. "Toroidal Rotation Driven by the Polarization Drift." In: *Phys. Rev. Lett.* 103 (20 2009), p. 205003. DOI: 10.1103/PhysRevLett.103.205003. URL: http://link.aps.org/doi/10.1103/PhysRevLett.103.205003.

[82] Ö. D. Gürcan et al. "Residual parallel Reynolds stress due to turbulence intensity gradient in tokamak plasmas." In: *Physics of Plasmas* 17.11 (2010). DOI: http://dx.doi.org/10.1063/1.3503624. URL: http://scitation.aip.org/content/aip/journal/pop/17/11/10.1063/1.3503624.

[83] T. Stoltzfus-Dueck. "Transport-Driven Toroidal Rotation in the Tokamak Edge." In: *Phys. Rev. Lett.* 108 (6 Feb. 2012), p. 065002. DOI: 10.1103/PhysRevLett.108.065002. URL: http://link.aps.org/doi/10.1103/PhysRevLett.108.065002.

[84] J. E. Rice et al. "Spontaneous core toroidal rotation in Alcator C-Mod L-mode, H-mode and ITB plasmas." In: *Plasma Physics and Controlled Fusion* 50.12 (2008), p. 124042. DOI: 10.1088/0741-3335/50/12/124042. URL: http://stacks.iop.org/0741-3335/50/i=12/a=124042.

[85]   J. E. Rice et al. "Inter-machine comparison of intrinsic toroidal rotation in tokamaks." In: *Nuclear Fusion* 47.11 (2007), p. 1618. DOI: 10.1088/0029-5515/47/11/025. URL: http://stacks.iop.org/0029-5515/47/i=11/a=025.

[86]   C. Angioni et al. "Intrinsic Toroidal Rotation, Density Peaking, and Turbulence Regimes in the Core of Tokamak Plasmas." In: *Phys. Rev. Lett.* 107 (21 2011), p. 215003. DOI: 10.1103/PhysRevLett.107.215003. URL: http://link.aps.org/doi/10.1103/PhysRevLett.107.215003.

[87]   C. Angioni et al. "Off-diagonal particle and toroidal momentum transport: a survey of experimental, theoretical and modelling aspects." In: *Nuclear Fusion* 52.11 (2012), p. 114003. DOI: 10.1088/0029-5515/52/11/114003. URL: http://stacks.iop.org/0029-5515/52/i=11/a=114003.

[88]   R. M. McDermott et al. "Effect of electron cyclotron resonance heating (ECRH) on toroidal rotation in ASDEX Upgrade H-mode discharges." In: *Plasma Physics and Controlled Fusion* 53.3 (2011), p. 035007. DOI: 10.1088/0741-3335/53/3/035007. URL: http://stacks.iop.org/0741-3335/53/i=3/a=035007.

[89]   J. E. Rice et al. "Non-local heat transport, rotation reversals and up/down impurity density asymmetries in Alcator C-Mod ohmic L-mode plasmas." In: *Nuclear Fusion* 53.3 (2013), p. 033004. DOI: 10.1088/0029-5515/53/3/033004. URL: http://stacks.iop.org/0029-5515/53/i=3/a=033004.

[90]   S. von Goeler, W. Stodiek, and N. Sauthoff. "Studies of Internal Disruptions and $m = 1$ Oscillations in Tokamak Discharges with Soft X-Ray Techniques." In: *Phys. Rev. Lett.* 33 (1974), pp. 1201–1203. DOI: 10.1103/PhysRevLett.33.1201. URL: http://link.aps.org/doi/10.1103/PhysRevLett.33.1201.

[91]   T. C. Hender et al. "Chapter 3: MHD stability, operational limits and disruptions." In: *Nuclear Fusion* 47.6 (2007), S128. DOI: 10.1088/0029-5515/47/6/S03. URL: http://stacks.iop.org/0029-5515/47/i=6/a=S03.

[92]   I. Furno et al. "Understanding sawtooth activity during intense electron cyclotron heating experiments on TCV." In: *Nuclear Fusion* 41.4 (2001), p. 403. DOI: 10.1088/0029-5515/41/4/306. URL: http://stacks.iop.org/0029-5515/41/i=4/a=306.

[93]   F. D. Halpern, H. Lütjens, and J-F. Luciani. "Diamagnetic thresholds for sawtooth cycling in tokamak plasmas." In: *Physics of Plasmas* 18.10 (2011). DOI: http://dx.doi.org/10.1063/1.3646305. URL: http://scitation.aip.org/content/aip/journal/pop/18/10/10.1063/1.3646305.

[94]   O. Sauter et al. "Beta limits in long-pulse tokamak discharges." In: *Physics of Plasmas* 4.5 (1997), pp. 1654–1664. DOI: 10.1063/1.872270. URL: http://link.aip.org/link/?PHP/4/1654/1.

[95]   G. P. Canal et al. "Fast seeding of NTMs by sawtooth crashes in TCV and their preemption using ECRH." In: *Nuclear Fusion* 53.11 (2013), p. 113026. DOI: 10.1088/0029-5515/53/11/113026. URL: http://stacks.iop.org/0029-5515/53/i=11/a=113026.

[96] O. Sauter et al. "Effects of ECH/ECCD on Tearing Modes in TCV and Link to Rotation Profile." In: *Proc. 23rd IAEA Fusion Energy Conference (Daejon, Korea)*. paper EXS/P2-17. 2010. URL: http://www-pub.iaea.org/mtcd/meetings/cn180_papers.asp.

[97] O. Sauter et al. "On the non-stiffness of edge transport in L-mode tokamak plasmas." In: *Physics of Plasmas* 21.5 (2014).

[98] Y. Martin et al. "Impurity Transport in TCV: Neoclassical and Turbulent Contributions." In: *Proc. 23rd IAEA Fusion Energy Conference (Daejon, Korea)*. paper EXS/P8-13. 2010. URL: http://www-pub.iaea.org/mtcd/meetings/cn180_papers.asp.

[99] A. Merle. In: *Private communication* (2013).

[100] C. Angioni et al. "Effects of localized electron heating and current drive on the sawtooth period." In: *Nuclear Fusion* 43.6 (2003), p. 455. DOI: 10.1088/0029-5515/43/6/308. URL: http://stacks.iop.org/0029-5515/43/i=6/a=308.

[101] B. P. Duval et al. "Momentum transport in TCV across sawteeth events." In: *Proc. 23rd IAEA Fusion Energy Conference (Daejon, Korea)*. paper EXS/P4-01. 2010. URL: http://www-pub.iaea.org/mtcd/meetings/cn180_papers.asp.

[102] B. P. Duval et al. "Effect of Sawteeth on the Spontaneous TCV Plasma Rotation." In: *35th EPS Conference on Plasma Physics (Hersonissos, Greece*. paper P-2.020. 2008. URL: http://epsppd.epfl.ch/Hersonissos/pdf/P2_020.pdf.

[103] D. L. Brower, W. X. Ding, and L. Lin. "Fluctuation-Induced Momentum Transport and Plasma Flows in the MST Reversed Field Pinch." In: *Proc. 23rd IAEA Fusion Energy Conference (Daejon, Korea)*. paper EXS/P4-02. 2010. URL: http://www-pub.iaea.org/mtcd/meetings/cn180_papers.asp.

[104] G. Hommen et al. "Optical boundary reconstruction of tokamak plasmas for feedback control of plasma position and shape." In: *Review of Scientific Instruments* 81.11 (2010). DOI: http://dx.doi.org/10.1063/1.3499219. URL: http://scitation.aip.org/content/aip/journal/rsi/81/11/10.1063/1.3499219.

[105] G. V. Pereverzev and P. N. Yushmanov. "ASTRA Automated System for TRansport Analysis in a Tokamak." In: *Tech. Rep* IPP Report.5/98 (2002).

[106] V. S. Udintsev et al. "Experimental observation of m/n = 1/1 mode behaviour during sawtooth activity and its manifestations in tokamak plasmas." In: *Plasma Physics and Controlled Fusion* 47.8 (2005), p. 1111. DOI: 10.1088/0741-3335/47/8/001. URL: http://stacks.iop.org/0741-3335/47/i=8/a=001.

[107] F. M. Levinton et al. "Improved Confinement with Reversed Magnetic Shear in TFTR." In: *Phys. Rev. Lett.* 75 (24 1995), pp. 4417–4420. DOI: 10.1103/PhysRevLett.75.4417. URL: http://link.aps.org/doi/10.1103/PhysRevLett.75.4417.

[108]   C. Gormezano et al. "Internal Transport Barriers in JET Deuterium-Tritium Plasmas." In: *Phys. Rev. Lett.* 80 (25 1998), pp. 5544–5547. DOI: 10.1103/PhysRevLett.80.5544. URL: http://link.aps.org/doi/10.1103/PhysRevLett.80.5544.

[109]   C. D. Challis et al. "Effect of q-profile modification by LHCD on internal transport barriers in JET." In: *Plasma Physics and Controlled Fusion* 43.7 (2001), p. 861. DOI: 10.1088/0741-3335/43/7/303. URL: http://stacks.iop.org/0741-3335/43/i=7/a=303.

[110]   Y. Koide et al. "Internal transport barrier on q=3 surface and poloidal plasma spin up in JT-60U high-β_p discharges." In: *Phys. Rev. Lett.* 72 (23 1994), pp. 3662–3665. DOI: 10.1103/PhysRevLett.72.3662. URL: http://link.aps.org/doi/10.1103/PhysRevLett.72.3662.

[111]   T. Fujita et al. "Internal Transport Barrier for Electrons in JT-60U Reversed Shear Discharges [Phys. Rev. Lett. 78, 2377 (1997)]." In: *Phys. Rev. Lett.* 78 (23 1997), pp. 4529–4529. DOI: 10.1103/PhysRevLett.78.4529. URL: http://link.aps.org/doi/10.1103/PhysRevLett.78.4529.

[112]   E. J. Strait et al. "Enhanced Confinement and Stability in DIII-D Discharges with Reversed Magnetic Shear." In: *Phys. Rev. Lett.* 75 (24 1995), pp. 4421–4424. DOI: 10.1103/PhysRevLett.75.4421. URL: http://link.aps.org/doi/10.1103/PhysRevLett.75.4421.

[113]   M. E. Austin et al. "Core barrier formation near integer q surfaces in DIII-D." In: *Physics of Plasmas* 13.8 (2006). DOI: http://dx.doi.org/10.1063/1.2245579. URL: http://scitation.aip.org/content/aip/journal/pop/13/8/10.1063/1.2245579.

[114]   R. C. Wolf et al. "Stationary advanced scenarios with internal transport barrier on ASDEX Upgrade." In: *Plasma Physics and Controlled Fusion* 41.12B (1999), B93. DOI: 10.1088/0741-3335/41/12B/306. URL: http://stacks.iop.org/0741-3335/41/i=12B/a=306.

[115]   O. Gruber et al. "Internal transport barrier discharges on ASDEX upgrade: progress towards steady state." In: *Plasma Physics and Controlled Fusion* 42.5A (2000), A117. DOI: 10.1088/0741-3335/42/5A/311. URL: http://stacks.iop.org/0741-3335/42/i=5A/a=311.

[116]   X. Litaudon et al. "Stationary magnetic shear reversal experiments in Tore Supra." In: *Plasma Physics and Controlled Fusion* 38.9 (1996), p. 1603. DOI: 10.1088/0741-3335/38/9/006. URL: http://stacks.iop.org/0741-3335/38/i=9/a=006.

[117]   G. T. Hoang et al. "Internal Transport Barrier with Ion-Cyclotron-Resonance Minority Heating on Tore Supra." In: *Phys. Rev. Lett.* 84 (20 2000), pp. 4593–4596. DOI: 10.1103/PhysRevLett.84.4593. URL: http://link.aps.org/doi/10.1103/PhysRevLett.84.4593.

[118]   S. Coda et al. "High-bootstrap, noninductively sustained electron internal transport barriers in the Tokamak à Configuration Variable." In: *Physics of Plasmas* 12.5 (2005), p. 056124. DOI: 10.1063/1.1896953. URL: http://link.aip.org/link/?PHP/12/056124/1.

[119]   O. Sauter et al. "Steady-state fully non-inductive reverse shear scenarios with electron ITB and dominant bootstrap current." In: *19th IAEA Fusion Energy Conference* Lyon (2002), EX/P5–06. URL: http://www-pub.iaea.org/mtcd/publications/pdf/csp_019c/html/node275.htm.

[120]   Z. A. Pietrzyk et al. "Long-Pulse Improved Central Electron Confinement in the TCV Tokamak with Electron Cyclotron Heating and Current Drive." In: *Phys. Rev. Lett.* 86 (8 2001), pp. 1530–1533. DOI: 10.1103/PhysRevLett.86.1530. URL: http://link.aps.org/doi/10.1103/PhysRevLett.86.1530.

[121]   M. A. Henderson et al. "Control of electron internal transport barriers in TCV." In: *Plasma Physics and Controlled Fusion* 46.5A (2004), A275. DOI: 10.1088/0741-3335/46/5A/030. URL: http://stacks.iop.org/0741-3335/46/i=5A/a=030.

[122]   J. W. Connor et al. "A review of internal transport barrier physics for steady-state operation of tokamaks." In: 44.4 (2004), R1. DOI: 10.1088/0029-5515/44/4/R01. URL: http://stacks.iop.org/0029-5515/44/i=4/a=R01.

[123]   F. Troyon et al. "MHD-Limits to Plasma Confinement." In: *Plasma Physics and Controlled Fusion* 26.1A (1984), p. 209. DOI: 10.1088/0741-3335/26/1A/319. URL: http://stacks.iop.org/0741-3335/26/i=1A/a=319.

[124]   L. L. Lao et al. "Rotational and magnetic shear stabilization of magnetohydrodynamic modes and turbulence in DIII-D high performance discharges." In: *Physics of Plasmas* 3.5 (1996), pp. 1951–1958. DOI: 10.1063/1.871991. URL: http://link.aip.org/link/?PHP/3/1951/1.

[125]   R. V .Budny et al. "Microturbulence and flow shear in high-performance JET ITB plasma." In: *Plasma Physics and Controlled Fusion* 44.7 (2002), p. 1215. DOI: 10.1088/0741-3335/44/7/311. URL: http://stacks.iop.org/0741-3335/44/i=7/a=311.

[126]   K. H. Burrell. "Effects of E x B velocity shear and magnetic shear on turbulence and transport in magnetic confinement devices." In: *Physics of Plasmas* 4.5 (1997), pp. 1499–1518. DOI: 10.1063/1.872367. URL: http://link.aip.org/link/?PHP/4/1499/1.

[127]   E. J. Synakowski. "Formation and structure of internal and edge transport barriers." In: *Plasma Physics and Controlled Fusion* 40.5 (1998), p. 581. DOI: 10.1088/0741-3335/40/5/006. URL: http://stacks.iop.org/0741-3335/40/i=5/a=006.

[128]   E. Joffrin et al. "MHD internal transport barrier triggering in low positive magnetic shear scenarios in JET." In: *Nuclear Fusion* 42.3 (2002), p. 235. DOI: 10.1088/0029-5515/42/3/302. URL: http://stacks.iop.org/0029-5515/42/i=3/a=302.

[129] T. P. Goodman et al. "Safety factor profile requirements for electron ITB formation in TCV." In: *Plasma Physics and Controlled Fusion* 47.12B (2005), B107. DOI: 10.1088/0741-3335/47/12B/S09. URL: http://stacks.iop.org/0741-3335/47/i=12B/a=S09.

[130] C. Zucca et al. "Current density evolution in electron internal transport barrier discharges in TCV." In: *Plasma Physics and Controlled Fusion* 51.1 (2009), p. 015002. DOI: 10.1088/0741-3335/51/1/015002. URL: http://stacks.iop.org/0741-3335/51/i=1/a=015002.

[131] A. Bottino et al. "Linear stability analysis of microinstabilities in electron internal transport barrier non-inductive discharges." In: *Plasma Physics and Controlled Fusion* 48.2 (2006), p. 215. DOI: 10.1088/0741-3335/48/2/004. URL: http://stacks.iop.org/0741-3335/48/i=2/a=004.

[132] X. Lapillonne et al. "Non-linear gyrokinetic simulations of microturbulence in TCV electron internal transport barriers." In: *Plasma Physics and Controlled Fusion* 53.5 (2011), p. 054011. DOI: 10.1088/0741-3335/53/5/054011. URL: http://stacks.iop.org/0741-3335/53/i=5/a=054011.

[133] T. Görler et al. "Flux- and gradient-driven global gyrokinetic simulation of tokamak turbulence." In: *Physics of Plasmas* 18.5 (2011), p. 056103. DOI: 10.1063/1.3567484. URL: http://link.aip.org/link/?PHP/18/056103/1.

[134] C. Angioni. "Modelling of electron transport and of sawtooth activity in tokamaks." PhD thesis. EPFL LAUSANNE, 2001. DOI: 10.5075/epfl-thesis-2469.

[135] O. Sauter et al. "Electron ITB in Fully Non-Inductive Reverse Shear Scenarios." In: *Proc. 29th EPS Conference on Controlled Fusion and Plasma Physics* 26B.Montreux (2002), P–2.087.

[136] S. Coda et al. "The physics of electron internal transport barriers in the TCV tokamak." In: *Nuclear Fusion* 47.7 (2007), p. 714. DOI: 10.1088/0029-5515/47/7/023. URL: http://stacks.iop.org/0029-5515/47/i=7/a=023.

[137] E. Fable et al. "Inward thermodiffusive particle pinch in electron internal transport barriers in TCV." In: *Plasma Physics and Controlled Fusion* 48.9 (2006), p. 1271. DOI: 10.1088/0741-3335/48/9/001. URL: http://stacks.iop.org/0741-3335/48/i=9/a=001.

[138] E. Fable, C. Angioni, and O. Sauter. "Gyrokinetic calculations of steady-state particle transport in electron internal transport barriers." In: *Plasma Physics and Controlled Fusion* 50.11 (2008), p. 115005. DOI: 10.1088/0741-3335/50/11/115005. URL: http://stacks.iop.org/0741-3335/50/i=11/a=115005.

[139] K. Ida. "Experimental studies of the physical mechanism determining the radial electric field and its radial structure in a toroidal plasma." In: *Plasma Physics and Controlled Fusion* 40.8 (1998), p. 1429. DOI: 10.1088/0741-3335/40/8/002. URL: http://stacks.iop.org/0741-3335/40/i=8/a=002.

[140] C. Chrystal et al. "Calculation of impurity poloidal rotation from measured poloidal asymmetries in the toroidal rotation of a tokamak plasma." In: *Review of Scientific Instruments* 83.10 (2012), p. 10D501. DOI: 10.1063/1.4728097. URL: http://link.aip.org/link/?RSI/83/10D501/1.

[141] O. Sauter and S.Yu. Medvedev. "Tokamak coordinate conventions: COCOS." In: *Computer Physics Communications* 184.2 (2013), pp. 293–302. DOI: http://dx.doi.org/10.1016/j.cpc.2012.09.010. URL: http://www.sciencedirect.com/science/article/pii/S0010465512002962.

[142] O. Sauter. "Notes on $\hat{u}$ and $\hat{\omega}$ using COCOS convention." In: *CRPP private communication* (2012).

[143] T. Vernay et al. "Synergy between ion temperature gradient turbulence and neo-classical processes in global gyrokinetic particle-in-cell simulations." In: *Physics of Plasmas* 19.4 (2012), p. 042301. DOI: 10.1063/1.3699189. URL: http://link.aip.org/link/?PHP/19/042301/1.

[144] M. A. Henderson et al. "Rapid and Localized Electron Internal-Transport-Barrier Formation During Shear Inversion in Fully Noninductive TCV Discharges." In: *Phys. Rev. Lett.* 93 (21 2004), p. 215001. DOI: 10.1103/PhysRevLett.93.215001. URL: http://link.aps.org/doi/10.1103/PhysRevLett.93.215001.

[145] P. H. Rebut, P. P. Lallia, and M. L. Watkins. "The critical temperature gradient model of plasma transport: Applications to JET and future tokamaks." In: *Plasma Physics and Controlled Nuclear Fusion Research* 2 (Proceedings of the 12th International Conference, Nice, 1988,(IAEA, Vienna, 1989)), p. 191.

[146] F. Ryter et al. "Experimental studies of electron transport." In: *Plasma Physics and Controlled Fusion* 43.12A (2001), A323. DOI: 10.1088/0741-3335/43/12A/325. URL: http://stacks.iop.org/0741-3335/43/i=12A/a=325.

[147] R. W. Harvey and M.G. McCoy. "The CQL3D Code." In: *Proc. IAEA TCM on Advances in Sim. and Modeling of Thermonuclear Plasmas,(Montreal)* (1992), pp. 489–526. URL: http://www.compxco.com/cql3d.html.

[148] J. Decker and Y. Pesson. In: *report EUR-CEA-FC-1736, Euratom-CEA* (2004).

[149] O. Sauter et al. "Steady-state fully noninductive operation with electron cyclotron current drive and current profile control in the tokamak à configuration variable (TCV)." In: *Physics of Plasmas* 8.5 (2001), pp. 2199–2207. DOI: 10.1063/1.1355317. URL: http://scitation.aip.org/content/aip/journal/pop/8/5/10.1063/1.1355317.

[150] C. Zucca. "Modeling and control of the current density profile in tokamaks and its relation to electron transport." PhD thesis. EPFL LAUSANNE, 2009. DOI: 10.5075/epfl-thesis-4360.

[151] A. Manini et al. "Role of Te / Ti and ∇v tor in ion heat transport of ASDEX Upgrade H-mode plasmas." In: *Nuclear Fusion* 46.12 (2006), p. 1047. DOI: 10.1088/0029-5515/46/12/007. URL: http://stacks.iop.org/0029-5515/46/i=12/a=007.

[152] S. Nowak et al. "Evidence of Neoclassical Toroidal Viscosity on the Neoclassical Tearing Modes in TCV tokamak." In: *Journal of Physics: Conference Series* 401.1 (2012), p. 012017. DOI: 10.1088/1742-6596/401/1/012017. URL: http://stacks.iop.org/1742-6596/401/i=1/a=012017.

[153] V. S. Udintsev et al. "Global plasma oscillations in electron internal transport barriers in TCV." In: *Plasma Physics and Controlled Fusion* 50.12 (2008), p. 124052. DOI: 10.1088/0741-3335/50/12/124052. URL: http://stacks.iop.org/0741-3335/50/i=12/a=124052.

[154] G. Turri et al. "MHD as trigger of electron temperature oscillations in ECCD discharges in TCV." In: *Plasma Physics and Controlled Fusion* 50.6 (2008), p. 065010. DOI: 10.1088/0741-3335/50/6/065010. URL: http://stacks.iop.org/0741-3335/50/i=6/a=065010.

[155] G. Giruzzi et al. "New Tokamak Plasma Regime with Stationary Temperature Oscillations." In: *Phys. Rev. Lett.* 91 (13 2003), p. 135001. DOI: 10.1103/PhysRevLett.91.135001. URL: http://link.aps.org/doi/10.1103/PhysRevLett.91.135001.

[156] A. Martynov. "Ideal MHD stability of tokamak plasmas with moderate and low aspect ratio." PhD thesis. EPFL LAUSANNE, 2005. DOI: 10.5075/epfl-thesis-3218.

[157] T. Vernay. "Collisions in Global Gyrokinetic Simulations of Tokamak Plasmas using the Delta-f Particle-In-Cell Approach: Neoclassical Physics and Turbulent Transport." PhD thesis. EPFL LAUSANNE, 2013. DOI: 10.5075/epfl-thesis-5638.

[158] X. Lapillonne. "Local and Global Eulerian Gyrokinetic Simulations of Microturbulence in Realistic Geometry with Applications to the TCV Tokamak." PhD thesis. EPFL LAUSANNE, 2010. DOI: 10.5075/epfl-thesis-4684.

[159] R. E. Waltz, G. D. Kerbel, and J. Milovich. "Toroidal gyro-Landau fluid model turbulence simulations in a nonlinear ballooning mode representation with radial modes." In: *Physics of Plasmas* 1.7 (1994), pp. 2229–2244. DOI: 10.1063/1.870934. URL: http://link.aip.org/link/?PHP/1/2229/1.

[160] R. E. Waltz, R. L. Dewar, and X. Garbet. "Theory and simulation of rotational shear stabilization of turbulence." In: *Physics of Plasmas* 5.5 (1998), pp. 1784–1792. DOI: 10.1063/1.872847. URL: http://link.aip.org/link/?PHP/5/1784/1.

[161] A. Bottino. "Modelling of global electrostatic microinstabilities in tokamaks : effects of ExB flow and magnetic shear." PhD thesis. EPFL LAUSANNE, 2004. DOI: 10.5075/epfl-thesis-2938.

[162] R. E. Waltz et al. "A gyro-Landau-fluid transport model." In: *Physics of Plasmas* 4.7 (1997), pp. 2482–2496. DOI: 10.1063/1.872228. URL: http://scitation.aip.org/content/aip/journal/pop/4/7/10.1063/1.872228.

[163] F. Jenko et al. "Electron temperature gradient driven turbulence." In: *Physics of Plasmas* 7.5 (2000), pp. 1904–1910. DOI: 10.1063/1.874014. URL: http://link.aip.org/link/?PHP/7/1904/1.

[164] G. Merlo. In: *Private communication* (2013).

[165] C. Angioni et al. "Theory-based modeling of particle transport in ASDEX Upgrade H-mode plasmas, density peaking, anomalous pinch and collisionality." In: *Physics of Plasmas* 10.8 (2003), pp. 3225–3239. DOI: http://dx.doi.org/10.1063/1.1589009. URL: http://scitation.aip.org/content/aip/journal/pop/10/8/10.1063/1.1589009.

[166] E. Fable, C. Angioni, and O. Sauter. "The role of ion and electron electrostatic turbulence in characterizing stationary particle transport in the core of tokamak plasmas." In: *Plasma Physics and Controlled Fusion* 52.1 (2010), p. 015007. DOI: 10.1088/0741-3335/52/1/015007. URL: http://stacks.iop.org/0741-3335/52/i=1/a=015007.

[167] Y. Camenen et al. "M111A: Poloidal (and toroidal) rotation in TCV." In: *TCV scientific meeting* (2013).

[168] M. Kotschenreuther, G. Rewoldt, and W.M. Tang. "Comparison of initial value and eigenvalue codes for kinetic toroidal plasma instabilities." In: *Computer Physics Communications* 88 (1995), pp. 128–140. DOI: http://dx.doi.org/10.1016/0010-4655(95)00035-E. URL: http://www.sciencedirect.com/science/article/pii/001046559500035E.

[169] D. Wágner et al. "Understanding the core density profile in TCV H-mode plasmas." In: *Plasma Physics and Controlled Fusion* 54.8 (2012), p. 085018. URL: http://stacks.iop.org/0741-3335/54/i=8/a=085018.

[170] P. Ricci et al. "Gyrokinetic linear theory of the entropy mode in a Z pinch." In: *Physics of Plasmas* 13.6 (2006), p. 062102. DOI: 10.1063/1.2205830. URL: http://link.aip.org/link/?PHP/13/062102/1.

[171] J. Kesner. "Interchange modes in a collisional plasma." In: *Physics of Plasmas* 7.10 (2000), pp. 3837–3840. DOI: 10.1063/1.1287915. URL: http://link.aip.org/link/?PHP/7/3837/1.

[172] A. N. Simakov, P. J. Catto, and R. J. Hastie. "Kinetic stability of electrostatic plasma modes in a dipolar magnetic field." In: *Physics of Plasmas* 8.10 (2001), pp. 4414–4426. DOI: 10.1063/1.1399058. URL: http://link.aip.org/link/?PHP/8/4414/1.

[173] A. Fasoli et al. "Electrostatic turbulence and transport in a simple magnetized plasma." In: *Physics of Plasmas* 13.5 (2006), p. 055902. DOI: 10.1063/1.2178773. URL: http://link.aip.org/link/?PHP/13/055902/1.

[174] F. M. Poli et al. "Experimental characterization of drift-interchange instabilities in a simple toroidal plasma." In: *Physics of Plasmas* 13.10 (2006), p. 102104. DOI: 10.1063/1.2356483. URL: http://link.aip.org/link/?PHP/13/102104/1.

[175]   F. M. Poli et al. "Transition from drift to interchange instabilities in an open magnetic field line configuration." In: *Physics of Plasmas* 15.3 (2008), p. 032104. DOI: 10.1063/1.2899303. URL: http://link.aip.org/link/?PHP/15/032104/1.

[176]   I. Furno et al. "Experimental Observation of the Blob-Generation Mechanism from Interchange Waves in a Plasma." In: *Phys. Rev. Lett.* 100 (5 2008), p. 055004. DOI: 10.1103/PhysRevLett.100.055004. URL: http://link.aps.org/doi/10.1103/PhysRevLett.100.055004.

[177]   C. Theiler et al. "The role of the density gradient on intermittent cross-field transport events in a simple magnetized toroidal plasma." In: *Physics of Plasmas* 15.4 (2008), p. 042303. DOI: 10.1063/1.2901188. URL: http://link.aip.org/link/?PHP/15/042303/1.

[178]   L. Federspiel et al. "Observation of a critical pressure gradient for the stabilization of interchange modes in simple magnetized toroidal plasmas." In: *Physics of Plasmas* 16.9 (2009), p. 092501. DOI: 10.1063/1.3204704. URL: http://link.aip.org/link/?PHP/16/092501/1.

[179]   A. Zeiler, J. F. Drake, and B. Rogers. "Nonlinear reduced Braginskii equations with ion thermal dynamics in toroidal plasma." In: *Physics of Plasmas* 4.6 (1997), pp. 2134–2138. DOI: 10.1063/1.872368. URL: http://link.aip.org/link/?PHP/4/2134/1.

[180]   P. Ricci, B. N. Rogers, and S. Brunner. "High- and Low-Confinement Modes in Simple Magnetized Toroidal Plasmas." In: *Phys. Rev. Lett.* 100 (22 2008), p. 225002. DOI: 10.1103/PhysRevLett.100.225002. URL: http://link.aps.org/doi/10.1103/PhysRevLett.100.225002.

[181]   A. E. Glassgold, S. Predrag Krstić, and D. R. Schultz. "$H^+ + H$ Scattering and Ambipolar Diffusion Heating." In: *The Astrophysical Journal* 621.2 (2005), p. 808. DOI: 10.1086/427686. URL: http://stacks.iop.org/0004-637X/621/i=2/a=808.

[182]   L. Federspiel. "Investigation of the excitation threshold for pressure gradient driven instabilities in TORPEX plasmas." In: *EPFL Master's Report (unpublished)* (2008).

[183]   K. Rypdal and S. Ratynskaia. "Fluctuation threshold and profile resilience in weakly ionized plasma in a curved, unsheared magnetic field." In: *Physics of Plasmas* 11.10 (2004), pp. 4623–4633. DOI: 10.1063/1.1785155. URL: http://link.aip.org/link/?PHP/11/4623/1.

[184]   M. Podestà et al. "Plasma production by low-field side injection of electron cyclotron waves in a simple magnetized torus." In: *Plasma Physics and Controlled Fusion* 47.11 (2005), p. 1989. DOI: 10.1088/0741-3335/47/11/008. URL: http://stacks.iop.org/0741-3335/47/i=11/a=008.

[185]   S. H. Müller et al. "Basic turbulence studies on TORPEX and challenges in the theory-experiment comparison." In: *Physics of Plasmas* 12.9 (2005), p. 090906. DOI: 10.1063/1.2034367. URL: http://link.aip.org/link/?PHP/12/090906/1.

[186] J. M. Beall, Y. C. Kim, and E. J. Powers. "Estimation of wavenumber and frequency spectra using fixed probe pairs." In: *Journal of Applied Physics* 53.6 (1982), pp. 3933–3940. DOI: 10.1063/1.331279. URL: http://link.aip.org/link/?JAP/53/3933/1.

[187] N. Iwama and T. Tsukishima. "A correlation method for estimating wave-number spectrum moments of fluctuations." In: *Applied Physics Letters* 31.11 (1977), pp. 783–785. DOI: 10.1063/1.89547.

[188] F. M. Poli, M. Podestà, and A. Fasoli. "A robust method for measurement of fluctuation parallel wavenumber in laboratory plasmas." In: *Review of Scientific Instruments* 80.5 (2009), p. 053501. DOI: 10.1063/1.3125627. URL: http://link.aip.org/link/?RSI/80/053501/1.

[189] F. M. Poli. "Electrostatic instabilities and turbulence in a toroidal magnetized plasma." PhD thesis. EPFL LAUSANNE, 2007. DOI: 10.5075/epfl-thesis-3849.

[190] D. T. Garnier et al. "Stabilization of a low-frequency instability in a dipole plasma." In: *Journal of Plasma Physics* 74 (06 Dec. 2008), pp. 733–740. DOI: 10.1017/S0022377808007071. URL: http://journals.cambridge.org/article-S0022377808007071.

[191] P. W. Terry. "Suppression of turbulence and transport by sheared flow." In: *Rev. Mod. Phys.* 72 (1 2000), pp. 109–165. DOI: 10.1103/RevModPhys.72.109. URL: http://link.aps.org/doi/10.1103/RevModPhys.72.109.

[192] R. K. Janev and J.J. Smith. "Cross sections for collision processes of hydrogen atoms with electrons, protons and multiply charged ions." In: *Supplement to the journal Nuclear Fusion* 4 (1993). DOI: 10.1007/978-3-642-71935-6.

[193] R. K. Janev et al. "Elementary Processes in Hydrogen-Helium Plasmas,Cross Sections and Reaction Rate Coefficients." In: *Springer Series on Atoms and Plasmas* 4 (1987). DOI: 10.1007/978-3-642-71935-6.

[194] R. A. Phaneuf, R.K. Janev, and M.S. Pindzola. "Collisions of Carbon and Oxygen Ions with Electrons, H, H_2 and He." In: *Oak Ridge National Laboratory Report ORNL-6090* Atomic Data for Fusion, Volume 5 (1987).

[195] R. Winston et al. "Nonimaging Optics." In: *Academic Press* (2004).

[196] J. M. Lerner and A. Thevenon. "The Optics of Spectroscopy." In: Section 2: MONOCHROMATORS & SPECTROGRAPHS (2013). URL: http://www.horiba.com/us/en/scientific/products/optics-tutorial/.

[197] Y. Camenen et al. "M111A: An indirect measurement of poloidal rotation in TCV." In: *TCV scientific meeting* (2012).

Acknowledgements-Remerciements

L'achèvement d'une thèse n'est pas seulement un travail individuel, mais se base sur le support d'un grand nombre de personnes sans lesquelles toute cette charge de travail serait insupportable.

Tout d'abord je voudrais remercier la direction du CRPP pour m'avoir permis de faire la thèse au CRPP à la suite de mon travail de Master avec l'équipe de TORPEX. Cette thèse a commencé comme étant complètement expérimentale, mais ensuite elle a nécessité une bonne base théorique, ce qui a impliqué la présence de deux superviseurs, les Dr. Basil Duval et Dr. Olivier Sauter, pour bien mélanger ces deux cotés complémentaires. Je remercie Basil pour m'avoir appris les particularités du système CXRS, pour m'avoir poussé à développer mon esprit critique et très indépendant et aussi pour m'avoir aidé à obtenir toutes mes sessions. Olivier de son coté m'a aidé à comprendre la physique à la base des barrières de transport et à chercher d'interpréter les profils expérimentaux obtenus avec le CXRS. Merci à vous deux pour le support pendant ces années de ma thèse, malgré les difficultés.

I also would like to kindly thanks the experts of my thesis committee: Dr. Yann Camenen, Dr. Rachael McDermott, Dr. Joe Lister and Prof. Olivier Schneider, for carefully reading my thesis manuscript and giving me important suggestions in order to still improve its quality.

Je remercie tous les pilotes (Ugo Siravo, PF Isoz, Yanis Andrèbe, Frédéric Dolizy), PdJ (Stefano Coda, Wouter Vijvers, Holger Reimerdes, Basil, Jean-Marc Moret, Duccio Testa, Roland Behn), les gyrotronistes (Miguel Silva, merci d'être toujours si disponible! et Tim Goodman), les informaticiens (Xavier LLobet, Pierre Etienne et PF), le team de "real-time control" (Bao Le et Federico Felici), les IdJ (Damien Fasel, Albert Perez, Jérémie Dubray et Ugo) et surtout les souvent oubliés DdJ, pour leur travail d'équipe et les discussions pendant mes nombreuses sessions à TCV. Tout le monde sait combien j'ai souffert pour obtenir mes eITBs!

Un merci à tous les techniciens et électriciens qui ont permis le bon fonctionnement du diagnostic CXRS, en particulier Pascal Conti (et son aide pour les calibrations absolues) et Claude Raggi (pour tous les plusieurs supports mécaniques construits).

Un grand merci à tous les membres du "CXRS team": Yanis Andrèbe, Alexander Karpushov, Alessandro Bortolon et Claudio Marini. Merci à Yanis pour sa disponibilité et son travail minutieux, et pour tous les moments passés à aligner ou calibrer les systèmes du CXRS. Thanks to Alexander to start taking care of the CXRS diagnostic during TCV operation after my back problems. You really help me in finally giving me some

---

Un grazie di cuore a tutto il clan Federspiel. In particolar modo al mio fratellone Matteo, per tutti gli anni passati qui insieme a Losanna durante i quali siamo diventati ottimi amici, con caratteri fin troppo simili, capaci di mandarci a quel paese in 2 secondi e poi far subito la pace ☺. Un mega grazie anche alla mia sorellona Sonja per tutti i suoi consigli (anche legali...) ed il suo punto di vista sempre obbiettivo e più deciso! Un abbraccio anche alle new entry della famiglia: i miei cognati Nicoletta ed Ugo e le piccole Sara e Giada, e pure a chi non c'è più come i miei nonni materni Ginetta e Giovanni Pellegrini che hanno sempre creduto in me.

Un bacione ai miei genitori Eliana e Marco che mi hanno lasciato scegliere liberamente la mia strada (professionale e privata): sono sempre stati presenti e mi hanno sostenuto nei momenti difficili della mia vita. È bello tornare a casa e trovare il vostro affetto e soprattutto sapere di poter contare sempre su tutti voi: grazie di esistere!

Un bacio a Silvano Gnesin per la sua amicizia, il suo conforto ed il suo amore durante questi due ultimi anni: non li dimenticherò! E mi raccomando, fai attenzione ai forconi... ☺.

Pour conclure un dernier remerciement un peu particulier à toutes mes Colnago (celle brûlée, celle volée et celles encore avec moi), fidèles amies d'aventures, de montées et de descentes (jusqu'à 74km/h...), de sueur et de joie. Elles ont jouées un rôle très important pour me faire oublier le stress de la thèse et la douleur physique ou mentale. Maintenant un nouveau chapitre de ma vie commence, j'ai vraiment envie de découvrir des nouveaux endroits avec vous et de faire des nouvelles expériences... forza Luciotta pedala!

Un abbraccio forte a tutti quanti!

Lucia

Lucia Federspiel

Engineering physicist EPFL

Av. de Beaulieu 20
1004 Lausanne
✆ *+41 79 373 97 33*
✉ *lucia.federspiel@gmail.com*
Personal situation:
born 26.12.1983
single
Swiss

Strengths

⟹ **Master EPFL in physics**
⟹ **Experienced in spectroscopy, nuclear physics, energy systems**
⟹ **Proven competences in the development and commissioning of new detection systems**

Education

9.2008-6.2014	**PhD in plasma physics at the Centre de Recherches en Physique des Plasmas (CRPP)**, *EPFL*, Lausanne.
2.2008	**Master EPFL in physics engineering**. Specialisation in plasma and nuclear physics, energy systems, biophysics and optics
9.2002-2.2008	**Physics engineering studies at EPFL**.
9.1998-6.2002	**High school diploma with physics, maths & biology options**, *Liceo Lugano 1*, Lugano (TI).

Projects and research experiences

PhD thesis	**Rotation and impurity studies in the presence of MHD activity and Internal Transport Barriers on TCV**.
	→ Improvements of a Charge eXchange diagnostic (CXRS) to determine impurity profiles in a plasma.
	→ Optimisation of optical components, cooling system and software elements. Purchase and installation of new CCD cameras under budget and time constraints. Obtained 8x enhanced Signal/Noise ratio with the new optimized hardware and faster data analysis after implementing new Matlab routines.
	→ Plasma rotation was investigated as an important element in reducing instabilities in fusion plasmas.
	→ Extensive experiments planned and performed on the TCV tokamak, the EPFL's largest experimental facility.
Master thesis	**Investigation of the excitation threshold for pressure gradient driven instabilities in TORPEX plasmas** by installing a low power microwave source and using a two point correlation technique.
Semester project	**Development, construction and calibration of a Mach probe** to study ion flow and blobs propagation with Conditional Average Sampling.
Semester project	**Pixel calibration of a fast frame rate visible camera FASTCAM** with an integrating sphere and identification of the spectral radiance emitted by TORPEX plasmas.

Relevant in-lab activities

Administrator	Responsible for the TCV diagnosticians' schedule (coordinating a team of 25 people involved in TCV daily operation).
Teaching	Assistant in computational physics course: tutoring exercise sessions where students write C++/Matlab code to solve physics problems.
Visitor's guide	Guide for visiting groups at the nuclear site TCV (presentation given in French, English or Italian)

Technical skills

Spectroscopy	Good knowledge in spectroscopy devices and components (monochromators, EMCCD cameras, lasers, optical fibers, lenses, integrating spheres,...), and related installation, calibration and data analysis
Energy & electricity	Broad knowledge in energy systems: nuclear energy, solar energy, fuel cells, heat pumps, hydro and wind power
IT	Matlab, LaTeX, Linux and MS Office environment, basic C++, AutoCAD

Languages

Italian	**Native**	
French	**Fluent C2**	*Bachelor + Master studies in French*
English	**Fluent C1**	*3 months language stay in London (UK)*
German	**Intermediate B1**	*1 month language stay in Sigmaringen (D)*

Extra-curricular activities

Sport | Competitive level cyclist, Volleyball player and swimmer

Humanitarian activities | Member of *Associazione DEDOME amici di don Franck*, *ONG based in Lugano*.
Training in Togo in 2002: support for the installation of the village electrical supply and primary school renovation.

Scientific publications and conference participations

Refereed scientific journals:

L. Federspiel, B. Labit, P. Ricci, A. Fasoli, I. Furno, C. Theiler, Observation of a critical pressure gradient for stabilisation of interchange modes in simple magnetized toroidal plasmas, *Phys. Plasmas*, vol. 16, p. 092501, 2009.

A. Bortolon, Y. Camenen, A.N. Karpushov, B.P. Duval, Y. Andrebe, L. Federspiel, O. Sauter and the TCV team, Indirect measurement of poloidal rotation using inboard-outboard asymmetry of toroidal rotation and comparison with neoclassical predictions, *Nuclear Fusion*, Vol. 53, 2013.

S. Nowak, E. Lazzaro, O. Sauter, G. Canal, B.P. Duval, L. Federspiel, A.N. Karpushov, D. Kim, H. Reimerdes, J. Rossel, D. Wagner and the TCV team, Evidence of neoclassical toroidal viscosity on the neoclassical tearing modes in TCV tokamak, *Joint Varenna-Lausanne International Workshop. Journal of Physics: Conference Series*, vol. 401, p. 012017, 2012.

Y. Camenen, A. Bortolon, B.P. Duval, L. Federspiel and A.G. Peeters et al., Evidence of Momentum Transport Induced by an Up-Down Asymmetric Magnetic Equilibrium in Toroidal Plasmas, *Physical Review Letters*, vol. 105, p. 135003, 2010.

Conference proceedings, refereed by abstract:

L. Federspiel, B.P. Duval, O. Sauter, Y. Andrebe and S. Coda et al., Rotation studies in electron Internal Transport Barriers on TCV, *54th Annual Meeting of the APS Division of Plasma Physics*, Providence, Rhode Island (USA), 2012.

L. Federspiel, B.P. Duval, A.N. Karpushov, Y. Andrebe and F.A.A. Felici et al., CXRS Acquisition Optimisation for Rotation Studies of Fast Events on TCV (Rotation studies in transport barriers on TCV), *38th EPS Conference on Plasma Physics*, poster & paper P2.117, Strasbourg (F), 2011.

L. Federspiel, B. Labit, P. Ricci, A. Fasoli, I. Furno, C. Theiler, Observation of a critical pressure gradient for the stabilization of interchange modes in simple magnetized toroidal plasmas, *Joint Annual Meeting of OPG/SPS/OGAA*, Innsbruck (A), 2009.

O. Sauter, A.N. Karpushov, S. Coda, B.P. Duval and L. Federspiel et al., The IN-mode in the TCV tokamak, *TTF 2013 - U.S. - E.U. Joint Transport Task Force Workshop*, Santa Rosa, California (USA), 2013.

A.N. Karpushov, Y. Andrebe, B.P. Duval, L. Federspiel, Charge exchange recombination spectroscopy measurement of ion temperature, rotation and impurity density profiles on the TCV tokamak, *EPS/ICPP 2012, 39th EPS conference on plasma physics, 16th international congress on plasma physics*, Stockholm (S), 2012.

Y. Martin, E. Fable, C. Angioni, Y. Camenen, D. Wagner, B.P. Duval, L. Federspiel, A. Karpushov, V. Piffl, O. Sauter, H. Weisen and the TCV team, Impurity transport in TCV; neoclassical and turbulent contributions, *23rd IAEA Fusion Energy Conference*, Daejon (Korea), 2010.

O. Sauter, B.P. Duval, L. Federspiel, F. Felici and T.P. Goodman et al., Effects of ECH/ECCD on Tearing Modes in TCV and Link to Rotation Profile, *23rd IAEA Fusion Energy Conference*, Daejon (Korea), 2010.

Y. Camenen, A. Bortolon, B.P. Duval, L. Federspiel and A.G. Peeters et al., Experimental demonstration of an up-down asymmetry effect on intrinsic rotation in the TCV tokamak, *37th EPS conference on plasma physics*, Dublin (Ireland), 2010.